

Developing Viable Catalysts for Ethanol Oxidation Using Electronic Structure Calculations

By

Lida Farsi

A Dissertation submitted to the Faculty of the
Worcester Polytechnic Institute

In partial fulfillment of the requirements for the
Degree of Doctor of Philosophy

in

Chemical Engineering

by

May 2019

APPROVED

Dr. N. Aaron Deskins, Advisor
Chemical Engineering Department, WPI

Dr. Ravindra Datta, Committee Member
Chemical Engineering Department, WPI

Dr. Nikolaos Kazantzis, Committee Member
Chemical Engineering Department, WPI

Dr. Pratap Rao, Committee Member
Mechanical Engineering Department, WPI

Dr. Susan Roberts, Head of Department
Chemical Engineering Department, WPI

Acknowledgments

There have been several people directly or indirectly involved in my research and have made my Ph.D. studies possible. First and foremost I would like to thank my advisor Professor N. Aaron Deskins who accepted me to his research group, guided me throughout my Ph.D. studies and was an understanding and fabulous mentor. I would like to thank Professor Datta, Professor Kazantzis, and Professor Rao who not only served as my Ph.D. committee, but also I had the great opportunity to serve as their teaching assistant and/or take their graduate courses. I would also like to acknowledge my former committee member, Professor Emmert.

I would like to thank Professor Deskins research group, most importantly Satish Kumar Iyemperumal who taught me VASP code when I first started my research at WPI and also provided me with his support and troubleshooting skills during my research at WPI. I also appreciate Satish's useful discussions and guidance on different research topics I conducted at WPI. I also would like to acknowledge my other labmates, Thang Pham, Tao Yan, Yuhan Mei, and Oskar Cheong for their support and useful discussions.

I would like to thank Professor Xiaowei Teng at University of New Hampshire and his research group specifically Guangxing Yang and Daniel Charles who performed experimental work of chapter 4.

I would like to thank Professor Jun Kawai and Koretaka Yuge who accepted me as a visiting scholar to perform research at Material Science Laboratory at Kyoto University. Professor Yuge was also my direct supervisor and mentor at Kyoto University, gave me permission to use his cluster expansion code, GCVC, and also bring it to WPI for future use. I also acknowledge the help of Takeuchi Kazuhito and Tanaka Ryohei at Kyoto University for their support of me to learn and also troubleshoot GCVC.

I would like to acknowledge the help of Sia Najafi, Raffaele Potami, Spencer Pruitt at WPI for their computational support.

I would also like to acknowledge Xsede supercomputing system for computational and also National Science Foundation (NSF), National Science Foundation East Asia and Pacific

Summer Institutes for U.S. Graduate Students (NSF EAPSI) and Japan Society for the Promotion of Science (JSPS) for their financial support.

I would like to acknowledge all faculty, students, and personnel at Chemical Engineering department, who directly or indirectly mentored and/or guided me at WPI. I would also acknowledge all Professors at WPI who taught me different courses during my Ph.D.

I would like to thank Azadeh Zaker for her useful discussions on surface segregation energy, regression models, and other research topics and also her unconditional support during my Ph.D. studies.

My special thanks to my dear friend, Mandana Mirrokni who has always supported me both academically and emotionally, even in the hardest life circumstances.

I would like to thank all my family and friends, specifically my parents Rahim Mehdizadegan Namin and Farzaneh Farsi who provided me in life with everything I ever needed. My unlimited thanks to my sisters Leila Namin, Sima Namin, and Sarah Mehdizadegan for their unconditional love and support during the years.

At the end I would like to dedicate my Ph.D. dissertation to my mom, Farzaneh Farsi, who is my greatest inspiration, valued education a lot, and is the main reason I became the person I am today.

Abstract

Fuel cells enable the conversion of different chemicals directly into electrical energy, and are much more efficient than conventional combustion engines. Direct ethanol fuel cells (DEFCs) use ethanol as a fuel source. However, DEFCs lack an efficient catalyst. In this study, using density functional theory (DFT) we modeled different catalysts, including alloys, to be used for the ethanol oxidation reaction (EOR) in DEFCs. We considered both stability and reactivity of such alloys. We modeled surface segregation energy as an indicator of the alloy's stability under reaction conditions. We modeled bimetallic Pt, Ir, Pd, and Rh alloys and developed a universal model for surface dependent segregation energies in bimetallic alloys. As an indicator of a catalyst's reactivity, we modeled C-C bond breaking in CH_xCO ($x=1,2,3$) as such reactions are the bottleneck of complete oxidation of ethanol. We modeled carbon-carbon bond breaking in transition metals including Pt, Ir, Rh, Au, Ag, alloys including Ir-Rh, Ir-Rh-Sn, metal-metal oxide interfaces including Pt-SnO₂, and Pt-Rh-SnO₂, and metal oxides including Rh₂O₃ and recognized Pt-Rh-SnO₂ to be the most effective catalyst for the C-C bond breaking. Finally we were interested in the design of bimetallic Ir-based alloys. For this purpose, we combined DFT with statistical physics based methods, specifically cluster expansion, to shed light on the ordering tendency of bimetallic Ir-based alloys. We found that Ir-Pt, Ir-Pd, and Ir-Cu tend to phase separate and do not form an alloy compound, while Ir-Rh, Ir-Ni, and Ir-Cr mix well and form an alloy. We also performed Monte Carlo simulations to investigate temperature effects on non-alloying mixtures. We showed as the temperature rises, non-alloys start to mix well and will form a homogeneous mixture, and as a result such mixtures may still be useful for the EOR. Our results show how atomistic modeling can predict stability and activity of potential alloy catalysts.

Table of Contents

Introduction.....	15
Chapter 1: Background.....	17
1.1. Ethanol Oxidation Fuel Cells.....	17
1.2. The Ethanol Oxidation Reaction.....	18
1.2.1. Complete Oxidation.....	19
1.2.2. Partial Oxidation.....	19
1.2.3. Density Functional Theory Modeling of Ethanol Oxidation.....	20
1.4. Catalysts for Ethanol Oxidation.....	22
1.4.1. Pt-based Catalysts.....	22
1.4.2. Pd-based Catalysts:.....	24
1.4.3. Other Catalysts Employed in Direct Ethanol Fuel Cells:.....	24
1.4.4. Why Ir-based Catalysts.....	25
Chapter 2: Methodology.....	27
2.1. Density Functional Theory.....	27
2.1.1. Schrodinger Equation.....	27
2.1.2. Born-Oppenheimer approximation.....	28
2.1.3. The Kohn and Hohenberg theorems.....	29
2.1.4. The Kohn-Sham Equation.....	29
2.1.5. Exchange Correlation Functional.....	30
2.1.6. Pseudopotential.....	31
2.1.7. Wave Function Modeling.....	31
2.1.7.1. Basis Set.....	31
2.1.8. Solving Algorithm.....	32
2.1.9. Periodic Boundary Conditions.....	33
2.2. Cluster Expansion Method.....	34
Chapter 3: Surface Dependent Segregation in Bimetallic Alloys.....	36
3.1. Introduction.....	36
3.2. Methodology.....	37
3.2.1. Simulation Parameters.....	37
3.2.2. Surface Models.....	38
3.2.3. Segregation definition.....	39
3.3. Results and discussion.....	40
3.3.1. Comparison of Segregation on (111) Surfaces.....	40

3.3.2.	Comparison of Segregation in the (111), (100), (110), and (210) Surfaces of Pt.....	42
3.3.3.	Surface Segregation in Pt, Ir, Pd, and Rh.....	44
3.3.4.	Bulk versus Second Layer Segregation.....	46
3.3.5.	Explanation and Analysis of Results.....	47
3.4.	Conclusions.....	51
Chapter 4: Comparison of different Catalysts for C-C Bond Scission in Ethanol Oxidation		53
4.1.	Introduction.....	53
4.2.	Methodology.....	55
4.3.	Results and discussion	62
4.3.1.	Pure Metals: Pt, Ir, Rh, Au, and Ag (111) Surfaces.....	62
4.3.2.	Alloys: Ir, Ir-Rh, Ir-Rh-Sn Alloys	63
4.3.3.	Metal/Metal Oxide Interfaces: Pt, Pt-SnO ₂ , and Pt-Rh-SnO ₂ Catalysts.....	66
4.3.4.	Rh and Rh ₂ O ₃	71
4.3.5.	Comparison of Pure Metals, Alloys, Metal/Metal Oxide Interfaces, and Metal Oxides	72
4.4.	Conclusions.....	74
Chapter 5: Iridium Alloy Structure from DFT and Cluster Expansion.....		75
5.1.	Introduction.....	75
5.2.	Methodology.....	77
5.2.1.	Computational details of First-Principle Calculations	77
5.2.2.	Computational details of Cluster Expansion.....	79
5.3.	Results and discussion	81
5.3.1.	Calculation of Substitution Energy per Atom for Ir-Pt (111) Surfaces	81
5.3.2.	CV Score Minimization:.....	87
5.3.3.	Construction of Formation Energy Diagrams to Find the Most Stable Configurations for Ir-M Alloys	88
5.3.4.	Performing Monte Carlo Simulations for Non-Compound Forming Alloys.....	97
5.4.	Conclusions.....	99
Chapter 6: Conclusions		100
Appendix A: The GCVC (Generalized Cluster-Expansion for Variable and Complex Systems) Code.....		102
Note on different cell sizes for DFT and cluster expansion calculations.....		105
Appendix B: Supporting Information: Surface Dependent Segregation in Bimetallic Alloys.....		107
B.1.	Nature of Metal Slabs	107
B.2.	Calculated Segregation Energies	109
B.3.	Comparison of two different definitions of segregation energy for Ir, Pd, and Rh surfaces....	113

B.4. Models for Predicting Surface Segregation	115
Appendix C: Supporting Information: Comparison of different Catalysts for C-C Bond Scission in Ethanol Oxidation.....	126
C.1. Adsorption of CH_xCO, CH_x, and CO Species on Transition Metals	126
C.2. Reaction modeling of C–C bond breaking at the surface of different Transition Metals	137
C.3. Adsorption of CH_xCO, CH_x, and CO Species on Ir-based Alloys.....	139
C.4. Adsorption of CH_xCO, CH_x, and CO Species on Metal-Metal Oxide Catalysts	143
C.5. Pt-SnO₂ interface model verification.....	153
C.6. CH_xCO C-C bond breaking over Pt, Pt-SnO₂, and three models of Pt-Rh-SnO₂ surfaces is depicted in Figures C.46-C.48:.....	154
C.7. CH_xCO C-C bond breaking over Rh₂O₃.....	158
C.8. CH_x, and CO oxidation over Rh and Rh₂O₃ surfaces	159
References.....	162

Table of Figures:

Figure 1.1. A schematic depiction of a direct ethanol fuel cell. The ethanol oxidation reaction occurs at the anode where ethanol and water react and generate carbon dioxide, protons, and electrons. Protons generated from the ethanol oxidation reaction transfer through the membrane to the cathode side where the oxygen reduction reaction happens. The electrons generated from the ethanol oxidation reaction go through the outer circuit and would be the source of electric current.....	17
Figure 2.1. A schematic of a 6×6 slab with periodic boundary conditions in all three directions. A vacuum layer is shown above and below the slab. The pictures on the left are top views, and the pictures in the middle and on the right are side views. The right pictures show the slab when periodic images are repeated to show neighboring cells.....	34
Figure 2.2. Demonstration of different types of clusters or interactions in a lattice. From left to right: empty, point, pair, triplet, and quadruplet clusters are depicted respectively.	35
Figure 3.1. Slab models used in the present study. For each surface, the left image shows the top view of the surface, while the right image shows the side view of the surface.	38
Figure 3.2. Illustration of different dopant positions within parent metals in slab and bulk structures. Side views of the slabs and bulk are shown.	40
Figure 3.3. Calculated segregation energies of single transition metal atoms within the (111) surfaces of Pt, Pd, Ir, and Rh.	42
Figure 3.4. Segregation energy comparison between the (110), (210), (100), and (111) surfaces of Pt. ...	44
Figure 3.5. Segregation energy comparisons between difference surfaces of Pt, Ir, Pd, and Rh.....	46
Figure 3.6. Calculated segregation energies in a Pt host metal involving sub-surface to surface segregation and also bulk to surface segregation. Segregation energies were calculated with Equations 1 and 2.	47
Figure 3.7. Comparison between segregation energies of various dopants in the (111), (100), (110), and (210) surfaces of Pt obtained with DFT and our developed model.	51
Figure 4.1. Pt, Ir, Au, Ag, and Rh (111) surfaces used in this work.	56
Figure 4.2. Top-view (far left) and side-view (second from left) of the Ir-Rh surface used in this work. Ir and Rh atoms are shown as blue and green spheres respectively. Top-view (second from right) and side-view (far right) of the Ir-Rh-Sn surface. Ir, Rh, and Sn atoms are shown as blue, green, and yellow spheres respectively.	56
Figure 4.3. Top-left: platinum adsorption energy on SnO ₂ , top-right: platinum adsorption energy on SnO ₂ with one oxygen vacancy present on SnO ₂ surface, bottom left: oxygen vacancy formation energy for Pt-SnO ₂ , bottom right: oxygen vacancy formation energy on SnO ₂ surface. For each case, we performed the calculations with and without freezing bottom layer(s) and compared the corresponding energies. In the case of freezing, one bottom layer of SnO ₂ was frozen. According to these results, SnO ₂ with three layers with freezing the bottom layer was implemented in our study.	58
Figure 4.4. Configuration of each model for the DFT calculations: (a) 1 st PtRh-SnO ₂ model, (b) 2 nd PtRh-SnO ₂ model, (c) 3 rd PtRh-SnO ₂ model, (d) Pt-SnO ₂ model, and (e) Pt (111).	59
Figure 4.5. Configuration of a) Rh ₂ O ₃ , top view (left) and side view (right) used in this work, which is a (0001) surface with O exposed. Blue and red spheres denote Rh and O atoms respectively.	60
Figure 4.6. CO adsorption on top, bridge, hcp, and fcc sites of the Ir surface. Ir, C, and O atoms are shown as blue, grey, and red spheres respectively.	61
Figure 4.7. Reaction energy for C-C bond splitting of (a) CHCO, (b) CH ₂ CO, and (c) CH ₃ CO over the Ag, Au, Ir, Rh, and Pt (111) surfaces.....	63
Figure 4.8. CHCO in different geometries and different sites over the Ir-Rh-Sn surface. CHCO was put on different areas including a) Rh atoms, b) Sn atoms, and c) in between those to investigate the effect of the	

area. Ir, Rh, Sn, C, H, and O atoms are shown as blue, green, yellow, grey, white, and red spheres respectively.	65
Figure 4.9. Calculated reaction energy diagram for C-C bond scission of <i>CHCO_{ads}</i> over Ir, Ir-Rh, and Ir-Rh-Sn surfaces. Reactant states are adsorbed intermediates (CHCO), and product states are adsorbed dissociated species (CH/CO). The transition state energy indicates the kinetic barrier for dissociation which is estimated by Bronsted-Evans-Polanyi (BEP) correlations. The reference state (adsorbed reactant) on all surfaces was taken to be 0 eV.	66
Figure 4.10. CH adsorption on Pt-SnO ₂ . Adsorption energies of CH are indicated. CH was placed to interact with Pt (the top), the Pt-SnO ₂ interface (bottom middle), or SnO ₂ (bottom right). To find the best CH adsorption energy on Pt-SnO ₂ , not only we put CH on different areas (metallic surface, oxide, and metal-oxide interface), but also we put CH on different adsorption configurations including hollow and top sites (these adsorption sites are depicted in Figure 4.6). The best adsorption configuration corresponds to the case in which CH is in a hollow site of the (111) facet (the top right configuration).	68
Figure 4.11. Adsorption energies of water on various catalyst surfaces.	69
Figure 4.12. Adsorption energies of *OH on various catalyst surfaces.	70
Figure 4.13. Reaction energy for C-C bond splitting of (a) CHCO, (b) CH ₂ CO, and (c) CH ₃ CO over the Pt (111), Pt-SnO ₂ , and PtRh-SnO ₂ surfaces.	71
Figure 4.14. Reaction energy for C-C bond splitting of (a) CHCO, (b) CH ₂ CO, and (c) CH ₃ CO over the Rh (111) and Rh ₂ O ₃ surfaces. The left, middle, and right pictures corresponds to CHCO, CH ₂ CO, and CH ₃ CO surfaces respectively.	72
Figure 4.15. Reaction energy for C-C bond splitting of (a) CHCO over most stable catalysts in each category: Ir (most reactive catalyst among Ir and Ir alloys), Rh (most reactive catalyst among transition metals), 2 nd model of Pt-Rh-SnO ₂ (most reactive catalyst among Metal/Metal Oxide interface), and Rh ₂ O ₃ (Metal Oxide), (b) CH ₂ CO over most stable catalysts in each category: Rh (most reactive catalyst among transition metals), 2 nd model of Pt-Rh-SnO ₂ (most reactive catalyst among Metal/Metal Oxide interface), and Rh ₂ O ₃ (Metal Oxide), (c) CH ₃ CO over most stable catalysts in each category: Pt (most reactive catalyst among transition metals), 2 nd model of Pt-Rh-SnO ₂ (most reactive catalyst among Metal/Metal Oxide interface), and Rh ₂ O ₃ (Metal Oxide).	74
Figure 5.1. Visual demonstration of Equation (5.1) for calculating substitution energy per atom using Ir-Pt (111) surfaces.	82
Figure 5.2. Ir-Pt (111) alloys modeled with the CP2K code. Three ratios are reported for each geometry. The first and second numbers denote number of Ir and Pt atoms in each layer respectively.	83
Figure 5.3. Ir-Pt (111) alloys modeled with the VASP code. Three ratios are reported for each geometry. The first and second numbers denote number of Ir and Pt atoms in each layer respectively.	85
Figure 5.4. Formation energies for bulk Ir-Pt obtained from cluster expansion (GCVC code) along with half-half composition (one of the most stable structures)	89
Figure 5.5. Formation energy diagram for the bulk Ir-Cr obtained from cluster expansion (GCVC code). In order to construct this formation energy diagram, lattice relaxation has not been performed. This resulted in getting a high CV score (13.8 meV/atom) along with much more negative formation energy compared to literature data. In order to modify this graph, full cell optimization has been performed for DFT calculations and the modified graph is depicted in Figure 5.	92
Figure 5.6. Formation energy diagram (left) and the most stable configuration (right) for the bulk Ir-Rh obtained from cluster expansion (GCVC code).	95
Figure 5.7. Formation energy diagram (left) and most stable configuration (right) for the bulk Ir-Cr obtained from cluster expansion (GCVC code).	95
Figure 5.8. Formation energy diagram (left) along with most stable configuration (right) for the bulk Ir-Ni obtained from cluster expansion (GCVC code).	96

Figure 5.9. Formation energy diagram (left) along with most stable configuration (right) for the bulk Ir-Pd obtained from cluster expansion (GVCV code).....	96
Figure 5.10. Formation energy diagram (left) along with most stable configuration (right) for the bulk Ir-Cu obtained from cluster expansion (GVCV code).	97
Figure 5.11. Monte Carlo simulations for Ir-Pt half-half composition. Increasing temperature enhances alloy mixing.	98
Figure A.1. Procedure of GVCV code (cluster expansion method). The first step is to construct clusters and then to perform DFT calculations. The non-optimized geometries from DFT calculations along with clusters would be used to find basis (correlation) functions. Having basis functions and DFT energies, cross validation (CV) score and then effective cluster interactions (ECIs) would be calculated. Based on these data, energies and geometries corresponding to all possible alloy configurations would be found. After this step, DFT and GVCV energies would be compared. If these values are within the defined accuracy, we are done; otherwise the found ground state configurations would be added to the pool of DFT geometries and the method repeated itself.	104
Figure B.1. Calculated segregation energies within (100) surfaces of Pt, Pd, Ir, and Rh.	110
Figure B.2. Calculated segregation energies within (110) surfaces of Pt, Pd, Ir, and Rh.	111
Figure B.3. Calculated segregation energies within (210) surfaces of Pt, Pd, Ir, and Rh.	112
Figure B.4. Comparison between (111) surfaces of Pt, Pd, Ir, and Rh as hosts. The segregation energies follow this trend: Pt > Rh > Pd > Ir.	112
Figure B.5. Calculated segregation energies from the bulk and sub-surface (second layer) sites. Results are for the (111), (100), (110), and (210) surfaces of Ir as host. Segregation energies were calculated with Equations 1 and 2 in the main text.	113
Figure B.6. Calculated segregation energies from the bulk and sub-surface (second layer) sites. Results are for the (111), (100), (110), and (210) surfaces of Pd as host. Segregation energies were calculated with Equations 1 and 2 in the main text.	114
Figure B.7. Calculated segregation energies from the bulk and sub-surface (second layer) sites. Results are for the (111), (100), (110), and (210) surfaces of Rh as host. Segregation energies were calculated with Equations 1 and 2 in the main text.	115
Figure B.8. Plot of segregation energy of Vanadium (V) as a dopant in (111), (100), (110), and (210) surfaces of Pt along with d-band properties of pure surfaces of Pt (without dopant). a) d-band center and segregation energy, b) d-band filling and segregation energy, and c) d-band width and segregation energy comparison for different surfaces of Pt. As it can be observed, there is not a linear correlation between different surfaces of Pt and d-band properties of the pure surfaces.	116
Figure B.9. Modified Yu et al.'s model segregation data.	116
Figure C.1. CH adsorption on fcc, hcp, bridge, and top sites of Rh (111).....	126
Figure C.2. CH adsorption on fcc, hcp, bridge, and top sites of Au (111).....	126
Figure C.3. CH adsorption on fcc, hcp, bridge, and top sites of Ag (111).....	126
Figure C.4. CH adsorption on fcc, hcp, bridge, and top sites of Pt (111).....	127
Figure C.5. CO adsorption on fcc, hcp, bridge, and top sites of Pt (111).....	127
Figure C.6. CO adsorption on fcc, hcp, bridge, and top sites of Rh (111).....	127
Figure C.7. CO adsorption on fcc, hcp, bridge, and top sites of Au (111).....	127
Figure C.8. CO adsorption on fcc, hcp, bridge, and top sites of Ag (111).....	128
Figure C.9. CH ₂ adsorption on fcc, hcp, bridge, and top sites of Pt (111).....	128
Figure C.10. CH ₂ adsorption on fcc, hcp, bridge, and top sites of Ir (111).....	128
Figure C.11. CH ₂ adsorption on fcc, hcp, bridge, and top sites of Rh (111).....	129
Figure C.12. CH ₂ adsorption on fcc, hcp, bridge, and top sites of Ag (111).....	129
Figure C.13. CH ₂ adsorption on fcc, hcp, bridge, and top sites of Au (111).....	129

Figure C.14. CH ₃ adsorption on fcc, hcp, bridge, and top sites of Ir (111).....	130
Figure C.15. CH ₃ adsorption on fcc, hcp, bridge, and top sites of Rh (111).....	130
Figure C.16. CH ₃ adsorption on fcc, hcp, bridge, and top sites of Au (111).....	130
Figure C.17. CH ₃ adsorption on fcc, hcp, bridge, and top sites of Ag (111).....	130
Figure C.18. CH ₃ adsorption on fcc, hcp, bridge, and top sites of Pt (111).....	131
Figure C.19. CHCO adsorption on Pt (111).....	131
Figure C.20. CHCO adsorption on Ag (111).....	132
Figure C.21. CHCO adsorption on Rh (111).....	132
Figure C.22. CHCO adsorption on Au (111).....	132
Figure C.23. CHCO adsorption on Ir (111).....	133
Figure C.24. CH ₂ CO adsorption on Ir (111).....	133
Figure C.25. CH ₂ CO adsorption on Ag (111).....	133
Figure C.26. CH ₂ CO adsorption on Rh (111).....	134
Figure C.27. CH ₂ CO adsorption on Pt (111).....	134
Figure C.28. CH ₂ CO adsorption on Pt (111).....	134
Figure C.29. CH ₃ CO adsorption on Ir (111).....	134
Figure C.30. CH ₃ CO adsorption on Au (111).....	135
Figure C.31. CH ₃ CO adsorption on Ag (111).....	135
Figure C.32. CH ₃ CO adsorption on Rh (111).....	135
Figure C.33. CH ₃ CO adsorption on Ag (111).....	136
Figure C.34. CH ₃ CO adsorption on Pt (111).....	136
Figure C.35. C-C bond breaking of CHCO, CH ₂ CO, and CH ₃ CO over Ag (111). The adsorption energies are listed below each structure.....	137
Figure C.36. C-C bond breaking of CHCO, CH ₂ CO, and CH ₃ CO over Au (111). The adsorption energies are listed below each structure.....	137
Figure C.37. C-C bond breaking of CHCO, CH ₂ CO, and CH ₃ CO over Ir (111). The adsorption energies are listed below each structure. The adsorption energies are listed below each structure.	138
Figure C.38. C-C bond breaking of CHCO, CH ₂ CO, and CH ₃ CO over Pt (111). The adsorption energies are listed below each structure.....	138
Figure C.39. C-C bond breaking of CHCO, CH ₂ CO, and CH ₃ CO over Rh (111). The adsorption energies are listed below each structure.....	139
Figure C.40. The most stable configuration for adsorption of CH and CO on Ir surface. Ir, C, H, and O atoms are shown in blue, grey, white, and red respectively. a) Top and b) side views of CH adsorption on hcp site of Ir surface. c) Top and d) side views of CO adsorption on top site of Ir surface.....	139
Figure C.41. Top-view (left) and side-view (right) of CHCO adsorption on Ir surface. Ir, C, H, and O atoms are shown in blue, grey, white, and red respectively.....	140
Figure C.42. The most stable configuration for adsorption of CH and CO on Ir-Rh surface. Ir, Rh, C, H, and O atoms are shown in blue, green, grey, white, and red respectively. a) Top and b) side views of CH adsorption on hcp site of Ir-Rh surface. c) Top and d) side views of CO adsorption on hcp site of Ir-Rh surface.....	140
Figure C.43. Top-view (left) and side-view (right) of CHCO adsorption on Ir-Rh surface. Ir, Rh, C, H, and O atoms are shown in blue, green, grey, white, and red respectively.	140
Figure C.44. The most stable configuration for adsorption of CH and CO on Ir-Rh-Sn surface. Ir, Rh, Sn, C, H, and O atoms are shown in blue, green, yellow, grey, white, and red respectively. a) Top and b) side views of CH adsorption on fcc site of Ir-Rh-Sn surface. c) Top and d) side views of CO adsorption on hcp site of Ir-Rh-Sn surface.....	141

Figure C.45. Top-view (left) and side-view (right) of CHCO adsorption on Ir-Rh-Sn surface. Ir, Rh, Sn, C, H, and O atoms are shown in blue, green, yellow, grey, white, and red respectively.	141
Figure C.46. Reaction energy of C-C bond scission of CHCO on various catalyst surfaces: (a) PtRh-SnO2 (1 st model), (b) PtRh-SnO2 (2 nd model), (c) PtRh-SnO2 (3 rd model), (d) Pt-SnO2 and (e) Pt (111). The adsorption energies are listed below each structure.	155
Figure C.47. Structures for C-C bond scission of CH ₂ CO on various catalyst surfaces: (a) PtRh-SnO2 (1 st model), (b) PtRh-SnO2 (2 nd model), (c) PtRh-SnO2 (3 rd model), (d) Pt-SnO2 and (e) Pt (111). The adsorption energies are listed below each structure.	156
Figure C.48. Reaction energy of C-C bond scission of CH ₃ CO on various catalyst surfaces: (a) PtRh-SnO2 (1 st model), (b) PtRh-SnO2 (2 nd model), (c) PtRh-SnO2 (3 rd model), (d) Pt-SnO2 and (e) Pt (111). The adsorption energies are listed below each structure.	157
Figure C.49. Reaction energy of C-C bond scission of CH _x CO (x=1,2,3) on Rh ₂ O ₃ . The adsorption energies are listed below each structure.	158
Figure C.50. Reaction energy of oxidation of CH _x species (x=1,2,3) on Rh. The adsorption energies are listed below each structure.	159
Figure C.51. Oxidation reaction of CH _x species (x=1,2,3) on Rh ₂ O ₃ . The adsorption energies are listed below each structure.	160
Figure C.52. Oxidation reaction of CO species on Rh. The adsorption energies are listed below each structure.	161
Figure C.53. Oxidation reaction of CO species on Rh ₂ O ₃ . The adsorption energies are listed below each structure.	161

Table of Tables:

Table 3.1. Comparison between various models to predict surface segregation and DFT data. In the case of Ruban et al. ¹¹³ and Wang et al. ¹⁰⁹ the models were compared with the DFT data in the original papers, while for Yu et al. ¹¹⁰ and our model our own DFT data was used for comparison.	50
Table 4.1. Calculated reaction energies of C-C bond breaking of CHCO on different alloy surfaces.	66
Table 4.2. Calculated reaction energies (eV) for C-C bond splitting over various catalyst surfaces ($\text{CH}_x\text{CO} \rightarrow \text{CH}_x + \text{CO}$).....	70
Table 5.1. Substitution energy per atom for Ir-Pt (111) surfaces modeled with CP2K code.....	84
Table 5.2. Substitution energy per atom for Ir-Pt (111) surfaces modeled with VASP code	86
Table B.1. Calculated surface energies and timing for the Pt (100) surface using different number of layers in the slab and considering freezing of Pt layers.	107
Table B.2. Calculated surface energies for the Pt (111) surface using different number of layers in the slab and considering different ways of freezing Pt layers.	108
Table B.3. Calculated surface energies for the Pt (110) surface using different number of layers in the slab.	108
Table B.4. Calculated surface energies for the Pt (210) surface using different number of layers in the slab.	108
Table B.5. Calculated segregation energies for the Pt (111) surface considering freezing different number of layers with Ag as a dopant. As it is evident, freezing does not have much effect on the segregation energy values. Since non-freezing needed the least computation time, while giving accurate results, we did not freeze any layer throughout our calculations.	109
Table B.6. Dopant data implemented in Equation 3. d-band width and d-band-filling are taken from Brejnak and Modrak ¹⁴⁹ . Surface energy and ban der Waals radius are taken from Yu et al ¹¹⁰	120
Table B.7. DFT based data for host metals implemented in Equation 3. d-band widths, d-band fillings, and surface energies were calculated with Equations (B.6), (B.7), and (B.8) respectively.	121
Table C.1. CH and CO adsorption energies on different sites of Ir, Ir-Rh, and Ir-Rh-Sn surfaces	139
Table C.2. CHCO adsorption energy on Ir, Ir-Rh, and Ir-Rh-Sn surfaces.....	141
Table C.3. Calculated CHCO adsorption energies in different geometries and different sites over the Ir-Rh-Sn surface. For these calculations, CHCO was put on different areas (including Rh atoms, Sn atoms, and in between those) to investigate the effect of the area. It was observed that the best adsorption energies were obtained when CHCO was put on Rh areas. In each area, CH and CO were adsorbed on different sites to investigate the most favorable geometry. As the adsorption on Sn and near Sn areas were unfavorable, most calculations were done regarding different sites on Rh areas.	142
Table C.4. CH and CO adsorption energies on different areas and different sites of Ir-Rh-Sn surface ...	142
Table C.5. Calculated CO adsorption energies on different sites over Pt (111)	143
Table C.6. Calculated CHCO adsorption energies on different sites over Pt (111).....	143
Table C.7. Calculated CH ₂ adsorption energies on different sites over Pt (111)	143
Table C.8. Calculated CH ₂ CO adsorption energies on different sites over Pt (111).....	143
Table C.9. Calculated CH ₃ CO adsorption energies on different sites over Pt (111).....	144
Table C.10. Calculated CH ₃ adsorption energies on different sites over Pt (111)	144
Table C.11. Calculated CH adsorption energies on different sites over Pt (111)	144
Table C.12. Calculated CH ₂ CO adsorption energies on different sites over Pt-SnO ₂	144
Table C.13. Calculated CH ₂ adsorption energies on different sites over Pt-SnO ₂	145
Table C.14. Calculated CH ₃ CO adsorption energies on different sites over Pt-SnO ₂	145
Table C.15. Calculated CH adsorption energies on different sites over Pt-SnO ₂	145
Table C.16. Calculated CH ₃ adsorption energies on different sites over Pt-SnO ₂	146

Table C.17. Calculated CHCO adsorption energies on different sites over Pt-SnO ₂	146
Table C.18. Calculated CO adsorption energies on different sites over Pt-SnO ₂	146
Table C.19. Calculated CH ₃ CO adsorption energies on different sites over Pt-Rh-SnO ₂ (first model) ..	147
Table C.20. Calculated CH ₃ adsorption energies on different sites over Pt-Rh-SnO ₂ (first model)	147
Table C.21. Calculated CHCO adsorption energies on different sites over Pt-Rh-SnO ₂ (first model)	148
Table C.22. Calculated CH adsorption energies on different sites over Pt-Rh-SnO ₂ (first model)	148
Table C.23. Calculated CO adsorption energies on different sites over Pt-Rh-SnO ₂ (first model)	148
Table C.24. Calculated CH ₂ adsorption energies on different sites over Pt-Rh-SnO ₂ (first model)	148
Table C.25. Calculated CH ₂ CO adsorption energies on different sites over Pt-Rh-SnO ₂ (first model) ..	149
Table C.26. Calculated CH ₃ CO adsorption energies on different sites over Pt-Rh-SnO ₂ (second model)	149
Table C.27. Calculated CH ₃ adsorption energies on different sites over Pt-Rh-SnO ₂ (second model) ...	149
Table C.28. Calculated CH adsorption energies on different sites over Pt-Rh-SnO ₂ (second model)	150
Table C.29. Calculated CH ₂ CO adsorption energies on different sites over Pt-Rh-SnO ₂ (second model)	150
Table C.30. Calculated CH ₂ adsorption energies on different sites over Pt-Rh-SnO ₂ (second model) ...	150
Table C.31. Calculated CHCO adsorption energies on different sites over Pt-Rh-SnO ₂ (second model)	150
Table C.32. Calculated CO adsorption energies on different sites over Pt-Rh-SnO ₂ (second model)	150
Table C.33. Calculated CH ₃ CO adsorption energies on different sites over Pt-Rh-SnO ₂ (third model) .	151
Table C.34. Calculated CH ₃ adsorption energies on different sites over Pt-Rh-SnO ₂ (third model)	151
Table C.35. Calculated CH ₂ CO adsorption energies on different sites over Pt-Rh-SnO ₂ (third model) .	152
Table C.36. Calculated CH ₂ adsorption energies on different sites over Pt-Rh-SnO ₂ (third model)	152
Table C.37. Calculated CH adsorption energies on different sites over Pt-Rh-SnO ₂ (third model)	152
Table C.38. Calculated CO adsorption energies on different sites over Pt-Rh-SnO ₂ (third model)	152
Table C.39. Number of layers' effect on oxygen vacancy formation energy for the Pt-SnO ₂ system.....	153
Table C.40. Number of layers' effect on oxygen vacancy formation energy for SnO ₂ system	153
Table C.41. Number of layers' effect on platinum adsorption energy for Pt-SnO ₂ system	153
Table C.42. Number of layers' effect on platinum adsorption energy for Pt-SnO ₂ system with oxygen vacancy	154
Table C.43. Calculated reaction energies (eV) for oxidation of CH _x and CO species (CH _x + O → CO + xH) and CO + O → CO ₂ . From this table, preferential effect of Rh ₂ O ₃ in oxidation reactions is evident.	161

Introduction

The current main sources of energy production in the world are coal, natural gas, and oil, all of which are fossil fuels. Fossil fuels are finite resources, so there is a need for alternative fuels. The other problem associated with fossil fuels is the pollution they produce. When fossil fuels are combusted, they produce diverse pollutants such as carbon monoxide, carbon dioxide, sulfur dioxide, nitrogen dioxide, and nitric oxide¹. Among these gases, nitrogen- and sulfur-containing species are extremely toxic and detrimental to health. Furthermore, many of these compounds are greenhouse gases and they generate several problems such as global warming and climate change, which in turn cause several problems for life on earth. Furthermore combustion is inefficient and the maximum efficiency taken from it belongs to Carnot cycle which gives efficiency about 35%². Fuel cells are an efficient alternative way of energy production, as they convert the chemical energy of the fuel directly into electricity, achieving very high theoretical efficiencies (~83%)³.

In the present work, we focused on developing catalysts for direct ethanol fuel cells (DEFCs), which utilize ethanol as their feed. Ethanol has several advantages compared to pure hydrogen and methanol, other popular fuel cell feeds^{4,5}. Specifically, ethanol has a higher boiling point compared to pure hydrogen, which makes it a much safer fuel. Furthermore, ethanol is less toxic than methanol and can be produced from biomass, which makes it potentially a renewable fuel type⁶.

A main problem associated with DEFCs is their lack of an efficient anode catalyst for ethanol oxidation. The conventional catalyst used in the fuel cell industry, Pt, is expensive and contributes an estimated 54% of the fuel cell stack cost⁷. Furthermore, in the case of DEFCs, Pt is not efficient in breaking carbon-carbon bonds during the ethanol oxidation reaction, and often leads to products like acetaldehyde⁸⁻¹¹, acetic acid (or acetate)^{8-10, 12-13}, carbon monoxide⁸⁻¹⁰, and carbohydrate (CH_x) fragments¹⁴⁻¹⁵, rather than the desired CO₂ product from full oxidation. One possible solution is to synthesize alloys that may involve cheaper elements, yet could in principle have desired efficiencies.

In this work, using density functional theory (DFT) we modeled different catalysts that could be used in DEFCs. We started our work modeling Pt-based catalysts and then extended our calculations to transition metals and alloys. We addressed both the stability of different alloys, as well as the reactivity of potential catalyst surfaces. For the reaction studies we focused our attention on C-C bond breaking in ethanol over different catalysts, including transition metals (Pt, Ir, Rh, Au, and Ag), alloys (Ir-Rh, Ir-Rh-Sn), and metal/metal oxide interfaces (Pt-SnO₂ and Pt-Rh-SnO₂). The C-C bond breaking is key towards complete oxidation of ethanol. C-C bond breaking in CHCO has reported to be rate determining step in ethanol oxidation reaction^{16,17}.

Our work shows that Ir, Pt, Rh have similar abilities to break C-C bonds, but that C-C bond breaking is much harder for Au and Ag. We also found that support effects can be important, and that an alloy of Pt and Rh supported on SnO₂ can break C-C bonds better than Pt/SnO₂, Pt, or SnO₂. This indicates that Rh and Sn could be useful for increasing the catalytic activity of Pt-based catalysts. We observed that Rh alloyed with Ir would slightly decrease C-C splitting, and Sn and Rh alloyed with Ir would have a detrimental effect for C-C splitting. We also compared the ability of Rh and Rh₂O₃ in breaking the C-C bond and their ability to oxidize intermediates resulting from C-C bond breaking including CH, CH₂, CH₃, and CO to CO₂. Our results show that Rh has a better ability in breaking the C-C bond, while Rh₂O₃ has a superior effect in oxidizing intermediate species resulting from C-C bond breaking to CO₂. We also combined DFT with statistical physics-based methods (cluster expansion) to model and design viable bimetallic Ir alloys. Finally we modeled surface segregation to understand and predict the stability of different alloyed surfaces and facets.

Chapter 1: Background

1.1. Ethanol Oxidation Fuel Cells

A fuel cell is a device, which directly converts the chemical energy of a fuel into electricity, and as a result is much more efficient than conventional heat engines relying on combustion. Several different types of fuel cells exist, including proton exchange membrane fuel cells, direct methanol fuel cells, and direct ethanol fuel cells (DEFCs), which utilize pure hydrogen, methanol, and ethanol as their feeds, respectively. Ethanol has a much higher boiling point compared to pure hydrogen and as a result is much safer. Ethanol is less toxic than methanol, and has a higher energy density compared to hydrogen and methanol⁴⁻⁶. Furthermore, ethanol can be produced from biomass and as a result, DEFCs can be considered a renewable way for energy production⁶. DEFCs have three main components: the anode, cathode, and electrolyte. A schematic of a DEFC is depicted in Figure 1.1.

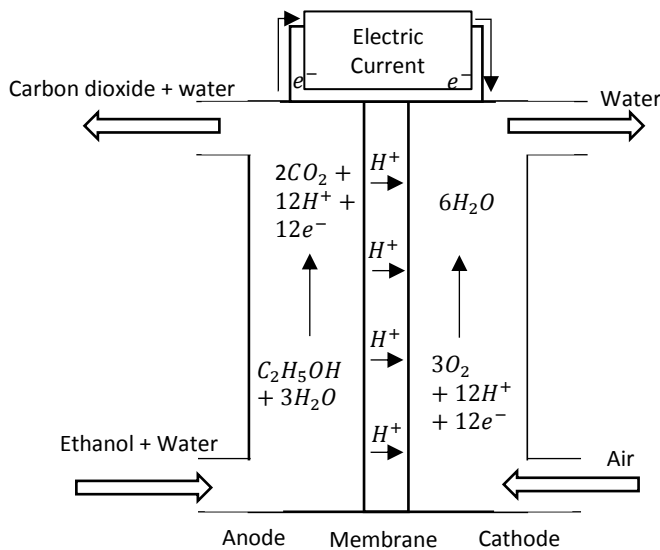
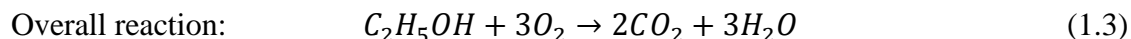
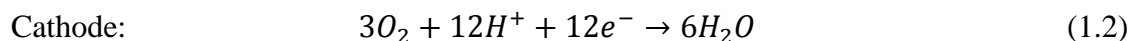
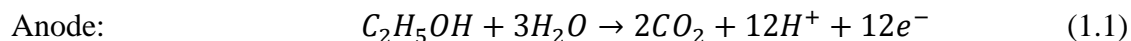


Figure 1.1. A schematic depiction of a direct ethanol fuel cell. The ethanol oxidation reaction occurs at the anode where ethanol and water react and generate carbon dioxide, protons, and electrons. Protons generated from the ethanol oxidation reaction transfer through the membrane to the cathode side where the oxygen reduction reaction happens. The electrons generated from the ethanol oxidation reaction go through the outer circuit and would be the source of electric current.

The overall desired reactions occurring in DEFCs can be summarized as the following:

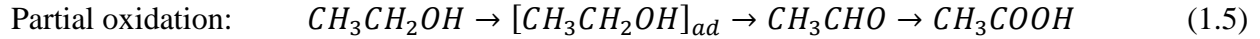
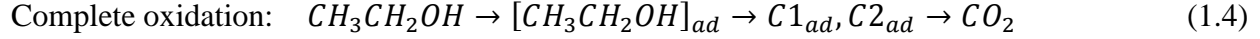


The ethanol oxidation reaction occurs in the anode compartment where in the presence of the catalyst, ethanol ideally oxidizes to produce carbon dioxide, protons, and electrons. The protons pass through the membrane, while electrons flow through the outer circuit. These electrons and protons then arrive at the cathode, where they react on a catalyst surface with the pure oxygen or air to produce water, known as the oxygen reduction reaction. Since ethanol contains only one oxygen atom, water or another oxygen-containing species will react with ethanol to facilitate the carbon dioxide generation. As can be seen in Equation 1.1, in the ethanol oxidation reaction ethanol oxidizes by reaction with water, or adsorbed species generated from water such as OH; therefore, an efficient catalyst should not only facilitate the chemisorption of ethanol, but should also activate the water molecule¹⁸.

1.2. The Ethanol Oxidation Reaction

The ethanol oxidation reaction, which occurs at the anode of a DEFC, has a complex mechanism as well as several side reactions. The ethanol oxidation reaction on the surface of different catalysts such as Pt^{17, 19-21}, Rh²²⁻²⁴, and Pd²⁵⁻²⁹ has been studied in the literature. The exact mechanism of the ethanol oxidation reaction is still being studied^{6, 11, 14, 21, 30-34}. To elucidate this mechanism, the nature of adsorbed intermediates on the catalyst surface has been investigated^{6, 11, 14, 21, 30-34}. For instance, differential electrochemical mass spectroscopy (DEMS), in situ Fourier transform infrared spectroscopy (FTIRS), and electrochemical thermal desorption mass spectroscopy (ECTDMS) techniques have been used to elucidate the ethanol oxidation mechanism^{11, 14, 30-32, 34}.

The ethanol oxidation reaction can occur via two parallel reactions, namely complete and partial oxidation. These reactions are indicated in the following Equations⁶:



Complete oxidation is desired since it produces a full $12 e^-$ per ethanol molecule (Equation 1.1), while partial oxidation is undesired since it produces fewer electrons per ethanol. Ethanol oxidation may involve a number of steps, including C-C breaking and C-H breaking. Souza-Garcia et al³⁵, stated that the first step in the ethanol oxidation reaction is the formation of acetaldehyde from ethanol which involves two electron transfer. The acetaldehyde then further oxidizes to acetic acid with the transfer of two electrons. The authors then argue that the acetic acid is the dominant product in the ethanol oxidation reaction and as a result, in practice, the ethanol oxidation reaction produces much less current density, $4 e^-$ instead of $12e^-$ (see Equation 1.1). The ethanol and acetaldehyde may also be decomposed to produce carbon monoxide and other carbon containing species, which then can lead to the production of carbon dioxide (leading to $12e^-$ produced).

1.2.1. Complete Oxidation

During complete oxidation (see Equation 1.4), the adsorbed ethanol species decomposes to $C1_{ad}$ and $C2_{ad}$ species, which contain one and two carbon atoms, respectively. Some research groups argue the main adsorbed intermediates for complete oxidation are $C1_{ad}$ species^{30,31}, while others argue $C2_{ad}$ are the major ones^{11, 14} Monyoncho et al.³³ emphasized the complexity of the ethanol oxidation reaction and reported that the straightforward reaction network for the ethanol oxidation includes 128 potential C2 and 21 potential C1 intermediates. These species then react to generate carbon dioxide. In order to maximize the production of carbon dioxide and thus to obtain the complete oxidation of ethanol, breaking the carbon-carbon bond in the carbon containing intermediates in the ethanol oxidation reaction is a necessity. To accomplish this goal, the first step is to have a more solid understanding of the nature of intermediates involved in the ethanol oxidation reaction.

1.2.2. Partial Oxidation

During partial oxidation, adsorbed ethanol can produce acetic acid and other carbon containing species rather than carbon dioxide. Because of partial oxidation, carbon dioxide, the main product of ethanol oxidation would not be generated and carbon-carbon bonds in products and intermediates remain intact. Wang et al²¹, showed that in the ethanol oxidation reaction over

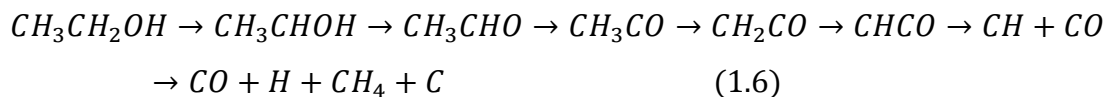
the Pt surface, carbon dioxide and acetic acid are generated from a CH₃CO intermediate, while acetaldehyde forms directly from ethanol. This indicates the importance of the CH₃CO intermediate in the ethanol oxidation reaction. Comparing Equations 1.4 and 1.5 with Equation 1.1 it is evident that complete oxidation of ethanol leads to the production of the main product, carbon dioxide, meaning that partial oxidation of ethanol should be minimized.

1.2.3. Density Functional Theory Modeling of Ethanol Oxidation

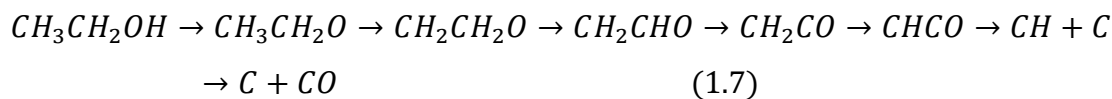
Alcala et al¹⁷. modeled ethanol decomposition on Pt (111) surface and specifically focused on C-C and C-O bond breaking of surface species derived from ethanol and reported that C-C bond breaking proceeds through CHCO. In another study, Alcala et al³⁶. also studied ethanol decomposition on PtSn-based catalysts and realized that the addition of Sn to Pt, prevents the decomposition of ethanol to CO, CH₄, and C₂H₆ species, while it activates dehydrogenation of ethanol to acetaldehyde. Furthermore, PtSn-based catalysts are selective for the conversion of acetic acid to ethanol, acetaldehyde, and ethyl acetate.

Ferrin et al.¹⁶ used Brønsted-Evans-Polanyi (BEP) correlations and scaling relations to minimize the required density functional theory calculations for modeling ethanol decomposition on ten transition metals. BEP correlations estimate the reaction barriers based on the reaction energy, and scaling relations predict the adsorption energy of complex adsorbates based on simple adsorbates. Ferrin et al.¹⁶ reported that C-C bond breaking in CH_xCO is the key process in ethanol oxidation reaction.

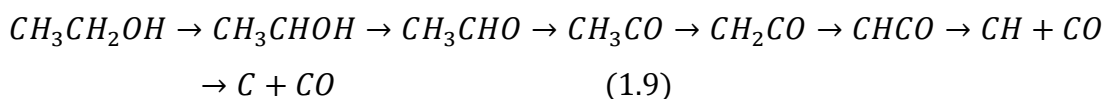
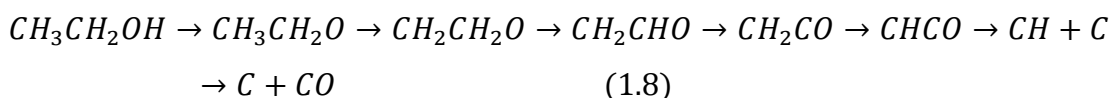
Li et al.³⁷ studied the ethanol decomposition on a Pd (111) surface and proposed the following reaction path for the ethanol decomposition:



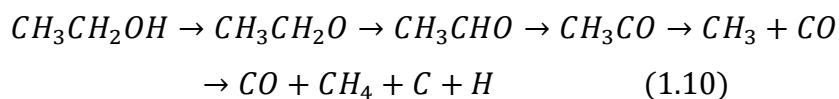
Li et al.³⁸ also proposed the following reaction pathway for the ethanol decomposition on Rh (111) surface with dehydrogenation of CH₃CH₂O being the rate determining step:



Choi et al.³⁹ used periodic density functional theory and kinetic Monte Carlo simulations to elucidate the ethanol decomposition on the Rh (111) surface. They proposed two reaction pathways for ethanol decomposition, the first through a CH₃CH₂O intermediate (similar to Li et al.³⁸. model for the ethanol decomposition on Rh (111)) and the second through a CH₃CHOH intermediate (similar to Li et al.³⁷. model for the ethanol decomposition on Pd (111)). They further explained that the first reaction involves the slow formation of CH₂CH₂O, which leads to the CHCO formation, a potential precursor for C-C bond cleavage. They emphasized that the dominant reaction mechanism is the first one and that both reactions could eventually produce C and CO. These reaction mechanisms can be written as the following³⁹:



Similarly Guo et al.⁴⁰ investigated ethanol decomposition on Pd (110) surface using periodic density functional theory calculations. They also proposed that ethanol decomposition occurs via CH₃CH₂O formation. Unlike Choi et al.³⁹ and Li et al.³⁸ who reported dehydrogenation happens through a CH bond in the CH₃ moiety of CH₃CH₂O, Guo et al.⁴⁰ stated that in the case of Pd (110), dehydrogenation occurs through a CH bond of the CH₂O moiety of CH₃CH₂O. In other words, they proposed the following mechanism for ethanol decomposition on Pd (110)⁴⁰:



They emphasized the fact that the first dehydrogenation step in the above reaction is the rate-limiting step and that there is no C-O bond scission involved in the above-mentioned mechanism.

Wu et al.⁴¹ stated that the key to obtain the transfer of 12-electrons and achieve complete oxidation is the competitive cleavage of C-C and C-H bonds in the ethanol oxidation reaction. They therefore considered CHCO, CH₂CO, and CH₃CO as important intermediates in the ethanol oxidation reaction and investigated C-C and C-H bond breaking of these species on the Cu (100) surface. They reported that the easiest C-C bond breaking among CH_xCO (x=1,2,3) species belongs to CH₂CO, while the hardest C-H bond breaking also belongs to CH₂CO, both with 1.02

eV activation barrier. The same research group also used the same rational to calculate reaction energies and activation barriers of C-C and C-H bond scission of CH_xCO ($x=1,2,3$) species over the Cu_2O (111) surface.⁴²

1.4. Catalysts for Ethanol Oxidation

1.4.1. Pt-based Catalysts

It is well established that when a molecule adsorbs on a surface of a heterogeneous catalyst, it can interact with many possible bonding sites.⁴³ For that matter, the catalyst surface and specifically the catalyst surface area is an important attribute for an efficient catalyst.⁴⁴ To increase the surface area, the active phase of a catalyst is usually dispersed on a conductive support, such as carbon.⁴⁴ Carbon-supported Pt is the most widely used catalyst in the fuel cell industry. However, carbon-supported Pt is far from being the most efficient catalyst for DEFCs, because of lack of its ability in breaking the C-C bond in the ethanol oxidation reaction.

To resolve this problem, alloying Pt with other transition metals or the addition of cocatalysts such as Ru and Sn to Pt have been investigated in the literature⁶. The most investigated alloy catalysts for the anode in DEFCs are binary Pt-Ru, Pt-Sn, and ternary Pt-Ru-based, Pt-Sn-based catalysts.⁶ The superior catalytic activity of these electrocatalysts compared to pure Pt is attributed to the bifunctional effect^{45,46} or the intrinsic mechanism effect (electronic model).^{45,47,48} According to the bifunctional effect – also known as a promoted mechanism – Ru or Sn will provide additional oxygen containing species, especially because these species will be easily oxidized at the catalyst surface. Some of the intermediates from the ethanol oxidation reaction would block the catalyst surface and would poison the catalyst; these oxygen containing species will then react with such intermediates and as a result, the complete oxidation of ethanol will be facilitated by the help of Ru or Sn.⁶ According to the intrinsic mechanism effect (electronic model), the second metal (for instance Ru or Sn) will modify the electronic structure of the pure noble metal (for example Pt) and as a result will modify the adsorption of the oxygen-containing species.^{6,49}

Zhou et al.⁵⁰ synthesized carbon supported Pt, Pt-Rh, and Pt-Sn catalysts with different atomic ratios and observed that Pt-Rh and Pt-Sn are more efficient in breaking the carbon-carbon bond in DEFCs. They emphasized the importance of using the right amount of Sn in Pt-Sn catalysts in order to have an efficient catalyst. In another study,⁵¹ Zhou et al. used the experimental method

developed by Wang et al.⁵² to synthesize carbon-supported Pt, Pt bi-metallic and tri-metallic catalysts such as Pt-Pd/C, Pt-Ru/C, Pt-Sn/C, Pt-W/C, Pt-Ru-W/C, and Pt-Ru-Mo/C. They showed that the activity of Pt towards electro-oxidation of ethanol increases with the addition of a second element to Pt in the following order: Pt₁Sn₁/C > Pt₁Ru₁/C > Pt₁W₁/C > Pt₁Pd₁/C > Pt/C. Furthermore, the Pt-Ru catalysts modified by W and Mo have shown to display superior electro-oxidation of ethanol while their DEFC performance is inferior compared to Pt-Sn catalysts.

Vigier et al.⁵³ synthesized and compared the activity of Pt, Pt-Re, and Pt-Sn catalysts. They reported that Pt-Sn is the most active catalyst towards electro-oxidation of ethanol among the three catalysts they studied. They also showed that the alloy composition is an important factor in determination of the alloy's activity. Lamy et al.⁵⁴ developed Pt-Sn catalysts and noticed superior electrocatalytic activity of Pt-Sn compared to pure Pt. They also realized these alloys have improved tolerance towards CO poisoning. The drawback of these catalysts however, is the fact that in the presence of these catalysts, C₂ species would still be generated. In other words, the complete oxidation of ethanol would not be achieved. To resolve this issue, one possible solution is to alloy Pt-Sn catalysts with a third element.

Riberio et al.⁵⁵ synthesized binary and ternary Pt-based catalysts. They specifically introduced Sn and Ir to Pt electrocatalysts and emphasized that Pt-Sn and Pt-Ir-Sn catalysts are superior for electrooxidation of ethanol compared to the pure Pt. This activation is mainly because Sn and Ir can adsorb OH species much better compared with Pt. OH species are important because they are necessary for the oxidation of adsorbed intermediates, specifically CH_x and CO to CO₂. In other words, Sn and Ir species would facilitate the complete oxidation of ethanol. Calegaro et al.⁵⁶ incorporated Ru oxide and Ir oxide into a carbon supported Pt catalyst. They showed Pt-RuO₂ catalysts have improved catalytic activity in the ethanol oxidation reaction compared with Pt and Pt-Ru. They also reported that Pt-RuO₂-IrO₂ possessed even better catalyst activity in the EOR. Zhang et al.⁵⁷ prepared Pt_x-WO₃/C catalysts and showed that these catalysts have superior catalytic activity in the EOR compared to Pt and also emphasized that this activity increases when the amount of utilized WO₃ increases.

In a review paper, Ermete Antolini⁶ summarized the research performed to develop catalysts for direct ethanol fuel cells. After considering all possible catalysts, Antolini concluded that Pt-Sn and Pt-Ru based catalysts are the most established catalysts for the EOR. He explained specifically for the anode reaction in direct ethanol fuel cells Pt-Sn catalyst is preferred. Ternary

Pt-Ru-based catalysts are always better than Pt-Ru, but whether or not they are superior than Pt-Sn is still unclear in the catalysis community.⁵⁸⁻⁶⁰ He also expressed that ternary Pt-Sn-based catalysts would always show better electrocatalytic activity compared with Pt-Sn in the EOR.⁶¹⁻⁶³

1.4.2. Pd-based Catalysts:

Pd as a member of the Pt group metals has also been investigated as a potential anode catalyst, especially in alkaline media. Ha et al.⁶⁴ synthesized Pd on carbon supported catalysts and compared their performance to the unsupported Pd catalyst in direct formic acid fuel cells. They reported that supported Pd/C shows less deactivation of the catalyst at high formic acid concentration. Chen et al.⁶⁵ considered the use of Pd and Pd-Ru catalysts in alkaline direct ethanol fuel cells. They stated that although Pd activity in acidic media is very low, in the alkaline media it possesses high catalytic activity. They prepared Pd/C and Pd-Ru/C catalysts and reported that Pd-Ru/C is extremely active in the ethanol oxidation reaction. In fact, Pd-Ru/C not only has higher catalytic activity compared with Pd/C, but also is almost four times more active than Pt-Ru/C (one of the best catalysts for ethanol oxidation reaction).

He et al.⁶⁶ synthesized Pd-Au and Pd-Sn-alloyed nanoparticles and compared their activity to conventional Pt/C catalysts for ethanol oxidation in alkaline fuel cells. They found that the commercial Pt/C had better kinetics for the ethanol oxidation reaction. However, they argued that in spite of more sluggish reaction kinetics of Pd-based catalysts, they are more tolerant towards poisoning and as a result are promising candidates for the electro-oxidation of ethanol in alkaline media. Among synthesized catalysts in this study⁶⁶, Pd-Au alloy catalyst had the highest activity towards ethanol oxidation. Nguyen et al.⁶⁷ prepared Pd/C and Pd-Ag/C alloyed nanoparticles and concluded that Pd-Ag/C alloyed nanoparticles have excellent catalytic activity, more CO tolerance, and higher stability compared to Pd/C and Pt/C catalysts which makes them potential candidates for ethanol oxidation in alkaline direct alcohol fuel cells.

1.4.3. Other Catalysts Employed in Direct Ethanol Fuel Cells:

Most research on anode electrocatalysts for DEFCs has been devoted to Pt-based catalysts and studies involving other catalysts are still in their early stages. The application of Rh as an anode catalyst was investigated by de Souza et al.⁶⁸ They reported that Rh is not an active catalyst for ethanol oxidation compared to Pt and that in fact Rh has a low reaction rate. De Souza et al.⁶⁸

attributed this low reaction rate to the low efficiency of Rh electrodes for the dehydrogenation reaction. They also investigated the effect of adding Rh to Pt and they realized the amount of Rh and Pt being used in electrode, affects the catalytic activity towards electrooxidation of ethanol. For instance, they reported that pure Pt and Pt₉₀Rh₁₀ have the same present normalized current density, while Pt₇₃Rh₂₇ possesses better CO₂ yield than pure Pt and therefore as the Rh/Pt ratio increases, the CO₂ production increases while acetaldehyde production decreases. This means adding Rh to Pt increases the selectivity toward the complete oxidation of ethanol. However, it does not decrease the barrier for the CO oxidation significantly.⁶⁸

1.4.4. Why Ir-based Catalysts

Pt group metals (PGMs) are well known for their good catalytic activity and therefore a large amount of studies have been devoted to the application of PGMs in the ethanol oxidation reaction. For instance, experimental or theoretical studies regarding Pt^{51, 69}, Rh⁶⁸, Ru⁷⁰, and Pd⁷¹ can be found in the literature. Riberio et al.⁵⁵ investigated the use of Ir as an additive to Pt/C and PtSn/C catalysts and reported that Ir will increase the electrocatalytic performance of these catalysts for the ethanol oxidation reaction. Calegaro et al.⁵⁶ observed that the addition of IrO₂ to Pt/C and PtRu/C catalysts would shift the onset potential of the ethanol oxidation reaction to less positive values. Cao et al.⁷² investigated the electrocatalytic activity of Ir-based catalysts towards the ethanol oxidation reaction and observed that the overall performance of Ir₃Sn/C is comparable to that of Pt₃Sn/C indicating that Ir-based catalysts are promising alternatives for the ethanol oxidation reaction. Du et al.⁷³ used experimental and theoretical tools and have shown that Ir-Sn-SnO₂/C catalysts possess high electrocatalytic activity for the ethanol oxidation reaction compared to Pt-Sn/C. The same research group⁷⁴ also considered the addition of Ir to Ru and observed that Ir-Ru/C catalyst has shown superior catalytic activity for the ethanol oxidation reaction compared to Ir/C and Pt/C catalysts. Their theoretical studies reveal that Ir-Ru alloys are preferable compared to Ir for the ethanol oxidation reaction.⁷⁴ Du et al.⁷⁴ also reported an increase in CO tolerance by Ir-Ru alloys compared with Pt. These studies encouraged us to investigate the effect of Ir and Ir alloys in the ethanol oxidation reaction, as they seem to be promising alternatives for the ethanol oxidation reaction in direct ethanol fuel cells.

In order to understand the macroscopic properties of the catalyst and to synthesize them experimentally, having a good understanding of the atomic-scale, microscopic properties of the

catalyst is necessary. This knowledge can be obtained via electronic structure calculations such as density functional theory (DFT). A discussion of DFT and its algorithms will be discussed in the next chapter.

Chapter 2: Methodology

2.1. Density Functional Theory

Density functional theory has been the most widely used method in condensed matter physics, computational chemistry, and quantum mechanics to describe the properties of bulk materials, surfaces, and nanoparticles. One excellent textbook on density functional theory (DFT) is “Density Functional Theory: A Practical Introduction” by Sholl and Steckel⁷⁵. In this section the DFT method is explained.

2.1.1. Schrodinger Equation

Density functional theory (DFT) is a computational chemistry method which tries to find the electronic structure of many-body systems such as atoms and molecules. Electronic structure theory deals with quantum states of electrons and it describes the forces and energies of electrons around nuclei.⁷⁶ In fact, the aim of DFT is to solve the most basic and important equation in quantum mechanics, the Schrodinger equation. The time-independent, non-relativistic Schrodinger Equation can be expressed as follows:

$$H_{op}\psi = E\psi \quad (2.1)$$

In this Equation H_{op} is the Hamiltonian operator which is associated with the system energy. ψ is a wavefunction, or eigenfunction for the Hamiltonian operator. The wavefunction, ψ , has an eigenvalue, E , associated with it which satisfies the eigenvalue equation. In quantum mechanics, a particle is characterized by ψ , the wavefunction, which contains information about the position and properties of the particle at time t ⁷⁷. To characterize a particle, it is necessary to solve the Schrodinger Equation and find the wavefunction. Substituting the full Hamiltonian in the above Equation and rewriting the Schrodinger Equation gives:

$$\left[-\frac{\hbar^2}{2m}\sum_{i=1}^N\nabla_i^2 + \sum_{i=1}^N V(r_i) + \sum_{i=1}^N\sum_{j<i} U(r_i, r_j)\right]\psi = E\psi \quad (2.2)$$

In this Equation m is the electron mass. $-\frac{\hbar^2}{2m}\sum_{i=1}^N\nabla_i^2$ is the kinetic energy of all the electrons. $\sum_{i=1}^N V(r_i)$ is the electrostatic energy between different electrons and atomic nuclei, and $\sum_{i=1}^N\sum_{j<i} U(r_i, r_j)$ is the electrostatic energy between electrons. ψ is the electronic wave function which is a function of the spatial coordinates of the N electrons that is $\psi = \psi(r_1, r_2, \dots, r_N)$ and E is the ground-state energy of the electrons. The wave function is a function of each of the

coordinates of all N electrons. However, an approximation named the Hartree product considers the wave function as a product of individual electron wave functions that is:

$$\psi = \psi_1(r)\psi_2(r), \dots, \psi_N(r) \quad (2.3)$$

It should be noted that the number of electrons, N, is usually considerably larger than the number of nuclei, M, as each atom has one nucleus and many electrons.

The wave function cannot be measured directly and the quantity which in principle can be measured directly is the probability of N electrons in a particular set of coordinates, r_1, \dots, r_N . This probability (p) can be written as follows:

$$p = \psi(r_1, r_2, \dots, r_N) \times \psi^*(r_1, r_2, \dots, r_N) \quad (2.4)$$

In the above equation the asterisk indicates the complex conjugate. A quantity analogous to the probability is the density of electrons at a position in space, $n(r)$, which can be written in terms of the individual electron wave functions as follows:

$$n(r) = \sum_i \psi_i(r) \times \psi_i^*(r) \quad (2.5)$$

In the above equation, the summation is over all the individual electron wave functions, which are occupied by electrons, so the term inside the summation is the probability that an electron is located at position r . Solving the Schrodinger equation to determine the system energy and wave function is not always straight forward, which is why we have methods like density functional theory.

2.1.2. Born-Oppenheimer approximation

To define the position of an atom, it is necessary to know where the nucleus and the electrons of an atom are. An important fact in quantum mechanics is that the atomic nuclei are much heavier than electrons ($m_{proton\ or\ neutron} \approx 1800\ m_{electron}$). This means that electrons respond more rapidly to the changes in their environment than the nucleus. The Born-Oppenheimer approximation is based on this fact and it assumes that the motion of electrons and the nuclei can be separated. Furthermore, the kinetic energy of the nucleus can be neglected as it is much heavier than the electrons. It assumes that the electrons are moving around the nuclei as quantum particles; the motion of the nucleus can be assumed to be governed by classical mechanics rather than quantum mechanics. For a set of electrons moving around a fixed set of nuclei, the lowest energy state of the electrons is defined as the ground state energy.

2.1.3. The Kohn and Hohenberg theorems

The aim of DFT is to find the energy of a collection of atoms and electrons. DFT relies on two fundamental theorems developed by Kohn and Hohenberg, named the first and the second Kohn and Hohenberg theorems. The first theorem states that *the ground-state energy from Schrodinger's Equation is a unique functional of the electron density*. This means that there is a direct correspondence between the electron wave function/electron density and the most stable configuration of the electrons. A functional is a mathematical operator which takes a function as an input and returns a value as an output. Mathematically the first Hohenberg-Kohn Equation can be summarized as:

$$E = E[n(r)] \quad (2.6)$$

The ground state energy is a functional which relies on $n(r)$, the electron density. It means that the ground-state electron density uniquely determines the energy and the wave function in the ground state.

The second Hohenberg-Kohn theorem states that the electron density that minimizes the energy of the overall functional is the true electron density corresponding to the full solution of the Schrodinger Equation, assuming we have the true exchange correlation functional (discussed later). This means that finding the ground state energy becomes a minimization problem.

2.1.4. The Kohn-Sham Equation

Kohn and Sham showed in order to find the right electron density, instead of solving the full Schrodinger Equation, one can solve a set of equations in which each equation involves just a single electron. In other words, the solution of the Kohn-Sham equations are single electron wavefunctions, $\psi_i(r)$, which depend merely on three spatial variables (x, y and z for the one electron). The Kohn-Sham equations have the following form:

$$\left[-\frac{\hbar^2}{2m} \nabla^2 + V(r) + V_H(r) + V_{XC}(r) \right] \psi_i(r) = \varepsilon_i \psi_i(r) \quad (2.7)$$

Three potentials in the above Equation V , V_H , V_{XC} represent interactions between an electron and the collection of atomic nuclei, the Hartree potential (electron-electron interactions), and exchange and correlation contribution to the single electron Equations, respectively. These potentials all depend on the electron density. The Hartree potential can be defined as follows:

$$V_H(r) = e^2 \int \frac{n(r')}{|r-r'|} d^3r' \quad (2.8)$$

This potential defines the repulsive electrostatic interaction between the electron being considered in one of the Kohn-Sham Equation and the total electron density defined by all the electrons in the system. This potential includes the interaction of the one electron with itself, the so called self-interaction phenomena which is unphysical and its correction is included in the exchange and correlation potential, V_{XC} . V_{XC} can be defined as a “functional derivative” of the exchange-correlation energy:

$$V_{XC} = \frac{\delta E_{XC}(r)}{\delta n(r)} \quad (2.9)$$

2.1.5. Exchange Correlation Functional

Kohn-Sham approach is built upon two assumptions⁷⁸: 1) The exact ground state density can be represented by the ground state density of an auxiliary fictitious system of non-interacting particles that generate the same density as any given system of interacting particles⁷⁹⁻⁸⁰. 2) The auxiliary Hamiltonian is chosen to have the usual kinetic operator and an effective local potential acting on an electron of spin σ at point \mathbf{r} . The exchange correlation functional corrects for any assumptions and as a result can be considered a correction term. The functional described by Hohenberg-Kohn theorem can be written in terms of the single-electron wave functions, ψ_i , which define the electron density, $n(\mathbf{r})$. The energy functional can be written as:

$$E[\{\psi_i\}] = E_{known}[\{\psi_i\}] + E_{XC}[\{\psi_i\}] \quad (2.10)$$

In the above Equation, the energy functional is divided into two parts, the known energy part and exchange correlation functional. The known part can be written as follows:

$$E_{known}[\{\psi_i\}] = -\frac{\hbar^2}{2m} \sum_i \int \psi_i^* \nabla_i^2 \psi_i d^3r + \int V(r)n(r)d^3r + \frac{e^2}{2} \int \int \frac{n(r)n(r')}{|r-r'|} d^3r d^3r' + E_{ion} \quad (2.11)$$

The terms in the right of the equation represent electronic kinetic energies, the electrostatic interactions between the electrons and the nuclei, the electrostatic interactions between pairs of electrons, and the electrostatic interactions between pairs of nuclei.

2.1.6. Pseudopotential

Pseudopotentials are a way of representing the interactions between the core and valence electrons. The core electrons are not typically represented by wave functions while valence electrons are. This is done to save computational time. The pseudopotential mimics the presence of the core electrons by a fixed potential. By using a pseudopotential, the number of wave functions required to be found and the number of electrons represented by the wave functions decreases, which makes computations faster.

2.1.7. Wave Function Modeling

Finding a wave function is a mathematical problem and there must be a way to define the wave functions for computational implementation. Such implementation should give accurate results while taking reasonable amount of time.

2.1.7.1. Basis Set

A basis set is a set of functions, ϕ_i , which are used to represent a wave function. The basis set does not fully represent the exact wavefunction, but a close approximation. The wave function is a linear combination of these basis sets:

$$\psi_i = \sum_i \mu_i \phi_i \quad (2.12)$$

As the basis sets in the above equation are known, if the coefficients, μ_i , be found, the wave function will be defined completely. The more basis sets used in the above equation, the more accurate the wave function will be but will require more computational time. An early implementation of the basis set was composed of atomic orbitals (AO) and this technique was called the linear combination of atomic orbitals (LCAO). The linear combination of atomic orbitals will form molecular orbitals. An atomic orbital is a wave function which represents only one electron in an atom and Slater type orbitals (STO's) can be used as basis set functions because of the similarities which they have with the atomic orbitals of hydrogen-like atoms. STO's can be shown mathematically with the following Equation:

$$\phi_i(\zeta, n, l, m, r, \theta, \phi) = Nr^{n-1}e^{-\zeta r}Y_{lm}(\theta, \phi) \quad (2.13)$$

In the above Equation, N is a normalization constant; r, θ , ϕ are spherical coordinates of the electron; Y_{lm} is the angular momentum part usually using spherical harmonic functions which

describe the shape of the wave function; and finally n , l , m are principal, angular, and magnetic quantum numbers respectively.

STO's are not usually computationally efficient, so Gaussian functions are often used instead to represent atoms and molecules. These functions are easier to work with mathematically. The general form of a Gaussian type orbital (GTO) can be written as follows:

$$g(\alpha, l, m, n, x, y, z) = N e^{-\alpha r^2} x^l y^m z^n \quad (2.14)$$

In the above Equation, N is a normalization constant, α is the “exponent”, x , y , and z are Cartesian coordinates, and l , m , and n are integral exponents which are fitted so that the orbital represents a real one. Another kind of basis set are plane waves, which are used for periodic systems such as solids or liquids. A plane waves basis set requires a good pseudopotential since the core region of an atom is not typically represented by the plane waves. A wave function which uses plane waves as basis set can be written mathematically as follows:

$$\psi_i(\mathbf{r}) = \sum_{\mathbf{G}} c_i \mathbf{G} e^{i(\mathbf{k}+\mathbf{G})\cdot\mathbf{r}} \quad (2.15)$$

In the above Equation, \mathbf{G} is the reciprocal lattice vector and c_i are coefficients to be found. Just as we define positions in real space in terms of lattice vectors, we define three vectors in reciprocal space in terms of vectors in real space. Larger lattice vectors in real space correspond to shorter lattice vectors in reciprocal space. For more information about reciprocal lattice vector please see DFT or solid state physics books^{75,81}. Another method, a hybrid Gaussian and plane wave (GPW) method⁸² utilizes both Gaussian and plane wave functions, such as with the CP2K code⁸²⁻⁸⁶.

2.1.8. Solving Algorithm

Performing a density functional theory calculation is equivalent to solving the Kohn-Sham Equations for a particular atomic configuration. However, this is not always straight forward, since there are two sets of unknowns, namely electron density and wavefunctions. The potentials in the Hamiltonian operator depend on the electron density (a function of the wave function), which in turn determines what the wave function is. Due to this circular nature, an iterative solution must be performed to find the correct density/wave function. To solve the Kohn-Sham equations, one of these variables has to be guessed and the other one is calculated by means of Kohn-Sham Equations. This procedure can be expressed by the following steps:

1. Guess the initial electron density, $n(\mathbf{r})$, and calculate the various potentials in the Hamiltonian operator.
2. Solve the Kohn-Sham Equation based on the trial electron density to find the wave function, $\psi_i(\mathbf{r})$.

$$\left[-\frac{\hbar^2}{2m} \nabla^2 + V(r) + V_H(r) + V_{XC}(r) \right] \psi_i(r) = \varepsilon_i \psi_i(r) \quad (2.16)$$

3. Calculate the electron density defined by the Kohn-Sham single-particle wave function from step 2, $n_{KS}(\mathbf{r}) = \sum_i \psi_i^*(\mathbf{r})\psi_i(\mathbf{r})$
4. Compare the electron density calculated in step 3, $n_{KS}(\mathbf{r})$, with the trial one in step 1, $n(\mathbf{r})$. If these two quantities are the same, this is the ground state electron density and the total energy can be computed based on this value. If this two densities are different, the electron density should be updated and the same procedure should be repeated from step 2.

2.1.9. Periodic Boundary Conditions

A well-known approach to define a solid or catalyst structure is to use periodic boundary conditions in which the user defines a cell containing the atoms of the systems. The cell repeats in all directions.⁷⁵ In the slab approach a surface is modeled with the atoms in the lower portion of the supercell, but an empty space is employed above the atoms in the top portion of the supercell. The surfaces are separated by empty spaces and any reactions/surface chemistry can occur on the surface of the slab. The empty space separating periodic image of slab in z-direction is called the vacuum region. It is important to use a vacuum region which is thick enough to prevent interactions between surfaces. Usually a vacuum region of at least 10 Å should be between two slabs. A schematic of a 6×6 slab with 10 Å vacuum layer is depicted in Figure 2.1.

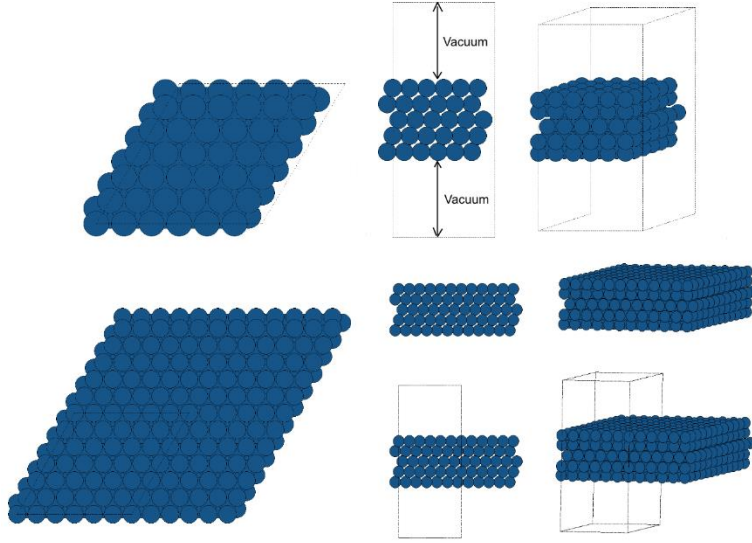


Figure 2.1. A schematic of a 6×6 slab with periodic boundary conditions in all three directions. A vacuum layer is shown above and below the slab. The pictures on the left are top views, and the pictures in the middle and on the right are side views. The right pictures show the slab when periodic images are repeated to show neighboring cells.

2.2. Cluster Expansion Method

The basic idea behind cluster expansion is that energy, enthalpy, or any other quantity (Q) which is related to atomic configuration, can be expressed in terms of sum over bonds (or interactions).⁸⁷ These bonds (or interactions) include pairs, triplets, quadruplets, and so forth.⁸⁷ In the cluster expansion community these bonds or interactions are referred to as clusters or figures. Subclusters are groups of clusters which share the same number of interactions. For example, pair interactions are subclusters which share interactions between two atoms, triplets are subclusters sharing interactions between three atoms and so on. One example of implementing the cluster expansion method is in configurational theory of alloys. In the present study we are dealing with bimetallic alloys. Mathematically, Q (which represents for instance the energy of an alloy) can be expressed in terms of correlation (basis) functions.⁸⁸

$$Q = \sum_n q_n \xi_n \quad (2.17)$$

In the above Equation, q_n are coefficients of correlation functions and are called effective cluster interactions (ECIs). ξ_n are multisite correlation functions (basis functions) for each of the

subclusters n . $n=0$ refers to the empty cluster, $n=1$ refers to the point cluster, $n=2$ refers to the pair cluster, and so forth. These cluster types are depicted in Figure 2.2.

$$\xi_n = \frac{1}{N_n} \sum_{P_i} \sigma_{p1} \sigma_{p2} \dots \sigma_{pn} \quad (2.18)$$

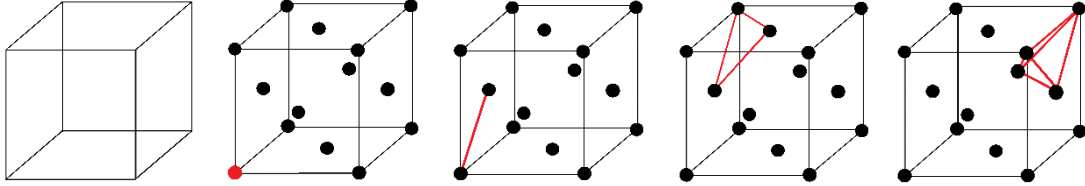


Figure 2.2. Demonstration of different types of clusters or interactions in a lattice. From left to right: empty, point, pair, triplet, and quadruplet clusters are depicted respectively.

ξ_n can be defined by Equation 2.18.⁸⁸ In Equation 2.18, σ_{pn} is a spin-like operator which takes the value of +1 or -1 depending on atom A or B occupy the lattice site p . n can take the values of 1,2,3,4, and so on. N_n is the total number of lattice subclusters (points, pairs, triplets, tetrahedrons, and so on). The main task in each cluster expansion code is to find ECIs. It is worth mentioning that the cluster expansion like other expansions (such as Fourier series and Taylor series) is exact when the summation (like in Equation 2.17) is infinite. However, it is not practical to use all terms in the cluster expansion summation, just like it is not possible to have all the terms in a Taylor expansion. In the present study, the “generalized cluster-expansion for variable and complex systems” (GCVC) code developed by Professor Koretaka Yuge at Kyoto University has been used to model bimetallic Ir based alloys. Further explanation of the GCVC code is presented in Appendix A.

Chapter 3: Surface Dependent Segregation in Bimetallic Alloys

3.1. Introduction

Platinum group metals, such as Pt, Pd, Rh, and Ir often display high catalytic activity for catalytic reactions. These metals can be expensive, so alloys are often used to decrease the amount of expensive metal being used, while also achieving high catalytic activity. Alloys have been investigated for instance in hydrogen generation^{89,90}, dehydrogenation⁹¹⁻⁹³, reforming processes^{94,95}, and fuel cells^{6, 96-98}. In order to design viable alloy catalysts, the materials should have high catalytic activity, but should also be stable. Depending on how well the two metals mix, different alloy structures may form⁹⁹. For instance, an alloy may form a homogenous structure for metals that mix well, while separation into distinct particles or core-shell particles may occur for metals that prefer to segregate.

Surface segregation leads to the surface of an alloy particle/crystal having a different alloy composition than the bulk. Surface segregation can influence many processes such as adsorption, wetting, crystal growth, oxidation, corrosion, and catalysis^{100,101}. Depending on the application of interest, surface segregation can be beneficial or detrimental^{102,103}. For instance, segregation of Pt atoms to the surface of a Pt₇₅Ni₂₅ alloy enhanced the catalytic activity for the oxygen reduction reaction (ORR).¹⁰⁴⁻¹⁰⁶ On the other hand, possible segregation of an element M in M (core)-Pt (shell) structures may decrease the stability of these alloys in acidic medium^{107,102}. Different parameters have been used to explain surface segregation. Atom size and surface energy difference between the host metal and the impurity element have been investigated^{108,102,109}. Elastic energy release¹¹⁰, heat of solution for the alloy¹¹⁰, composition of the elements in the alloy¹⁰², and cohesive energy¹⁰⁹ are other properties tied to surface segregation.

Segregation has already been studied in previous reports using modeling tools, such as density functional theory (DFT). Ruban et al¹¹¹⁻¹¹³ for instance calculated segregation energies of single impurity atoms in several low-index surfaces¹¹¹⁻¹¹³. Segregation behavior for the (111) surfaces of platinum^{102,114,115}, palladium^{108,116,117}, and iridium¹⁰⁷ has been investigated. Segregation behavior can be surface dependent, meaning that it can depend on what surface is exposed. Ruban et al.¹¹³ reported that the segregation energy is related to the nature of d-bands which vary across the different transition metals. Surface segregation at the (111)^{106, 118-125}, (110)^{106, 118-121, 123-125}, and (100)^{106, 118-126} surfaces of Pt has been studied. Surface segregation at

the (111)^{121, 127-129}, (110)^{121,128,129}, and (100)^{121, 126-129} surfaces of Pd has also been investigated. Such studies have shown that segregation behavior could occur differently at various surfaces. A potential shortcoming in existing studies is the limited number of impurities that have been considered. For instance, several of these studies only considered binary Pt-Ni^{106, 118-119, 123, 125} and Pt-Pd¹²⁷⁻¹²⁹ alloys. The segregation energy, a measure of how much an impurity element prefers to segregate from a parent element, can be a good indicator of the alloy's stability^{108,107}. While published literature has determined segregation energies for select metals in select surfaces, a comparison of many different surface facets (e.g. open and closed) is not currently available. Furthermore, the most comprehensive collection¹¹²⁻¹¹³ of segregation energies in the literature uses the local density approximation (LDA), while in the present study, we performed DFT calculations using generalized gradient approximation (GGA) functionals, which are more common for modeling metals.

We have performed a systematic study of the (111), (110), (100), and (210) surfaces using Pt, Pd, Rh, and Ir as host metals. We considered all transition metals as dopants, and investigated how segregation compares for the different surface facets. It is important to note that segregation energy also depends on the alloy's composition and depending on how many atoms are being segregated, different segregation energies can be obtained. In the present study, we considered dilute alloys, specifically we modeled a single impurity (dopant) in the host metal. We also addressed how different types of segregation (surface to sub-surface versus surface to bulk) affect segregation energy results. Finally, we presented models that may explain these surface segregation processes, and can be used to make predictions of alloy segregation.

3.2. Methodology

3.2.1. Simulation Parameters

Density functional theory (DFT) calculations were performed using the CP2K package⁸²⁻⁸⁶ which uses the Gaussian and plane waves (GPW) method⁸². Electron densities were treated by plane waves and electronic orbitals were treated by double-zeta Gaussian basis sets.¹³⁰ The Perdew, Burke, and Ernzerhof (PBE) exchange correlation functional¹³¹ was used throughout the present study. Core electrons were represented by Goedecker-Teter-Hutter (GTH) pseudopotentials^{132,133}. All calculations were spin-polarized. CP2K uses periodic boundary

conditions and samples reciprocal space only at the Γ point. To compensate for any error associated with small k-point sampling, large cells have been used.

3.2.2. Surface Models

In order to build surfaces, first we calculated lattice parameters of bulk metals that were used as alloy hosts: 3.86 Å (Ir), 3.96 Å (Pt), 3.95 Å (Pd), and 3.84 Å (Rh). These values match well with other density functional theory studies: 3.86 to 3.89 Å for Ir¹³⁴⁻¹³⁵, 3.99 Å for Pt¹³⁵⁻¹³⁶, 3.93-3.96 Å for Pd^{135, 137-141}, and 3.80 Å to 3.86 Å for Rh^{135, 142-144}. Next we modeled surfaces using periodic boundary conditions, or the slab approach. For (111) and (100) surfaces, 6×6 super cells were used. Both (111) and (100) surfaces were 5 atomic layers thick consisting of 180 atoms. For (110) surfaces, 4×6 super cells with 7 atomic layers consisting of 168 atoms were used. For (210) surfaces, 2×4 supercells with 5 atomic layers consisting of 160 atoms were used. All atoms were allowed to relax for the various slabs. The corresponding slab models are depicted in Figure 3.1. We investigated how the number of layers affected our results. We also examined how freezing the bottom layers compared to not freezing the bottom layers affected our results. We discuss these aspects in the Appendix B.1.

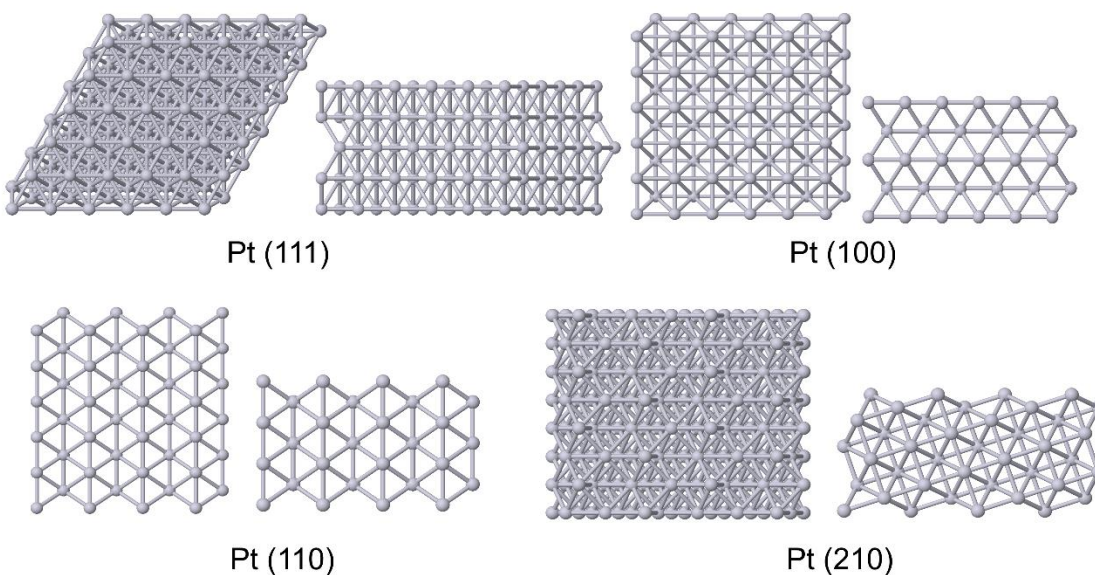


Figure 3.1. Slab models used in the present study. For each surface, the left image shows the top view of the surface, while the right image shows the side view of the surface.

3.2.3. Segregation definition

In order to model segregation, we considered a dopant atom in the first (top) surface layer, in the second surface layer, or in a larger bulk structure. The bulk structure was of size $5 \times 5 \times 5$ and had 500 atoms. The dopant atom may transfer from the second surface layer to the first surface layer, or from the bulk to the first surface. Both segregation processes were considered in this work. The positions of a dopant in the alloy are depicted in Figure 3.2. The segregation energy, $E_{seg-1-2}$, is defined as the total energy difference of the alloy with dopant in the first layer and second layer. An alternative definition, $E_{seg-1-bulk}$, is defined as the total energy difference of the alloy with dopant in the first layer and bulk structure. The segregation energy is calculated by equations (3.1) and (3.2):

$$E_{seg-1-2} = E_{1st\ layer} - E_{2nd\ layer} \quad (3.1)$$

$$E_{seg-1-bulk} = E_{pure\ bulk} + E_{1st\ layer} - E_{impurity\ in\ bulk} - E_{pure\ surface} \quad (3.2)$$

In these equations E_{seg} is the calculated segregation energy, $E_{1st\ layer}$ is the total energy of the alloy with the dopant in the first layer, and $E_{2nd\ layer}$ is the total energy of the alloy with the dopant in the second layer. The bulk energies, $E_{pure\ bulk}$ and $E_{impurity\ in\ bulk}$, are the total energies of a dopant-free bulk cell and the bulk structure with a single atom dopant. A negative segregation energy indicates that the dopant prefers to segregate towards the surface, while positive segregation energy indicates the dopant does not prefer to segregate towards the surface. Unless noted in the text, when we refer to segregation energy, this indicates the $E_{seg-1-bulk}$ value.

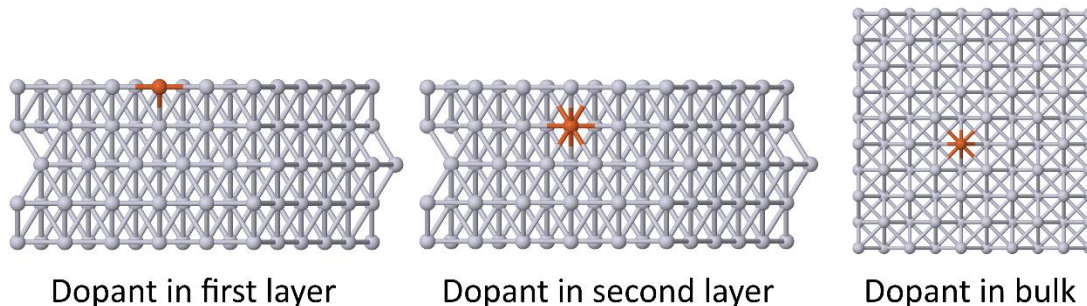


Figure 3.2. Illustration of different dopant positions within parent metals in slab and bulk structures. Side views of the slabs and bulk are shown.

3.3. Results and discussion

3.3.1. Comparison of Segregation on (111) Surfaces

We first examined segregation of transition metals at the (111) surfaces. Calculated segregation energies ($E_{seg-1-bulk}$) are given in Figure 3.3. The segregation energy curves have a characteristic U shape, where early and late transition metals have the most negative segregation energies while middle transition metals have the most positive segregation energies. This is similar to previous work, such as Ruban et al¹¹³, Chelikowsky¹⁴⁵, and Mukherjee et al¹⁴⁶. However, there is anomalous segregation behavior for 3d metals, especially middle metals like Cr, Mn, and Fe. The segregation energy curve for the 3d metals does not have a full U shape, but rather dips for the middle transition metals, in contrast to the 4d and 5d metals. Such anomalous behavior can be attributed to magnetic effects, which are present in 3d metals, as discussed by Sutton¹⁴⁷. Such magnetic effects do not occur as profoundly for 4d and 5d metals. This dip for mid transition metals occurring in the 3d row can be observed for other properties, such as surface enthalpy¹⁴⁵.

We calculated the average segregation energies in the different host metals Pt, Pd, Ir, and Rh to be 0.58, 0.53, 0.00, and -0.02 eV, respectively. Ranges of segregation energies in the host metals were as follows: Pt (-0.92 to 1.4 eV), Pd (-0.43 to 1.19 eV), Ir (-1.89 to 0.98 eV), and Rh (-1.42 to 0.67 eV). The segregation energies in general follow this trend: Pt > Rh > Pd > Ir for 4d and 5d dopants. That is, the segregation energies in the Pt (111) surface tend to be most positive, while the segregation energies in the Ir (111) surface tend to be most negative. Thus, segregation is least likely to occur within Pt and most likely to occur within Ir. For 3d transition metals

however, Pd and Ir possess the least segregation energy values among other hosts. Due to oscillatory behavior of surface segregation in 3d transition metals, it is hard to report a monotonic segregation trend as was done for 4d and 5d dopants.

One factor affecting surface segregation is the metal atomic size. When the dopant atom is bigger than the host metal, strain occurs. In order for this strain to be released, the dopant could segregate to the surface and leave the metal lattice. For a given dopant, the bigger the host metal, the less likely segregation occurs due to strain. Pt has the largest van der Waals radius among the four host metals, while Rh and Ir have the smallest radii. As a result, surface segregation is least likely to occur in Pt, and more likely to occur in other hosts. As we show in section 3.e, there are also other factors affecting surface segregation. Therefore, our results cannot be interpreted merely by metal atomic size.

As can be seen in Figure 3.3, segregation energies are most negative for early and late transition metals and most positive for the middle transition metals. In other words, early and late transition metals are most likely to segregate from the parent metal. Chelikowsky et al.¹⁴⁵ used Miedema¹⁴⁸ theory to examine such trends. Chelikowsky showed that the segregation energy is proportional to the cohesive energy of the metal. As discussed by Sutton¹⁴⁷, a transition metal's cohesive energy can be estimated from the number of d electrons (n_d) based on a Friedel model approximation. The maximum cohesive energy occurs for when $n_d = 5$, or for middle transition metals. Thus, middle transition metals have the largest cohesive energies and correspondingly the largest segregation energies. Brejnak and Modrak¹⁴⁹ attempted to explain segregation based on number of d electrons, and suggest that for host metals with $n_{d\text{-host}} > 5$, segregation will occur when $n_{d\text{-dopant}} > n_{d\text{-host}}$. We do observe favorable segregation for metals having $n_{d\text{-dopant}} > n_{d\text{-host}}$, as seen in Figure 3.3, but favorable segregation also occurs for some early transition metals, in contrast to the predictions of Brejnak and Modrak¹⁴⁹.

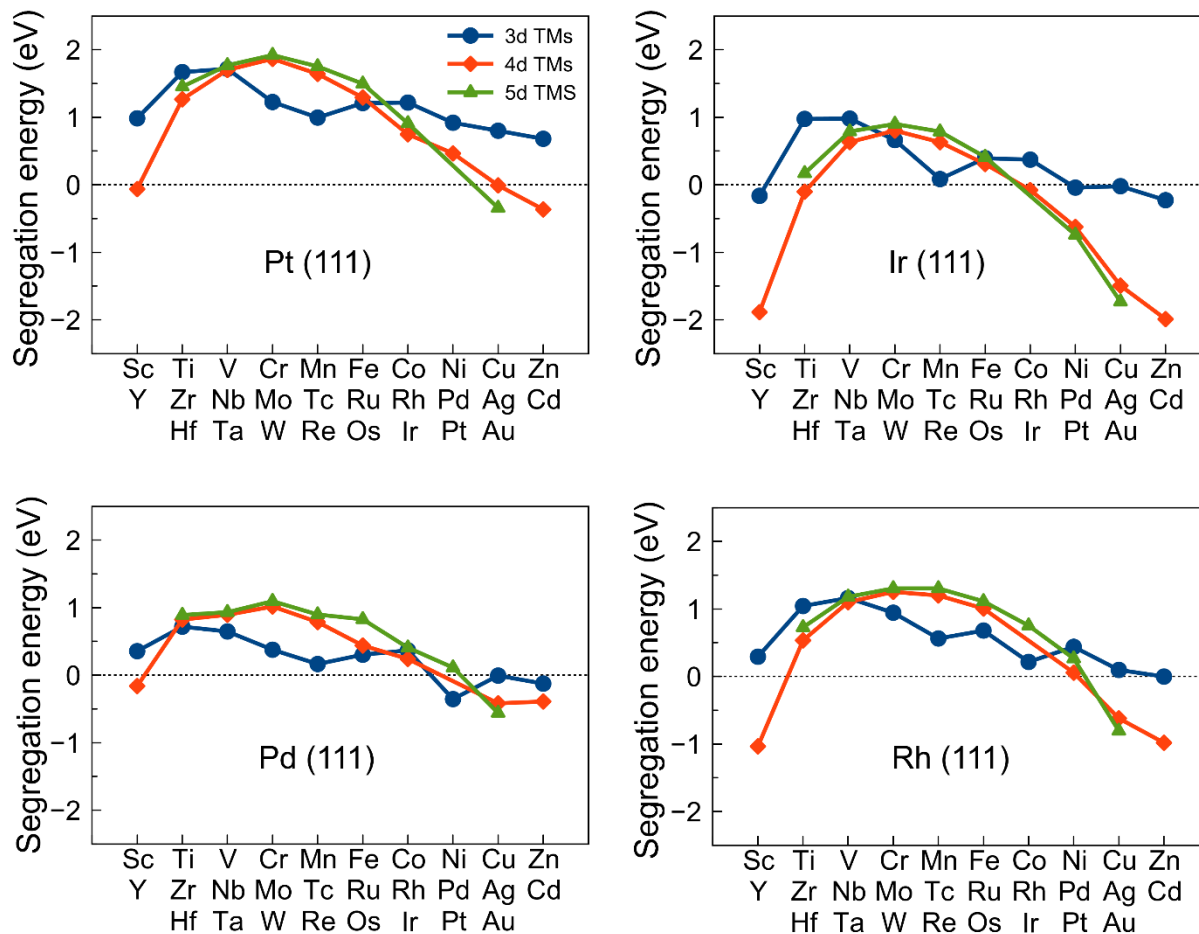


Figure 3.3. Calculated segregation energies of single transition metal atoms within the (111) surfaces of Pt, Pd, Ir, and Rh.

3.3.2. Comparison of Segregation in the (111), (100), (110), and (210) Surfaces of Pt

Surface segregation can be surface dependent, meaning that it may depend on what parent surface the segregation is occurring at. For instance, Duan et al.¹²⁸ studied surface segregation with Pt-Pd alloyed nanoparticles and observed different segregation tendencies for (100), (110) and (111) surfaces of these particles. To demonstrate this point, we show surface segregation energies for Pt (111), (100), (110), and (210) surfaces in Figure 3.4. For some dopants, there is a large segregation energy difference between the Pt surfaces. For instance, several dopants (e.g. Co, Ti, V, Sc) have large segregation energy differences (0.9 to 0.6 eV) between the (110) and (100) surfaces. In general the lowest segregation energies occur for the (110) surface, while the

highest segregation energies occur for the (100) surface. Other metals (e.g. Pd, Os, Ir, Au) have much smaller differences (≈ 0.1 eV) between the (110) and (100) surfaces. The average segregation energies are 1.2, 1.1, 1.0, and 0.7 eV for the Pt (100), (111), (210), and (110) surfaces, respectively, or $(100) > (111) > (210) > (110)$.

An examination of the different dopant metals provides details on segregation. Surface-dependent segregation is most pronounced for the 3d transition metals. The average segregation energy difference between (100) and (110) surfaces for 3d metals was calculated to be 0.6 eV. The average segregation energy differences between (100) and (110) surfaces for 4d and 5d transition metals was calculated to be 0.3 eV for both cases. The relative order of segregation energies across the various surfaces were different for the 3d, 4d, and 5d metals. For 3d metals the segregation energies were generally as follows: $(100) > (111) > (210) > (110)$. For a few later transition metals (Ni, Cu, Zn), however, the (111) segregation energies are higher than the (100) segregation energies. The segregation energies of many middle 4d and 5d transition metals follow this trend: $(100) \approx (210) > (111) > (110)$. For early and late transition 4d and 5d metals, however the segregation energies across the different surfaces become closer, and it becomes difficult to distinguish surface-dependent segregation. For instance, segregation energies of 5d metals for the (100) and (210) surfaces are very close, with a mean absolute difference of 0.04 eV between the two surfaces. Of note is that segregation energies with 4d and 5d metals have a much greater range (-0.8 to 2.1 eV) than the range of the 3d segregation energies (0.2 to 1.9 eV). 3d metals behave differently than 4d and 5d metals due to their unique magnetic properties as discussed before¹⁴⁷.

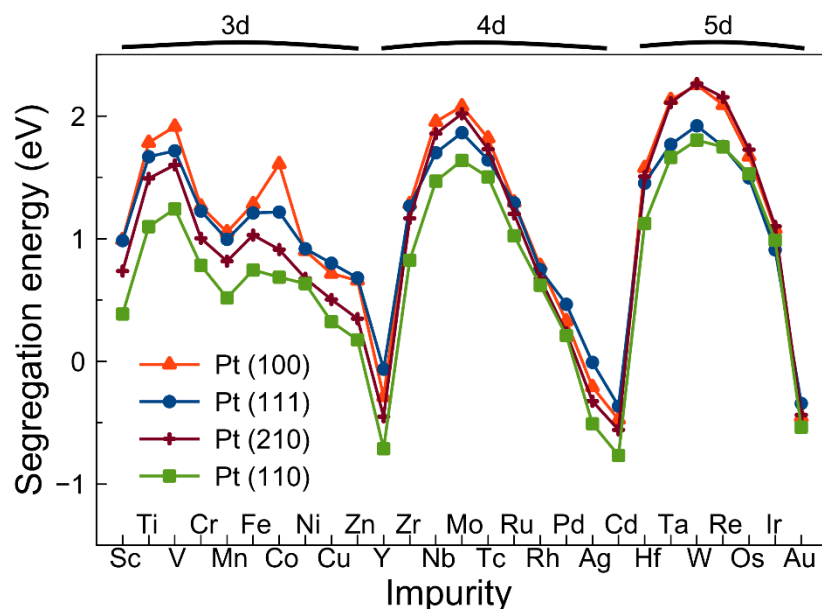


Figure 3.4. Segregation energy comparison between the (110), (210), (100), and (111) surfaces of Pt.

3.3.3. Surface Segregation in Pt, Ir, Pd, and Rh

Segregation energy comparisons between different surfaces of Pt, Ir, Pd, and Rh are shown in Figure 3.5. In the case of Pt and Pd as host, segregation energies for (111), (100), (110), and (210) surfaces converged to almost the same number at the start and the end of the transition metal series. For Ir and Rh, this is not the case and for Ir as host, the values of segregation energies at the beginning and the end of transition metals differs the most for (111), (100), (110), and (210) surfaces (compared with Pt, Pd, and Rh as hosts). The segregation energies with Ir as host are between -3.10 and 1.30 eV. The corresponding ranges for Pt, Pd, and Rh surfaces as hosts are -0.77 to 2.26, -0.56 to 1.97, and -1.40 to 2.15 eV, respectively. The most positive segregation energies occurred with Pd as the host. Pt had the highest segregation energy, at 2.26 eV for W in (210) surface. The lowest segregation energy value occurred with Ir, at -3.10 eV for Y in the (210) surface. The average segregation energies for Pt, Ir, Pd, and Rh are 0.99, -0.22, 0.50, and 0.57 eV, respectively. The segregation energy trends are thus roughly Pt > Rh > Pd > Ir when considering all the (111), (100), (110), and (210) surfaces. (Shown in Figure B.4 in Appendix B)

As evident from Figure 3.5, segregation energy might be surface dependent and in some cases surface dependent segregation energy exists more. For Pt and Ir as host, the 3d dopant

segregation energies depended strongly on the surface, meaning that there is up to 1.5 eV energy difference between segregation of 3d dopants when different facets of Ir or Pt occur. In the case of Pd as a host, there is up to a 1 eV energy difference in segregation for 4d and 5d dopants within different facets of Pd. For Rh as host the surface dependent segregation is most pronounced for 5d transition metals with about an 0.8 eV energy difference between different facets. From Figure 3.5 it can be observed that there is not a consistent trend in preferred surface dependent segregation. For example, with Pt as host and 3d transition metals as dopants the segregation energies follow this trend: (100)>(111)>(210)>(110). On the other hand with Rh as host and 5d transition metals as dopants this trend occurs: (210)>(100)>(110)>(111). That's while in some cases such as Pd as host and 3d transition metals as dopants, there is not an obvious trend in surface dependent segregation energy. In order to further explain such trends, we have developed a model to predict surface dependent segregation energies, as discussed in Section 3.e.

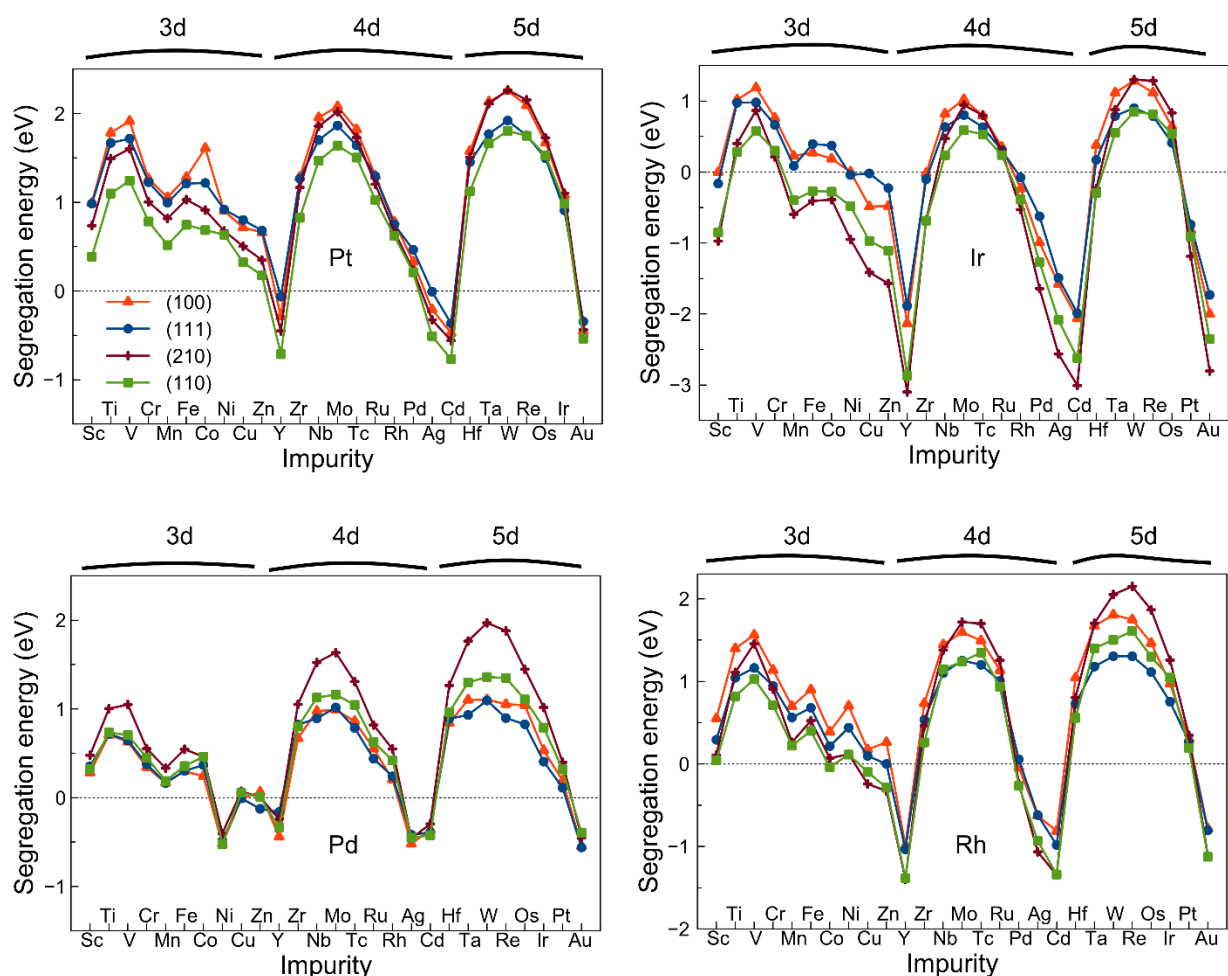


Figure 3.5. Segregation energy comparisons between difference surfaces of Pt, Ir, Pd, and Rh.

3.3.4. Bulk versus Second Layer Segregation

We next address segregation from sub-surface sites to the surface compared to segregation from the bulk to surface. Both processes have been studied in the literature^{102, 108, 110, 113}. Figure 3.6 shows the calculated segregation energies using Equation 3.1 (sub-surface to surface segregation) and Equation 3.2 (bulk to surface segregation) with Pt as the host. A clear trend in the results is that sub-surface segregation energies are lower than bulk segregation energies, indicating that bulk segregation is harder. This would suggest that as the dopant metal gets closer and closer to the surface, it becomes less stable relative to the bulk, until at the surface it may or may not reach a stable state. The plots all have similar shapes indicating that the segregation energies are largely

just shifted relative to each other. The mean absolute differences between bulk and sub-surface segregation energies are 0.49 eV (111), 0.54 eV (100), 0.60 eV (110), and 0.82 eV (210), with standard deviations of 0.35 eV (111), 0.38 eV (100), 0.42 eV (110), and 0.58 eV (210). The corresponding graphs for Ir, Pd, and Rh as hosts are depicted in Figures B.5-B.7. For Ir and Pd as host, the two segregation processes have similar segregation energies, as evident in Figures B.5 and B.6. The mean absolute differences between bulk and sub-surface segregation energies for Ir was 0.24 eV, while the similar value for Pd was 0.14 eV.

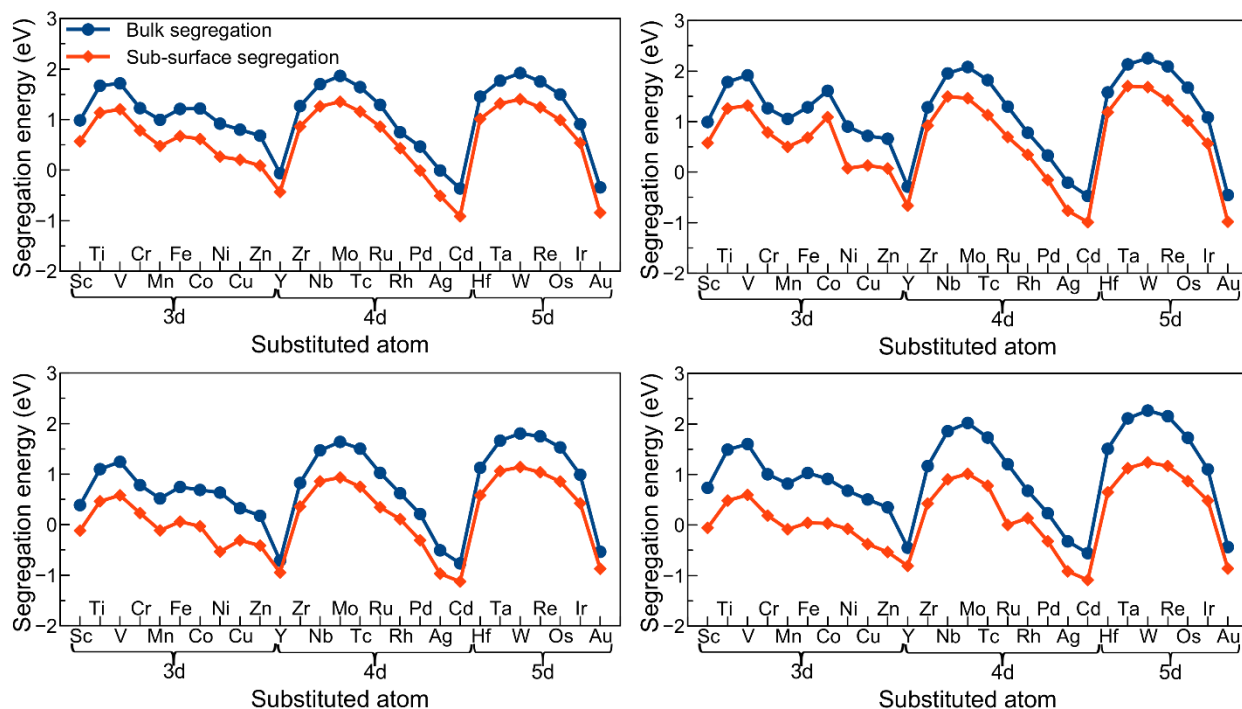


Figure 3.6. Calculated segregation energies in a Pt host metal involving sub-surface to surface segregation and also bulk to surface segregation. Segregation energies were calculated with Equations 1 and 2.

3.3.5. Explanation and Analysis of Results

We next sought to develop a mathematical model that could explain and predict surface segregation. Such a model could be used to quickly screen potential alloys without having to run more time-intensive DFT calculations. Several models have already been published to predict segregation energies. Brejnak and Modrak¹⁴⁹ developed a model to predict segregation energies using properties of pure metals, such as lattice structure, d-band center, d-band width, d-band

filling, and atomic volume. They discussed that the sign of the product of $\Delta N \alpha_s$ determines whether a dopant atom would segregate to the surface. In the above product, ΔN is the difference between number of d-electrons for alloy components (solute and the solvent) and α_s denotes the surface potential. They used d-band properties of the surface and the bulk simultaneously in order to predict surface segregation, although they did not distinguish between different surfaces. Motivated by this, we also calculated the d-band filling, d-band center, and d-band width for the different surfaces of our host metals we studied: (111), (100), (110), and (210). These results are tabulated in Table B.7 in Appendix B. We plotted d-band properties of Pt along with segregation energy of vanadium as dopant as an example to see if there is a linear correlation between d-band properties and segregation energy. As it can be seen in Figure B.8 in Appendix B, there is no direct correlation between d-band properties of the host and segregation energies in (111), (100), (110), and (210) surfaces of Pt. This suggests that other properties of the dopants and hosts may be needed for a more complete prediction of segregation energies.

Ruban et al.¹¹³ used Friedel's rectangular state density model¹⁵⁰⁻¹⁵¹ to predict segregation energies in transition metal alloys. In their paper they directly compared surface segregation energies of 4d metals calculated using both DFT and their model. Comparing their DFT data with their model indicates how closely the two match. We analyzed their data to calculate an R^2 value of 0.53 between the two data sets, and a root mean square error (RMSE) between the two data sets of 0.41 eV. Furthermore, Ruban et al.¹¹³ acknowledged that their model is limited in how it considers the structure of surfaces. A more robust model is needed to better consider segregation behavior between different surfaces.

Another model, based on universal tight-binding (TB) and Friedel's model, developed by Wang and Johnson¹⁰⁹ was used to predict segregation in alloy particles. Wang and Johnson compared segregation energies obtained from their model to their DFT segregation energies in their work. Their model captured the general segregation trends correctly, but there was up to a 3 eV energy difference between their DFT and model results. The R^2 and a root mean square error (RMSE) from comparing their DFT data and model was 0.19 and 0.93 eV respectively.

Yu et al¹¹⁰. developed a model to predict segregation energies based on the surface energy, elastic energy, and heat of solution of the impurity and the host metal. Unlike the two previous models which used Friedel's model and tight-binding theory without any regression to fit their

data, Yu et al.¹¹⁰, took advantage of linear regression to find coefficients for their utilized parameters. They only modeled Ni (111) as a host metal. We refitted their parameters to our own DFT data, and calculated a RMSE of 0.58 eV, R^2 of 0.63, and adjusted R^2 of 0.73 when using their model (with refitted parameters) to our DFT data. The drawback of this model however is that it does not predict surface dependent segregation energies since it uses generic experimental surface energies. When we used DFT-calculated surface energies (for the host metals), the RMSE and R^2 were calculated to be 0.48 eV and 0.76, respectively, which was a slight improvement. Unlike a previous model¹¹³, which predicted segregation energies to follow an exact parabola for each facet of Pt with the trend of 210>110>100>111 (contradictory to DFT results), this modified version of Yu et al.'s model captured segregation trends much more realistically. It even captured the oscillatory behavior of the 3d dopants. Data using this model for Pt as host can be found in Figure B.9 in Appendix B. This model distinguishes between the (111) surface of Pt and the other surfaces and predicts segregation trends to be (111) > (100) \approx (110) \approx (210). However DFT predicts the following order of segregation energies: (100)>(111)>(210)>(110). Therefore, similar to previous segregation models, the Yu et al.¹¹⁰ model did not fully capture surface dependent segregation energies.

We therefore developed our own model to predict surface-dependent segregation energies. We took common features of previous models to derive the model shown in Equation 3.3. Our model uses d-band width (W^B), d-band filling of the dopant (N_B), coordination number in the surface (Z_s) and in the bulk (Z_b), a term representing the elastic energy release ($\left[\left(\frac{r_B}{r_A}\right)^3 - 1\right]^2 r_A^3$), and surface energy difference of the host and the dopant ($E_{surface}^B - E_{surface}^A$). This model takes elements of Ruban et al.¹¹³ (coordination numbers and d-band properties), but also adds in features from Yu et al.¹¹⁰ (difference in surface energies and elastic energy). The model also includes adjustable parameters, which allows more flexibility. This model was directly fitted to all our DFT data (all Pt, Ir, Pd, Rh host surfaces), and is given in Equation 3.3, where the β coefficients are the fitted parameters. The model gave a RMSE of 0.51 eV and an adjusted R^2 of 0.89. The exact parameters of the model can be found in Appendix B.

$$E_{segregation}^{B \rightarrow A} = \beta_0 + \beta_1 W^B + \beta_2 N_B + \beta_3 (E_{surface}^B - E_{surface}^A) + \beta_4 \left[\left(\frac{r_B}{r_A} \right)^3 - 1 \right]^2 r_A^3 + \beta_5 \left[1 - \left(\frac{Z_b}{Z_s} \right)^{\frac{1}{2}} \right] \quad (3.3)$$

Further explanation of all the parameters and how we developed this model can be found in the Appendix B. Figure 3.7 shows how our DFT data compares to our model. Table 3.1 shows a summary of how our model compares to our DFT data, as well as some other models in the literature. Overall, our model captures the features of the DFT model quite well.

The large adjusted R^2 value of 0.89 and low $RMSE$ of 0.51 eV indicate the accuracy of our model. The largest difference between the DFT data and our model belongs to Pd as the host with a difference of 1.96 eV. The comparison between segregation energies calculated with DFT and our model for (111), (100), (110), and (210) surfaces of Pt is depicted in Figure 3.7. As is evident from the figure, our model mirrors the DFT results well. Our model is able to describe surface-dependent segregation, a feature previously not included in segregation models. The corresponding figures for Ir, Pd, and Rh can be found in Figures B.10, B.11, and B.12. Our model takes into account d-band properties of the dopant (d-band filling and d-occupation number), surface energy of the host dopant, atomic radii of the host and impurity, and also coordination numbers in the bulk and at the surface. All these parameters combined give a surface dependent segregation model that agrees well with DFT. Previous models did not consider all these parameters at the same time and as a result were not able to achieve such good agreement with DFT.

Table 3.1. Comparison between various models to predict surface segregation and DFT data. In the case of Ruban et al.¹¹³ and Wang et al.¹⁰⁹ the models were compared with the DFT data in the original papers, while for Yu et al.¹¹⁰ and our model our own DFT data was used for comparison.

Model	R^2	Adjusted R^2	RMSE (eV)	Largest Difference (eV)	Smallest Difference (eV)
Ruban et al. ¹¹³	0.53	-	0.41	1.32	0.01
Wang et al. ¹⁰⁹	0.19	-	0.93	3.16	0.00
Yu et al. ¹¹⁰	0.63	0.63	0.58	1.96	0.00
Our Model	0.89	0.89	0.51	1.96	0.01

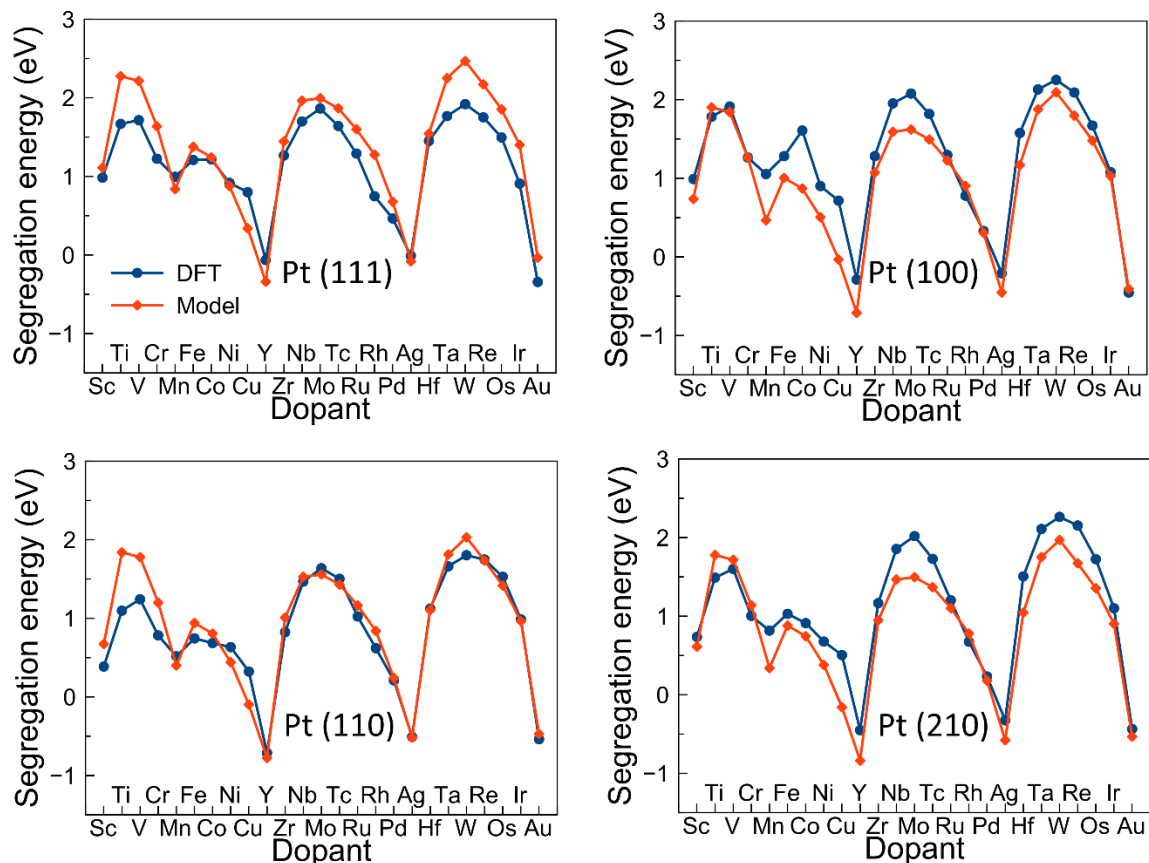


Figure 3.7. Comparison between segregation energies of various dopants in the (111), (100), (110), and (210) surfaces of Pt obtained with DFT and our developed model.

3.4. Conclusions

We calculated bulk and sub-surface segregation energies by means of DFT. We realized although these definition predict the same trends for segregation energies, they might result in different absolute values. Thus it is crucial to consider how one defines segregation phenomenon while comparing segregation energies with literature values. Our calculations proved segregation can be surface dependent. For instance for Pt as the host and 3d transition metals as dopants segregation energy follows the trend of: $100 > 111 > 210 > 110$. That's while for 4d and 5d transition metals as dopants $100 \approx 210 > 111 > 110$ trend is observed. In general, early and late transition metals segregate more and have more negative segregation energies, while mid-transition metals possess positive segregation energies and do not tend to segregate. An oscillatory segregation

behavior is observed in 3d transition metals due to magnetism. We also calculated segregation energies in other hosts including Ir, Rh, and Pd. When considering all the (111), (100), (110), and (210) surfaces, the general trend of Pt > Rh > Pd > Ir is observed. We further developed a statistical model which predicts segregation of a transition metal dopants. This model used several parameters, including d-band width and d-band filling of the dopant, surface energies of the host and impurity, an elastic energy release term, and coordination number. This model is able to predict surface-dependent segregation, and predict for instance segregation energies to follow this trend for segregation of 3d dopants in Pt (in agreement with the DFT data): (100) > (111) > (210) > (110). Our model is an improvement on previous models in that it can distinguish segregation at different host surfaces, and has high accuracy. For this work we have illustrated how DFT and our model can predict segregation at different metal surfaces. Such results are important for predicting and understanding the stability of different metal alloy crystals/particles, and will allow faster screening of potential alloys.

Chapter 4: Comparison of different Catalysts for C-C Bond Scission in Ethanol Oxidation

4.1. Introduction

One of the biggest challenges associated with direct ethanol fuel cells (DEFCs) is efficiently and fully oxidizing ethanol. Fully oxidation of ethanol is a complicated reaction network involving at least 128 different C₂ species and at least 21 different C₁ species³³. Carbon-carbon bond breaking is an important step in complete oxidation of ethanol since it is necessary to form CO₂. Other products can form in the absence of C-C bond breaking, such as acetaldehyde. For instance C-C bond breaking in CHCO at the Rh (111)^{39,38}, Pd (111)³⁷, Cu (100)⁴¹ surfaces, C-C bond breaking in CH₂CO at the Cu (100)⁴¹ surface, and C-C bond breaking in CH₃CO at the Pd (110)⁴⁰ and Cu (100)⁴¹ surfaces have all been studied. Some studies report C-C breaking to occur through CH₃CO in the ethanol oxidation reaction (EOR)^{21,152}. Ferrin et al¹⁶ reported that C-C bond scission in CH_xCO is the key process in EOR and that carbon-carbon bond breaking in CHCO is the rate determining step in the EOR for most transition metals.

Since C-C bond breaking in CH_xCO (x=1,2,3) is the bottleneck of complete EOR, in the present study, these reactions were modelled to investigate different catalysts' effects in C-C bond scission in the EOR. The most common fuel cell catalyst, Pt, does not break the C-C bond completely and as a result incomplete oxidation of ethanol occurs at the surface of Pt. This leads to production of different reaction intermediates in which some of them will poison the catalyst surface. In other words, Pt would be poisoned rapidly by strongly adsorbed intermediates coming from dissociative adsorption of ethanol⁵⁴. To improve the activity of Pt in C-C bond scission, alloying one or more elements with Pt has been investigated by different research groups^{6, 50-51, 60}.

In the present study, different catalysts have been employed in the EOR and their effects in C-C bond breaking as indicator of the alloys' catalytic activities have been compared. We started with transition metals including Pt, Ir, Rh, Au, and Ag and compared their abilities in C-C bond breaking. Ir^{55, 72, 74}, Rh³⁸⁻³⁹, Au¹⁵³⁻¹⁵⁶, and Ag¹⁵⁷ in the ethanol oxidation reaction have also been investigated in the literature. For that matter it is worth to compare their ability in the carbon-carbon bond breaking with Pt. We then considered Ir and Ir-based alloys. Ir and Ir alloys^{55, 72, 74} have shown to have high catalytic activity, close to Pt, in the ethanol oxidation reaction. Since Rh⁶,

¹⁵⁸⁻¹⁵⁹ and Sn^{6, 71, 73, 160-161} can improve the catalytic activity of most metals, we investigated their effect on carbon-carbon bond breaking when alloying with Ir. Specifically we compared the ability of Ir, Ir-Rh, and Ir-Rh,Sn for carbon-carbon bond breaking.

Some research¹⁶¹⁻¹⁶⁴ reported that platinum-tin oxides (non-alloys) have faster kinetics for the ethanol oxidation reaction (EOR) compared to platinum-tin (alloys). However, other research¹⁶⁵⁻¹⁶⁸ provides contradictory results and reported PtSn alloys to be better candidates for the EOR compared to Pt-SnO₂. To address this dilemma, understanding the metal-oxide interface is required. Based on the research in this area, platinum-tin oxide has better catalytic activity compared to pure platinum and this superior catalytic activity is attributed to the large fraction of undercoordinated atoms¹⁶⁹. To investigate how this undercoordinated atoms relate to bi-functional mechanism and changing the d-band properties, having a good understanding of metal/metal oxide interfaces is a necessity. Interactions between the metal and metal oxide are especially important because they can change the chemical and physical properties of the two components¹⁷⁰.

We have therefore modeled Pt and Pt-SnO₂ catalysts. Rh and Sn are elements which have shown to increase the catalytic activity of the pure metal or alloy and as a result were chosen to be used with Pt. We also considered supported Pt-based catalysts including Pt-SnO₂ and Pt-Rh-SnO₂ and compared their activity to pure Pt. Pt and Pt-Rh interfaced with SnO₂ have been investigated. Platinum-tin alloys^{160, 171-172} have shown to have considerable catalytic activity and as a result have found broad applications in industry. For instance, platinum-tin catalysts have shown to be really effective in the naphtha reforming processes¹⁷³⁻¹⁷⁴. As another example, the application of silica-supported Pt-Sn catalysts in dehydrogenation processes were investigated by different research groups¹⁷⁵⁻¹⁷⁶. Besides, platinum-tin catalysts have shown to be potential candidates for the use in direct methanol¹⁷⁷⁻¹⁷⁹ and direct ethanol^{6, 54, 160} fuel cells. Specifically, the application of platinum-tin catalysts in direct ethanol fuel cells (DEFCs) is of special importance. Along with platinum-tin catalysts, platinum-tin oxide catalysts are also of interest^{160, 180}. Tin-oxide is especially important due to the fact that it can provide O-species which can facilitate the oxidation of CO produced during dissociative adsorption of ethanol on platinum active sites. This phenomena is known as the bi-functional mechanism^{165, 181-182}. Furthermore, the use of SnO₂ as an additive to Pt in the ethanol oxidation reaction could increase the Pt surface area and/or change the “d” band level of the material which causes more efficient oxidation of the intermediates generated in the ethanol

oxidation reaction (EOR) and decreases the poisoning effect caused by some of these intermediates¹⁶⁴.

Finally we have modeled Rh and Rh₂O₃ surfaces and compared their abilities in C-C bond breaking in CH_xCO species. Rh may become oxidized, and these calculations assess how oxidation of a metal affects its ability for C-C bond breaking. For example, it has been shown that activating the lattice oxygen on the surface of partially oxide metal, like Rh₂O₃, or metal oxide materials enhances activity for CO oxidation, oxygen evolution reaction, lithium ion batteries, and electro-oxidation of ethanol¹⁸³⁻¹⁹³. These various catalysts may be considered as promising materials in DEFCs. Our results show how pure metals, alloys, and metal-metal oxide interfaces may all enable C-C bond breaking.

4.2. Methodology

All geometry optimization DFT calculations were performed with the CP2K package.⁸²⁻⁸⁶ CP2K uses the Gaussian and plane wave⁸² (GPW) method which treats molecular orbitals as Gaussian functions and electronic density by plane waves. The Perdew, Burke, and Ernzerhof (PBE) exchange correlation functional¹³¹ was used throughout the present study. Core electrons were represented by Goedecker-Teter-Hutter (GTH) pseudopotentials^{132,133}. All calculations were spin-polarized. CP2K uses only a Gamma point for reciprocal space sampling so we used a rather large slab to assure convergence with respect to k-points. We used a double-zeta Gaussian basis set for the metals and a triple-zeta Gaussian basis set for adsorbates¹³⁰. For charge analysis, the optimized geometries obtained from CP2K then were used for single point calculations with the Vienna ab initio simulation package (VASP)¹⁹⁴⁻¹⁹⁸ code to analyze the electronic properties of the interface. The Perdew-Burke-Ernzerhof (PBE) exchange correlation functional¹³¹, a cutoff energy of 400 eV for the plane wave basis set and a 1×1×1 Monkhorst-Pack uniform k-point grid over the Brillion zone has been used for the VASP calculations.

For all geometries modeled in this study we used the slab approach with periodic boundary conditions. The Pt (111), Ir (111), Au (111), Ag (111), and Rh (111) surfaces were modeled using a 6 × 6 super cell. Each slab was four atomic layers thick with the two bottom layers frozen. The corresponding structures are shown in Figure 4.1. Rh and Rh-Sn were used to alloy Ir. The reason for alloying Ir with Rh and Sn is that alloying a transition metal surface with other metals (as discussed in detail in the introduction section) might lead to more catalytic activity. Ir-Rh was

modeled by substituting the first layer of Ir with Rh. In other words, an overlayer structure was used in order to model Ir-Rh. The corresponding geometry is depicted in Figure 4.2. For the Ir-Rh-Sn surface, three atoms of Rh in the Ir-Rh surface, have been replaced with Sn. The corresponding geometry can be found in Figure 4.2.

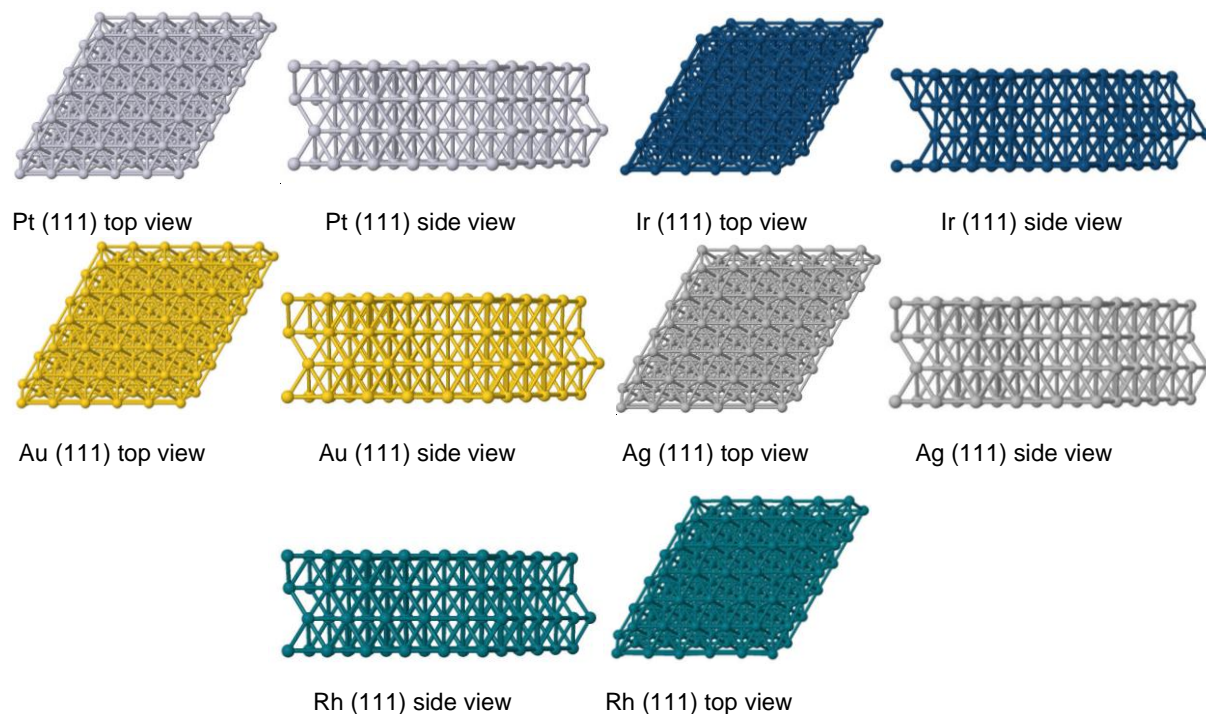


Figure 4.1. Pt, Ir, Au, Ag, and Rh (111) surfaces used in this work.

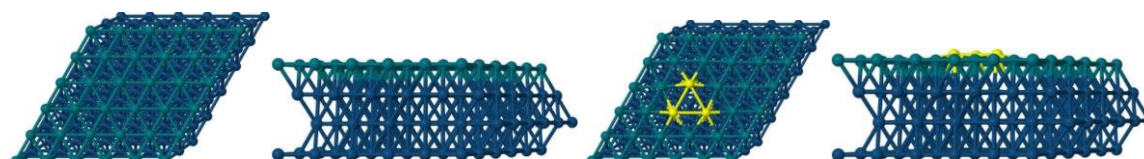


Figure 4.2. Top-view (far left) and side-view (second from left) of the Ir-Rh surface used in this work. Ir and Rh atoms are shown as blue and green spheres respectively. Top-view (second from right) and side-view (far right) of the Ir-Rh-Sn surface. Ir, Rh, and Sn atoms are shown as blue, green, and yellow spheres respectively.

To model interfaces between Pt and SnO₂, and also PtRh and SnO₂, we used the “rod” approach, as described by Molina et al.¹⁹⁹. A similar approach by Du et al.¹⁶⁰ has been used. This approach forms an interface between a metal rod and metal oxide support, with (111) facets exposed by the metal rod. Such facets are the most stable surface of Pt, and this rod represents a potential Pt-SnO₂ interface. A cell size of 13.7 Å by 16.4 Å by 35 Å was used to model this system. A three-layer (9 atomic layer) SnO₂ surface with dimensions of 13.7 Å and 16.4 Å, or 5×2, (180 atoms) was used as a support for either Pt or PtRh rods (containing 36 atoms). The total number of atoms in Pt-SnO₂ cell was therefore 216 atoms. We have frozen the bottom layer of SnO₂ (60 atoms) in its bulk position to save computational time. Figure 4.4 shows the structures used in the simulations.

Besides a 3 layer SnO₂ slab, different layers including 4, 5, 6, 7, and 8 were also modeled and the results have shown that 3 layer SnO₂ will give reasonably good results. We also performed the calculations with and without freezing the bottom layers to find a balance between accuracy and timing. To find the optimum number of layers to be used in the simulation and also to see whether or not freezing is required, two test parameters were calculated and compared. The first test value was the oxygen vacancy formation energy. To calculate the oxygen vacancy formation energy, E_{vac} , the following formula was employed:

$$E_{vac} = E(cell_{vac}) + \frac{1}{2}E(O_2) - E(cell)$$

Where $E(cell_{vac})$ is the total energy of Pt-SnO₂ with vacancy, $E(O_2)$ represents the energy of the oxygen molecule, and $E(cell)$ is the energy of the Pt-SnO₂. The above formula was also used to calculate the oxygen vacancy formation energy for the SnO₂ system. In that case, $E(cell_{vac})$ and $E(cell)$ represent total energy of SnO₂ with vacancy and total energy of SnO₂ system respectively. To calculate the adsorption energy of platinum on the SnO₂ surface (E_{ads}), the following formula were used:

$$E_{ads} = [E(Pt_{36} - SnO_2) - E(SnO_2) - E(Pt_{36})]/36$$

Where $E(Pt_{36} - SnO_2)$ is the energy of the Pt-SnO₂ system, $E(SnO_2)$ represents the energy of the bare metal oxide in the absence of platinum and $E(Pt_{36})$ is the energy of platinum cluster (with 36 atoms) in the absence of SnO₂. The summary of such calculations are depicted in Figure 4.3. The details of such calculations are tabulated in Tables C.39-C.42. As it can be inferred from

Figure 4.3, using 3 layers of SnO₂ with freezing bottom layer gives equivalently good results to using eight layers without freezing. As a result, we used three layers and we froze the bottom layer of SnO₂ for constructing Pt-SnO₂ structures.

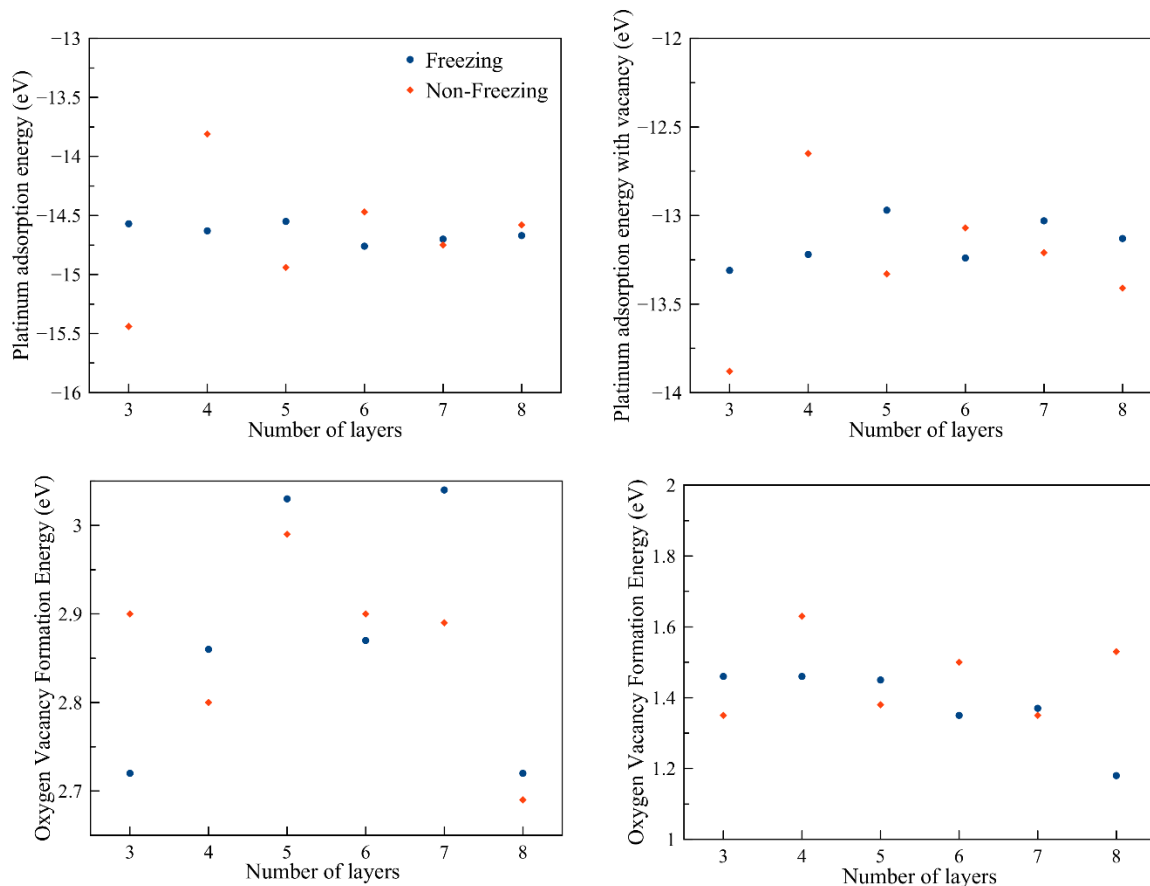


Figure 4.3. Top-left: platinum adsorption energy on SnO₂, top-right: platinum adsorption energy on SnO₂ with one oxygen vacancy present on SnO₂ surface, bottom left: oxygen vacancy formation energy for Pt-SnO₂, bottom right: oxygen vacancy formation energy on SnO₂ surface. For each case, we performed the calculations with and without freezing bottom layer(s) and compared the corresponding energies. In the case of freezing, one bottom layer of SnO₂ was frozen. According to these results, SnO₂ with three layers with freezing the bottom layer was implemented in our study.

The Pt-SnO₂ and PtRh-SnO₂ systems had 216 total atoms. The PtRh rods had 18 Pt atoms and 18 Rh atoms. The three different PtRh rods had Rh atoms in various locations in the alloy

(such as on top of the rod or on one rod face). These models are depicted in Figure 4.4. The structures of the three different models utilized to model PtRh-SnO₂ catalysts are also depicted in Figure 4.4.

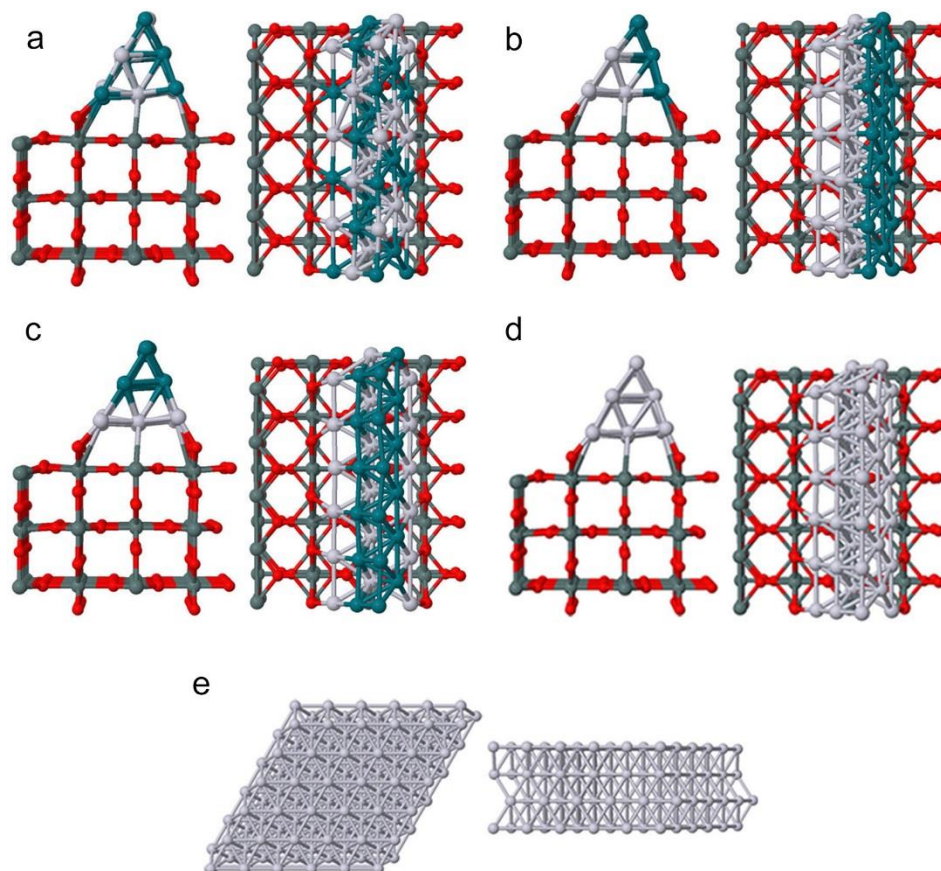


Figure 4.4. Configuration of each model for the DFT calculations: (a) 1st PtRh-SnO₂ model, (b) 2nd PtRh-SnO₂ model, (c) 3rd PtRh-SnO₂ model, (d) Pt-SnO₂ model, and (e) Pt (111).

For bulk Rh₂O₃, we calculated lattice parameters for corundum structure which has hexagonal structure to be $a = 5.22 \text{ \AA}$ and $c = 13.82 \text{ \AA}$. For the Rh₂O₃ surface, we used a model developed by Scherson et al.²⁰⁰ which is an oxygen terminated (0001) surface. Scherson et al.²⁰⁰ modeled 7 possible surface terminations of Rh₂O₃ (three surfaces corresponding to (0001) surfaces and four surfaces corresponding to (1102) surface terminations). They constructed density of states and free energy plots for these surfaces and compared these surfaces to one another. They

concluded that (0001) and (1102) surfaces have similar stability and as a result we used (0001) surface since it was more straightforward to be built. For each (0001) surface termination, Scherson et al. built three surface terminations and showed the oxygen exposed cell is the most reactive and stable one. Our cell size was $10.44 \times 10.44 \times 37.37 \text{ \AA}^3$ containing 40 Rh and 72 O atoms. In order to have an oxygen terminated surface (as Scheron et al's work), we removed the second two top layers of (0001) surface which resulted in an O-exposed non-stoichiometric surface. The corresponding geometry is depicted in the following Figure 4.5.

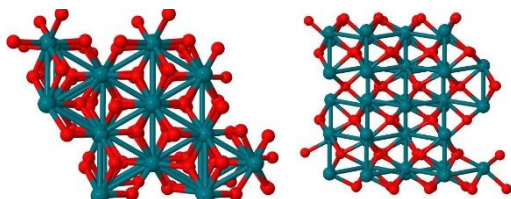


Figure 4.5. Configuration of a) Rh₂O₃, top view (left) and side view (right) used in this work, which is a (0001) surface with O exposed. Blue and red spheres denote Rh and O atoms respectively.

Over the metal surfaces we calculated carbon-carbon bond breaking reaction energies. In order to find reaction energies, first we found the most stable configuration for the adsorption of each species on the surface. To do so, we put adsorbates (CH_x, CO, and CH_xCO) on top, hcp, fcc, and bridge sites and in each case and then calculated the adsorption energies. Such adsorption sites are depicted in Figure 4.6. In the top position the adsorbate directly binds to an atom in the first layer. In the bridge position, the adsorbate binds to two atoms in the first layer forming two bonds; basically the atom adsorbs in between two atoms forming a bridge. In the hcp position, the adsorbate would be put parallel to an atom in the second layer (in other words, if hypothetically we shift the second layer to the first layer, we put the adsorbate on top position of this atom in the second layer). In the fcc position, the adsorbate would be put parallel to an atom in the third layer and similar analogy to the hcp position can be make.

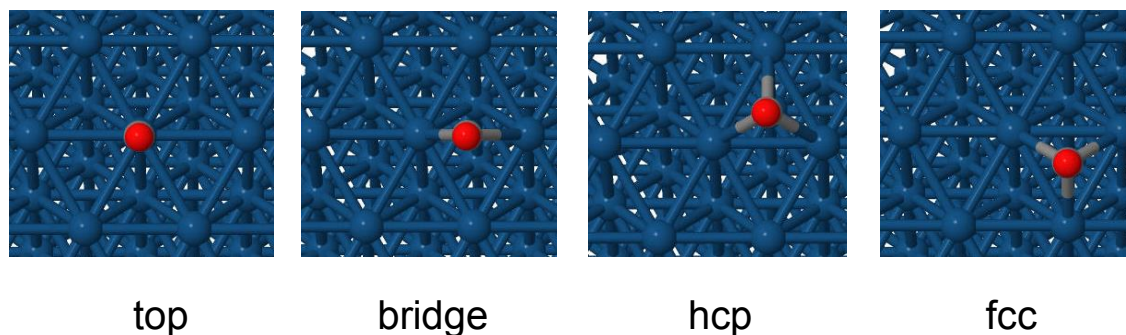


Figure 4.6. CO adsorption on top, bridge, hcp, and fcc sites of the Ir surface. Ir, C, and O atoms are shown as blue, grey, and red spheres respectively.

The most negative adsorption energy corresponds to the most favorable and most stable configuration. The following formula was used to calculate adsorption energies:

$$E_{adsorption} = E_{adsorbate/surface} - E_{surface} - E_{adsorbate\ in\ gas\ phase}$$

In the above equation $E_{adsorbate/surface}$ represents the energy of the adsorbate/surface system, $E_{surface}$ is the energy of the bare surface, and $E_{adsorbate\ in\ gas\ phase}$ is the energy of the gas-phase molecule. In order to calculate adsorption energy on metal-oxide or oxide surfaces, similar strategy has been implemented. The adsorbate was put in different adsorption sites and in different areas (oxide, metallic site, metal/oxide interface) and in each case adsorption energy was calculated with the above formula. After finding the most stable configurations, we proceeded to calculate reaction energies with the following formula:

$$E_{reaction(c-c\ bond\ breaking)} = E_{CH_x} + E_{CO} - E_{CH_xCO} - E_{bare\ surface}$$

In the above equation, $E_{reaction(c-c\ bond\ breaking)}$ corresponds to the reaction energy of the C-C bond breaking in CH_xCO species. E_{CH_x} , E_{CO} , E_{CH_xCO} , and $E_{bare\ surface}$ are the DFT energies corresponding to CH_x , CO, CH_xCO , and bare surface respectively.

In order to find activation energies, Brønsted-Evans-Polanyi (BEP) correlations has been used which estimates reaction barriers based on reaction energies. It is important to note the

reaction energy implemented in the BEP correlations has different definition and uses the gas phase reactant (CH_xCO) as its reference state. In other words, the reaction energy implemented in BEP correlations has been calculated with the following formula:

$$E_{\text{reaction (for BEP correlations)}} = E_{\text{CH}_x} + E_{\text{CO}} - E_{\text{CH}_x\text{CO (gas phase)}} - 2E_{\text{bare surface}}$$

The following linear BEP relation was used to connect transition state and reaction energies:

$$E_{\text{transition state}} = \gamma E_{\text{reaction (for BEP correlations)}} + \xi$$

And to find activation energies the value of the $E_{\text{transition state}}$ was added to the adsorption energy of the CH_xCO species:

$$E_{\text{activation energy}} = E_{\text{transition state}} - E_{\text{CH}_x\text{CO adsorption}}$$

We used parameters published by Wang et al. to calculate activation energies for CHCO , CH_2CO , and CH_3CO bond breaking. The values of $\gamma = 0.85 \text{ eV}$ and $\xi = 2.05 \text{ eV}$ for CHCO , $\gamma = 0.62 \text{ eV}$ and $\xi = 2.73 \text{ eV}$ for CH_2CO , and $\gamma = 0.75 \text{ eV}$ and $\xi = 1.82 \text{ eV}$ for CH_3CO has been used.

4.3. Results and discussion

4.3.1. Pure Metals: Pt, Ir, Rh, Au, and Ag (111) Surfaces

C-C bond breaking of CHCO , CH_2CO , and CH_3CO at the surfaces of Pt, Ir, Au, Ag, and Rh (111) surfaces were modeled. The gaseous species were put in different adsorption sites (top, hcp, fcc, and bridge) and the most negative adsorption energies corresponding to the most stable configurations were determined. Based on the most stable geometries, reaction energies for breaking the C-C bonds were calculated. The corresponding geometries for the C-C bond scission over Ag, Au, Ir, Pt, and Rh (111) surfaces, are summarized in Figures C.35-C.39 in Appendix C respectively. The reaction energy diagrams for the C-C bond scission are summarized in Figure 4.7 in which transition state energies are estimated by Brønsted-Evans-Polanyi (BEP) correlations. As it can be seen from these graphs, Ag (111) and Au (111) surfaces are not favorable for breaking the C-C bond in CHCO , CH_2CO , and CH_3CO . In the case of CHCO and CH_2CO , Ag (111) is the worst metal for C-C bond scission. In the case of CH_3CO , Au and Ag are almost the same (not favorable) in breaking the C-C bond with Au being slightly worse. Our studies show that in the case of CHCO and CH_2CO bond breaking, Ir (111) and Rh (111) have close ability to that of Pt (111) in breaking the C-C bond with Rh being slightly better than the other metals. In the case of

CH₃CO, Ir (111) and Rh (111) are slightly worse than Pt (111) for the C-C bond scission with all three metals having really similar abilities in the C-C bond breaking. Based on these results, Rh is the best metal for breaking the C-C bond in the EOR. Ag and Au both have sluggish tendency to break C-C bond and as a result, using Rh, Ir, and Pt is highly preferred for the C-C bond breaking.

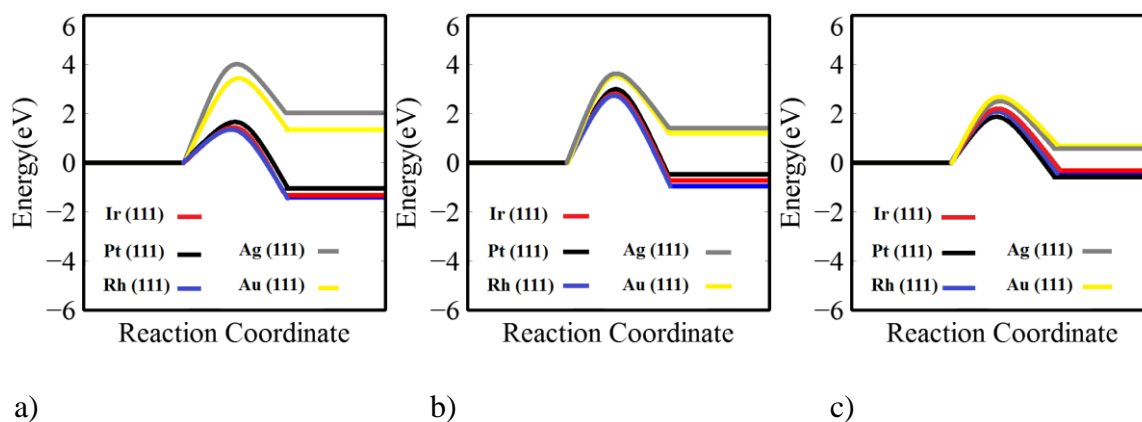


Figure 4.7. Reaction energy for C-C bond splitting of (a) CHCO, (b) CH₂CO, and (c) CH₃CO over the Ag, Au, Ir, Rh, and Pt (111) surfaces.

4.3.2. Alloys: Ir, Ir-Rh, Ir-Rh-Sn Alloys

We modeled carbon-carbon bond breaking of CHCO at the surface of Ir, Ir-Rh, and Ir-Rh-Sn alloys. We chose this specific reaction since it is reported to be the rate determining step in the ethanol oxidation reaction.¹⁶⁻¹⁷ To calculate these reaction energies, we calculated adsorption energies of CH, CO, and CHCO at the surface of Ir, Ir-Rh, and Ir-Rh-Sn. For the adsorption of CH and CO on Ir and Ir-Rh surfaces, three different adsorption sites, namely fcc, hcp, and top, have been modeled. These reaction sites have been shown in Figure C.40-C.45 in Appendix C. If the adsorbate is put on top of the metallic surface in the first layer, we call this adsorption position, top site. If the adsorbate is put on top the metallic surface in the second layer, we call this adsorption position, hcp, and if the adsorbate is put on the top of the metallic surface in the third layer (parallel to the third layer), we call it a fcc site. The hcp and fcc sites are also referred to hollow sites. To elucidate the most negative reaction energy and therefore in order to find the most stable CH adsorption configuration, it is important to consider all possible configurations to

calculate the most negative adsorption energy. Therefore we put adsorbates in top, fcc, and hcp configurations and calculate adsorption energies in each case.

CH and CO adsorption energies in top, hcp, and fcc sites of Ir, Ir-Rh, and Ir-Rh-Sn are summarized in Table C.1. We conclude from these data that CH is most likely to be adsorbed in the hcp site of Ir, Ir-Rh and fcc site of Ir-Rh-Sn. We also can realize that CO is most likely to be adsorbed in a top site of Ir, and hcp site of Ir-Rh and Ir-Rh-Sn surfaces. The most stable configuration for the adsorption of CHCO on Ir, Ir-Rh, and Ir-Rh-Sn is when CH is in bridge and CO is put on top site. The most stable configurations for CH and CO adsorption on Ir surface and that of CHCO are depicted in Figures C.40 and C.41 respectively. The most stable configurations for CH and CO adsorption on Ir-Rh surface and that of CHCO are depicted in Figures C.42 and C.43 respectively. For the adsorption of gaseous species on Ir-Rh-Sn, we also considered the effect of adsorption area (Rh or Sn) on the adsorption energy, meaning we put CH, CO, and CHCO on Rh, Sn, and interface of these metals. Such consideration is depicted in Figure 4.8. The adsorption sites near Sn are highly unfavorable meaning that these adsorbates do not tend to adsorb on. The adsorption energies improve when the adsorbates move away from Sn. The most stable configurations for CH and CO adsorption on the Ir-Rh-Sn surface and for CHCO are depicted in Figures C.44 and C.45 respectively.

CH and CO adsorption energies on different areas and different adsorption sites of Ir-Rh-Sn surface are summarized in Table C.1 and such energies for CHCO adsorptions are summarized in Table C.3. The most negative adsorption energies (corresponding to the most stable configurations) for CHCO adsorption on Ir, Ir-Rh, and Ir-Rh-Sn are shown in Table C.2.

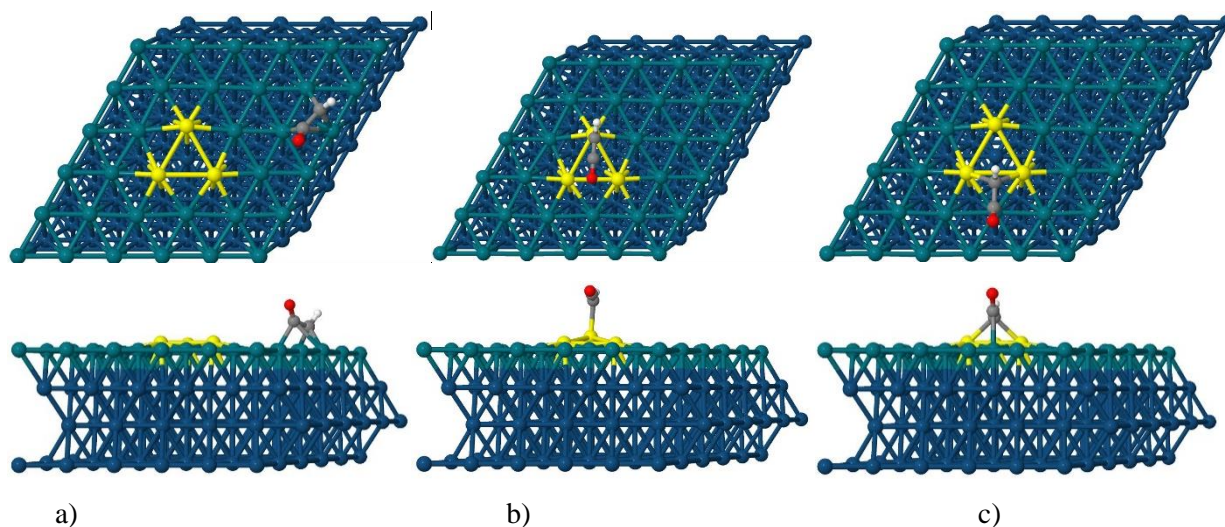


Figure 4.8. CHCO in different geometries and different sites over the Ir-Rh-Sn surface. CHCO was put on different areas including a) Rh atoms, b) Sn atoms, and c) in between those to investigate the effect of the area. Ir, Rh, Sn, C, H, and O atoms are shown as blue, green, yellow, grey, white, and red spheres respectively.

In order to calculate reaction energy over different surfaces, the most stable configuration of each of the products and the reactant is considered. The reaction energy calculations are summarized in Figure 4.9 and Table 4.1. In this figure, the transition state energies are estimated by Brønsted-Evans-Polanyi (BEP) correlations. As it can be seen from Figure 4.9 and Table 4.1, Ir has the most negative reaction energy for C-C bond scission of CHCO. This contradicts our expectation about Rh and Sn improving the ability of Ir in breaking the C-C bond. This contradiction is even more pronounced in the case of Sn. Although the use of Rh and Sn has been recommended for the use in DEFCs^{6, 201}, We hypothesize they had a detrimental effect in C-C bond breaking mainly due to the fact that Rh and Sn tend to oxidize in reaction environment, a feature which has not been considered in our alloy models. Basically, if we model Ir-RhO₂, or Ir-SnO₂, the catalytic activity increases. This is mainly due to the fact that oxide species will provide oxygen containing species such as OH which when react with CH_x or CO species, produce CO₂, the ultimate product for the complete oxidation. This OH concentration is also correlated with the pH of the reaction conditions. In our DFT calculations, we did not consider different concentrations of OH species and in general, we did not consider the presence of different co-adsorbates. Modeling such species, potentially may change the activity of our alloys. In the next

sections we have modeled different oxides specifically Pt-SnO₂, Pt-Rh-SnO₂, and Rh₂O₃ and we confirmed our hypothesis that using oxides of Rh and Sn, will improve C-C bond breaking ability of alloy species.

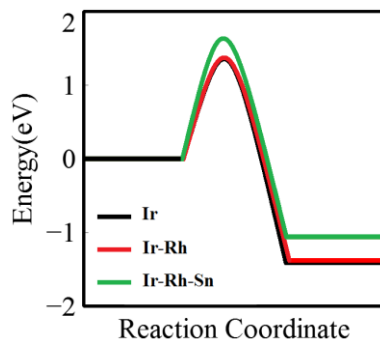


Figure 4.9. Calculated reaction energy diagram for C-C bond scission of $CHCO_{ads}$ over Ir, Ir-Rh, and Ir-Rh-Sn surfaces. Reactant states are adsorbed intermediates (CHCO), and product states are adsorbed dissociated species (CH/CO). The transition state energy indicates the kinetic barrier for dissociation which is estimated by Bronsted-Evans-Polanyi (BEP) correlations. The reference state (adsorbed reactant) on all surfaces was taken to be 0 eV.

Table 4.1. Calculated reaction energies of C-C bond breaking of CHCO on different alloy surfaces.

Surface	Reaction energy(eV)
Ir	-1.41
Ir-Rh	-1.38
Ir-Rh-Sn	-1.06

4.3.3. Metal/Metal Oxide Interfaces: Pt, Pt-SnO₂, and Pt-Rh-SnO₂ Catalysts

We modeled carbon-carbon bond breaking over Pt, Pt-SnO₂, and three different models of Pt-Rh-SnO₂. For Pt-SnO₂ and Pt-Rh-SnO₂ we used the nanorod-oxide model which had been implemented in the literature previously^{199, 202-205}. For Pt-Rh-SnO₂ we used a model similar to Pt-SnO₂ with the difference that we substituted half of Pt atoms with Rh. In the first Pt-Rh-SnO₂

model, we alternatively substituted Pt atoms with Rh. In the second model, we substituted Pt with Rh, in the 3 nanorod layers on the right. For the third model, we substituted 3 nanorod layers on the top with Rh. The corresponding geometries can be found in Figure 4.4. We used the corresponding models for Pt, Pt-SnO₂ and Pt-Rh-SnO₂ to investigate how SnO₂ and Rh would change Pt ability to break the carbon-carbon bond in CH_xCO (x=1,2,3).

To find energies of the above reactions, first we adsorbed CHCO, CH, CO, CH₂CO, CH₂, CH₃CO, and CH₃ species to different areas (Pt, Rh, SnO₂, and metallic- oxide interface) and different adsorption sites (hollow, bridge, and top). We calculated adsorption energies in each case, and using structures with the most negative adsorption energies, we calculated the reaction energies. An example of such geometries and adsorption energies associated with them is depicted in Figure 4.10. The geometries corresponding to most negative adsorption energies (most stable configurations) along with their adsorption energies of the species for the carbon-carbon bond scission in CHCO, CH₂CO, and CH₃CO are summarized in Figures C.46-C.48 respectively.

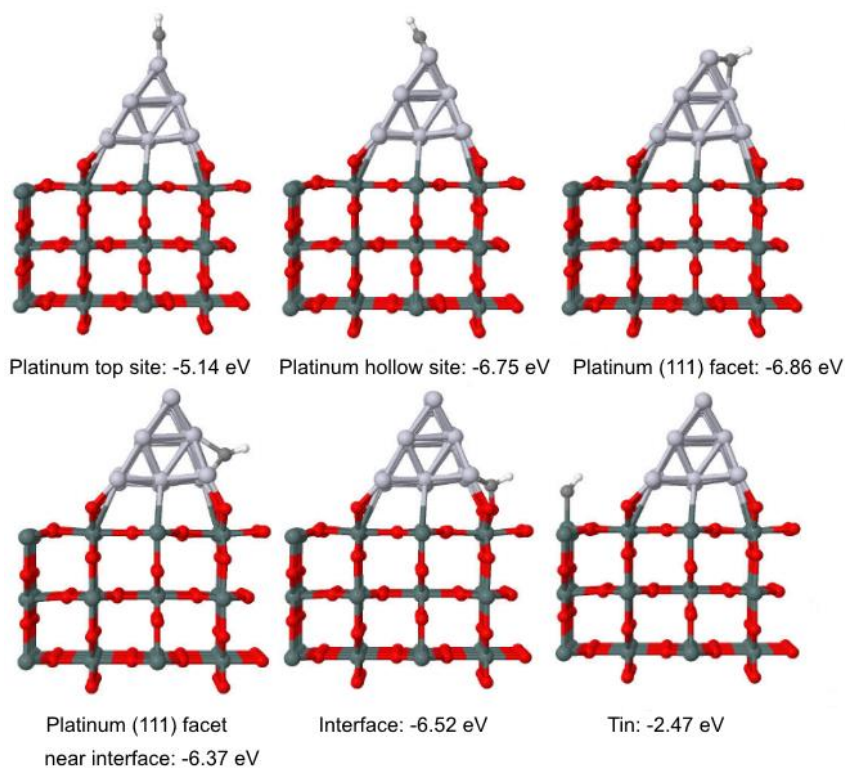


Figure 4.10. CH adsorption on Pt-SnO₂. Adsorption energies of CH are indicated. CH was placed to interact with Pt (the top), the Pt-SnO₂ interface (bottom middle), or SnO₂ (bottom right). To find the best CH adsorption energy on Pt-SnO₂, not only we put CH on different areas (metallic surface, oxide, and metal-oxide interface), but also we put CH on different adsorption configurations including hollow and top sites (these adsorption sites are depicted in Figure 4.6). The best adsorption configuration corresponds to the case in which CH is in a hollow site of the (111) facet (the top right configuration).

Our calculations show the preferential tendency of metallic sites to adsorb CH_xCO, CH_x, and CO species. The adsorption of these gaseous species on different adsorption sites of Pt (111) are summarized in Tables C.5-C.11. The corresponding energies for Pt-SnO₂, Pt-Rh-SnO₂ (first model), Pt-Rh-SnO₂ (second model), and Pt-Rh-SnO₂ (third model) are presented in Tables C.12-C.18, C.19-C.25, C.26-C.32, and C.33-C.38 respectively. These tables contain adsorption energies on all different adsorption sites and all adsorption areas (metallic surface, metal-metal oxide interface, and oxide). The most stable adsorption configurations along with their corresponding energies are depicted in Figures C.46-C.48. We also modeled adsorption of H₂O and OH on Pt, Pt-SnO₂, and three surfaces of Pt-Rh-SnO₂. The most stable configurations for H₂O and OH

adsorption on these surfaces along with their adsorption energies are depicted in Figures 4.11 and 4.12 respectively. In most cases we realized metallic surface is not the preferred adsorption site. Water adsorbed on the top site of Pt, SnO₂ for the 1st and 2nd model of Pt-Rh-SnO₂ and metal-metal oxide interface of 3rd model of Pt-Rh-SnO₂ and Pt-SnO₂. OH adsorbed on the hollow site of Pt, SnO₂ for the 2nd model of Pt-Rh-SnO₂, metallic site next to the metal-metal oxide interface of 1st and 3rd model of Pt-Rh-SnO₂, and metal-metal oxide interface of Pt-SnO₂. In general as evident by these preferred adsorption sites, SnO₂ promotes dissociative adsorption of water to OH. This OH will then react with CH_x and CO species resulting from C-C bond splitting and leads to the production of carbon dioxide. In other words, SnO₂ facilitates complete oxidation of ethanol.

Water adsorption on each model

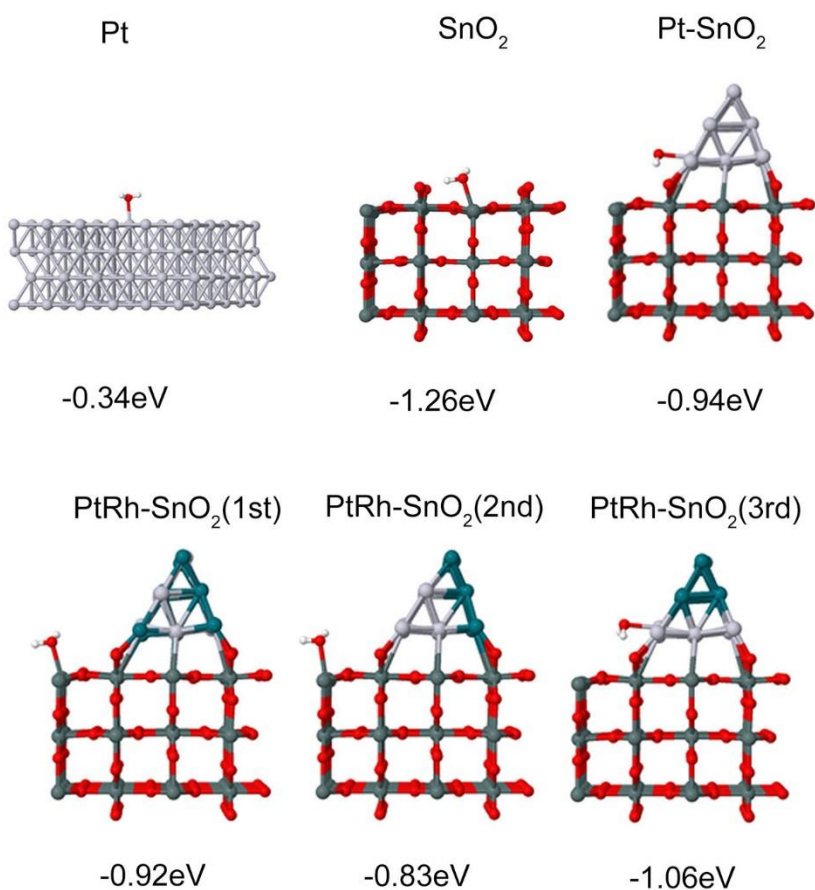


Figure 4.11. Adsorption energies of water on various catalyst surfaces.

*OH adsorption on each model

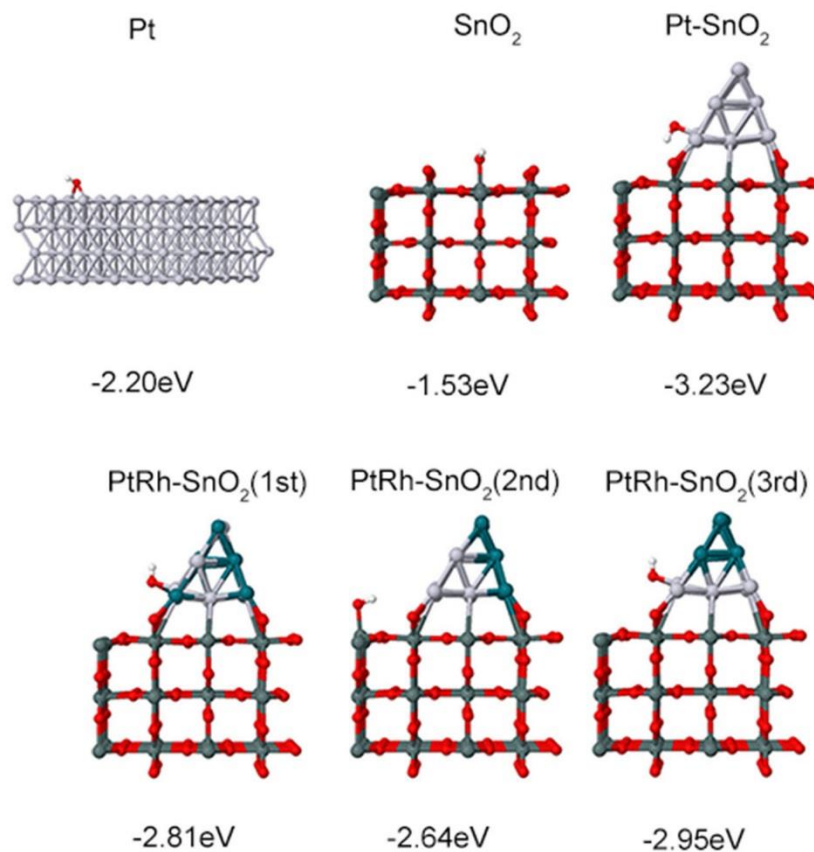


Figure 4.12. Adsorption energies of $*\text{OH}$ on various catalyst surfaces.

Table 4.2. Calculated reaction energies (eV) for C-C bond splitting over various catalyst surfaces ($\text{CH}_x\text{CO} \rightarrow \text{CH}_x + \text{CO}$).

Catalyst	Reactant		
	CHCO	CH_2CO	CH_3CO
Pt(111)	-1.08	-0.5	-0.63
Pt- SnO_2	-1.07	-0.58	-0.45
PtRh- SnO_2 (1 st model)	-1.36	-1.51	-1.08
PtRh- SnO_2 (2 nd model)	-1.62	-1.77	-1.57
PtRh- SnO_2 (3 rd model)	-1.34	-1.33	-0.94

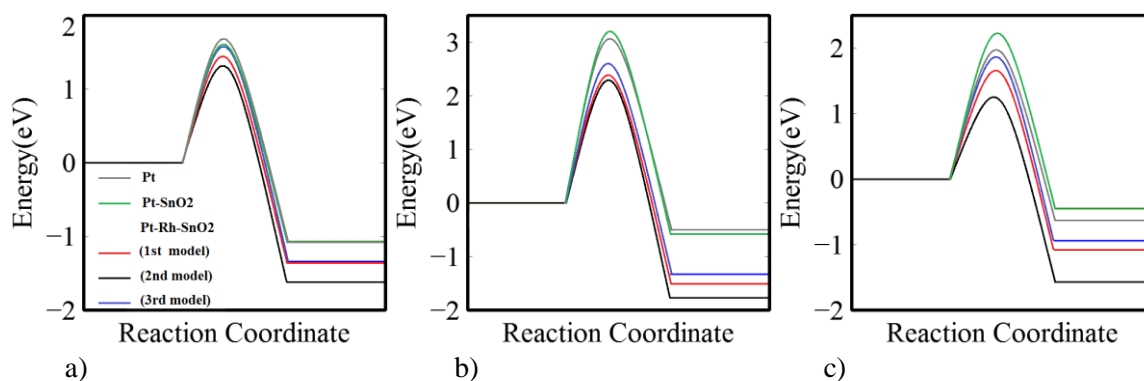


Figure 4.13. Reaction energy for C-C bond splitting of (a) CHCO, (b) CH₂CO, and (c) CH₃CO over the Pt (111), Pt-SnO₂, and PtRh-SnO₂ surfaces.

Table 4.2 and Figure 4.13 show the calculated reaction energies for C-C bond splitting. All the Rh-containing models had lower reaction energies compared to Pt-SnO₂ and Pt (111) demonstrating that Rh facilitates C-C bond spilling. The promotional effect of Rh on C-C bond splitting could be due to the fact that Rh had strong ability to promote β -dehydrogenation of CH₃CHO. CH₃CHO is a reaction intermediate generated from dehydrogenation of α -carbon and hydroxyl group of ethanol molecule; after β -dehydrogenation of CH₃CHO, CH₂CHO is generated, which is a preferred precursor for C-C bond splitting²⁰⁶⁻²⁰⁸. On the other hand, SnO₂ had stronger interactions with water and formed OH via dissociative adsorption of water. The resulting OH species would oxidize adjacent CO or CH_x occupied on Pt and/or Rh sites to CO₂ as reactions $CH_x + OH \rightarrow CO_2$ and $CO + OH \rightarrow CO_2$. In other words, SnO₂ provides OH containing species which when react with CH_x and CO, would lead to the complete oxidation of ethanol by producing CO₂.

4.3.4. Rh and Rh₂O₃

We modeled carbon-carbon bond breaking of CH_xCO (x=1,2,3) over the surfaces of Rh and Rh₂O₃ to see how implementing the lattice oxygen at the surface of Rh will change activity. The reaction energies for C-C bond breaking of CHCO, CH₂CO, and CH₃CO over Rh (111) and Rh₂O₃ are compared in Figure 4.14. As it can be seen, in all cases, Rh₂O₃ is more active towards breaking the carbon-carbon bond and in the case of CH₃CO, this superior effect is more pronounced. As it was mentioned in the introduction section, it has been shown in the literature

that activating the lattice oxygen on the surface of partially oxide metal or metal oxide nanomaterials enhances catalytic activity for CO oxidation, oxygen evolution reaction, lithium ion batteries, and electro-oxidation of ethanol¹⁸³⁻¹⁹³. This enhanced activity may be due to the fact that such oxidized structures possess different electronic structures compared to bulk materials. For instance, metal-oxygen hybridization may occur for such oxides which potentially increases catalytic activity of such materials including Rh₂O₃. Oxide materials also possess preferential tendency to oxidize CH_x and CO species resulting from C-C bond breaking. Such calculations are summarized in Appendix C.8.

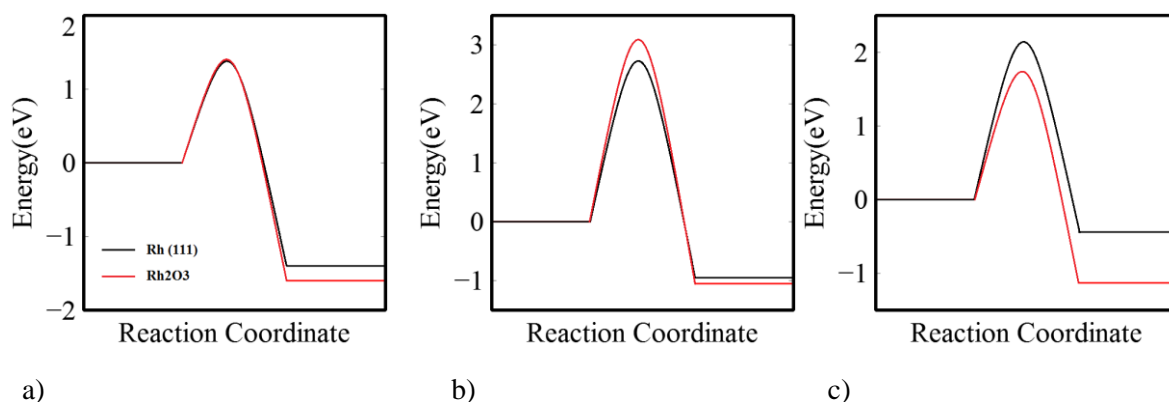


Figure 4.14. Reaction energy for C-C bond splitting of (a) CHCO, (b) CH₂CO, and (c) CH₃CO over the Rh (111) and Rh₂O₃ surfaces. The left, middle, and right pictures corresponds to CHCO, CH₂CO, and CH₃CO surfaces respectively.

4.3.5. Comparison of Pure Metals, Alloys, Metal/Metal Oxide Interfaces, and Metal Oxides

In this section, we compared the ability of pure metals, alloys, metal/metal oxides, and also partially oxide metals in breaking carbon-carbon bond for the ethanol oxidation reaction. For C-C bond breaking in CHCO, the best catalyst among Ir and Ir alloys is Ir. The reaction energy for C-C bond scission in CHCO over Ir (111) surface, was calculated to be -1.41 eV and 1.32 eV with two different versions of CP2K (2.1 and 2.6 versions respectively). We used the second number for the sake of our comparisons since all other calculations (in spite of alloys) has been performed with the newer version of CP2K. We then compared the ability of Ir (111), Rh (111), 2nd model of Pt-Rh-SnO₂, and Rh₂O₃ which are representative of best metal/alloy, transition metal, metal-metal oxide, and metal oxide for C-C bond breaking in CHCO. This comparison is depicted in Figure 4.15 (a). We constructed similar graph for the comparison of the ability of different catalysts in C-

C bond breaking in CH_2CO (Figure 4.15 (b) and also CH_3CO (depicted in Figure 4.15 (c)). For C-C bond breaking of CH_2CO and CH_3CO , we did not perform alloy calculations, specifically Ir, Ir-Rh, and Ir-Rh-Sn. Since Ir-Rh and Ir-Rh-Sn did not improve C-C bond breaking of CHCO , we expect they behave similarly for C-C bond breaking over CH_2CO and CH_3CO . In other words, we expect Ir would be the best metal for breaking the C-C bond among Ir, Ir-Rh, and Ir-Rh-Sn. Rh is the best metal for breaking the C-C bond of CHCO and CH_2CO . That's while in the case of CH_3CO , Pt is slightly better. Comparing different catalysts in Figure 4.15 one can notice the superior catalytic activity of 2nd model of Pt-Rh-SnO₂, specifically for C-C bond breaking in CH_2CO and CH_3CO and therefore Pt-Rh-SnO₂ has the highest ability to break the C-C bond, showing metal-metal oxides in general are better for C-C bond breaking and if one wants a catalyst which works well for C-C bond breaking, they should have some sort of metal oxides present. This is mainly because of the different chemistry involved in each of these categories (metals, alloys, metal-metal oxides, oxides). One involves metallic bonds (the alloys and metals), the other involves more ionic bonds (metal oxides). Formations of the product species are more stable in metal oxides compared to metals and therefore make C-C bond breaking reactions more exothermic. Such metal-metal oxide interfaces with nanorod/oxide models are already investigated^{199, 202-204} in the literature and their superior catalytic activity are attributed to the charge transfer between metal and metal oxide interface^{199, 202-204}.

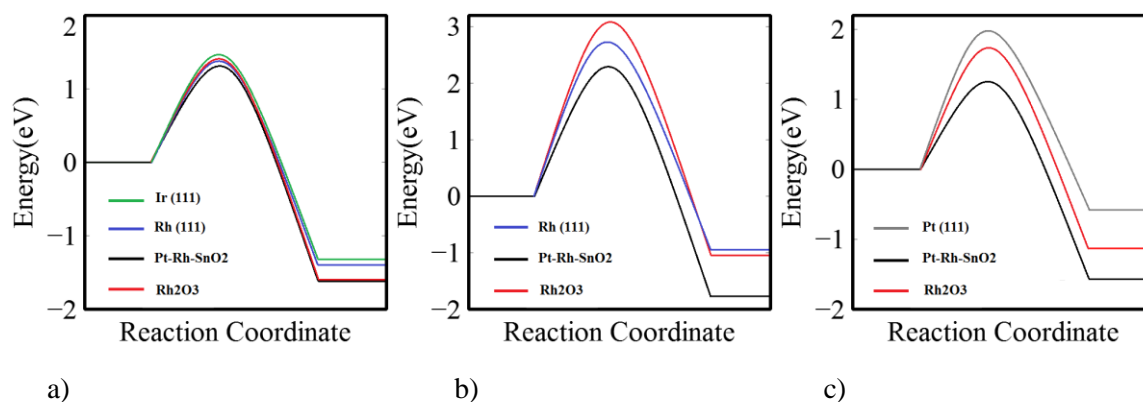


Figure 4.15. Reaction energy for C-C bond splitting of (a) CHCO over most stable catalysts in each category: Ir (most reactive catalyst among Ir and Ir alloys), Rh (most reactive catalyst among transition metals), 2nd model of Pt-Rh-SnO₂ (most reactive catalyst among Metal/Metal Oxide interface), and Rh₂O₃ (Metal Oxide), (b) CH₂CO over most stable catalysts in each category: Rh (most reactive catalyst among transition metals), 2nd model of Pt-Rh-SnO₂ (most reactive catalyst among Metal/Metal Oxide interface), and Rh₂O₃ (Metal Oxide), (c) CH₃CO over most stable catalysts in each category: Pt (most reactive catalyst among transition metals), 2nd model of Pt-Rh-SnO₂ (most reactive catalyst among Metal/Metal Oxide interface), and Rh₂O₃ (Metal Oxide).

4.4. Conclusions

Different catalysts including transition metals (Pt, Ir, Rh, Ag, Au), Ir and Ir alloys (Ir-Rh, Ir-Rh-Sn), metal-metal oxide interfaces (Pt, Pt-SnO₂, three models of Pt-Rh-SnO₂), and Rh and partially oxide Rh (Rh₂O₃) were modeled and their abilities in breaking the carbon-carbon bond in the ethanol oxidation reaction has been compared. Based on our calculations, 2nd model of Pt-Rh-SnO₂ is the best proposed catalyst for C-C bond breaking in the ethanol oxidation reaction.

Chapter 5: Iridium Alloy Structure from DFT and Cluster Expansion

5.1. Introduction

Alloys can have a number of structures, such as ordered, fully mixed, segregated, shell-core, or near surface. The alloy structure in turn determines the electronic and catalytic properties of the alloy. Ir-based alloys have shown promise in a number of catalytic applications, including ethanol oxidation^{72,73}, oxygen reduction²⁰⁹, and hydrogen generation²¹⁰. Ir alloys are especially important as they possess high melting point, high corrosion and oxidation tolerance, and excellent mechanical properties which broaden their applications. Our goal was to provide a systematic understanding of realistic Ir alloys, such as their stability at various temperatures and synthesis conditions. As a preliminary study, we modeled Ir-Pt (111) surfaces to grasp an understanding of these alloys' structures. We then modeled some bulk Ir-Pt alloys and combined DFT with cluster expansion method to identify stable bimetallic Ir alloys. For the bulk structures we specifically focused our attention on Ir-Rh, Ir-Ni, Ir-Cr, Ir-Pt, Ir-Pd, and Ir-Cu alloys. Ir-Pt^{209, 211-214}, Ir-Ni²¹⁵⁻²¹⁷, Ir-Rh²¹⁸, Ir-Pd²¹⁹, and Ir-Cu²²⁰ alloys specifically have been investigated in the literature. In each Ir-M case, we modeled 100 structures with DFT and gave the results to the cluster expansion code. The code then found the energies corresponding to all possible atomic configurations. Here we performed a combination of DFT with cluster expansion results on six bimetallic Ir-M (M=Rh, Ni, Cr, Pt, Pd, and Cu) alloys. One can use the same procedure to model other bimetallic alloys.

It is well established that the physical properties of alloys strongly depend on the alloy structure (configuration and composition). Furthermore, the thermodynamics of alloys such as phase equilibria are greatly influenced by alloy structure. In order to design suitable catalysts knowing the preferred alloy structure is necessary. Furthermore, the alloy structure is susceptible to change in reaction condition, for instance temperature change. Knowing how alloy structure will potentially change in the reaction environment therefore is required to design viable catalysts. Empirical, trial-and-error techniques to synthesize different catalysts may not be efficient, and a combination of theoretical techniques such as density functional theory (DFT) and experimental techniques are desirable. Synthesizing all possible alloys experimentally is a burdensome task and not usually economically efficient. It can save time to model different alloys by means of DFT to propose possible options for catalytic applications. Such desirable alloys then would be synthesized experimentally to make sure they are viable catalysts to be used in desired reactions.

A potential drawback of DFT simulations is the computational cost. This issue arises in modeling alloys with different compositions. A specific alloy, in our case, Ir-M (M=Rh, Ni, Cr, Pt, Pd, Cu), can be modeled with many different structures, meaning that it can have different compositions and configurations. If the Ir-M alloy being modeled for instance contains 16 atoms, there are $2^{16} = 65536$ different configurations for this alloy (as each lattice point can contain either Ir or M). Not all of these configurations are stable. To determine which alloys are stable, the formation energy of these alloys should be compared. To do so, DFT calculations should be performed to obtain electronic energies of these alloys. By obtaining DFT energies, formation energies can be calculated. Conducting 65536 DFT calculations would require a large amount of computation power. To resolve this computational hindrance, a combination of DFT with statistical physics methods, such as the cluster expansion method, has been suggested in literature.

A combination of DFT with the cluster expansion method allows a large number of alloy configuration calculations to be completed in much shorter time. Among the different properties that can be obtained with the cluster expansion method, we focused our attention on determining ground-state energies (among all possible configuration). Having ground state energies, the formation energy diagrams for each bimetallic alloy can be constructed. Formation energy diagrams provide us with valuable information about alloys' formation and we constructed such diagrams for Ir-M (M=Pt, Pd, Cu, Rh, Cr, and Ni) alloys. Formation energy diagrams for these bimetallic Ir alloys then can be compared. Formation energy diagrams inform us about the alloys' ordering tendencies. Such tendencies inform us whether or not synthesizing a specific alloy for our catalytic application is feasible or not.

Formation energy diagrams of different alloys such as Fe-Cr^{221,222}, Ru-Al²²³, Fe-V²²⁴, Co-Yb¹⁴⁸, Pd-Pt²²⁵, Rh-Pt²²⁵, Ag-Au²²⁵, Al-Li²²⁶, Cu-Rh²²⁷, Ag-Pd²²⁸, Cu-Zn²²⁸, Al-Zn²²⁸, Co-Al²²⁸, Fe-Co²²⁹, Cu-Au²³⁰, Pt-Rh²³¹, Pd-V²³², Ni-Pt²³³, Mo-Ta²³⁴, and Pt-Rh²³⁵ have been constructed by different research groups. Our calculations add to the collection of formation energy diagrams and shedlight on the understanding of bimetallic Ir-M alloys' structures.

5.2. Methodology

5.2.1. Computational details of First-Principle Calculations

In first step we modeled Ir-Pt (111) surfaces. Initially we were trying to find the best bimetallic Ir-Pt (111) surface merely by means of DFT. For that matter we used both CP2K⁸²⁻⁸⁶ and VASP¹⁹⁴⁻¹⁹⁸ codes to construct Ir-Pt (111) alloys to see working with which code was easier for future cluster expansion calculations (more description of cluster expansion code will be provided in the next section). In order to compare different alloy structures, we calculated substitution energy per atom (explained in results section) for each structure. After finding potential structures for such surfaces, we decided to combine DFT with cluster expansion code to find the best bulk structure for such alloys. The main motivation to use cluster expansion was computation limitation associated with DFT calculations. We modeled 27 and 34 structures for Ir-Pt (111) surfaces with CP2K and VASP respectively. After modeling such structures, we decided to use VASP code for cluster expansion calculations as it gives us the opportunity to use a smaller cell for the computation ease.

As it was explained in Chapter 2, in order to perform cluster expansion calculations, one needs to have input data from DFT. These data include both structures and energies of the modeled alloys. Having these structures and energies enable the cluster expansion code, GCVC, to find ground state energies for all possible Ir-M alloy configurations (a thorough explanation of cluster expansion method and GCVC code can be found in chapter 2 and Appendix A respectively). After validating the fact that CP2K and VASP codes gave similar results, and after finding the best bimetallic Ir-Pt (111) structures, we decided to use the VASP code to model our bulk structures for use with the cluster expansion code. The reason was the fact that Professor Koretaka Yuge who developed the cluster expansion code (GCVC), used VASP code to model input structures. Technically any DFT code can be used to model input structures. The difficulty associated with CP2K is that to model any input structure, the modeled geometry should be much bigger than the equivalent structure modeled with VASP code. This means an input geometry with VASP code should be repeated to make the cell much bigger. The reason is that CP2K uses only a Gamma point for reciprocal space sampling (more information on reciprocal space can be found in Chapter 2). Using VASP would eliminate this difficulty as instead of increasing the cell size, we only need to use higher k-points.

CP2K uses the Gaussian and plane waves (GPW) method⁸². The Perdew, Burke, and Ernzerhof (PBE) exchange correlation functional¹³¹ along with cutoff energy of 480 eV was used throughout CP2K calculations. Core electrons were represented by Goedecker-Teter-Hutter (GTH) pseudopotentials^{132,133}. All calculations were spin-polarized. We used a double-zeta Gaussian basis set for the Pt and Ir metals¹³⁰. CP2K uses only a Gamma point for reciprocal space sampling so we used a rather large slab to assure convergence with respect to k-points. we used 6×6 Ir (111) cell which was 5 atomic layers thick to model Ir surface. We froze the bottom two layers to the bulk position. We substituted a different number of Ir atoms with Pt in the first, second, and third layers and modeled 27 different Ir-Pt (111) alloys with different Pt compositions. Such geometries are depicted in Figure 5.2. To model Ir-Pt (111) surfaces with VASP, we used a 3×3 Ir (111) cell which was 5 atomic layers thick and again we froze the bottom two layers to the bulk position. The corresponding cell contained 45 atoms. We modeled 34 different configurations with different Pt compositions. Such geometries are depicted in Figure 5.3. We used the PBE¹³¹ exchange correlation functional and the cutoff energy of 400 eV throughout the VASP calculations. Brillouin zone sampling was performed on the basis of the Gamma point with k-point sampling of $4 \times 4 \times 1$ for surface and Monkhost-Pack with k-point sampling of $6 \times 6 \times 6$ for bulk calculations. Method of Methfessel-Paxton order of one with the width of 0.15 eV were employed for VASP calculations. In order to calculate the substitution energy per atom we also needed the bulk energy for Ir and Pt. Our simulation cell for the bulk Ir and Pt contained 500 atoms for CP2K and 4 atoms for VASP. It is worth mentioning that as it was stated before, with VASP we are able to use a small cell since we can implement a large number of k-points. We used a $12 \times 12 \times 12$ k-points Monkhorst-Pack²³⁶ for bulk Ir and Pt.

To model input structures (which are the bulk Ir-Pt alloys) for the cluster expansion code, GCVC²³⁷, we used the VASP code¹⁹⁴⁻¹⁹⁸. We used the same parameters which we used for the Ir-Pt (111) surfaces. We calculated the lattice parameter of Ir to be 3.88 Å. Throughout the calculations, we have used this number as the lattice parameter of the Ir-M systems. Changing the composition of Ir-M alloys does change the lattice parameter. However, such change would be small if the lattice parameters of the two elements in the alloy are close enough. We will show in the results section that for instance in the case of Ir-Pt alloys, using lattice parameter of Ir for the whole system is a valid approximation since Ir and Pt possess similar lattice parameters. We will also show that this is not the case for Ir-Cr if lattice parameter of Ir be used for the whole system

as Ir and Cr do not possess similar lattice parameters. Our simulation cell for Ir-M bulk calculations had 32 atoms. To construct DFT geometries required for the cluster expansion calculations, random and ordered alloys were constructed by substituting different number of Ir atoms in Ir-M alloys with M.

5.2.2. Computational details of Cluster Expansion

To run cluster expansion code, one needs to have input structures along with energies of these structures. These geometries and their energies are calculated by means of DFT. In other words, we have modeled finite number of alloy configurations by means of DFT and calculated their corresponding energies. Such geometries along with their energies then were given to the cluster expansion code, GCVC as the input. Based on these input configurations and energies, GCVC have found configurations and energies corresponding to all possible atomic configurations. In other words, if the modeled cell consists of 16 atoms, there will be 2^{16} possible atomic configurations. We modeled only 100 structures with DFT. We then gave such structures along with their corresponding energies to cluster expansion code and GCVC code found configurations and energies corresponding to 2^{16} possible atomic configurations. The general idea behind the cluster expansion code is presented in section 2.2 of Chapter 2. The detailed explanation of cluster expansion code, GCVC can be found in Appendix A. We generated 100 ordered and random structures of Ir-M (M=Pt, Pd, Rh, Cu, Cr, Ni) alloys and performed geometry optimization DFT calculations to find energies corresponding to these structures. The initial geometries and corresponding energies were given as input to the cluster expansion code. The generalized cluster-expansion for variable and complex systems (GCVC) code²³⁷ developed by Professor Koretaka Yuge at Kyoto University has been used in this work.

To run the GCVC code, we used a lattice comprised of 256 atoms. It is important to note that the cell being used for cluster expansion calculations should be big enough so that more number of clusters (interactions) can be employed. For instance, imagine a cell containing only 4 atoms. The number of four body interactions (an interaction between four atoms) is only one. That's while if we have 256 atoms in our cell, this number is 35, meaning there are 35 different clusters corresponding to four body interactions. Using a small cell therefore, decreases cluster expansion accuracy considerably and it is almost impossible to get accurate results with a small cell size. So using a large cell is necessary in cluster expansion calculations. In the present study,

we have considered up to quadruplet interactions and for each interaction, we specified a cut off radius specifying to the code to consider n-body interactions up to the defined radius. We specified 6 Å for pair, triplet, and quadruplet clusters resulting in 4, 12, and 35 clusters for two, three, and four body interactions respectively. We also have one empty cluster and one point cluster which will result in 53 clusters overall. Based on these specific criteria, GCVC will find the coordinates of all clusters along with their lengths. We originally used 4 Å, 4 Å, and 80 Å for pair, triplet, and quadruplet clusters resulting in 2, 2, and 152 clusters for two, three, and four body interactions respectively, which considering empty and point clusters it resulted in 158 clusters overall. These settings resulted in considerably high CV score (20 meV/atom). The high CV score is directly correlated with the choice of cut off radius. As the number of interactions increases, their importance in cluster expansion decreases. In other words, pair interactions have much bigger effect in summation in Equation (2.17) in Chapter 2. Triplet interactions are more important than quadruplet and so on. 4 Å, 4 Å, and 80 Å cut off radii would result in low number of clusters for two and three body interaction, while resulting in high number of clusters for four body interactions which is not much important. We tried different cut off radii and in each case calculated CV score and confirmed using 4 Å, 4 Å, and 80 Å for pair, triplet, and quadruplet clusters would result in reasonable number of clusters.

There are different sub codes implemented within the GCVC code. The reader is encouraged to refer to Appendix A for more detailed explanation of these sub codes. It is important to note that each sub code has a different function and different settings and it is possible to use different cell sizes for each sub code, since we divide the energy by number of atoms and report eV/atom for our calculations, using different cell sizes would not harm our calculations. It is also important to note that the cell used for DFT calculations can be of different size of cluster expansion codes for the same reason. We used a cell comprising 256 atoms to construct our clusters. We started with a small cell for the DFT calculations (containing 32 atoms) and expanded to a cell with 256 atoms in the cluster expansion calculations to get correlation (basis) functions. More detailed explanation can be found in Appendix A.

Having basis functions and DFT energies, the GCVC code will find effective cluster interactions and eventually all possible geometries with their corresponding energies. The explanation of effective cluster interactions and how GCVC finds them is explained in section 2.2

in Chapter 2 and Appendix A respectively. The energies obtained with DFT and GCVC are compared. If these energies are within the accuracy which user defines, the cluster expansion has converged. Otherwise, the most stable configurations found with the cluster expansion method will be added to the DFT database and the same procedure will be performed until required accuracy is achieved.

5.3. Results and discussion

5.3.1. Calculation of Substitution Energy per Atom for Ir-Pt (111) Surfaces

Before running the cluster expansion code, we generated Ir-Pt (111) alloys with different atomic compositions and also different geometries, and ran the calculations with CP2K and VASP to compare substitution energies per atom for Ir-Pt alloys to determine which atomic configurations are preferred. This parameter can also be an indicator of segregation phenomena which was explained in detail in Chapter 3. Substitution energy per atom can be determined by the following formula:

$$\Delta E_{\text{substitution energy per atom}} = \frac{1}{n} (E_{\text{alloy}} + n \times E_{\text{Ir}} - n \times E_{\text{Pt}} - E_{\text{Ir}(111)}) \quad (5.1)$$

In the above equation, substitution energy per atom is denoted by $\Delta E_{\text{substitution energy per atom}}$. n is the number of Pt atoms in the Ir-Pt (111) alloy. E_{alloy} is the DFT energy for the Ir-Pt (111) alloy, E_{Ir} is the DFT bulk energy of Ir divided by number of Ir atoms used in the simulation bulk cell. In other words, E_{Ir} is the bulk energy per atom of Ir. E_{Pt} is the DFT bulk energy of Pt divided by number of atoms in the bulk (bulk energy per atom for bulk Pt). $E_{\text{Ir}(111)}$ is the DFT energy obtained for the Ir (111) surface. The above equation can be visualized as the following:

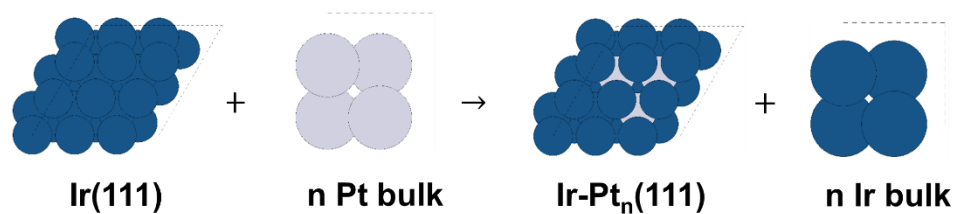


Figure 5.1. Visual demonstration of Equation (5.1) for calculating substitution energy per atom using Ir-Pt (111) surfaces.

We generated surfaces with VASP and CP2K and in each case calculated substitution energy per atom. The modeled Ir-Pt (111) surface with CP2K code are depicted in Figure 5.2. and the calculated substitution energies per atom are summarized in Table 5.1. The simulated geometries for Ir-Pt (111) surfaces using VASP code are demonstrated in Figure 5.3. and calculated substitution energies per atoms are summarized in Table 5.2. We substituted a different number of Ir atoms in different layers with Pt. Thus to refer to each configuration, we used this notation:

$$n_{Ir \text{ in } 1st \text{ layer}} : n_{Pt \text{ in } 1st \text{ layer}} \quad n_{Ir \text{ in } 2nd \text{ layer}} : n_{Pt \text{ in } 2nd \text{ layer}} \quad n_{Ir \text{ in } 3rd \text{ layer}} : n_{Pt \text{ in } 3rd \text{ layer}}$$

In other words, for each layer, we reported the number of Ir and Pt atoms respectively. Figure 5.2 shows examples using this notational system.

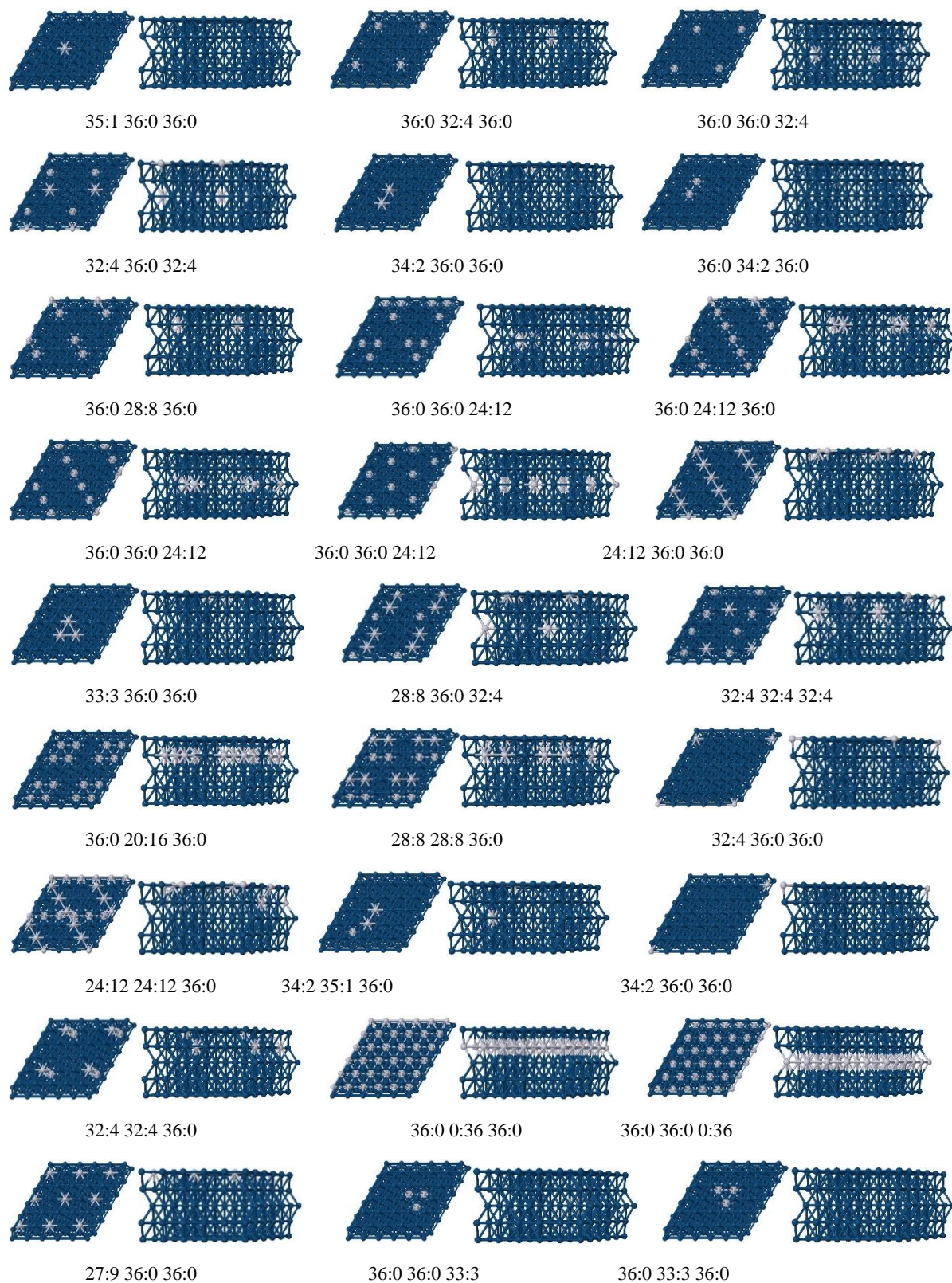


Figure 5.2. Ir-Pt (111) alloys modeled with the CP2K code. Three ratios are reported for each geometry. The first and second numbers denote number of Ir and Pt atoms in each layer respectively.

Table 5.1. Substitution energy per atom for Ir-Pt (111) surfaces modeled with CP2K code

Composition profile	Substitution energy per atom	Position of impurity
24:12 36:0 36:0	-0.44	1 st layer
32:4 36:0 36:0	-0.42	1 st layer
33:3 36:0 36:0	-0.41	1 st layer
35:1 36:0 36:0	-0.39	1 st layer
34:2 36:0 36:0	-0.38	1 st layer
34:2 36:0 36:0	-0.38	1 st layer
27:9 36:0 36:0	-0.29	1 st layer
28:8 36:0 32:4	-0.22	1 st and 3 rd layers
32:4 32:4 36:0	-0.21	1 st and 2 nd layers
24:12 24:12 36:0	-0.19	1 st and 2 nd layers
28:8 28:8 36:0	-0.14	1 st and 2 nd layers
32:4 36:0 32:4	-0.13	1 st and 3 rd layers
34:2 35:1 36:0	-0.10	1 st and 2 nd layers
32:4 32:4 32:4	-0.07	1 st , 2 nd and 3 rd layers
36:0 32:4 36:0	-0.02	2 nd layer
36:0 34:2 36:0	0.03	2 nd layer
36:0 36:0 33:3	0.06	3 rd layer
36:0 33:3 36:0	0.06	2 nd layer
36:0 28:8 36:0	0.08	2 nd layer
36:0 20:16 36:0	0.09	2 nd layer
36:0 0:36 36:0	0.09	2 nd layer
36:0 24:12 36:0	0.11	2 nd layer
36:0 36:0 0:36	0.13	3 rd layer
36:0 36:0 24:12	0.15	3 rd layer
36:0 36:0 24:12	0.16	3 rd layer
36:0 36:0 32:4	0.17	3 rd layer
36:0 36:0 24:12	0.17	3 rd layer

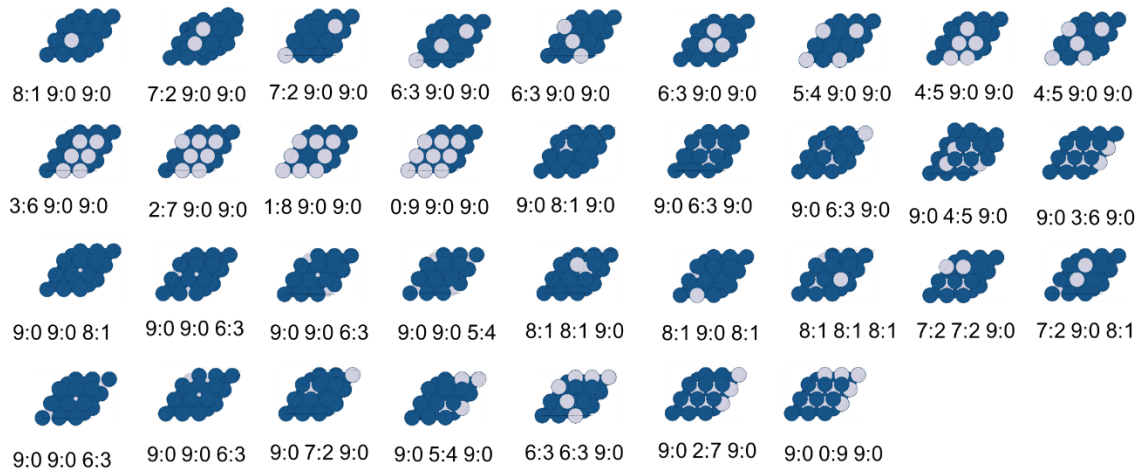


Figure 5.3. Ir-Pt (111) alloys modeled with the VASP code. Three ratios are reported for each geometry. The first and second numbers denote number of Ir and Pt atoms in each layer respectively.

Table 5.2. Substitution energy per atom for Ir-Pt (111) surfaces modeled with VASP code

Composition profile	substitution energy per atom (eV)	Position of impurity
6:3 9:0 9:0	-0.38	1 st layer
1:8 9:0 9:0	-0.37	1 st layer
0:9 9:0 9:0	-0.37	1 st layer
2:7 9:0 9:0	-0.37	1 st layer
3:6 9:0 9:0	-0.36	1 st layer
4:5 9:0 9:0	-0.36	1 st layer
4:5 9:0 9:0	-0.36	1 st layer
7:2 9:0 9:0	-0.36	1 st layer
8:1 9:0 9:0	-0.36	1 st layer
6:3 9:0 9:0	-0.36	1 st layer
6:3 9:0 9:0	-0.35	1 st layer
5:4 9:0 9:0	-0.35	1 st layer
7:2 9:0 9:0	-0.35	1 st layer
7:2 9:0 8:1	-0.13	1 st and 3 rd layers
8:1 8:1 9:0	-0.08	1 st and 2 nd layers
6:3 6:3 9:0	-0.07	1 st and 2 nd layers
8:1 9:0 8:1	-0.05	1 st and 3 rd layers
7:2 7:2 9:0	-0.03	1 st and 2 nd layers
8:1 8:1 8:1	0.05	1 st , 2 nd , and 3 rd layers
9:0 9:0 8:1	0.21	3 rd layer
9:0 9:0 6:3	0.22	3 rd layer
9:0 9:0 6:3	0.23	3 rd layer
9:0 9:0 6:3	0.23	3 rd layer
9:0 9:0 5:4	0.24	3 rd layer
9:0 9:0 6:3	0.24	3 rd layer
9:0 0:9 9:0	0.24	2 nd layer
9:0 8:1 9:0	0.25	2 nd layer
9:0 2:7 9:0	0.26	2 nd layer
9:0 3:6 9:0	0.27	2 nd layer
9:0 7:2 9:0	0.27	2 nd layer
9:0 6:3 9:0	0.27	2 nd layer
9:0 4:5 9:0	0.28	2 nd layer
9:0 6:3 9:0	0.29	2 nd layer
9:0 5:4 9:0	0.29	2 nd layer

As it can be seen from Tables 5.2 and 5.3 using CP2K and VASP codes gave consistent results: putting Pt as an impurity in the first layer, independent of its composition, gave the most negative substitution energy per atom, meaning that Pt prefers to be in the first layer. Putting Pt in the second or third layer generally gave positive substitution energies per atom. This demonstrates the fact that Pt being in the second or third layer is unfavorable. We also modeled Pt in a combination of layers. If we have more Pt atoms in first layer (and less Pt atoms in second and third layers), we get negative substitution energy per atom. That's while if we put more Pt atoms in second and/or third layers (and less Pt atoms in first layer) we get positive substitution energy per atom. For example, when we consider the case of a 7:2 9:0 8:1 composition profile the calculated substitution per atom was -0.13 eV, while in the case we used a 8:1 8:1 8:1 composition profile the substitution energy per atom was calculated to be 0.05. In the first case since we have more Pt atoms in the first layer, we have an overall negative substitution energy per atom while in the second case we have two Pt atoms in the second and third layers, so the corresponding energy is positive. This observation about Ir-Pt (111) alloys is consistent with what we showed for the segregation tendency of Ir-Pt alloys in chapter 3. In chapter 3 we calculated segregation energy of Pt dopants from the bulk to the surface and from the second layer to the surface of Ir (111) to be -0.74 and -0.39 eV, respectively. This demonstrates the fact that Pt prefers to segregate to the surface of Ir (111). In order to rationalize the reasoning behind this segregation tendency we developed a model in Chapter 3 which predicts segregation behavior in different surfaces of Ir, Pt, Pd, and Rh as host metals.

5.3.2. CV Score Minimization:

As it was explained in Appendix A, the Cross Validation (CV) score is an indicator of cluster expansion accuracy. The CV score can be calculated by Equation (5.2):

$$CV\ score = \sqrt{\frac{1}{N_s} \sum_{m=1}^{N_s} (E_{DFT}^m - E_{CE}^m)^2} \quad (5.2)$$

In the above equation, N_s is the total number of input structures and E_{DFT}^m and E_{CE}^m are the energies of structure m obtained with the DFT and cluster expansion methods, respectively. In order for the cluster expansion to give reliable results, the CV score should be as small as possible which implies that the energies obtained from the cluster expansion method are close to the DFT energies. It has been established in the cluster expansion community^{235, 238-239} that usually CV

scores should be below 1 meV/atom for the cluster expansion method to give accurate results. To accomplish this goal two different factors should be taken into account. The first one is the choice of DFT geometries and the second is using a wise choice of clusters. To choose good DFT geometries which are geometries resulting in lowest CV score, there is a sub code embedded in GCVC which enables the user to find the best input DFT structures. To find such structures, one needs to guess initial geometries, run the cluster expansion code to find correlation functions and effective cluster interactions to enable the cluster expansion code to find best configurations to be used for DFT calculations. More detailed explanation of constructing such geometries with the cluster expansion code and different sub-codes embedded in GCVC can be found in Appendix A. After performing DFT calculations for these geometries and then using the GCVC code, we then calculated the CV score for the binary Ir-M alloys. Initially we obtained a value of 20 meV/atom (as it was explained earlier) for the Ir-Pt system, which was not within our desired accuracy. The reason was the choice of cut off radii which resulted in high number of quadruplet clusters and low number of pair and triplet clusters. After correcting the cut off radii, we got higher number of pair and triplet clusters along with lower number of quadruplet clusters which improved our cluster choice. As a rule of thumb, using 50-60 total clusters is sufficient to run GCVC for binary alloys. As a result we changed the parameters in getCluster (a sub-code of GCVC) so that we got 53 total clusters. After running GCVC code with the new settings we managed to decrease CV score to 0.72 meV/atom which is accurate enough for our purposes. The CV score for Ir-Pd, Ir-Cr, Ir-Ni, Ir-Cu, and Ir-Rh systems were calculated to be 1.1, 11.5, 1.4, 4.9, and 0.1 meV/atom respectively. The high CV score for Ir-Cr is due to the fact that Cr possess body-centered cubic (bcc) crystal structure while Ir has face-center cubic (fcc) crystal structure. We used the GCVC code assuming Ir-M alloys possesses fcc structures. This is only problematic for the case of Ir-Cr alloys with Cr being the only non-fcc metal. In spite of having relatively high CV score, the formation energy obtained from GCVC code is still predicts a negative value which is an indication of alloy formation. In the next section we discuss the sources of error in this calculation and the ways to improve this number.

5.3.3. Construction of Formation Energy Diagrams to Find the Most Stable Configurations for Ir-M Alloys

The following formula has been used to calculate the formation energy of the binary Ir-M alloys:

$$E_{formation}(\sigma) = E(\sigma) - (E_{Ir}^{pure} \cdot x_{Ir} + E_M^{pure} \cdot x_M) \quad (5.3)$$

In the above equation $E_{formation}(\sigma)$ denotes the formation energy per atom for a specific configuration σ . $E(\sigma)$ is the energy per atom for configuration σ obtained from simulation. E_{Ir}^{pure} and E_M^{pure} are the energies per atom for pure iridium and pure M metal, and x_{Ir} and x_M denote the atomic fractions of iridium and metal M in the alloy respectively. It is important to note when calculating formation energies based on DFT, all values should be extracted from DFT simulations including $E(\sigma)$, E_{Ir}^{pure} , and E_M^{pure} . The same thing applies when calculating formation energies based on cluster expansion. The formation energy diagram for Ir-Pt alloy obtained from cluster expansion method is depicted in Figure 5.4.

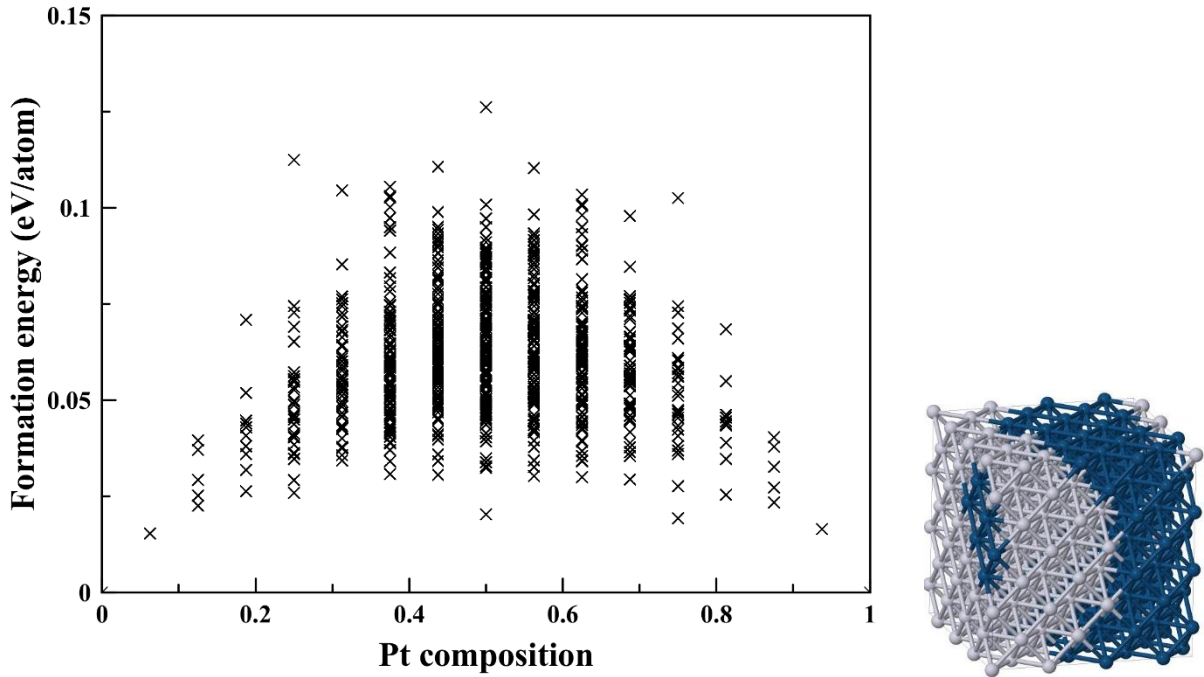


Figure 5.4. Formation energies for bulk Ir-Pt obtained from cluster expansion (GCVC code) along with half-half composition (one of the most stable structures)

Figure 5.4 shows that the formation energies for the Ir-Pt system are positive. It also shows one of the most stable structures for Ir-Pt alloys. The positive formation energy values imply phase separation.²⁴⁰ Generally speaking, negative formation energy is an indicative of ordering, while positive values imply phase separation.²⁴⁰ This observation is consistent with the geometry

depicted in Figure 5.4. The most stable structures correspond to the geometries which possess the least formation energies. It is evident from Figure 5.4 that most stable structures tend to phase separate. This is consistent with the Ir-Pt phase diagram²⁴¹. According to Ir-Pt phase diagram, these alloys tend to form solid solutions at high temperatures regardless of their compositions. It is also observed²⁴¹ that at lower temperatures, two phase (Pt-rich and Ir-rich) equilibrium is thermodynamically favorable. In another study²⁴², Pt-Ir nanoparticles loaded on activated carbon support were synthesized with Pt, Ir, and C atomic compositions being 5.9, 4.3, and 89.8 respectively. The authors also incorporated 1:1 Pt/Ir ratio in Pt-Ir/C electro-catalyst in the molecular structural design of the DFT calculations²⁴². In another study²⁴³, Pr-Ir/C catalysts were prepared by having 20% platinum, 20% iridium, and 60% carbon. These results are aligned with our cluster expansion results. Based on our results, one of the most stable Ir-Pt alloys corresponds to the geometry where iridium and platinum have the same compositions in the alloy. The corresponding geometry is depicted in Figure 5.4.

We conducted the same procedure (which has been conducted for Ir-Pt alloys) for Ir-Rh, Ir-Ni, Ir-Cr, Ir-Pd, and Ir-Cu alloys. In each case, we constructed about 100 Ir-M bulk alloys consisting of different M compositions and different atomic configurations. Then we used the GCVC code and constructed formation energy diagrams in each case. The corresponding diagrams are depicted in Figures 5.8-5.12. In each case, the most stable configuration, corresponding to the lowest formation energy is also demonstrated in the right of the formation energy diagram in each case. As evident from these figures (and also Figures 5.4 and 5.5 for Ir-Pt), some alloys including Ir-Pt, Ir-Pd, and Ir-Cu phase segregate and do not tend to form an alloy. On the other hand, some alloys including Ir-Rh, Ir-Ni, and Ir-Cr mix well and form alloys.

For Ir-Pt, formation energy were between 0.0153 ($x_{Pt} = 0.0165$) and 0.12619 ($x_{Pd} = 0.5$) eV/atom. The most favorable alloy configurations correspond to these formation energies: 0.0153 ($x_{Pt} = 0.0625$), 0.0165 ($x_{Pt} = 0.9375$), 0.01927 ($x_{Pt} = 0.75$), and 0.02032 ($x_{Pt} = 0.5$). The 50-50 % atomic configurations' formation energies were between 0.020 and 0.126 eV/atom. Kolb et al.²⁴⁴ reported the value of 0.065 eV/atom for this atomic composition which validates the accuracy of our procedure.

For Ir-Pd, formation energy were between 0.019 ($x_{Pd} = 0.0625$) and 0.194 ($x_{Pd} = 0.5$) eV/atom. The most favorable alloy configurations correspond to these formation energies: 0.0193

($x_{Pd} = 0.0625$), 0.0285 ($x_{Pd} = 0.9375$), 0.031305 ($x_{Pd} = 0.125$). The 50-50 % atomic configurations' formation energies were between 0.04013 and 0.19392 eV/atom. Kolb et al.²⁴⁴ reported the value of 0.098 eV/atom for this atomic composition which validates the accuracy of our procedure.

For Ir-Cu, the formation energies were between 0.0226 ($x_{Cu} = 0.0625$) and 0.265905 ($x_{Cu} = 0.5$) eV/atom. The most stable configurations have formation energies of 0.0226 ($x_{Cu} = 0.0625$), 0.0296 ($x_{Cu} = 0.9375$), and 0.037249 ($x_{Cu} = 0.125$) eV/atom. The 50-50 % atomic configurations' formation energies were between 0.060785 and 0.265905 eV/atom.

For Ir-Rh, formation energies were between -0.00271 ($x_{Rh} = 0.75$) and -0.02027 ($x_{Rh} = 0.5$) eV/atom. The most negative formation energy corresponds to a half-half composition (-0.02027 eV/atom). The half-half compositions are between -0.00807 to -0.02027 eV/atom. Kolb et al.²⁴⁴ reported a value of -0.016 eV/atom for this atomic composition which again validates the accuracy of our cluster expansion method.

Originally for Ir-Cr system, we used lattice parameter of Ir for the whole system. After performing cluster expansion calculations, not only we got relatively a high CV score (13.8 meV/atom), we also got a value of -0.4 eV/atom for formation energy of half/half composition which is almost twice the value reported in the literature (-0.239 eV/atom)²⁴⁵. The source of this error is the fact that Ir (lattice parameter = 3.84 Å) and Cr (lattice parameter = 2.91 Å) do not possess similar lattice parameters. For that matter we performed new sets of calculations in which we also optimized the cell's lattice parameter. With this method we improved CV score to 11.5 meV/atom and also improved our formation energy diagram (Figure 5.9). In the first case, when we did not optimize lattice parameter for each geometry, we used 95 atomic configurations. However, for the second case when we optimized lattice parameter, we used 31 different atomic configurations due to time limitation. We suspect if we increase number of input geometries, we can improve CV score, as evident for our other Ir-M alloys.

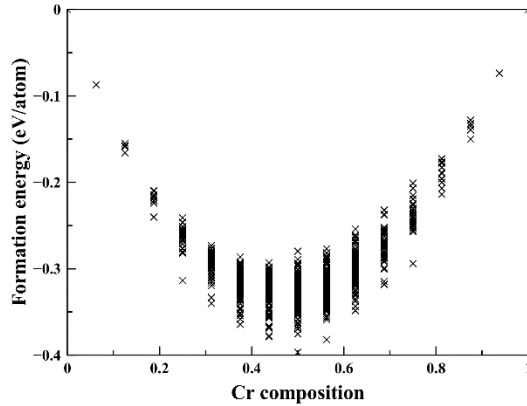


Figure 5.5. Formation energy diagram for the bulk Ir-Cr obtained from cluster expansion (GCVC code). In order to construct this formation energy diagram, lattice relaxation has not been performed. This resulted in getting a high CV score (13.8 meV/atom) along with much more negative formation energy compared to literature data. In order to modify this graph, full cell optimization has been performed for DFT calculations and the modified graph is depicted in Figure 5.

For Ir-Cr, formation energies were between -0.21473 to 0.069008 eV/atom (both correspond to $x_{Cr} = 0.75$). The most stable structures have formation energies of -0.21473 ($x_{Cr} = 0.75$) and -0.203 ($x_{Cr} = 0.625$) eV/atom. The half-half composition has formation energies between -0.1967 and -0.03192 eV/atom. This number is reported to be -0.239 eV/atom in the literature²⁴⁵. The slight difference between our reported formation energy and literature value is the fact that Ir and Cr have different crystal structures, Ir and Cr possess fcc and bcc crystal structures respectively, that's while we considered fcc crystal structure for all atomic compositions. This might be a source of error, especially for structures which have high atomic Cr compositions. The other source of error might be due to lower number of input geometries for Ir-Cr calculations. Increasing number of input geometries (as evident by our other Ir-M alloys) would potentially improve our calculated CV score. Still our calculations give reasonable formation energies for Ir-Cr and gives negative value for formation energies which is consistent with literature value²⁴⁵.

For Ir-Ni, the formation energies were between -0.11569 eV/atom ($x_{Ni} = 0.5$) and 0.008788 eV/atom ($x_{Ni} = 0.25$). The most negative formation energies were -0.11569 ($x_{Ni} = 0.5$), -0.11183 ($x_{Ni} = 0.375$), and -0.11128 ($x_{Ni} = 0.4375$). The half-half composition had

formation energies between -0.11569 and -0.05148 eV/atom. Based on Hart et al.'s paper²⁴⁵, at low temperatures, Ir-Ni alloys with negative formation energies have been found with DFT calculations. They reported based on experiments however, Ir and Ni do not form compounds. They reported the value of -0.0358 eV/atom for the formation energy of Ir-Ni. The slight difference between Hart et al.'s value and our formation energy is due to lattice mismatch for Ir and Ni. We did not optimize our lattice cell during our VASP calculations (We only performed lattice optimization for Ir-Cr alloys). This is not problematic for Ir-Pt, Ir-Pd, and Ir-Rh, since lattice parameters of Ir, Pt, Pd, and Rh are 3.84, 3.92, 3.89, and 3.80 Å respectively. For Ir-Ni alloys however, Ir and Ni have lattice parameters of 3.84 and 3.52 Å respectively. Using the same lattice parameter for the alloy has caused a slight error in our calculations. Still our value is close to the literature data²⁴⁵ and we got negative formation energy for Ir-Ni alloys which means Ir and Ni would form compound at low temperatures which is consistent with Hart et al.'s observations.²⁴⁵

There are two different ways to rationalize these trends. The first one is through a model developed by Miedema et al.²⁴⁶ which is expressed by Equation (5.4):

$$\Delta H \propto -Pe (\Delta\phi^*)^2 + Q_0 \left(\Delta n_{WS}^{\frac{1}{3}} \right)^2 \quad (5.4)$$

Equation (5.4) denotes ΔH (heat of formation) can be expressed as the sum of two terms, $-Pe (\Delta\phi^*)^2$ and $Q_0 \left(\Delta n_{WS}^{\frac{1}{3}} \right)^2$. The first term in Equation (5.4) relates to the difference in chemical potential of electrons, ϕ^* , for pure metals A and B. This difference ($\Delta\phi^*$) causes displacement of electrons to places with lower energies (more favorable potential) and has a negative contribution to the heat of formation of alloys. The second term in Equation (5.4) relates to the discontinuity in the electron density that occurs in the interface between dissimilar atoms when atoms A and atoms B are put together. Thus difference in electron density (Δn_{WS}) leads to a positive contribution to the heat of formation of the alloy. Basically in the case of Ir-M alloys, if the difference between chemical potential of electrons for Ir and M is big, the mixing driving force is much higher and as a result, enthalpy of formation would be lower. When putting Ir and M atoms together, the atoms in the alloy (in the interface) should adapt a new electron density which is unfavorable. Bigger the difference in electron density of Ir and M atoms individually, harder it is to form a compound. Such contributions can be seen in Equation 5.4.

In the Equation 5.4, P and Q_0 are empirical constants and e is the elementary charge. Expression 5.4 then can determine the formation enthalpy sign and as a result will determine the mixing tendency of the alloy.

The second way to rationalize when enthalpy of formation of alloys is negative (compound forming) or positive (phase separating) is provided by Kolb and co-workers.²⁴⁴ They studied ordering tendency of binary alloys of Rh, Pd, Ir, and Pt. They divided enthalpy of formation into three separate components: volume deformation energy, chemical energy, and relaxation energy. Volume deformation energy is defined as the energy required to isothermally deform the pure constituents of the alloy so that they fit the final volume of the alloy and depends on the bulk moduli of the pure metals and to the degree these metals need to be distorted to fit the average volume of the alloy. Chemical energy is defined as the energy given off when two pure end points (deformed to the final volume of the alloy) are brought together to form the alloy²⁴⁴. Finally relaxation energy is defined as the energy released when all internal degrees of freedom of the alloy are allowed to relax²⁴⁴. Kolb et al.²⁴⁴ then tabulated these contributions for their binary systems and realized chemical energy contribution determines the sign of enthalpy of formation and as a result is the dominating factor.

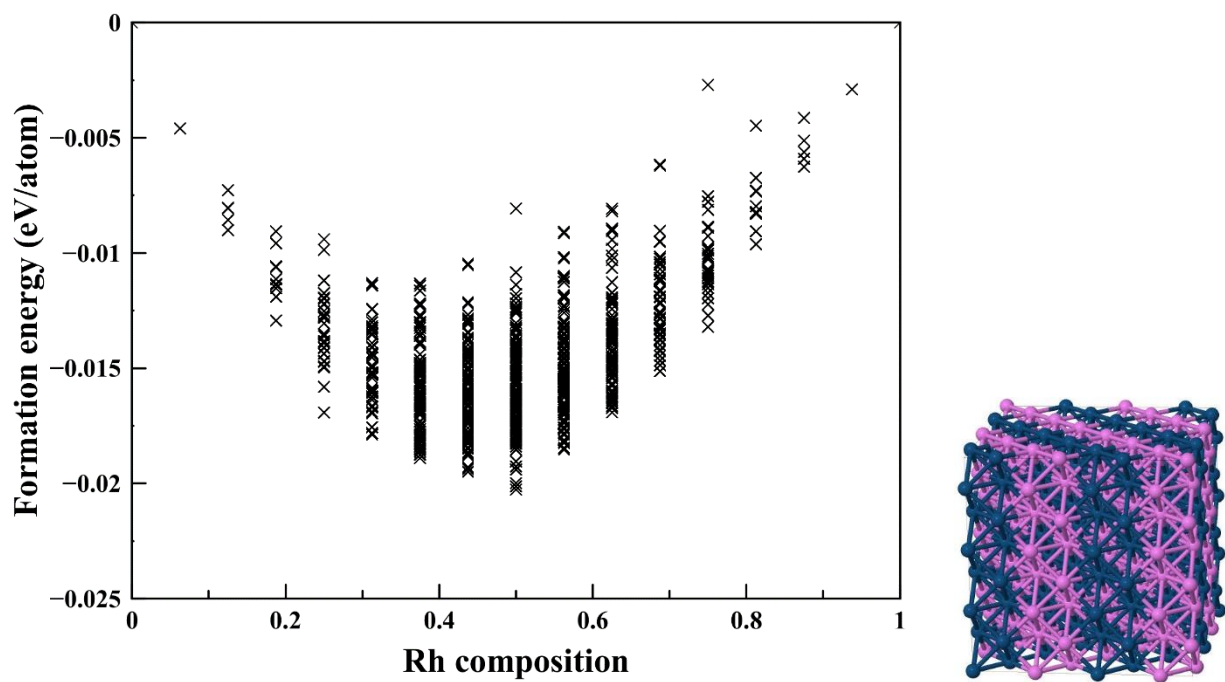


Figure 5.6. Formation energy diagram (left) and the most stable configuration (right) for the bulk Ir-Rh obtained from cluster expansion (GCVC code).

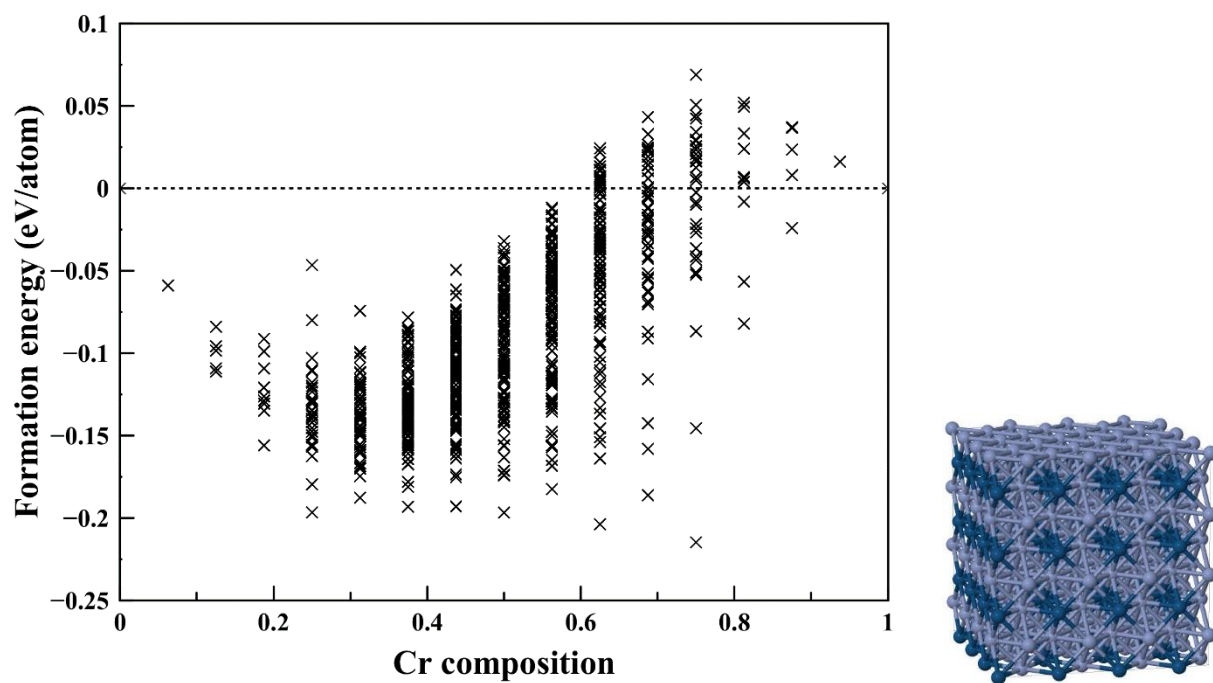


Figure 5.7. Formation energy diagram (left) and most stable configuration (right) for the bulk Ir-Cr obtained from cluster expansion (GCVC code).

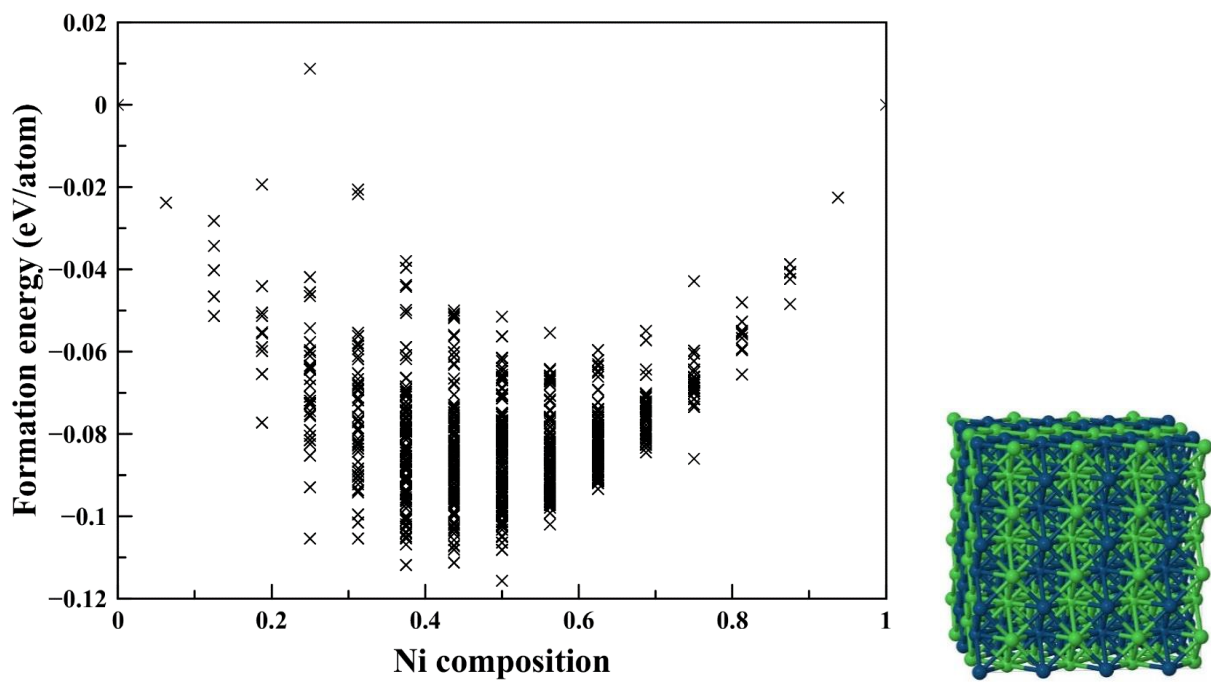


Figure 5.8. Formation energy diagram (left) along with most stable configuration (right) for the bulk Ir-Ni obtained from cluster expansion (GCVC code).

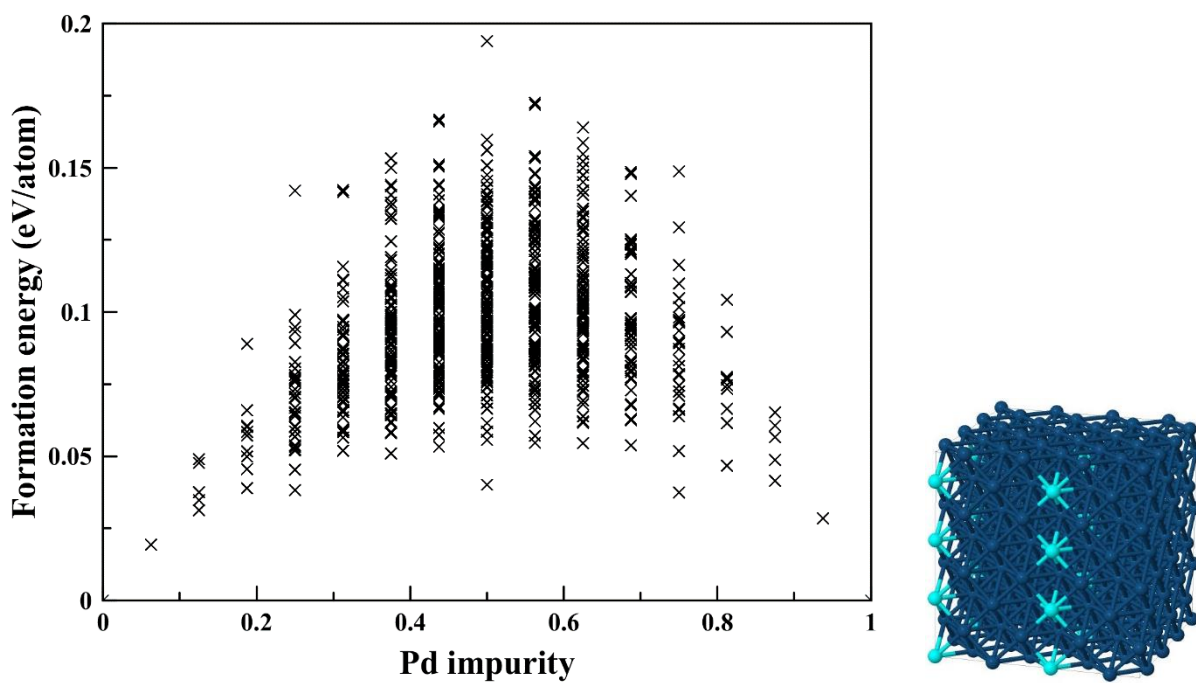


Figure 5.9. Formation energy diagram (left) along with most stable configuration (right) for the bulk Ir-Pd obtained from cluster expansion (GCVC code).

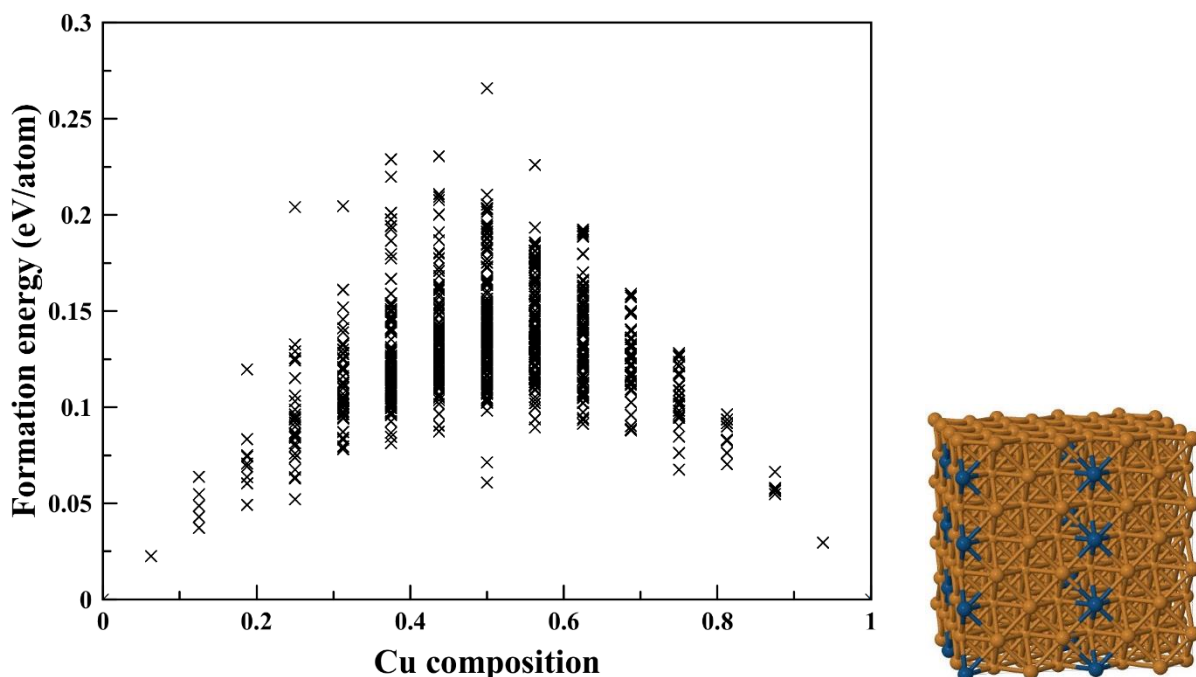


Figure 5.10. Formation energy diagram (left) along with most stable configuration (right) for the bulk Ir-Cu obtained from cluster expansion (GCVC code).

5.3.4. Performing Monte Carlo Simulations for Non-Compound Forming Alloys

It is important to note that DFT calculations gives energies corresponding to 0 K. Ground state energies obtained from formation energy diagrams therefore are representative of alloy formation or segregation at 0K. One of the important factors at fuel cell conditions is temperature. In the case of DFFCS, in real reaction conditions, one is dealing with temperatures in the range of 350-570 K^{62, 247-249}. To see how phase separating (non-compound forming alloys) behave with temperature increase, we performed Monte Carlo simulation through GCVC code. With having a specific configuration (for instance half-half atomic composition for Ir-Pt alloy, and specifying a temperature in Monte Carlo code in GCVC, the code finds the final atomic configuration for the specified temperature. In other words, GCVC provides the user with the snapshot of equilibrium state at a given temperature. We performed such calculations for Ir-Pt half-half atomic composition at 100, 200, 300, 400, 500, 600, 700, and 800 K. The snapshot of equilibrium state for this composition at these temperatures are depicted in Figure 5.11. As it can be seen from Figure 5.11,

the alloy miscibility enhances with the temperature rise. Such effects can be attributed to entropy and temperature effects in alloy mixing. As the temperature increase (considering Gibbs free energy formula presented by $\Delta G = \Delta H - T\Delta S$), entropy contribution to the free energy of the alloy becomes more dominant, leading to alloy mixing. This observation is consistent with previous findings on temperature effect on alloy mixing²⁵⁰. For instance, Zhang et al²⁵⁰. studied two structures of $\text{Cd}_{1-x}\text{Zn}_x\text{S}$ alloys (wurtzite and zinc-blende). They reported these two structures to have positive formation energies and as a result phase segregate. They then performed Monte Carlo simulations and reported miscibility for both structures at higher temperatures. These results directly confirm our observation that increasing the temperature enhances alloy's mixing. This explains the use of non-compound forming alloys such as Ir-Pt in fuel cells^{242-243, 251}. Although, some alloys tend to phase segregate and do not form compounds, still at higher temperatures they mix well and as a result may find their use in fuel cells.

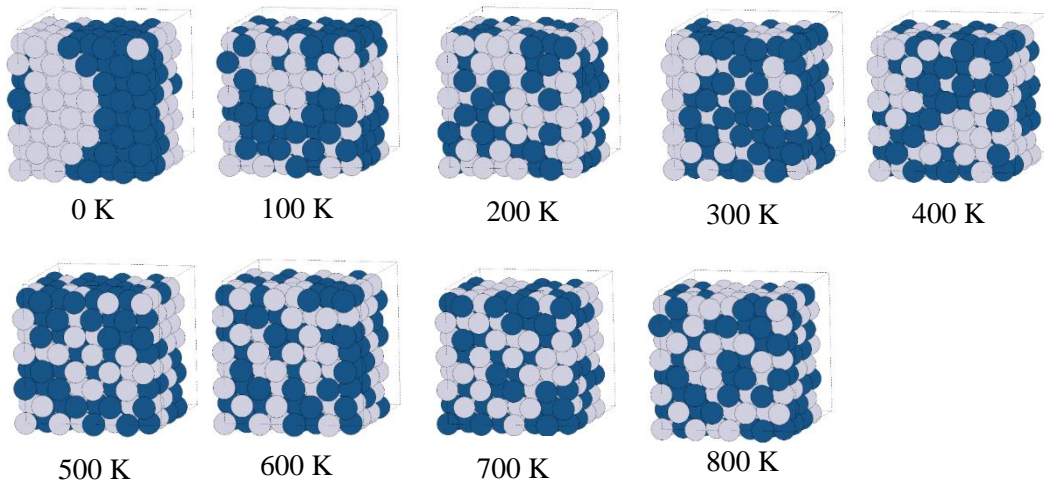


Figure 5.11. Monte Carlo simulations for Ir-Pt half-half composition. Increasing temperature enhances alloy mixing.

5.4. Conclusions

In this chapter first we modeled different compositions and configurations of Ir-Pt (111) surfaces to recognize most favorable atomic structures. For comparing these structures, we calculated substitution energy per atom for each configuration. Based on such calculations, we concluded the most stable structures (with most negative energies for substitution energy per atom) correspond to the geometries in which Pt is put in the first atomic layer. This finding is consistent with what we have shown in Chapter 3 where we showed Pt tend to segregate to the first layer of Ir-Pt alloys. We then focused our attention to bimetallic Ir-M bulk structures and investigated ordering tendency (compound forming or phase separation) for bimetallic Ir-based alloys. We categorized such ordering tendencies by calculating formation energy diagrams by the combination of density functional theory and cluster expansion methods. We recognized Ir-Pt, Ir-Pd, and Ir-Cu as non-compound forming and Ir-Rh, Ir-Ni, and Ir-Cr as compound forming alloys. Finally, we performed Monte Carlo simulations to investigate the temperature effect on alloy mixing. Our calculations suggest as the temperature increases, phase separating Ir-Pt alloys tend to mix well and as a result can be used in fuel cell operating conditions.

Chapter 6: Conclusions

In this work we used computational tools, including density functional theory (DFT) and cluster expansion, to model viable catalysts for the ethanol oxidation reaction (EOR) in direct ethanol fuel cells. A desired catalyst not only should possess high catalytic activity, but also should be stable in the reaction conditions. We modeled surface segregation in bimetallic alloys as an indicator of the alloy's stability. Our calculations show segregation energies are most negative for early and late transition metals and most positive for the middle transition metals. In order to rationalize these results we developed a universal model (for transition metals as host and dopants) for the prediction of surface segregation energy in bimetallic alloys. Based on our model, surface segregation depends on coordination numbers, d-band properties of the dopant and also surface energy and atomic size of alloy constituents. Next step for this work is to also consider post-transition metal as dopants and develop a model for post-transition metals. We already performed such calculations (can be found in Appendix B, Figure B.14) and as a future work we would develop a model for post-transition metals as dopants.

In the next part of our work, we modeled different catalysts including transition metals (Pt, Ir, Rh, Au, Ag), alloys (Ir, Ir-Rh, Ir-Rh-Sn), metal-metal oxide interfaces (Pt, Pt-SnO₂, three models of Pt-Rh-SnO₂), and metal oxides (Rh, Rh₂O₃) and compared their ability in breaking the C-C bond in the EOR. In each category, we recognized the best catalyst for C-C bond breaking. Specifically among transition metals, Rh, among Ir and Ir alloys, Ir, among metal-metal oxide interfaces, 2nd model of Pt-Rh-Sn O₂, and among Rh and Rh₂O₃, Rh₂O₃ are superior in C-C bond breaking. Among all the catalysts considered, Pt-Rh-SnO₂ has the highest ability to break the C-C bond, showing metal-metal oxides in general are better for C-C bond breaking and if one wants a catalyst which works well for C-C bond breaking, they should have some sort of metal oxides present. This is mainly because of the different chemistry involved in each of these categories (metals, alloys, metal-metal oxides, oxides). One involves metallic bonds (the alloys and metals), the other involves more ionic bonds (metal oxides). Formations of the product species are more stable in metal oxides compared to metals and make C-C bond breaking reactions more exothermic. The promotional catalytic activity of metal-metal oxide interfaces is also attributed to the charge transfer between metal and metal oxide interface.^{199, 202-204} Based on our calculations, Pt-Rh-SnO₂ is the best catalyst for C-C bond breaking in the EOR.

Finally we were interested in the design of the best bimetallic Ir-based alloys to be used in DEFCs. We realized some alloys including Ir-Pt, Ir-Pd, and Ir-Cu possess positive formation energies and as a result phase separate. Other alloys (Ir-Rh, Ir-Ni, and Ir-Cr) mix well and form stable compounds. Based on these findings, Ir-Rh, Ir-Ni, and Ir-Cr could be potential alloys to be used in the EOR. Considering chapters 4 and 5 together, Ir-Rh seems to be a promising candidate for the EOR. We also performed Monte Carlo simulations for Ir-Pt to investigate temperature effects on non-alloying mixtures. We showed as the temperature rises, Ir-Pt starts to mix well and as a result may still be useful for the EOR. In the next step, cluster expansion can be used to model other bimetallic Ir and also generally other alloys. We performed such calculations for bulk structures. One may extend such analysis to alloy surfaces. In this work we performed Monte Carlo simulations for Ir-Pt alloys. It would be valuable to also perform such calculations to other non-alloys to investigate the interplay between enthalpy and entropy in other non-alloys.

Our results in these three chapters show how atomistic modeling can predict stability and reactivity of potential catalysts. We proposed potential catalysts including Pt-Rh-SnO₂ for C-C bond breaking, a crucial step in the complete oxidation of ethanol. We designed potential bimetallic Ir-based alloys including Ir-Rh by the combination of DFT with cluster expansion method, and also developed a model for surface dependent segregation energy which is an indicator of the alloy's stability in the reaction conditions. Such calculations can potentially be performed for other bimetallic alloys including Rh-M, Pt-M, and other Ir-M alloys (M being a transition or post transition metal). We also developed a model for surface dependent segregation energy in dilute limit. One may perform such calculations in other atomic compositions as surface segregation is composition dependent. Finally we considered metal-metal oxide interfaces including Sn and Rh oxides and used them with the combination of Pt and Rh. One may perform such calculations for Ir and other metallic oxides to investigate the activity of such interfaces.

Appendix A: The GCVC (Generalized Cluster-Expansion for Variable and Complex Systems) Code

The first step in using the GCVC code is to find independent clusters for a given lattice. In order to find independent number of clusters, “getCluster” code is used. This step is independent of arrangement of atoms in the lattice. In this step, in one of the input files (gcvc-cluster.in) we specify how many subclusters we want to consider in the summation in Equation 1.27. We also define a radius in which each of the interactions should be truncated. For instance, we specify to the program to consider two-body interactions (pair interactions) within the radius of 6 Å of each lattice site. In the present study, we used up to four-body interactions and for two, three, and four body interactions we considered the truncation radius of 6 Å. This gives us enough terms to consider in Equation 1.27 while not being too complicated for the code to perform the calculations. In other words, it maintains a good balance between timing and accuracy.

The second step is to perform DFT calculations for a number of atomic configurations and variety of compositions. From these calculations there are two different things in which we use in the cluster expansion code: 1) Input geometries, 2) Input energies.

The third step is to find basis (correlation) functions. For that matter there is a code implemented in GCVC named “getBasis-conf”. In this step input geometries from DFT calculations would be used. Each configuration would be repeated to match the size of geometry which has been used for cluster expansion. For instance we used a cell for DFT calculations containing 32 atoms, after repeating the unit cell, it contained 256 atoms. In an input file named “gcvc-basis-conf.in” the sequence of spin variables would be specified. For instance atoms A and B would be assigned to +1 and -1 respectively. Based on DFT input geometries, basis (correlation) functions then would be calculated.

The fourth step is to calculate Cross Validation (CV) score, a parameter in cluster expansion community which defines the accuracy of cluster expansion. CV score can be calculated by Equation A.1:

$$CV\ score = \sqrt{\frac{1}{N_s} \sum_{m=1}^{N_s} (E_{DFT}^m - E_{CE}^m)^2} \quad (A.1)$$

In the above Equation, N_s is the total number of input structures and E_{DFT}^m and E_{CE}^m are the energies of structure m obtained with DFT and cluster expansion, respectively. In order for cluster expansion giving reliable results, CV score should be as small as possible; meaning that the energies obtained with cluster expansion should be close to DFT ones. “opt-basis” code implemented in GCVC, calculates CV score based on DFT energies, an input file named “enecar”, basis functions, an input file named “CORRELATION”, and other parameters such as temperature and number of clusters implemented in “gvc-opt-basis-in”.

The fifth step is to find ECIs (the main task in performing cluster expansion). This can be accomplished by “lsfit” code. In this step also energies obtained from DFT calculations and also basis functions would be implemented in order to find ECIs “ecicar”.

The sixth step is to construct coordination information for each lattice points “mccar.conf”. This would be performed by means of “setMC-conf” code.

The seventh step is to find optimal set of DFT input structures. Whether or not to perform this step depends on the CV score. If the CV score is within the desired accuracy, this step could be skipped. Otherwise, “mccar.conf”, basis functions, ECIs would be used to construct recommended DFT structures to be used to run for the cluster expansion. This task would be accomplished by means of “str-select” code.

The final step is to find geometries and energies corresponding to the ground state structures (geometries which possess lowest energies). ECIs and “mccar.conf” and other parameters implemented in “gvc-gs-conf.in” would be used to find energies and geometries of all possible configurations. This task would be accomplished by means of “gs-conf” code. For instance if we specify in the input file for “gs-conf” named “gvc-gs-conf.in” that we want to have a cell comprising 16 atoms, the code calculations energies and geometries corresponding to 2^{16} configurations. Note that we are dealing with binary systems, so there would be two possibilities for each lattice site, and overall there would be 2^{16} possible configurations. After finding all energies and atomic configurations, ground state geometries could be found. The general scheme of GCVC (cluster expansion code) is summarized in Figure A.1.

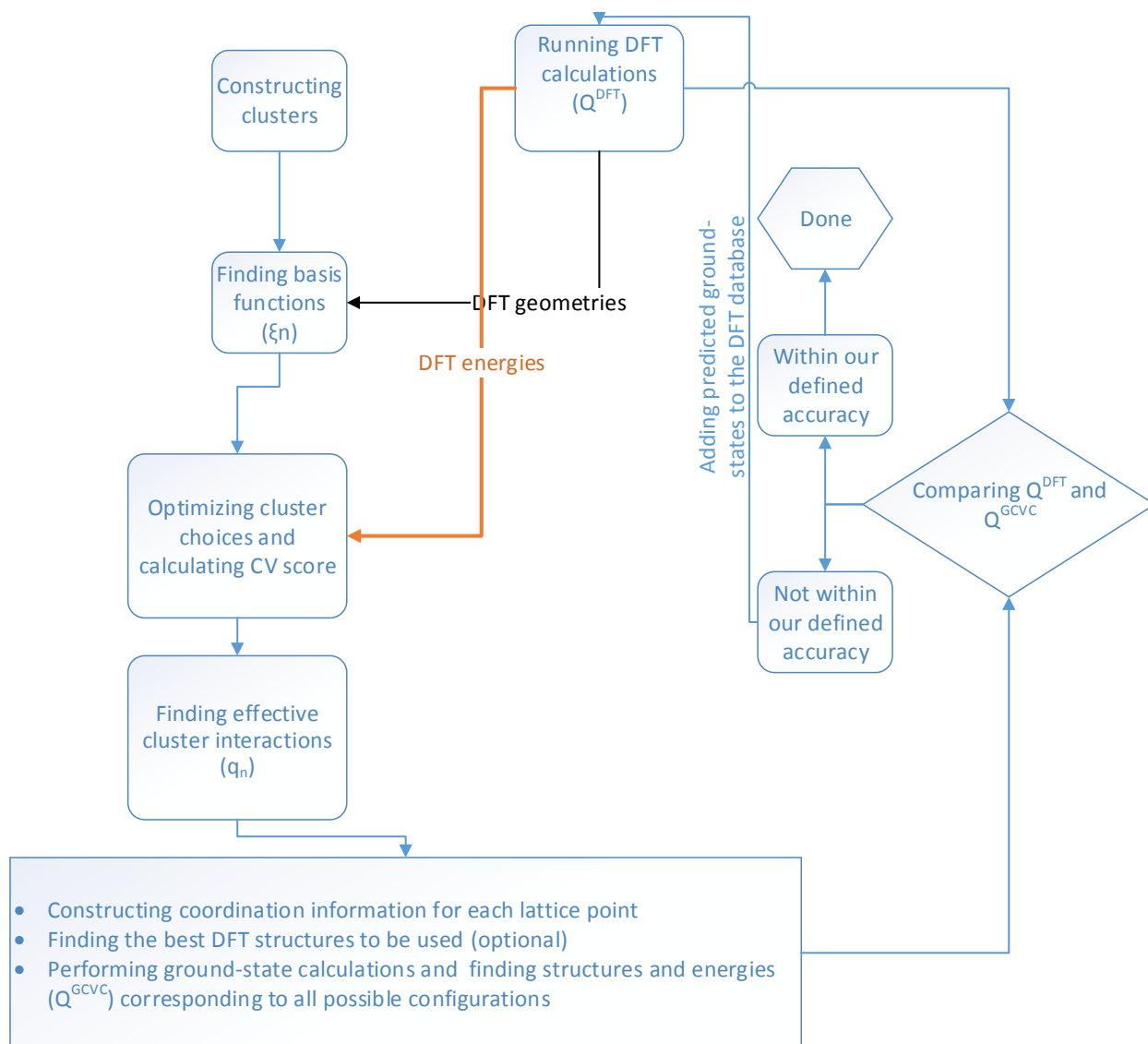


Figure A.1. Procedure of GVCV code (cluster expansion method). The first step is to construct clusters and then to perform DFT calculations. The non-optimized geometries from DFT calculations along with clusters would be used to find basis (correlation) functions. Having basis functions and DFT energies, cross validation (CV) score and then effective cluster interactions (ECIs) would be calculated. Based on these data, energies and geometries corresponding to all possible alloy configurations would be found. After this step, DFT and GVCV energies would be compared. If these values are within the defined accuracy, we are done; otherwise the found ground state configurations would be added to the pool of DFT geometries and the method repeated itself.

Note on different cell sizes for DFT and cluster expansion calculations

It is important to note the difference between the cell sizes in different simulations. To do cluster expansion calculations (to use GCVC code) the cell size being used should be large. However, since DFT calculations suffer from computational limitation, the cell size cannot be the same size of the one used for cluster expansion calculations. On the other hand, the cell size cannot be too small either, because as it was mentioned earlier, small unit cell will not give us the desirable variety of different configurations. To strike a balance between accuracy and computational limitations, we have used 32 and 256 atoms for DFT and cluster expansion calculations respectively. After running the DFT calculations, we expanded each of the configurations consisting 32 atoms with repeating their supercell to obtain the supercell containing 256 atoms. This is specifically important because in order to find the basis (correlation) functions, the DFT geometries are needed and without extending the DFT configurations, there would be discrepancy between DFT and cluster expansion supercells. Another important factor to consider, is DFT energies. In order for cluster expansion to use DFT energies, we have divided the energies by 32. In other words, we calculated the energy per atom for each specific configuration. Dividing by number of atoms enables us to use different number of atoms for DFT and cluster expansion calculations (32 and 256 in this study respectively). There are different subcodes embedded in GCVC to accomplish different tasks such as constructing the clusters, finding basis functions, CV score, effective cluster interactions, constructing coordination information for each lattice points, and ground states. In other word, there are at least 6 codes which should be run in order to get ground states and these codes should be performed in the order which is listed above. In other words, first DFT calculations should be run; second with the first code embedded in GCVC (getCluster) clusters should be constructed. Third with the second code of GCVC (getBasis) basis (correlation) functions should be constructed. Fourth with the third GCVC code (opt-basis) CV score will be calculated. Fifth with the fourth GCVC code (lsfit) the effective cluster interactions would be calculated. Sixth with the fifth GCVC code (setMC-conf) coordination information for each lattice points will be calculated, and finally with the sixth GCVC code (gs-conf) all possible configurations for this alloy (including ground states) will be found. It is important to note that there is a parameter in gs-conf which divides the original cell for GCVC calculations (256 atoms) to smaller cell size. In other words, to find the all possible configurations for a binary alloy, there are $2^{\text{number of atoms}}$ different ways. If we do not divide the cell, there would be 2^{256} different

possible alloy configurations to be found which is beyond the computational power of GCVC. So, we divided the unit cell by $2 \times 2 \times 4$ to obtain 16 atoms in the cell. Doing so, there are $2^{16} = 65536$ different alloy configurations to be calculated which is within the computation power of GCVC.

Appendix B: Supporting Information: Surface Dependent Segregation in Bimetallic Alloys

B.1. Nature of Metal Slabs

We performed calculations to determine the effect of freezing bottom layers versus allowing full relaxation of the layers. We also performed calculations to determine the effect of the number of layers in the slab. Table B.1 shows calculated surface energies for the Pt (100) surface. Table B.2 shows calculated surface energies for the Pt (111) surface using different number of layers and with and without freezing bottom layer(s). Tables B.3 and B.4 show surface energies for Pt (110) and (210). The analysis shows that the number of layers did not affect surface energies significantly. Freezing layers did also not have a significant effect on the surface energy. In our work we therefore allowed full relaxation of the slabs and used five layers for the (100) surfaces, 5 layers for the (111) surfaces, 7 layers for the (110) surfaces, and 5 layers for the (210) surfaces. These choices gave slabs that were at least 8 Å thick, to ensure a reasonably thick slab.

Table B.1. Calculated surface energies and timing for the Pt (100) surface using different number of layers in the slab and considering freezing of Pt layers.

Number of layers	Frozen Layers	Surface Energy (eV/Å ²)
3	None	0.12
4	None	0.11
5	None	0.11
5	Bottom Layer	0.11
6	None	0.10
7	None	0.10
7	Bottom 3 Layers	0.10
8	None	0.10
8	Bottom 4 Layers	0.10

Table B.2. Calculated surface energies for the Pt (111) surface using different number of layers in the slab and considering different ways of freezing Pt layers.

Number of layers	Frozen Layers	Surface Energy (eV/Å ²)
3	Bottom Layer	0.09
4	None	0.08
5	None	0.08
5	Bottom 2 Layers	0.08
6	None	0.07
7	None	0.07
7	Bottom 4 Layers	0.07
8	Bottom 5 Layers	0.06

Table B.3. Calculated surface energies for the Pt (110) surface using different number of layers in the slab.

Layers	Surface energy (eV/A ²)
4	0.12
5	0.12
6	0.12
6-bottom layer frozen	0.12
7	0.12
7-bottom layer frozen	0.12

Table B.4. Calculated surface energies for the Pt (210) surface using different number of layers in the slab.

Number of layers	Surface energy eV(A ²)
4	0.12
5	0.12
6	0.12
7	0.12

We also performed segregation energy calculations using a 5-layer Pt (111) surface and Ag as a dopant with different number of frozen layers, as given in Table B.5. Again these results verify that a fully relaxed 5 layer slab is sufficient for this work.

Table B.5. Calculated segregation energies for the Pt (111) surface considering freezing different number of layers with Ag as a dopant. As it is evident, freezing does not have much effect on the segregation energy values. Since non-freezing needed the least computation time, while giving accurate results, we did not freeze any layer throughout our calculations.

Number of frozen layers	Segregation energy
0	-0.51
1	-0.51
2	-0.50
3	-0.48

B.2. Calculated Segregation Energies

Segregation energies in (100) surfaces of Pt, Pd, Ir, and Rh are depicted in Figure B.1. Segregation energies for (110) and (210) surfaces of Pt, Pd, Ir, and Rh are also shown in Figures B.2 and Figures B.3 respectively. As was explained in the main text for (111) surfaces and as it is also evident from Figures B.2 and Figures B.3, Ir has the most negative segregation energies, while Pd has the most positive segregation energies.

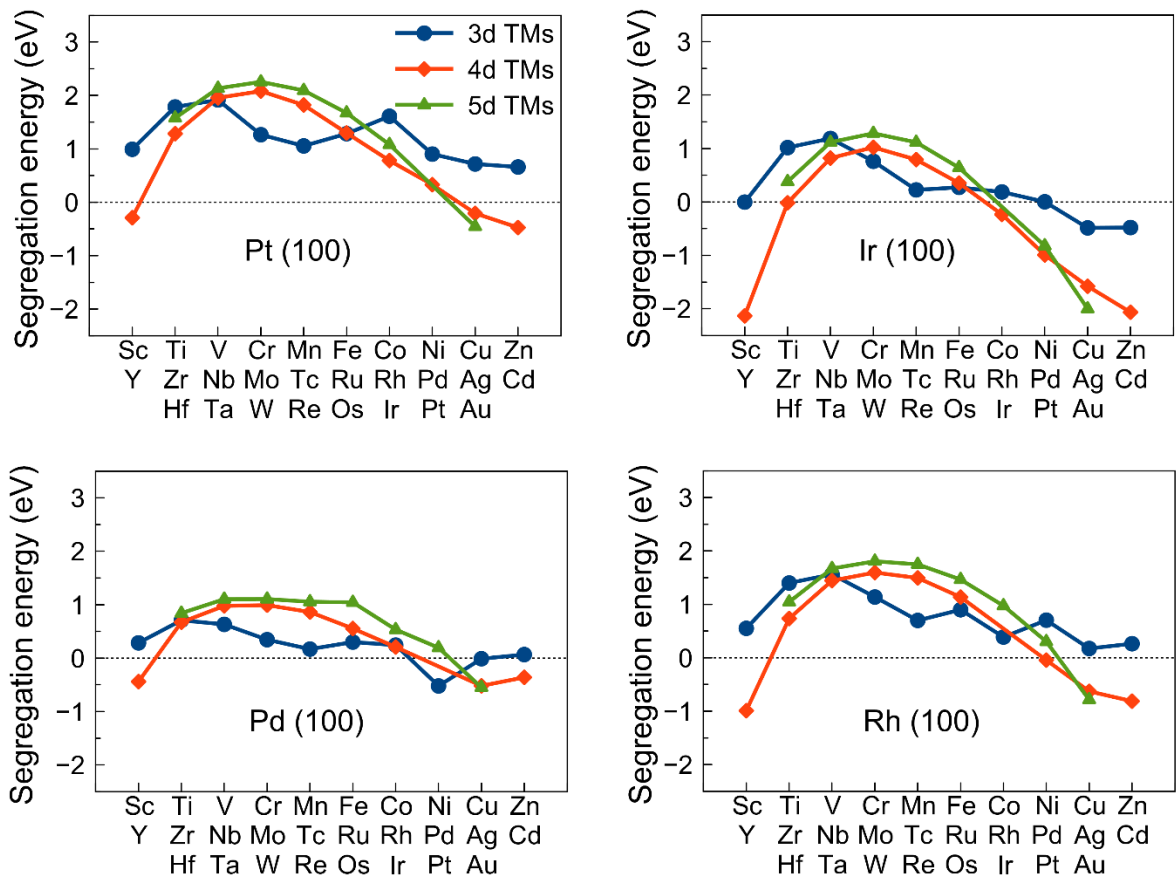


Figure B.1. Calculated segregation energies within (100) surfaces of Pt, Pd, Ir, and Rh.

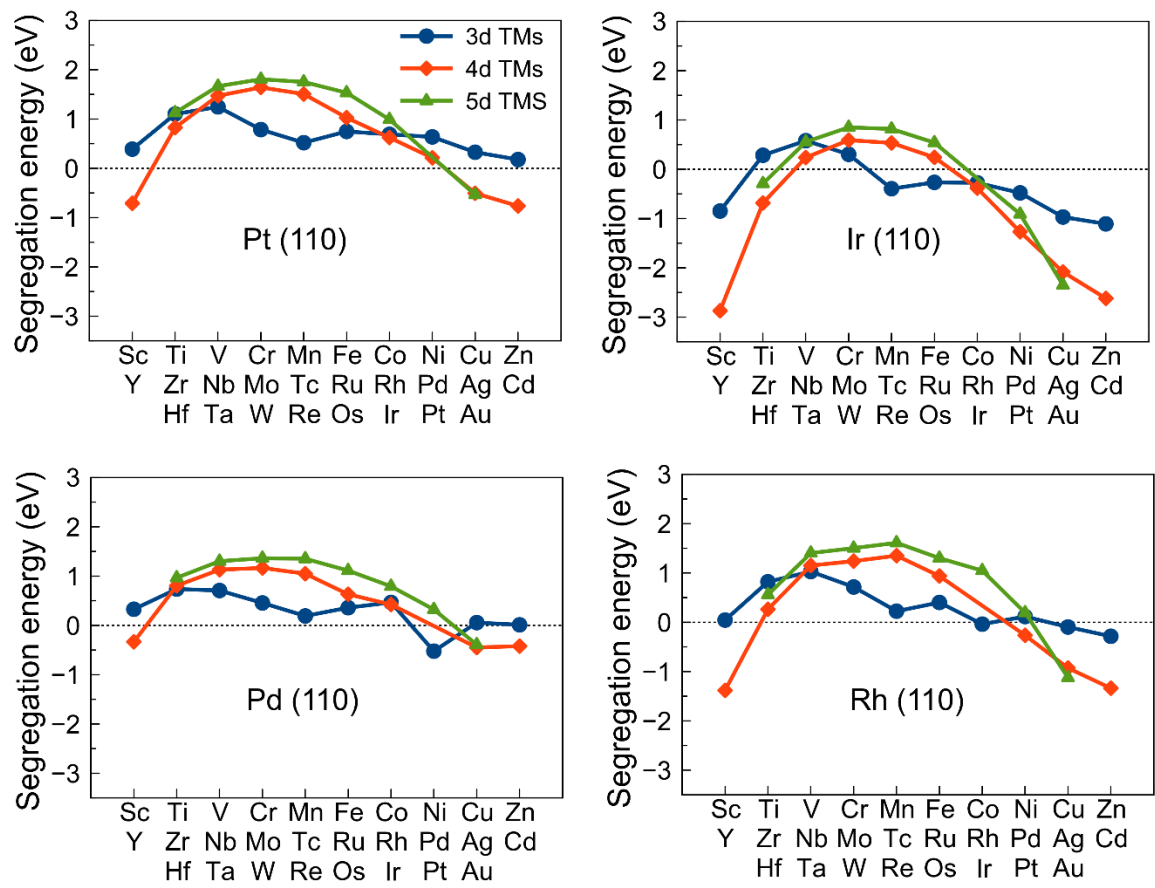


Figure B.2. Calculated segregation energies within (110) surfaces of Pt, Pd, Ir, and Rh.

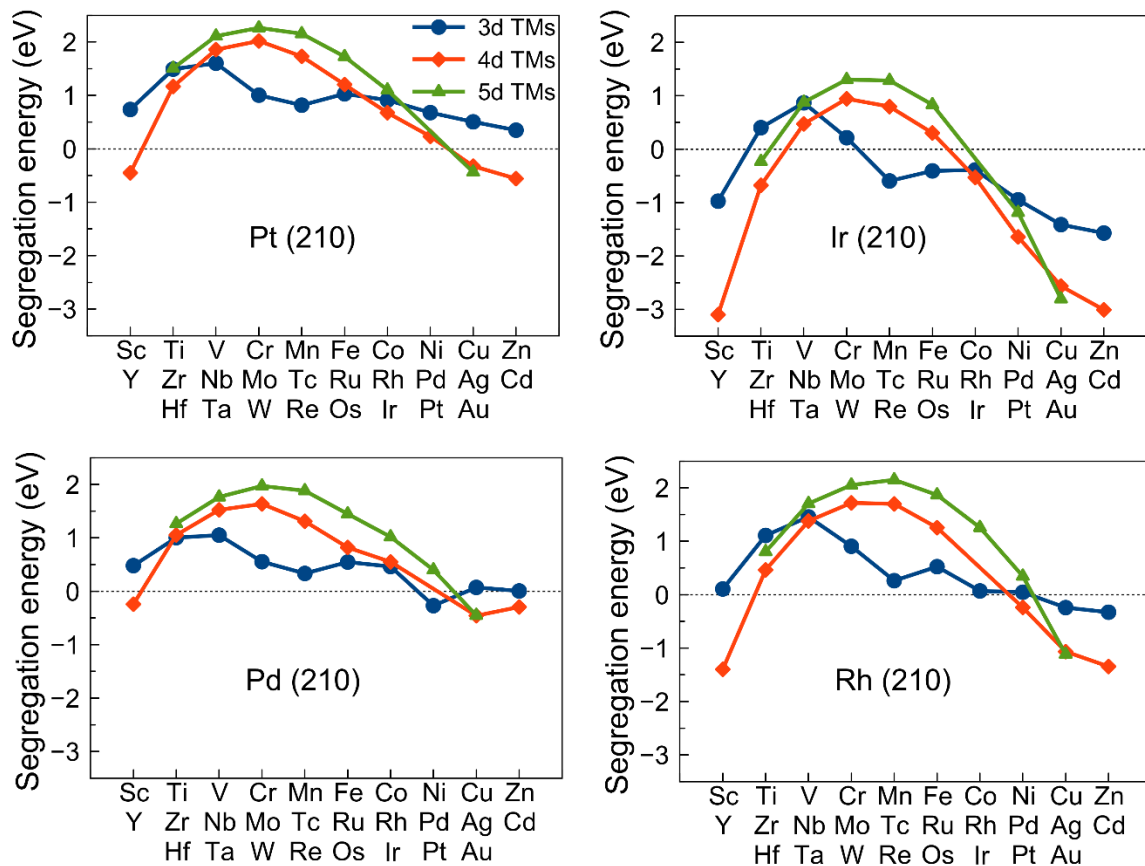


Figure B.3. Calculated segregation energies within (210) surfaces of Pt, Pd, Ir, and Rh.

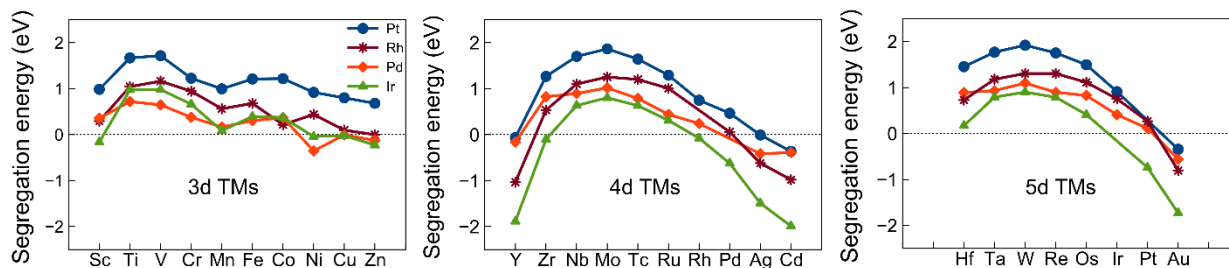


Figure B.4. Comparison between (111) surfaces of Pt, Pd, Ir, and Rh as hosts. The segregation energies follow this trend: Pt > Rh > Pd > Ir.

B.3. Comparison of two different definitions of segregation energy for Ir, Pd, and Rh surfaces

Segregation energies defined by two different definitions (Equations 1 and 2 in the main text) for Ir, Pd, and Rh as hosts are compared in Figure B.5-B.7. In the case of Ir and Pd, the two definitions almost give the same values. For Rh, the values do not match but the trends are similar for the two definitions (like Pt which was discussed in the main text).

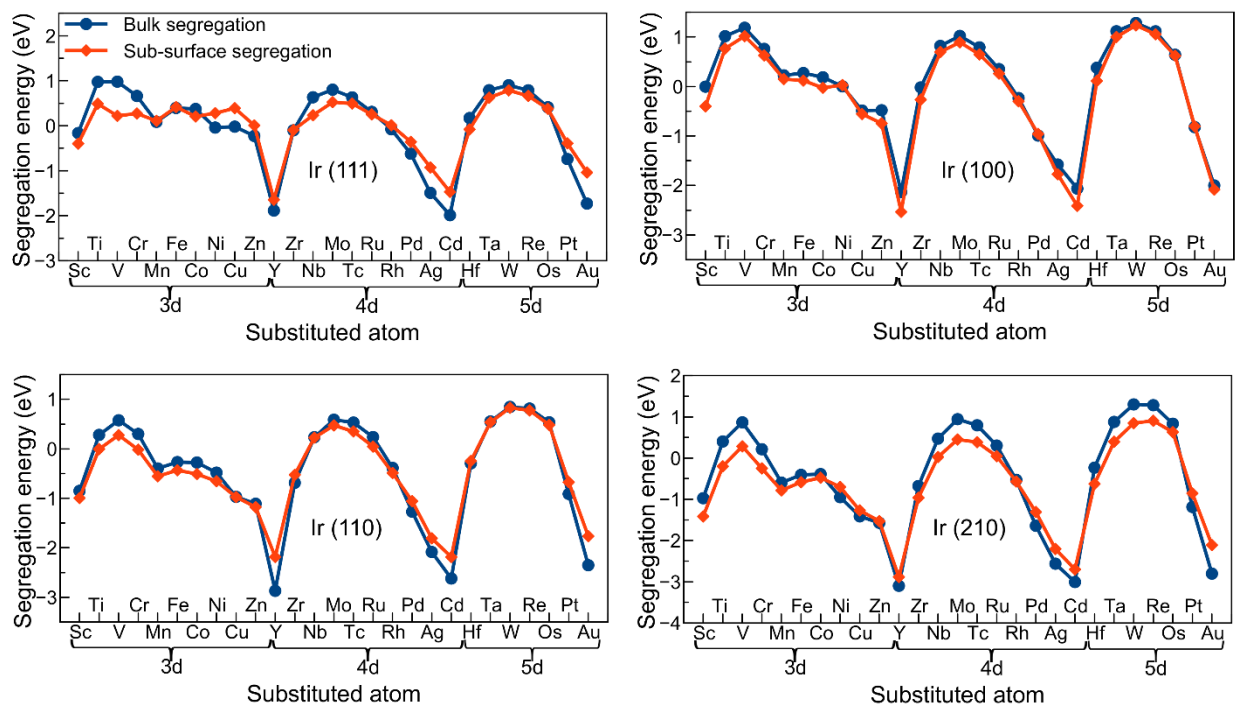


Figure B.5. Calculated segregation energies from the bulk and sub-surface (second layer) sites. Results are for the (111), (100), (110), and (210) surfaces of Ir as host. Segregation energies were calculated with Equations 1 and 2 in the main text.

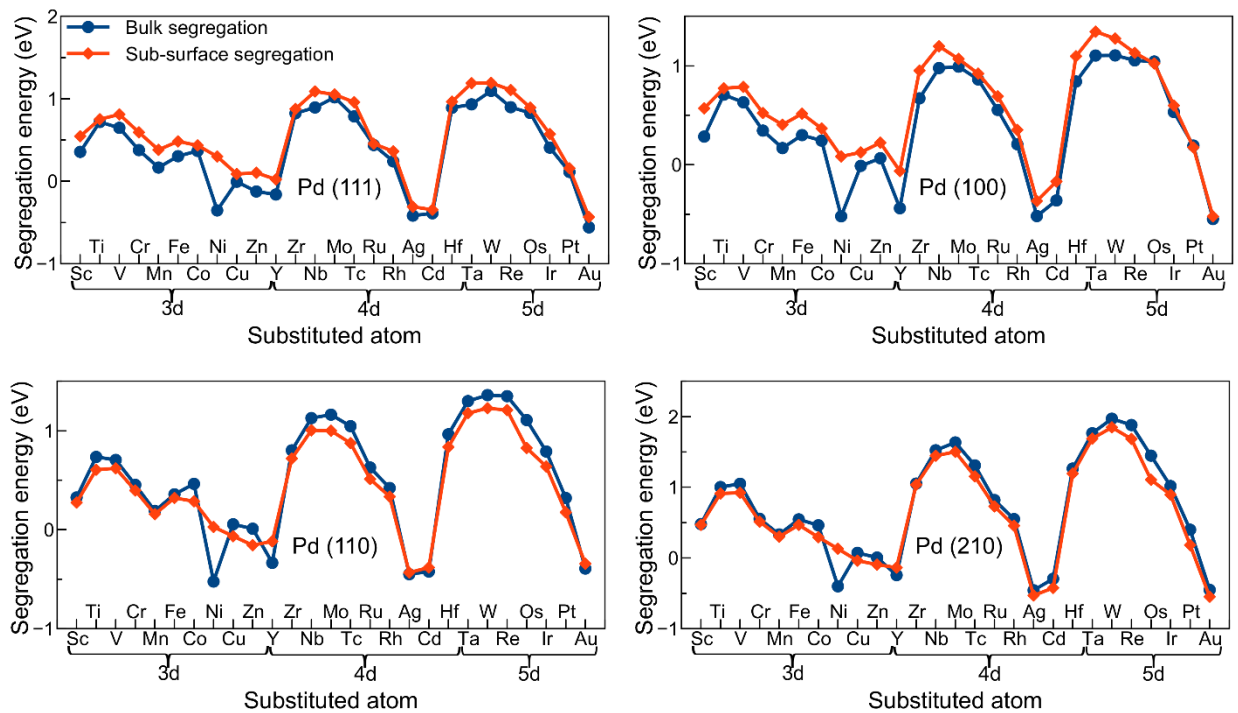


Figure B.6. Calculated segregation energies from the bulk and sub-surface (second layer) sites. Results are for the (111), (100), (110), and (210) surfaces of Pd as host. Segregation energies were calculated with Equations 1 and 2 in the main text.

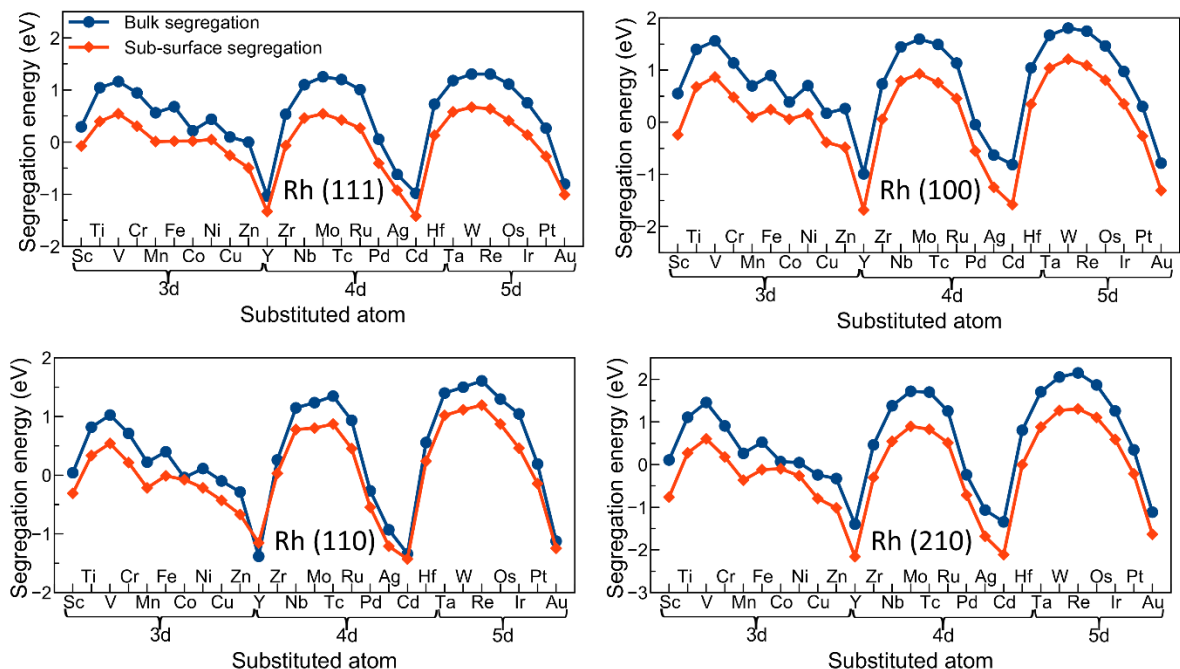


Figure B.7. Calculated segregation energies from the bulk and sub-surface (second layer) sites. Results are for the (111), (100), (110), and (210) surfaces of Rh as host. Segregation energies were calculated with Equations 1 and 2 in the main text.

B.4. Models for Predicting Surface Segregation

We were interested to see if there is an correlation between d-band properties of different surfaces of host metals with segregation energy values. We calculated d-band width, d-band filling, and d-band center for (111), (100), (110), and (210) of our host metals. To investigate such a correlation, we considered V as the dopant and Pt as the host as we observed the trend of $(100) > (111) > (210) > (110)$. Figure B.8 shows d-band width versus segregation energy, d-band filling versus segregation energy, and d-band center versus segregation energy. As it can be seen there is no obvious correlation between d-band properties of the host and segregation energy values. Later we showed comparing equations B.8 and B.13 that d-band properties of the host played a slight role in predicting segregation energies of dopants in our host metals. In other words, adding a term which takes into account d-band properties of the host, improved the adjusted R^2 only by 0.01.

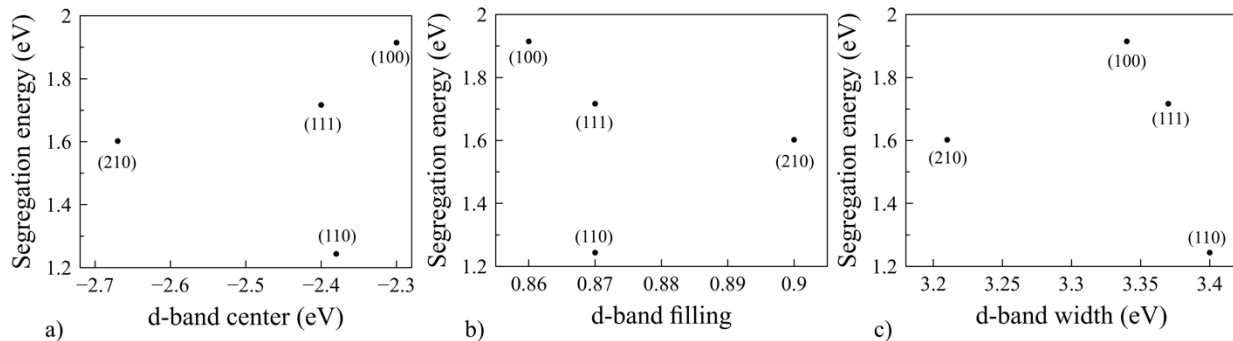


Figure B.8. Plot of segregation energy of Vanadium (V) as a dopant in (111), (100), (110), and (210) surfaces of Pt along with d-band properties of pure surfaces of Pt (without dopant). a) d-band center and segregation energy, b) d-band filling and segregation energy, and c) d-band width and segregation energy comparison for different surfaces of Pt. As it can be observed, there is not a linear correlation between different surfaces of Pt and d-band properties of the pure surfaces.

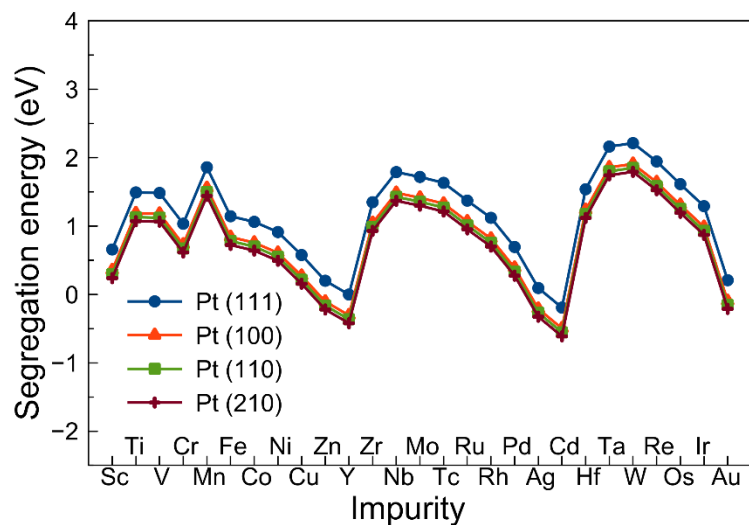


Figure B.9. Modified Yu et al.'s model segregation data.

Yu et al¹¹⁰. developed a model for segregation energy based on difference in surface energy, elastic energy, and heat of solution of the impurity and the host metal. Their model can be written as the following:

$$E_{seg} = C_1\Delta E_{surf} + C_2\Delta E_{elast} + C_3E_{sol} \quad (B.1)$$

They explained that based on previous literature, the ΔE_{elast} term can be written as the following:

$$\Delta E_{elast} \propto \left[\left(\frac{r_B}{r_A} \right)^3 - 1 \right]^2 r_A^3 \quad (B.2)$$

In this equation B represents the impurity. r_B and r_A denote the Van der Waals radii of the impurity and the host respectively. The heat of solution can be calculated by the following formula:

$$E_{sol} = E_{A_nB_m} - nE_A - mE_B \quad (B.3)$$

$E_{A_nB_m}$ is the total energy of the $E_{A_nB_m}$ unit cell that contains n number of A atoms and m number of B atoms. E_A and E_B are the total energy of one A or B atom in the bulk. All these energies are calculated with DFT. Figure B.9. shows a comparison of different segregation energies calculating using Yu et al.'s model for Pt, after refitting the parameters to our data.

In order for us to develop a model to predict surface dependent segregation energy, we considered different parameters which could potentially affect surface segregation energies including: d-band width and d-occupation number of the host, d-band width and d-occupation number of the dopant, geometric mean of d-band width of the host and the dopant, electronegativity of the transition metals used as dopants, Ionization potential, electron affinity, number of d-electrons, cohesive energy, polarizability, atomic and group number of dopants involved, work function, surface energy, surface energy difference between host and the dopant, Wigner-Seitz radius, Van Der Waals radius, the $\left[\left(\frac{r_B}{r_A} \right)^3 - 1 \right]^2 r_A^3$ term (taken from Yu et al.¹¹⁰ which is correlated with elastic energy) using Wigner-Seitz radii of host and dopant (referred to WS correlation), the $\left[\left(\frac{r_B}{r_A} \right)^3 - 1 \right]^2 r_A^3$ term (taken from Yu et al.¹¹⁰), this time using Van der Waals radii of host and dopant (referred to VDW correlation), the $\left[1 - \left(\frac{Z_b}{Z_s} \right)^{\frac{1}{2}} \right]$ term named coordination contribution and the $\{W^A N_A(10 - N_A) - W^{B \rightarrow A} N_B(10 - N_B)\}$ term named as bandwidth contribution. (both taken from Ruban et al¹¹³).

We then performed different linear and non-linear regression models to investigate which terms to keep and also to see which parameters to use in our model. While making different models, we tried different combination of parameters and whichever gave the best adjusted R^2 , we chose that. The details of different models in which we used are not presented here for brevity. After trying out multiple models we proposed Equation (B.4) to predict surface dependent segregation energy. In our Equation (B.4), we used the terms implemented in Ruban et al¹¹³ (coordination numbers and d-band properties) and Yu et al¹¹⁰ models (surface energy and VDW correlation).

Our model we developed to predict surface is as follows:

$$E_{segregation}^{B \rightarrow A} = 2.34 - 0.09W^B - 0.24N_B + 0.81(E_{surface}^B - E_{surface}^A) - 0.60 \left[\left(\frac{r_B}{r_A} \right)^3 - 1 \right]^2 r_A^3 - 1.13 \left[1 - \left(\frac{Z_b}{Z_s} \right)^{\frac{1}{2}} \right] \quad (B.4)$$

The parameters implemented in our model (Equation 3) are $\beta_0 = 2.34, \beta_1 = -0.09, \beta_2 = -0.24, \beta_3 = 0.81, \beta_4 = -0.60, \beta_5 = -1.13$. In the above equation, $E_{segregation}^{B \rightarrow A}$ denotes the segregation energy of dopant B in the host of A. W^B is the d-bandwidth of dopant, N_B is the d-occupation number of the dopant, $E_{surface}^A$ and $E_{surface}^B$ are surface energies of the bare metals, r_A and r_B are Van der Waals radii, and Z_b and Z_s are coordination numbers. In all cases A refers to the host and B represents the dopant. The $\left[\left(\frac{r_B}{r_A} \right)^3 - 1 \right]^2 r_A^3$ term is associated with elastic energy release and was inspired by Yu et al.¹¹⁰ The variables $\left[1 - \left(\frac{Z_b}{Z_s} \right)^{\frac{1}{2}} \right]$, W^B , and N_B are inspired by Ruban et al.¹¹³. The values in equation (3) for the dopant (B) are summarized in Table B.6. The values of d-band width and d-band filling in Table B.6 are taken from Table 1 in Brejnak and Modrak paper¹⁴⁹. The values of surface energy (for dopants) and van der Waals radius are taken from Table 2 in Yu et al.'s paper¹¹⁰. Surface energy, d-band width, and d-band filling of the host metal are calculated with DFT. For calculating d-band width and d-band filling, we used Equations (2) and (3) from Xu and Kitchin's paper²⁵². In order to calculate d-band width, first we calculated d-band center using Equation (1) from their paper²⁵². These equations are listed as equations B.5-B.7:

$$E_l = \frac{\int \rho E dE}{\int \rho dE} \quad (\text{B.5})$$

$$W_l^2 = \frac{\int \rho (E - E_l)^2 dE}{\int \rho dE} \quad (\text{B.6})$$

$$f_l = \frac{\int_{-\infty}^{E_f} \rho dE}{\int_{-\infty}^{\infty} \rho dE} \quad (\text{B.7})$$

In Equations B5-B6, E_l denotes the d-band center corresponding to the state l and is computed based on the first moment of the projected density of states about the Fermi level (E_f). W_l is calculated based on square root of second moment of the projected density of states about the d-band center; and the fractional d-band filling is calculated based on the integral over states up to Fermi level divided by the integral over all states. In order to calculate surface energies for (111), (100), (110), and (210) of our host metals, we used the following formula²⁵³:

$$E_{surface} = \frac{E_{tot}^{slab} - N E_{tot}^{bulk}}{2A} \quad (\text{B.8})$$

In the above formula $E_{surface}$ is the calculated surface energy, E_{tot}^{slab} is the total energy of the slab containing N number of atoms, E_{tot}^{bulk} is the energy per atom of the bulk system, A is the surface area of the slab, and the factor 1/2 takes into account the presence of two equivalent surfaces of the slab.

We also used the term associated with d-band width and d-band filling of the host and impurity ($W^A N_A (10 - N_A) - W^{B \rightarrow A} N_B (10 - N_B)$) as proposed by Ruban et al¹¹³. Based on our analysis, adding this term did not increase the accuracy of our model considerably. Using the following model, which adds these d-band properties of the host and impurity, results in a R^2 value of 0.90 and $RMSE$ of 0.50 eV which is not much of an improvement compared to our original model:

$$E_{segregation}^{B \rightarrow A} = 2.68 - 0.18W^B - 0.20N_B - 0.007\{W^A N_A (10 - N_A) - W^{B \rightarrow A} N_B (10 - N_B)\} + 0.83(E_{surface}^A - E_{surface}^B) - 0.54 \left[\left(\frac{r_B}{r_A} \right)^3 - 1 \right]^2 r_A^3 + 0.11 \left[1 - \left(\frac{Z_b}{Z_s} \right)^{\frac{1}{2}} \right] \quad (\text{B.9})$$

Tables B.6 and B.7 shows the values we used for fitting our model

Table B.6. Dopant data implemented in Equation 3. d-band width and d-band-filling are taken from Brejnak and Modrak¹⁴⁹. Surface energy and van der Waals radius are taken from Yu et al¹¹⁰.

Transition metal	d-band width(eV)	d-band-filling	Surface energy (J/m ²)	van der Waals radius (Å)
Sc	5.1	1.76	1.275	2.61
Ti	5.8	2.90	2.1	2.39
V	6.1	3.98	2.55	2.29
Cr	6.0	4.96	2.3	2.25
Mn	5.0	6.02	1.6	2.24
Fe	4.5	6.93	2.475	2.23
Co	4.1	7.87	2.55	2.23
Ni	3.7	8.97	2.45	2.22
Cu	2.8	9.91	1.825	2.26
Y	7.4	1.68	1.13	2.71
Zr	8.9	2.96	2	2.54
Nb	10.0	4.10	2.7	2.43
Mo	10.0	5.07	3	2.39
Tc	9.5	6.23	3.15	2.36
Ru	8.6	7.24	3.05	2.34
Rh	7.1	7.99	2.7	2.34
Pd	5.5	8.96	2.05	2.37
Ag	3.6	10.00	1.25	2.43
Hf	10.2	2.69	2.15	2.53
Ta	11.6	3.78	3.15	2.43
W	11.7	4.73	3.675	2.39
Re	11.4	5.73	3.6	2.37
Os	10.7	6.70	3.45	2.35
Ir	9.2	7.65	3	2.36
Pt	7.3	8.74	2.475	2.39
Au	5.3	9.89	1.5	2.43

Table B.7. DFT based data for host metals implemented in Equation 3. d-band widths, d-band fillings, and surface energies were calculated with Equations (B.6), (B.7), and (B.8) respectively.

Host	d-band width (eV)	d-band filling	Surface energy (J/m ²)	Coordination number at the surface	Coordination number in the bulk
Pt (111)	3.37	0.87	1.332	9	12
Pt (100)	3.34	0.86	1.773	8	12
Pt (110)	3.40	0.87	1.857	7	12
Pt (210)	3.21	0.90	1.941	6	12
Ir (111)	3.75	0.76	2.624	9	12
Ir (100)	3.74	0.76	3.096	8	12
Ir (110)	3.77	0.76	3.133	7	12
Ir (210)	3.62	0.76	3.226	6	12
Pd (111)	2.52	0.89	1.404	9	12
Pd (100)	2.51	0.90	1.616	8	12
Pd (110)	2.50	0.89	1.673	7	12
Pd (210)	2.48	0.89	1.707	6	12
Rh (111)	2.89	0.79	2.336	9	12
Rh (100)	2.88	0.79	2.506	8	12
Rh (110)	2.89	0.78	2.534	7	12
Rh (210)	2.83	0.79	2.574	6	12

Comparison between segregation energies calculated with DFT and our model for (111), (100), (110), and (210) surfaces of Ir, Pd, and Rh are shown in Figures B.10, B.11, and B.12 respectively. Our model follows segregation behavior very well, especially for the Ir and Rh surfaces.

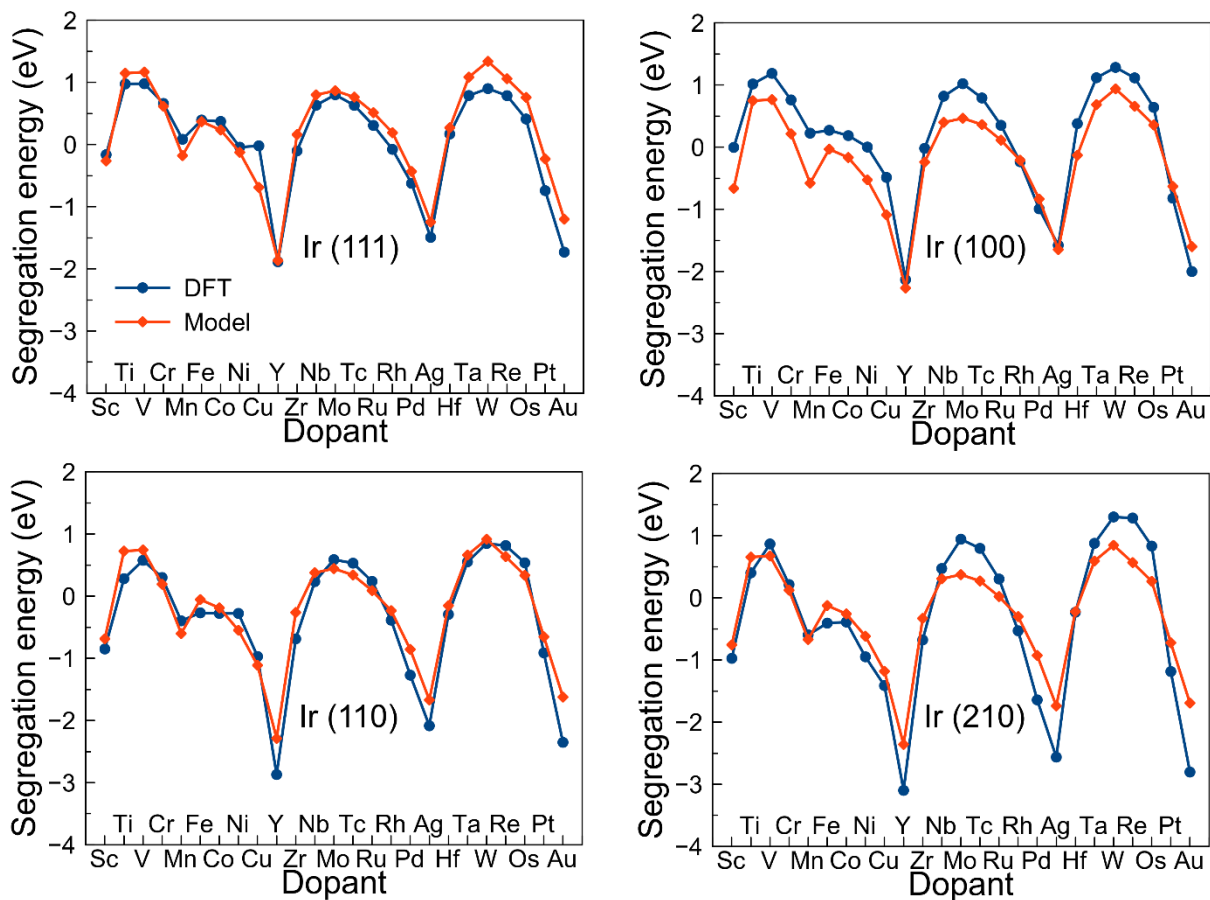


Figure B.10. Comparison of segregation energies for dopants in (111), (100), (110), and (210) surfaces of Ir obtained with DFT and our model.

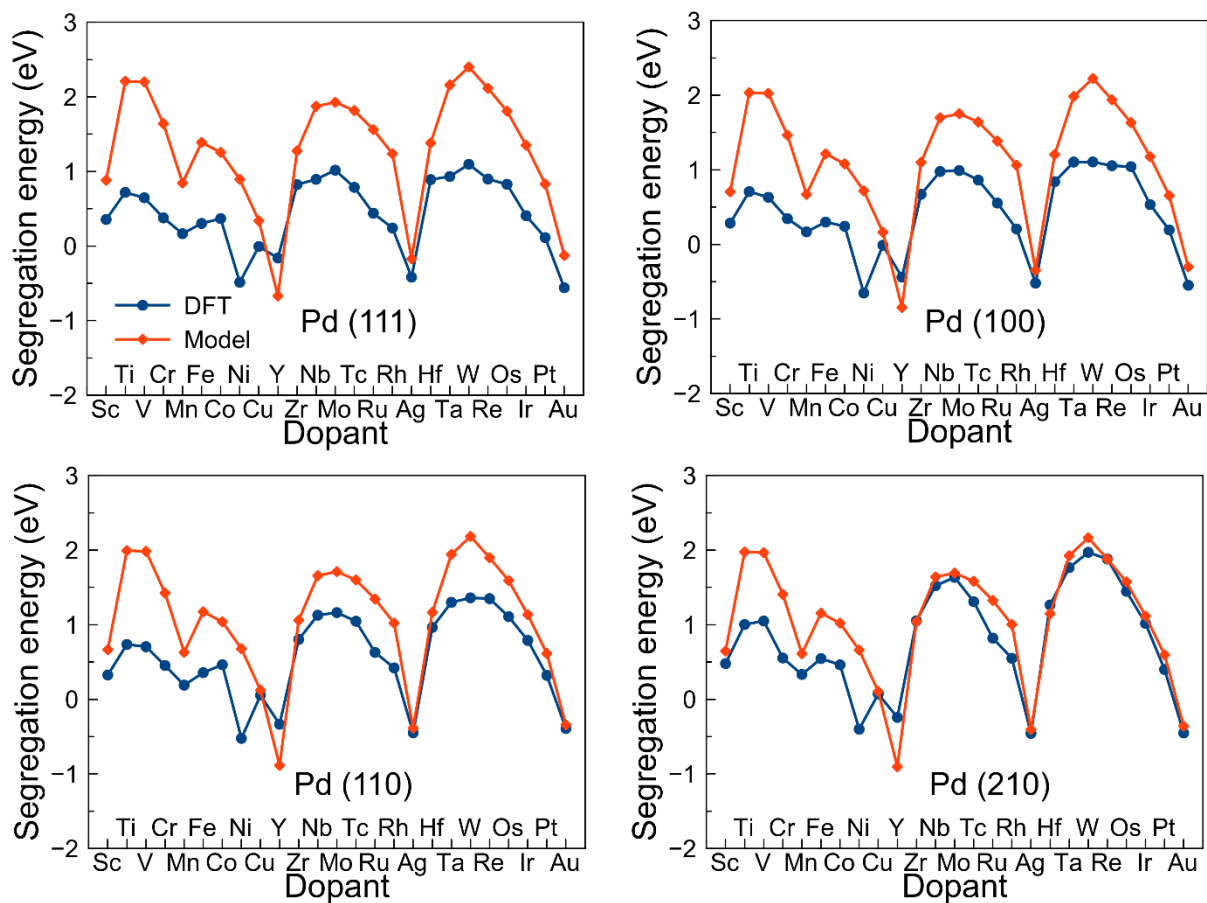


Figure B.11. Comparison of segregation energies for dopants in (111), (100), (110), and (210) surfaces of Pd obtained with DFT and our model.

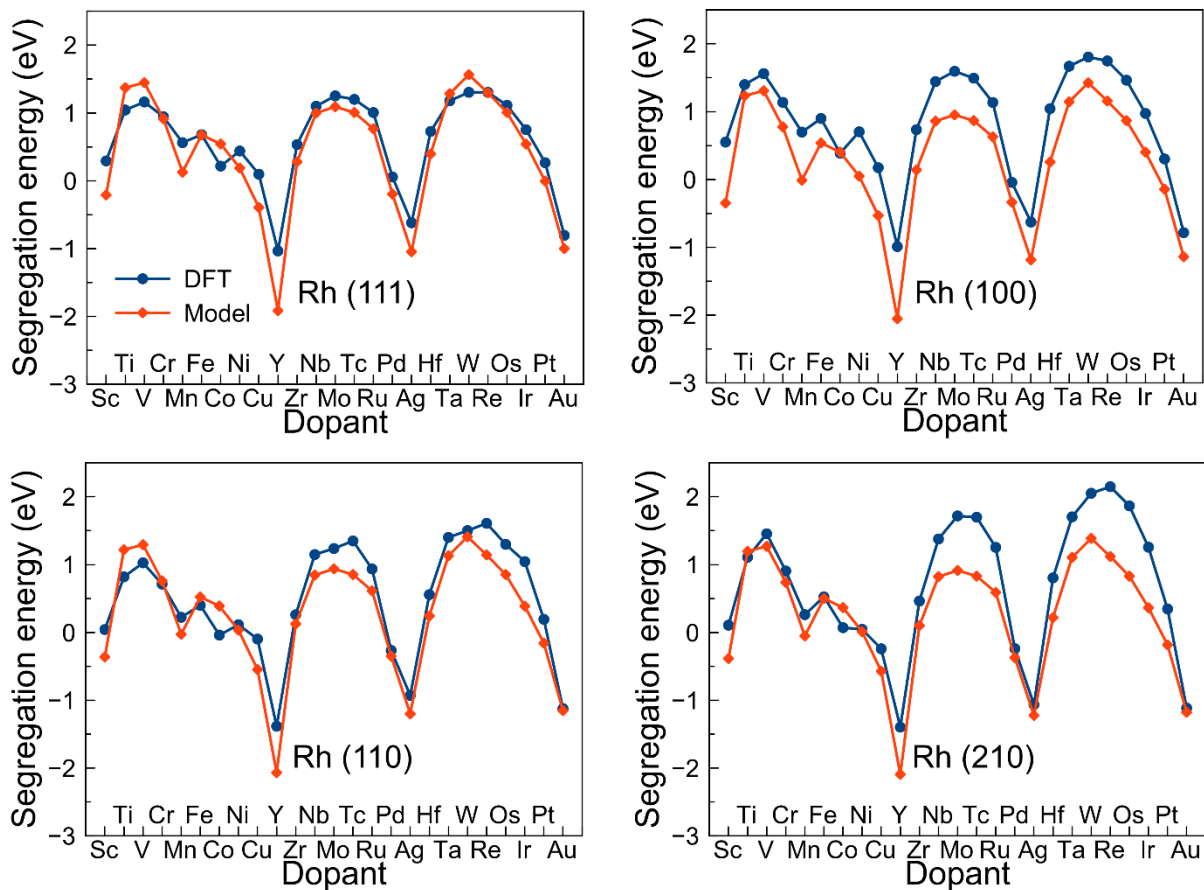


Figure B.12. Comparison of segregation energies for dopants in (111), (100), (110), and (210) surfaces of Rh obtained with DFT and our model.

Surface dependent segregation energy in (111), (100), (110), and (210) surfaces of Pt, Ir, Pd, and Rh as hosts and post-transition metals as dopant is depicted in Figure B.13.

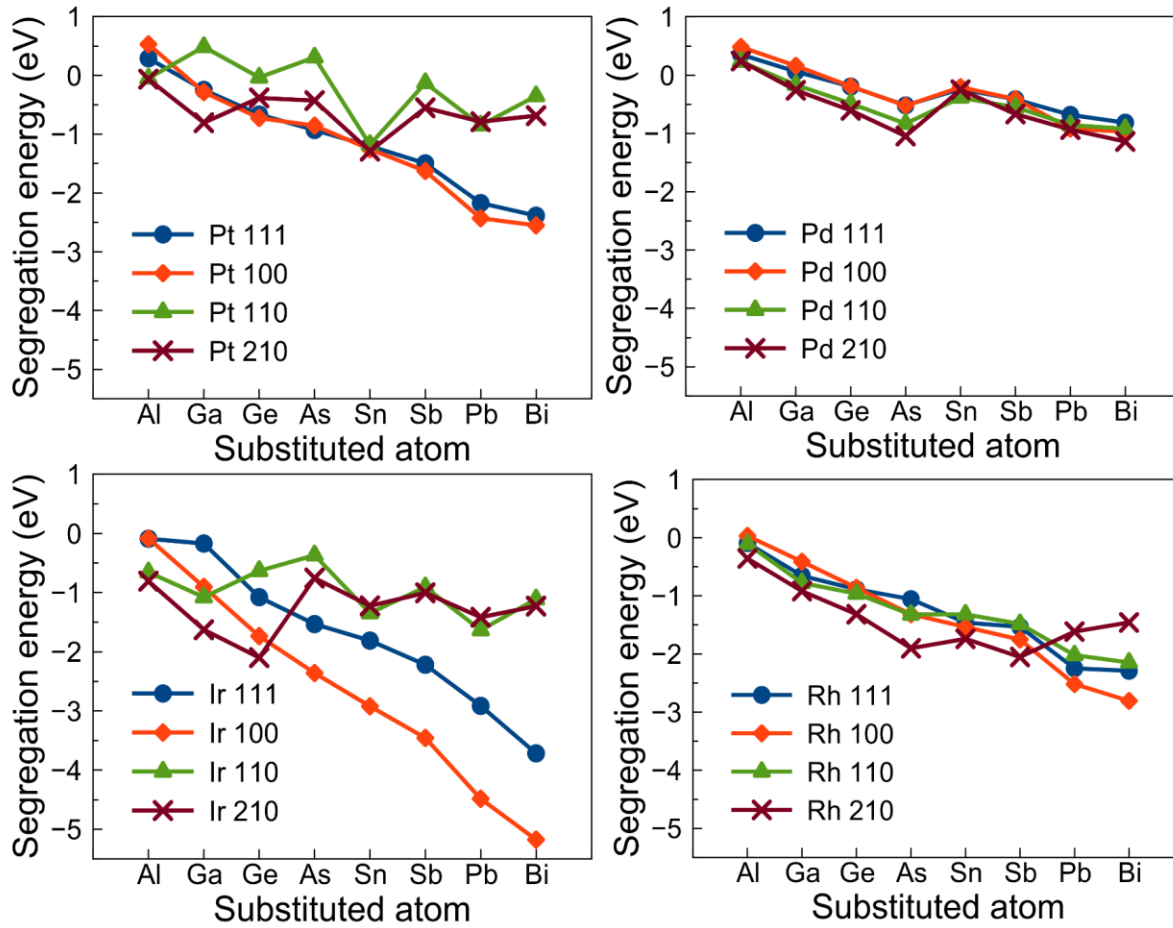


Figure B.13. Surface dependent segregation energy of post-transition metal dopants in (111), (100), (110), and (210) surfaces of Pt, Pd, Ir, and Rh as host metals.

Appendix C: Supporting Information: Comparison of different Catalysts for C-C Bond Scission in Ethanol Oxidation

C.1. Adsorption of CH_xCO , CH_x , and CO Species on Transition Metals

In this appendix the adsorption configurations over different surfaces is presented. In Figures C.1-C.4, adsorption energy of CH over metallic surfaces is demonstrated.

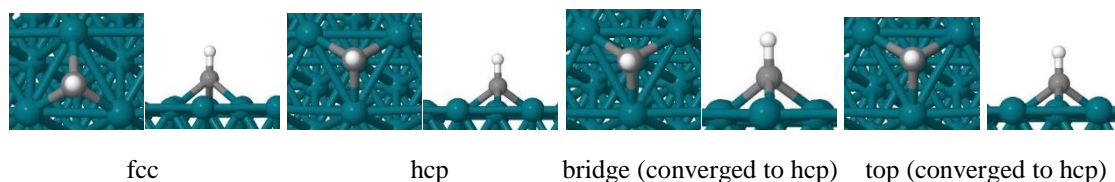


Figure C.1. CH adsorption on fcc, hcp, bridge, and top sites of Rh (111)

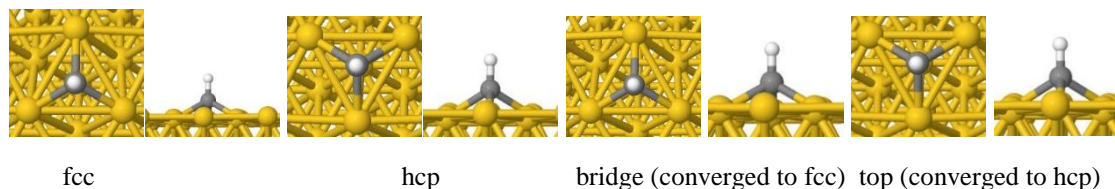


Figure C.2. CH adsorption on fcc, hcp, bridge, and top sites of Au (111)

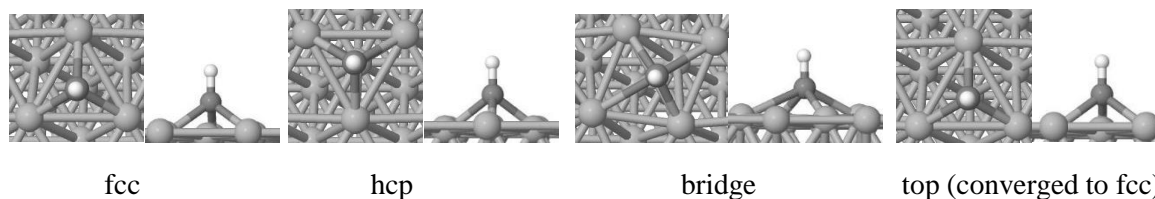


Figure C.3. CH adsorption on fcc, hcp, bridge, and top sites of Ag (111)

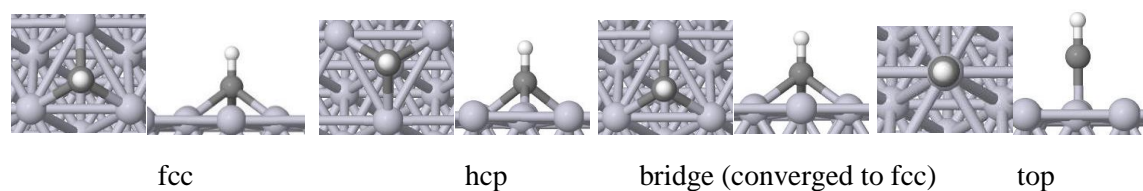


Figure C.4. CH adsorption on fcc, hcp, bridge, and top sites of Pt (111)

In Figures C.5-C.8, adsorption energy of CO over metallic surfaces has been shown.

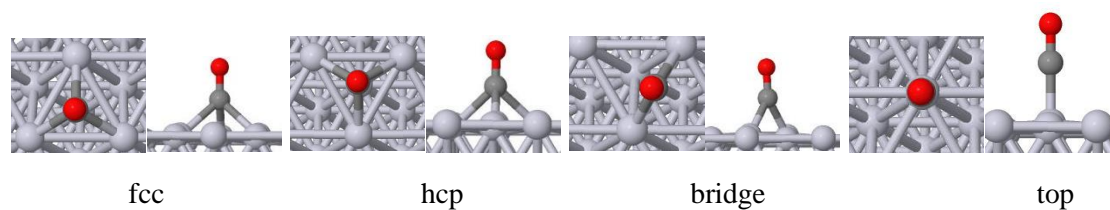


Figure C.5. CO adsorption on fcc, hcp, bridge, and top sites of Pt (111)

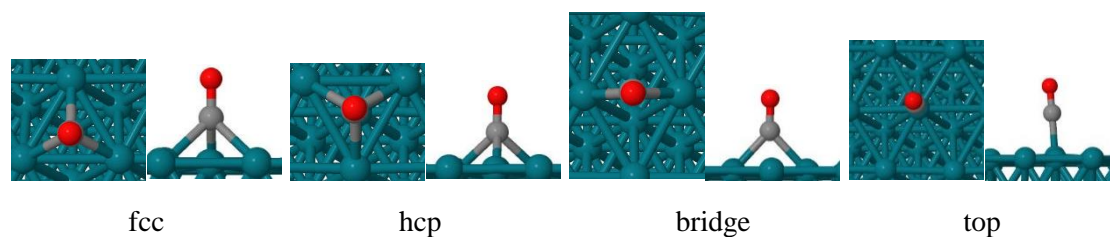


Figure C.6. CO adsorption on fcc, hcp, bridge, and top sites of Rh (111)

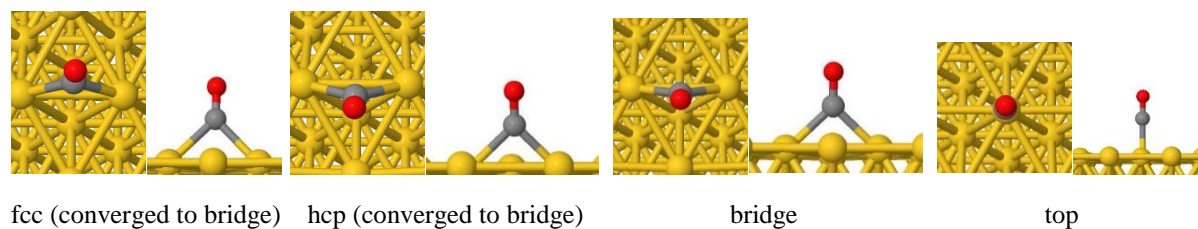


Figure C.7. CO adsorption on fcc, hcp, bridge, and top sites of Au (111)

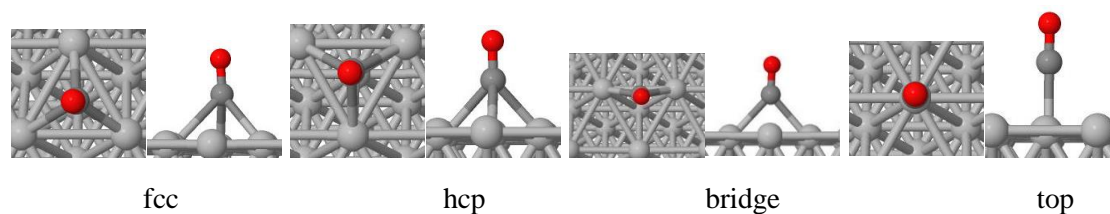


Figure C.8. CO adsorption on fcc, hcp, bridge, and top sites of Ag (111)

Figures C.9-C.13 shows the adsorption energy of CH₂ over metallic surfaces.

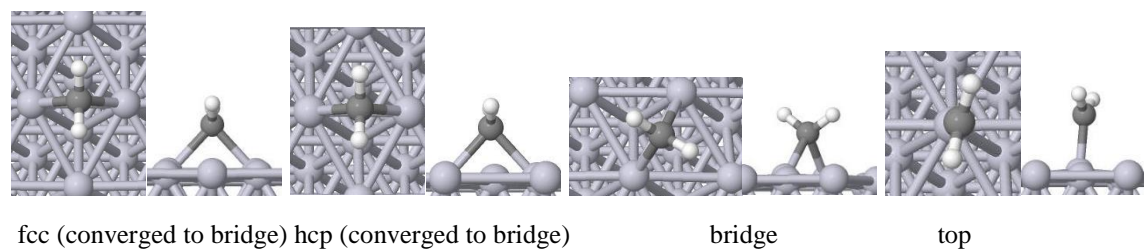


Figure C.9. CH₂ adsorption on fcc, hcp, bridge, and top sites of Pt (111)

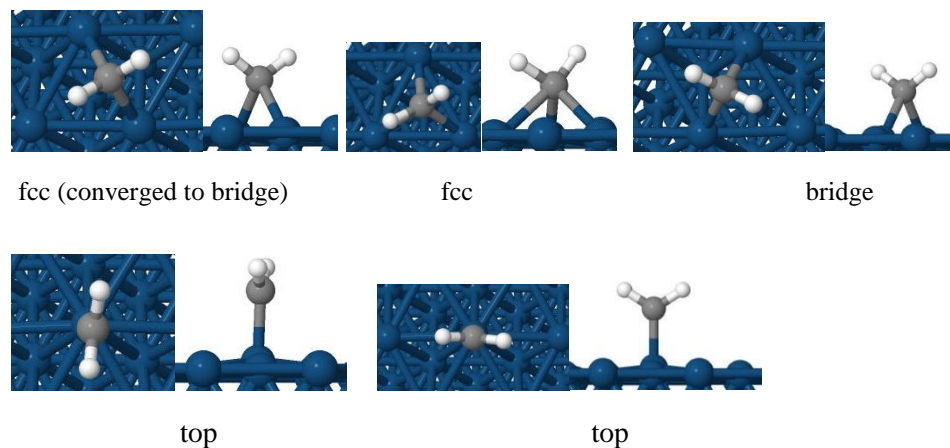


Figure C.10. CH₂ adsorption on fcc, hcp, bridge, and top sites of Ir (111)

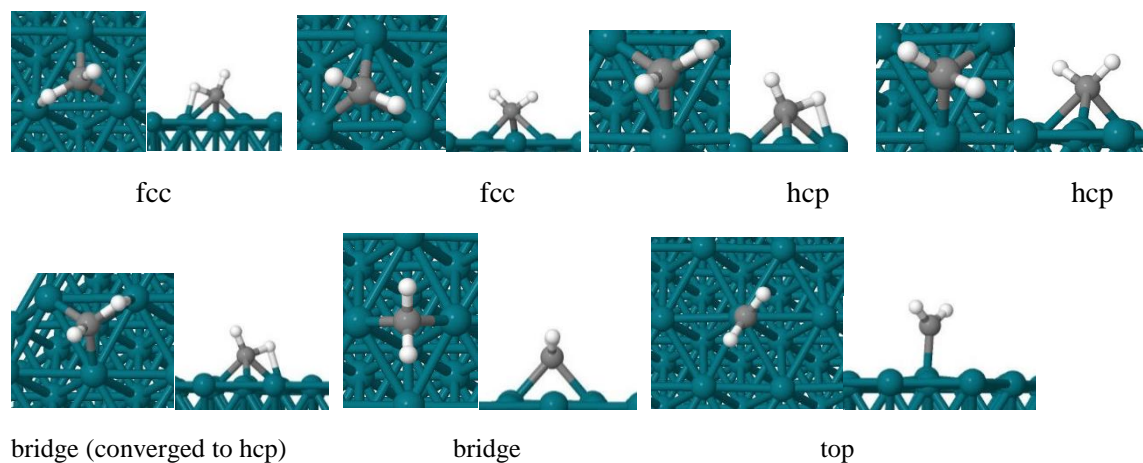


Figure C.11. CH₂ adsorption on fcc, hcp, bridge, and top sites of Rh (111)

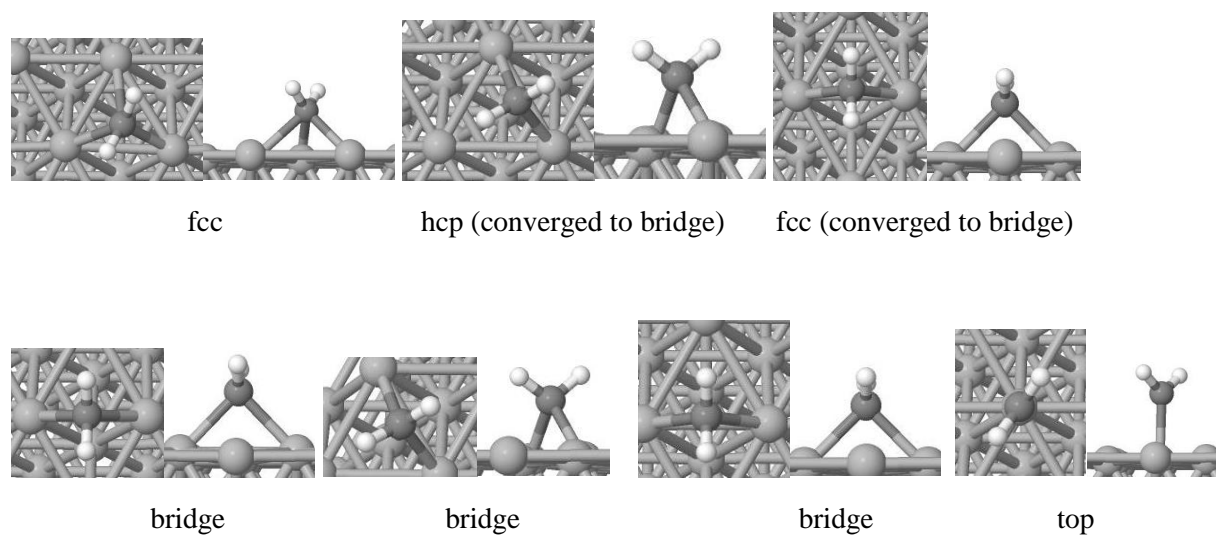


Figure C.12. CH₂ adsorption on fcc, hcp, bridge, and top sites of Ag (111)

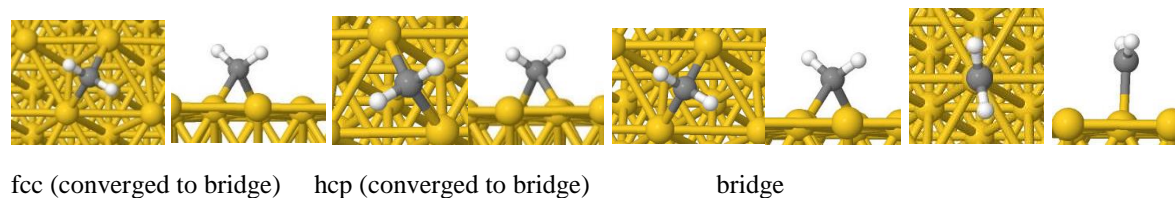


Figure C.13. CH₂ adsorption on fcc, hcp, bridge, and top sites of Au (111)

Adsorption energy of CH₃ over different adsorption sites of Ir, Rh, Pt, Au, and Ag has been shown in Figures C.14-C.18.

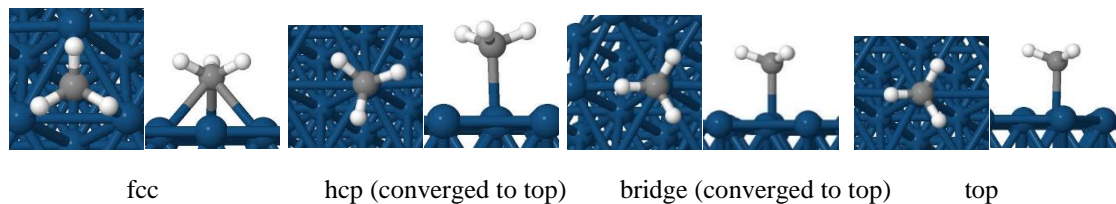


Figure C.14. CH₃ adsorption on fcc, hcp, bridge, and top sites of Ir (111)

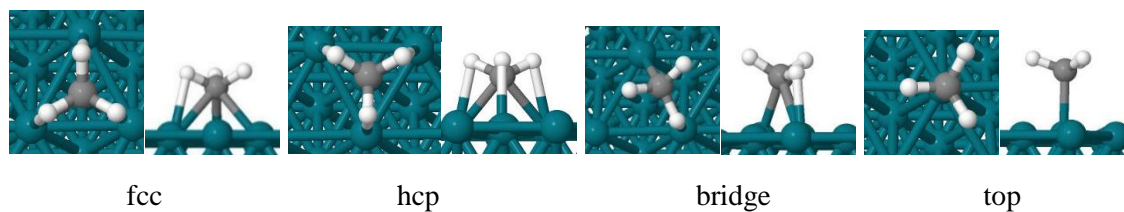


Figure C.15. CH₃ adsorption on fcc, hcp, bridge, and top sites of Rh (111)

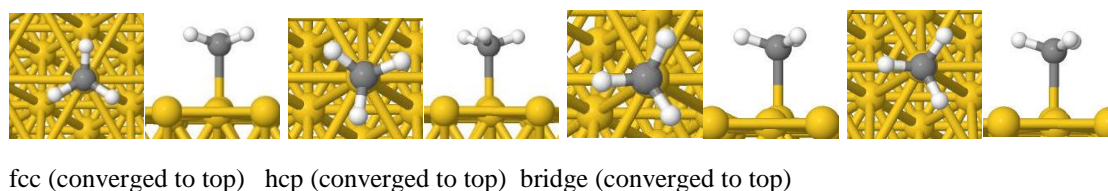


Figure C.16. CH₃ adsorption on fcc, hcp, bridge, and top sites of Au (111)

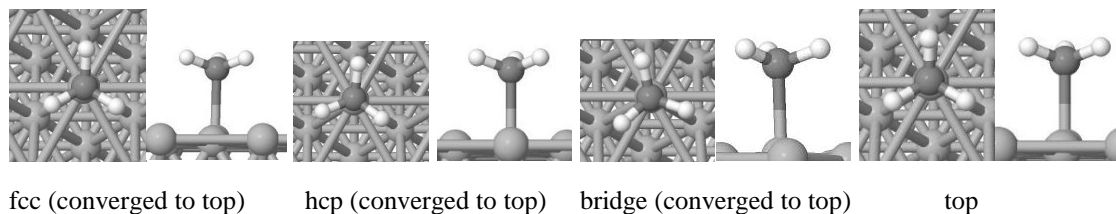
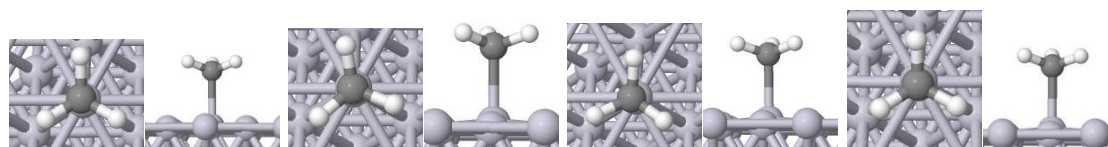


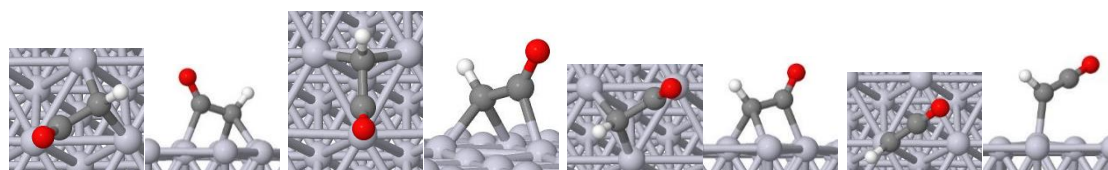
Figure C.17. CH₃ adsorption on fcc, hcp, bridge, and top sites of Ag (111)



fcc (converged to top) hcp (converged to top) bridge (converged to top) top

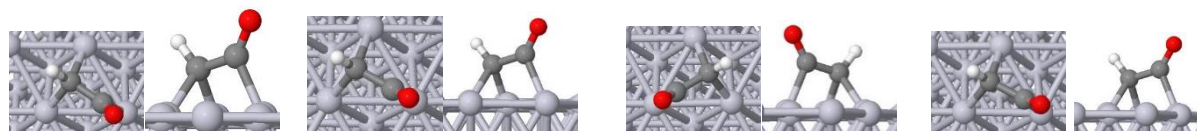
Figure C.18. CH₃ adsorption on fcc, hcp, bridge, and top sites of Pt (111)

Adsorption energy of CHCO over different adsorption sites of Ir, Rh, Pt, Au, and Ag has been shown in Figures C.19-C.22.



Initial: CO -top-CH-fcc Initial: CO-top-CH-hcp Initial: CO and CH top Initial: CO fcc, CH top

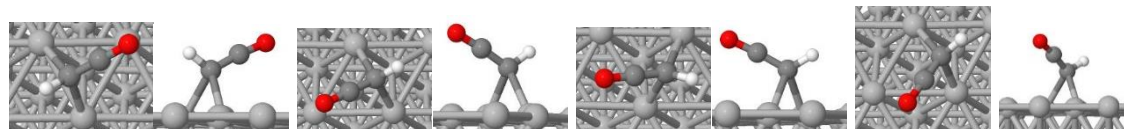
Final: CO top-CH- bridge Final: CO-top-CH-bridge Final: CO top-CH bridge Final: Bond through C in CH



Initial: CH fcc, CO hcp Initial: CO fcc, CH hcp Initial: CO top, CH fcc Initial: CO hcp, CH bridge

Final: CH Bridge,
CO near top Final: CO near top,
CH bridge Final: CO top, CH bridge

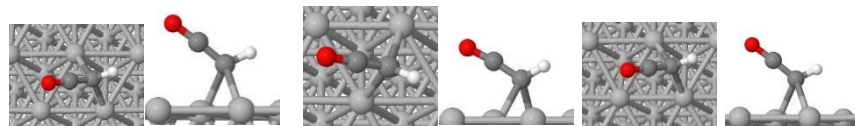
Figure C.19. CHCO adsorption on Pt (111)



Initial: CO top, CH fcc

Initial: CHCO hcp

Initial: CHCO top



Initial: CO top, CH hcp

Initial: CHCO fcc

Initial: CO top, CH hcp

Figure C.20. CHCO adsorption on Ag (111)

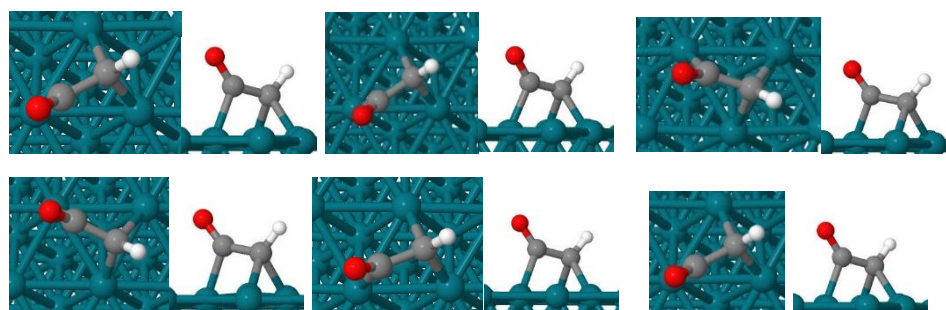


Figure C.21. CHCO adsorption on Rh (111)

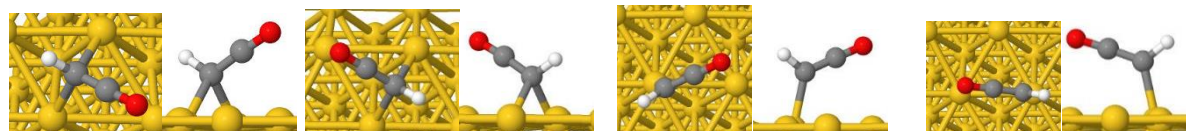
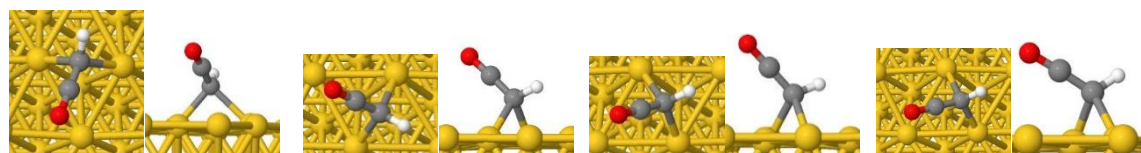


Figure C.22. CHCO adsorption on Au (111)

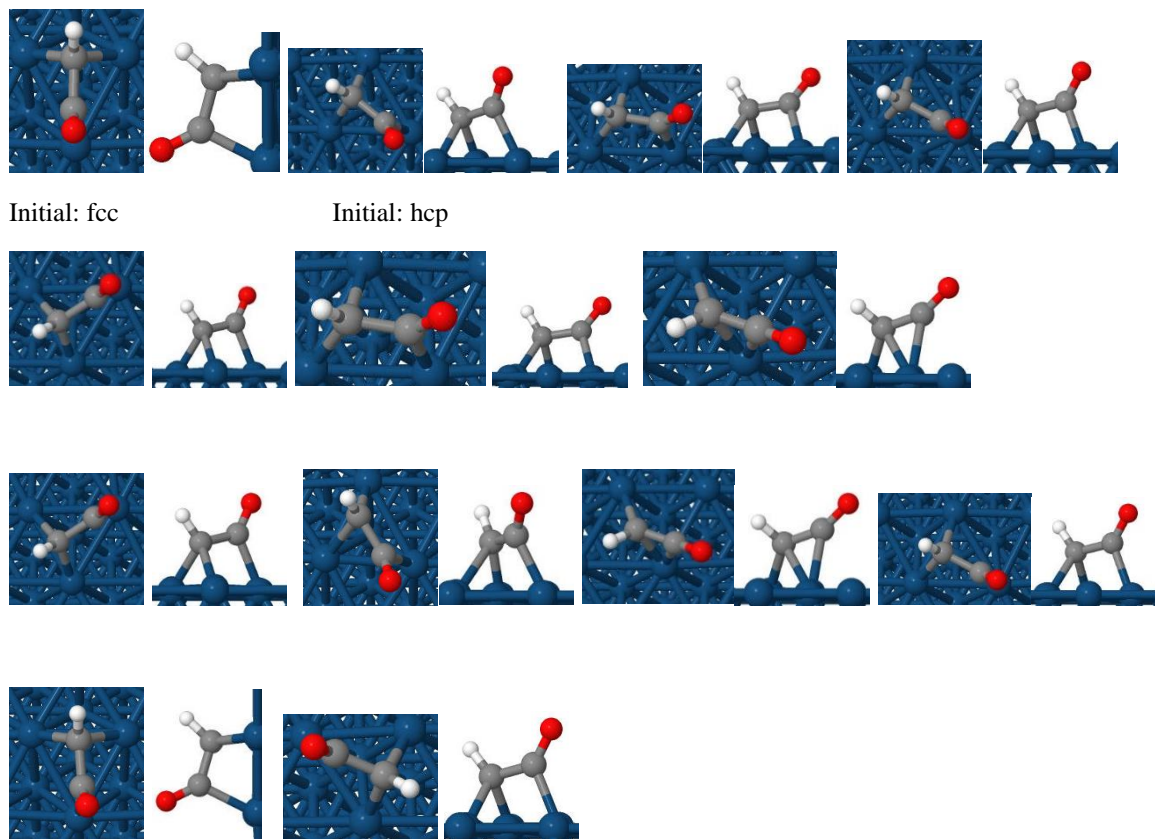


Figure C.23. CHCO adsorption on Ir (111)

Adsorption energy of CH_2CO over different adsorption sites of Ir, Rh, Pt, Au, and Ag has been shown in Figures C.24-C.28.

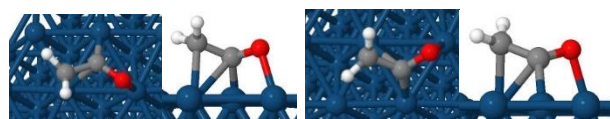


Figure C.24. CH_2CO adsorption on Ir (111)

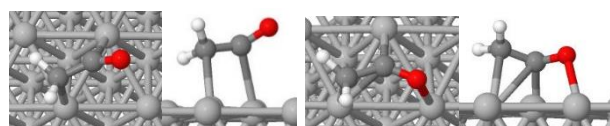


Figure C.25. CH_2CO adsorption on Ag (111)

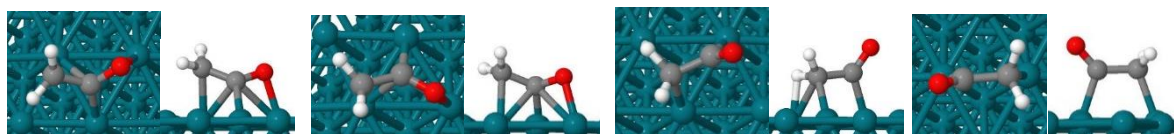


Figure C.26. CH₂CO adsorption on Rh (111)

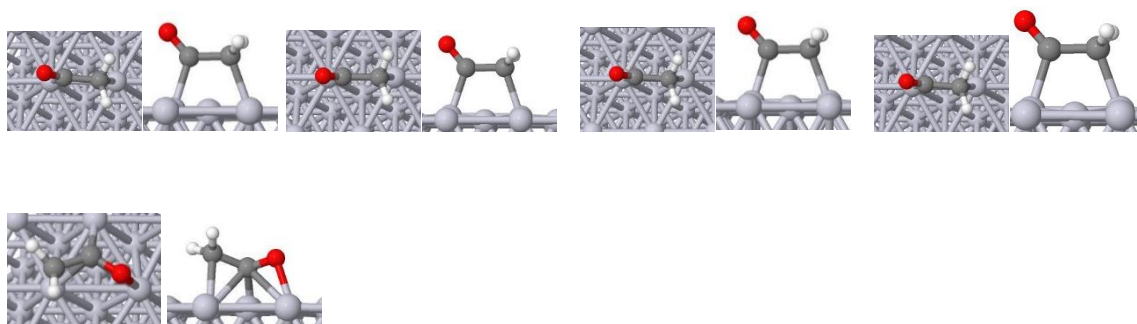


Figure C.27. CH₂CO adsorption on Pt (111)

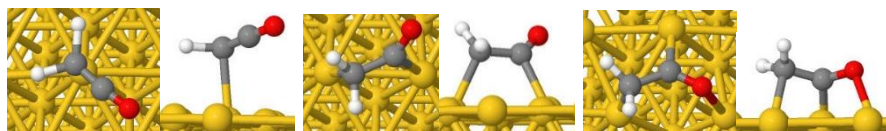


Figure C.28. CH₂CO adsorption on Pt (111)

Adsorption energy of CH₃CO over different adsorption sites of Ir, Rh, Pt, Au, and Ag has been shown in Figures C.29-C.34.

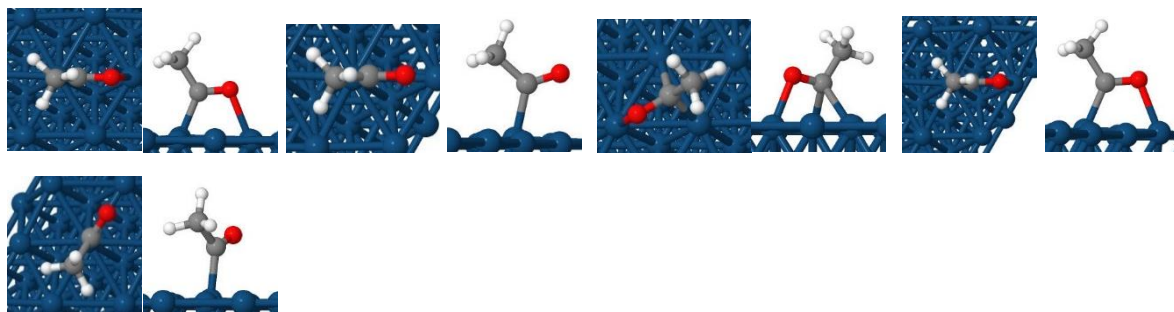


Figure C.29. CH₃CO adsorption on Ir (111)

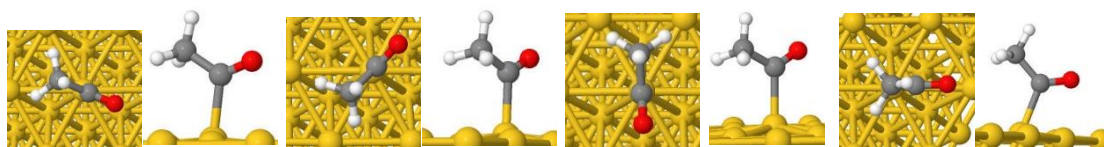


Figure C.30. CH₃CO adsorption on Au (111)

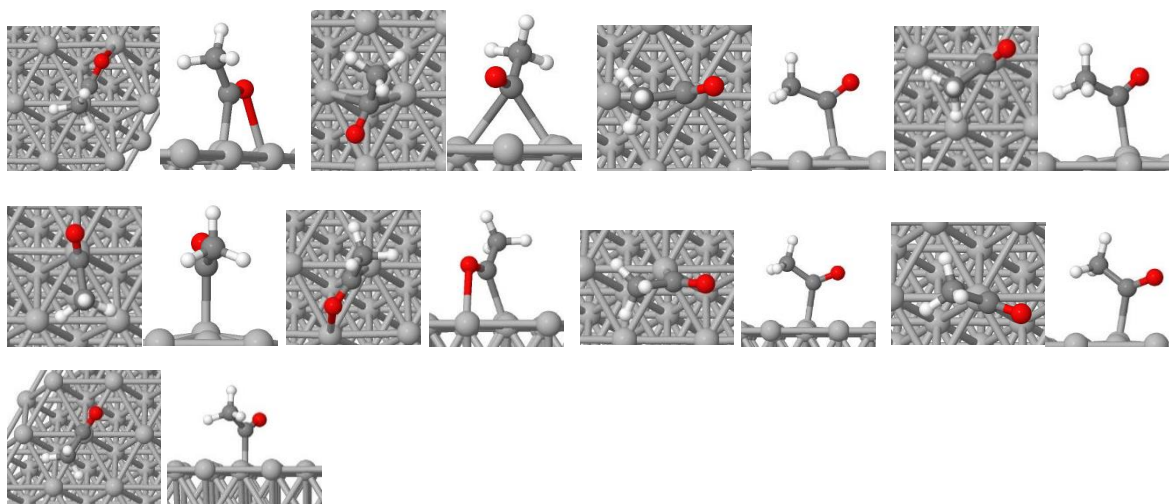


Figure C.31. CH₃CO adsorption on Ag (111)

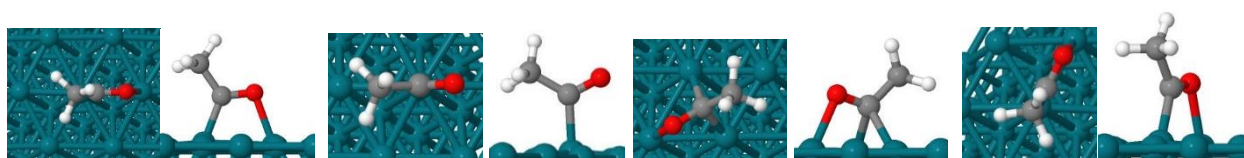


Figure C.32. CH₃CO adsorption on Rh (111)

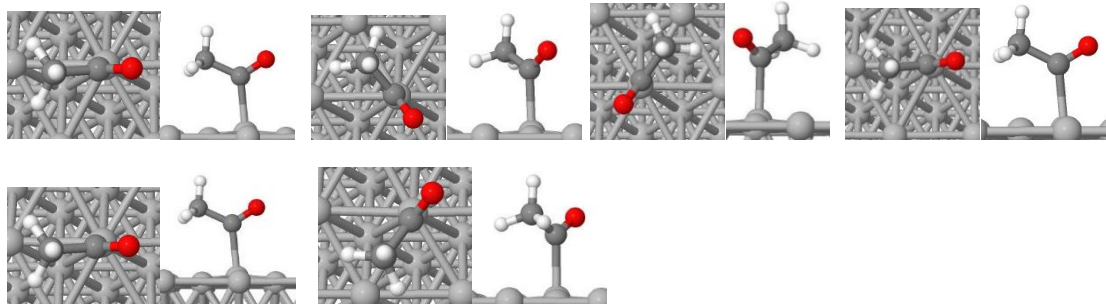


Figure C.33. CH₃CO adsorption on Ag (111)

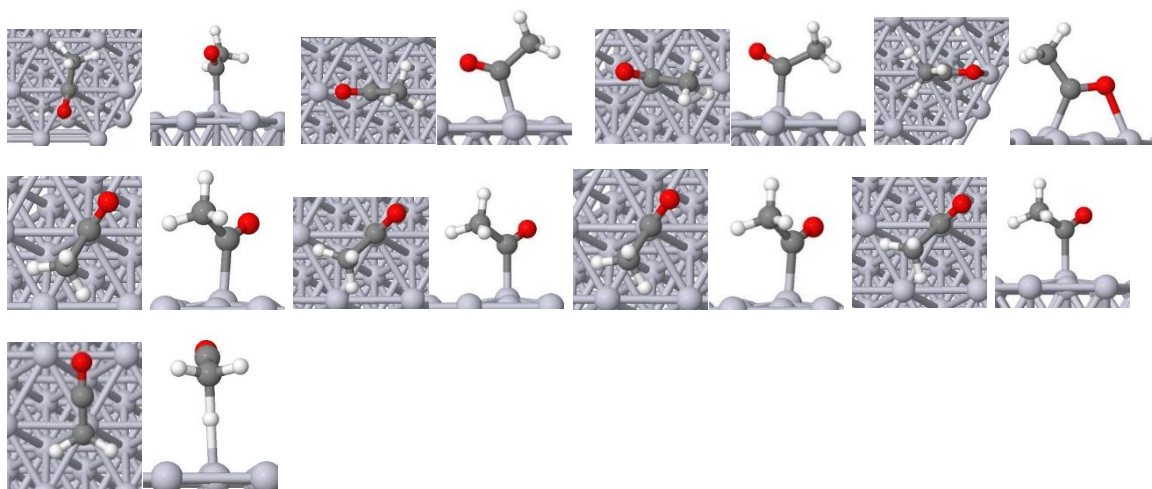


Figure C.34. CH₃CO adsorption on Pt (111)

C.2. Reaction modeling of C–C bond breaking at the surface of different Transition Metals

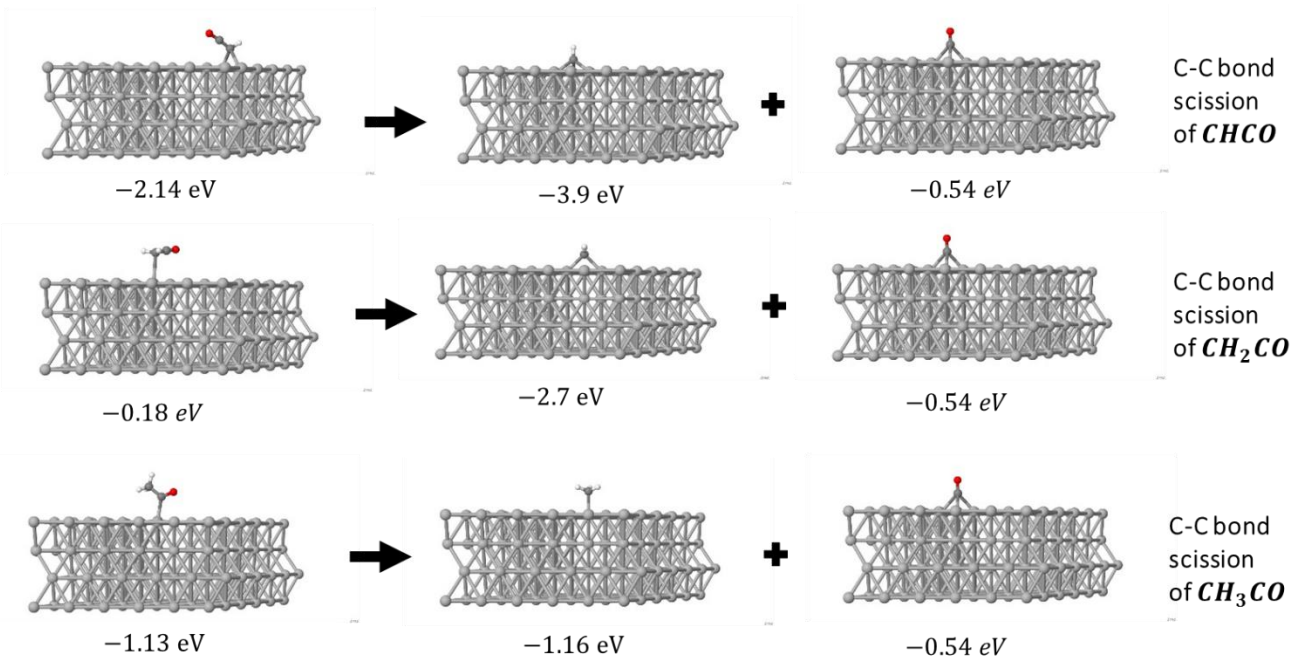


Figure C.35. C-C bond breaking of CHCO, CH₂CO, and CH₃CO over Ag (111). The adsorption energies are listed below each structure.

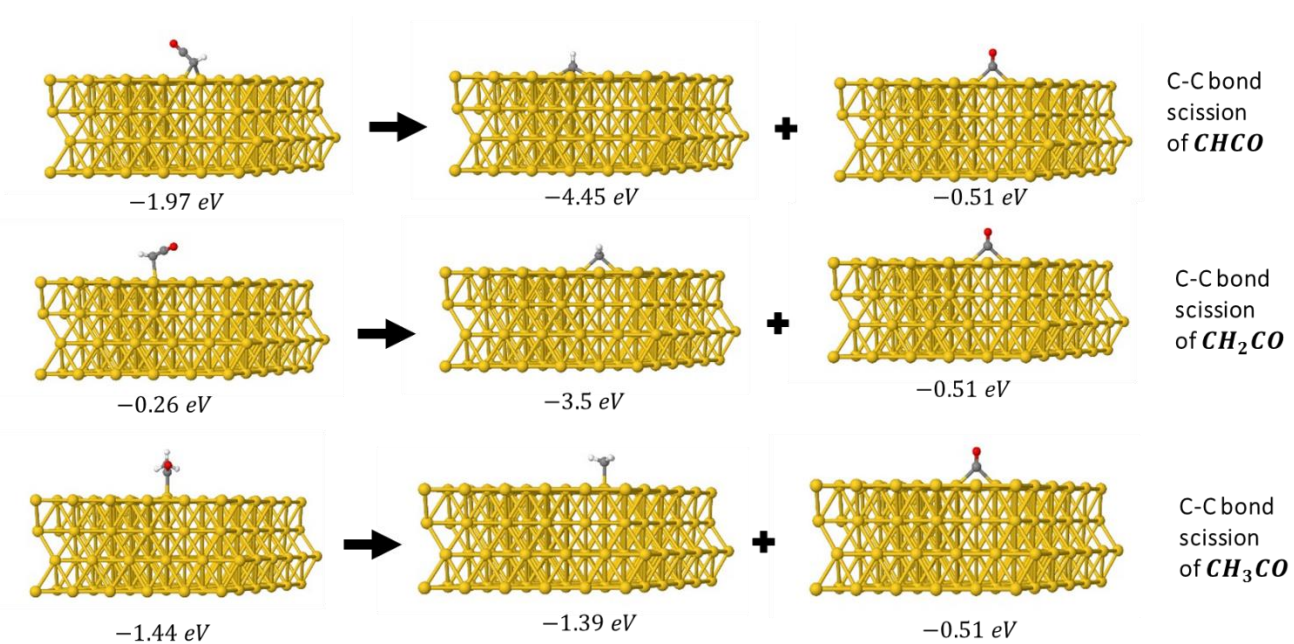


Figure C.36. C-C bond breaking of CHCO, CH₂CO, and CH₃CO over Au (111). The adsorption energies are listed below each structure.

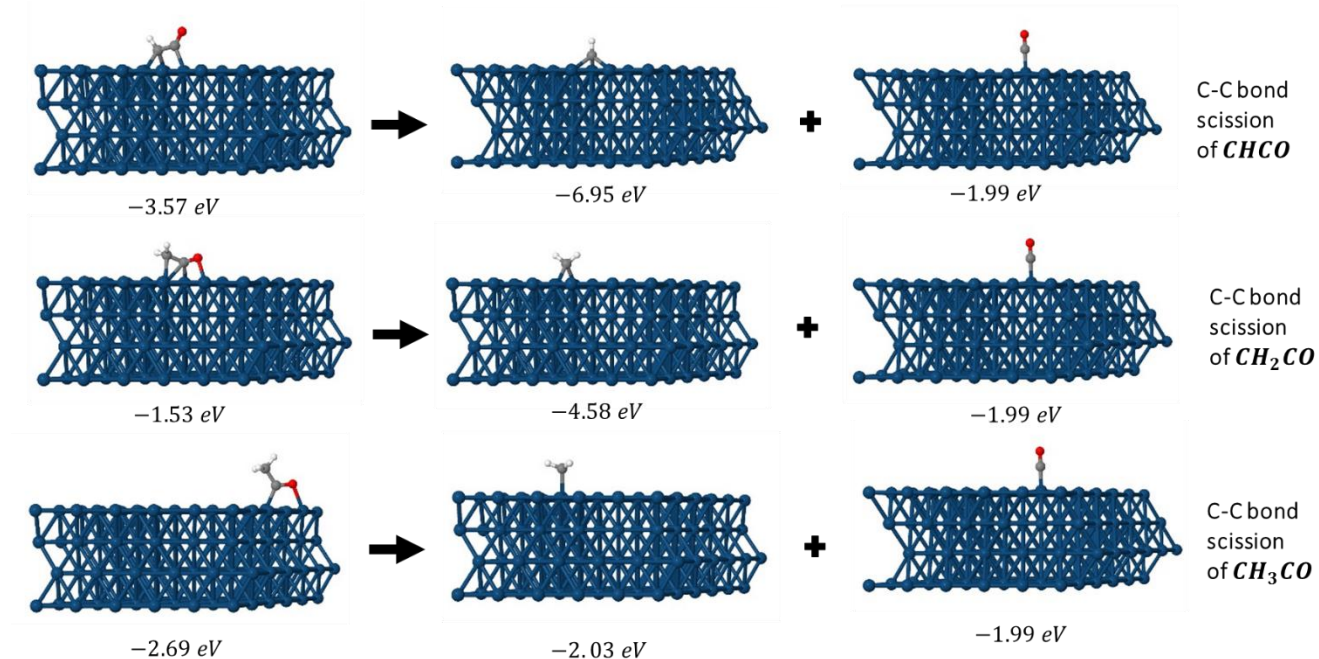


Figure C.37. C-C bond breaking of CHCO, CH₂CO, and CH₃CO over Ir (111). The adsorption energies are listed below each structure. The adsorption energies are listed below each structure.

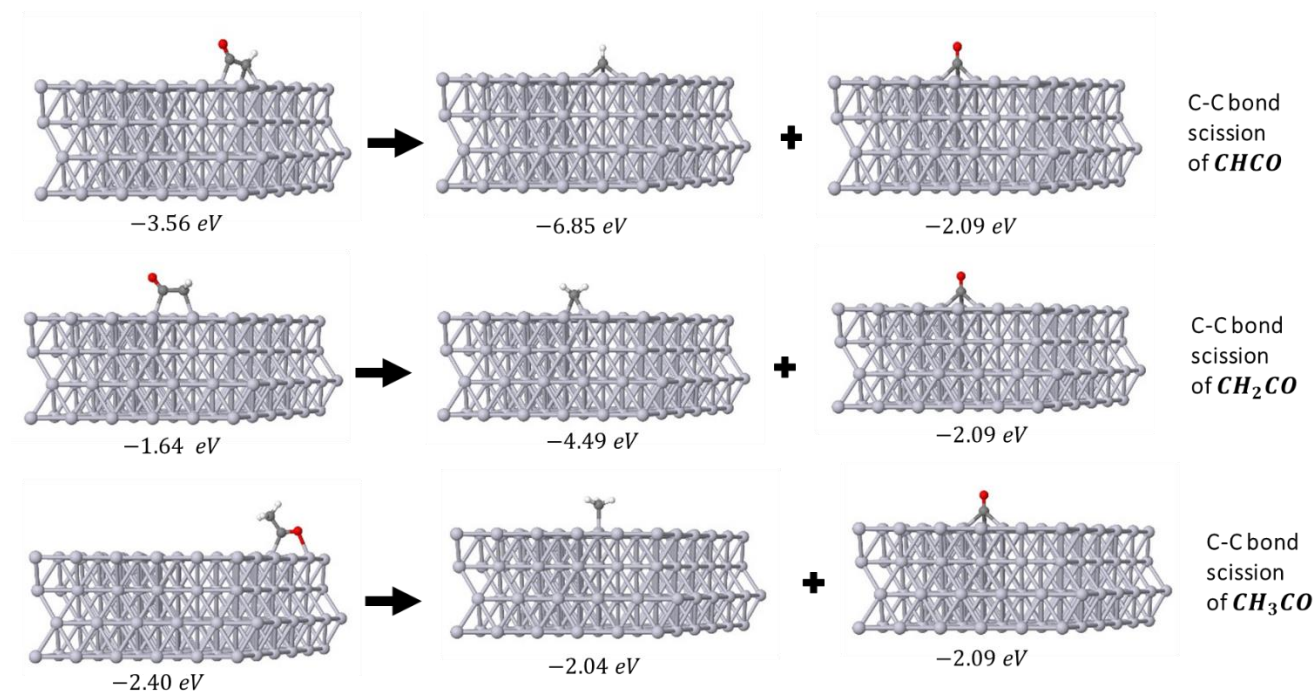


Figure C.38. C-C bond breaking of CHCO, CH₂CO, and CH₃CO over Pt (111). The adsorption energies are listed below each structure.

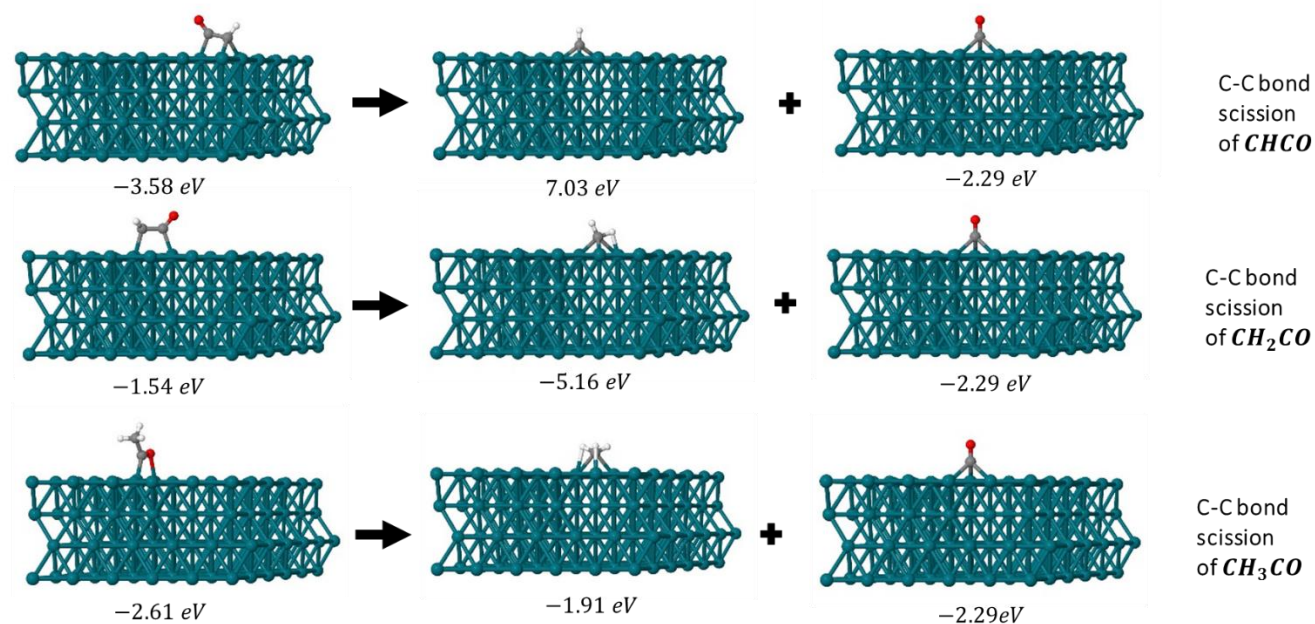


Figure C.39. C-C bond breaking of $CHCO$, CH_2CO , and CH_3CO over Rh (111). The adsorption energies are listed below each structure.

C.3. Adsorption of CH_xCO , CH_x , and CO Species on Ir-based Alloys

Table C.1. CH and CO adsorption energies on different sites of Ir, Ir-Rh, and Ir-Rh-Sn surfaces

	Adsorption energy(eV)								
	Ir			Ir-Rh			Ir-Rh-Sn		
	top	hcp	fcc	top	hcp	fcc	top	hcp	fcc
CH	-4.99	-7.11	-6.79	-4.72	-6.91	-6.75	-6.53	-6.53	-6.61
CO	-2.15	-1.84	-1.77	-2.04	-2.17	-2.13	-1.74	-2.15	-2.12

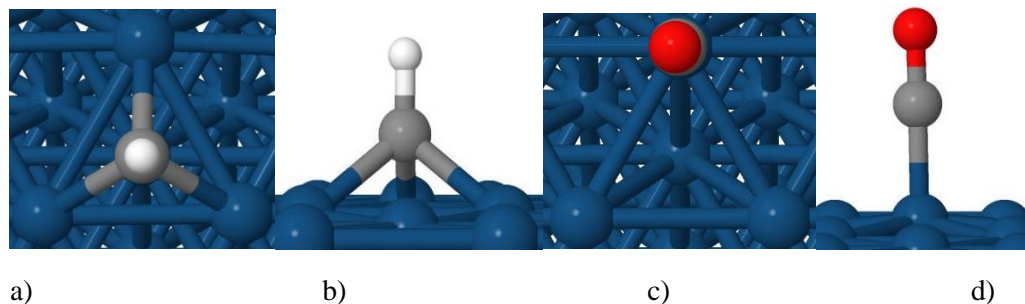


Figure C.40. The most stable configuration for adsorption of CH and CO on Ir surface. Ir, C, H, and O atoms are shown in blue, grey, white, and red respectively. a) Top and b) side views of CH adsorption on hcp site of Ir surface. c) Top and d) side views of CO adsorption on top site of Ir surface.

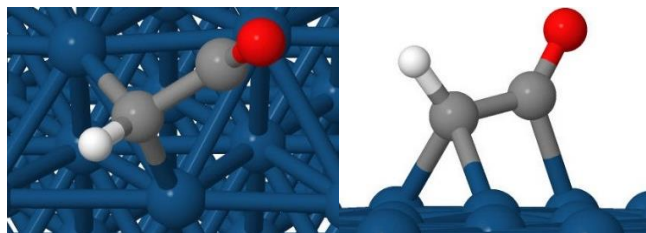


Figure C.41. Top-view (left) and side-view (right) of CHCO adsorption on Ir surface. Ir, C, H, and O atoms are shown in blue, grey, white, and red respectively.

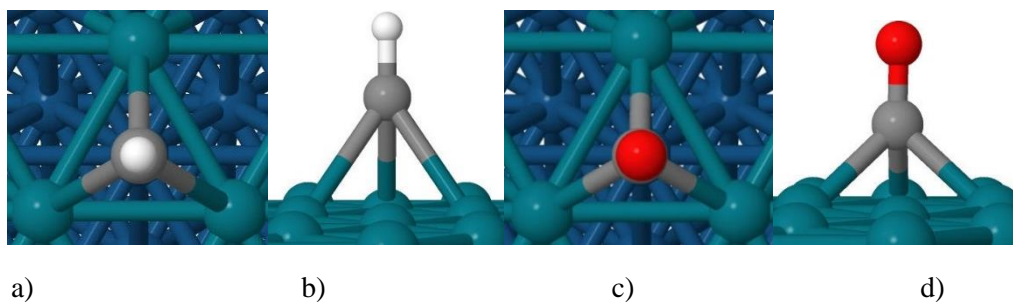


Figure C.42. The most stable configuration for adsorption of CH and CO on Ir-Rh surface. Ir, Rh, C, H, and O atoms are shown in blue, green, grey, white, and red respectively. a) Top and b) side views of CH adsorption on hcp site of Ir-Rh surface. c) Top and d) side views of CO adsorption on hcp site of Ir-Rh surface.

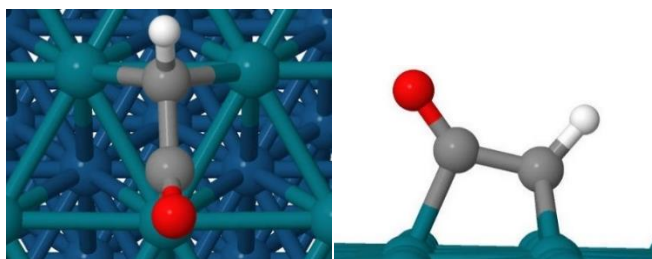


Figure C.43. Top-view (left) and side-view (right) of CHCO adsorption on Ir-Rh surface. Ir, Rh, C, H, and O atoms are shown in blue, green, grey, white, and red respectively.

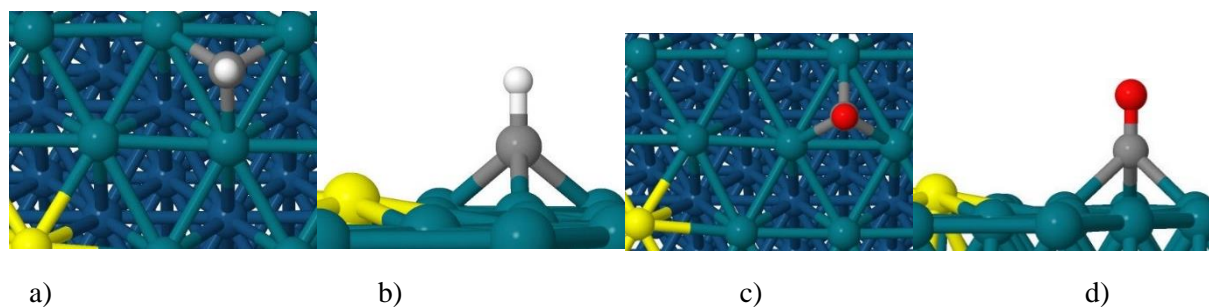


Figure C.44. The most stable configuration for adsorption of CH and CO on Ir-Rh-Sn surface. Ir, Rh, Sn, C, H, and O atoms are shown in blue, green, yellow, grey, white, and red respectively. a) Top and b) side views of CH adsorption on fcc site of Ir-Rh-Sn surface. c) Top and d) side views of CO adsorption on hcp site of Ir-Rh-Sn surface.

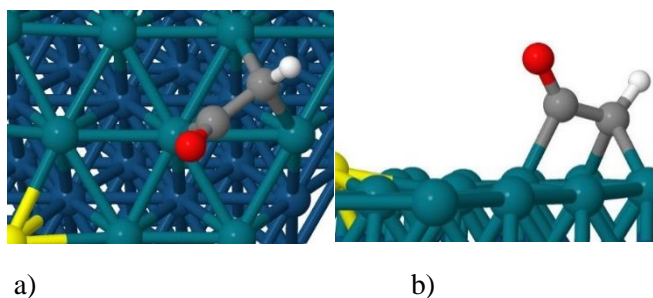


Figure C.45. Top-view (left) and side-view (right) of CHCO adsorption on Ir-Rh-Sn surface. Ir, Rh, Sn, C, H, and O atoms are shown in blue, green, yellow, grey, white, and red respectively.

Table C.2. CHCO adsorption energy on Ir, Ir-Rh, and Ir-Rh-Sn surfaces

Surface	Adsorption energy(eV)
Ir	-3.51
Ir-Rh	-3.36
Ir-Rh-Sn	-3.37

Table C.3. Calculated CHCO adsorption energies in different geometries and different sites over the Ir-Rh-Sn surface. For these calculations, CHCO was put on different areas (including Rh atoms, Sn atoms, and in between those) to investigate the effect of the area. It was observed that the best adsorption energies were obtained when CHCO was put on Rh areas. In each area, CH and CO were adsorbed on different sites to investigate the most favorable geometry. As the adsorption on Sn and near Sn areas were unfavorable, most calculations were done regarding different sites on Rh areas.

Adsorption of CHCO on Different areas	Different Sites for CH and CO		Adsorption energies(eV)
	CH	CO	
Rh	hcp	fcc	-3.185
	top	top	-3.182
	top	hcp	-3.37
	top	hcp*	-2.38
	bridge	top	-3.31
	bridge	bridge	-3.22
	top	top	-3.33
Sn	top	hcp	-1.80
	top	bridge	-1.79
Between Rh/Sn	fcc	hcp	-2.92
	fcc	top	-1.42
	hcp	fcc	-1.87
	top	hcp	-1.83
	bridge	top	-3.27
	bridge	bridge	-1.81

* The difference between this site with the previous one is that in the latter case, CH and CO were put closer to Sn area. As it can be seen, the latter case has less negative energy, proving the fact that Sn areas are highly unfavorable.

Table C.4. CH and CO adsorption energies on different areas and different sites of Ir-Rh-Sn surface

	Adsorption energy on Ir-Rh-Sn surface (eV)						
	Rh			Sn		Between Rh and Sn	
	top	hcp	fcc	top	hcp	hcp	fcc
CH	-6.53	-6.53	-6.61	-2.23	-3.97	-6.46	-4.42
CO	-1.74	-2.15	-2.12	-0.08	-0.08	-1.84	-0.03

C.4. Adsorption of CH_xCO , CH_x , and CO Species on Metal-Metal Oxide Catalysts

Table C.5. Calculated CO adsorption energies on different sites over Pt (111)

Adsorption site	Adsorption energy (eV)
top	-2.38
fcc	-2.51
hcp	-2.45
bridge	-2.44

Table C.6. Calculated CHCO adsorption energies on different sites over Pt (111)

Adsorption site	Converged adsorption site	Adsorption energy (eV)
CO-top-CH-hcp	converged to CO-top-CH-bridge	-3.63
CH-fcc-CO-hcp	converged to CO-top-CH-bridge	-3.67
CO-top-CH-bridge	converged to CO-top-CH-bridge	-3.68
CO-top-CH-fcc	converged to CO-top-CH-bridge	-3.68

Table C.7. Calculated CH_2 adsorption energies on different sites over Pt (111)

Adsorption site	Adsorption energy (eV)
top	-4.34
fcc converged to bridge	-5.16
hcp converged to bridge	-5.16
bridge	-5.16

Table C.8. Calculated CH_2CO adsorption energies on different sites over Pt (111)

Adsorption site	Converged adsorption site	Adsorption energy (eV)
COtop-CH2bridge	COtop-CH2top	-1.69
CObridge-CH2top	COtop-CH2top	-1.68
COhcp-CH2top	COtop-CH2top	-1.69
Cofcc-CH2hcp	COtop-CH2top	-1.68
Cobridge-CH2top	COtop-CH2top	-1.7

Table C.9. Calculated CH₃CO adsorption energies on different sites over Pt (111)

Adsorption site	Adsorption energy (eV)
H bond with surface	-1.17
C (top)in CO bond with surface-CH ₃ hcp	-2.53
C (top) in CO bond with surface-CH ₃ bridge	-2.54

Table C.10. Calculated CH₃ adsorption energies on different sites over Pt (111)

Adsorption site	Adsorption energy (eV)
fcc-converged to top site	-2.12
top	-2.12
hcp-converged to top site	-2.12
bridge-converged to top site	-2.12

Table C.11. Calculated CH adsorption energies on different sites over Pt (111)

Adsorption site	Adsorption energy (eV)
hcp	-7.09
fcc	-7.19
top	-4.44
bridge converged to fcc	-7.19

Table C.12. Calculated CH₂CO adsorption energies on different sites over Pt-SnO₂

Adsorption site	Adsorption energy (eV)
O-bond-with-surface	-2
on top of Pt-O and C bond with Pt	-1.82
on oblique site	-2.15
on top site	-1.82
on Pt, third layer	-0.78
Tin-oxide	-0.25
Tin-oxide	-0.73
Tin-oxide	-0.75

Table C.13. Calculated CH₂ adsorption energies on different sites over Pt-SnO₂

Adsorption site	Adsorption energy (eV)
on-Pt-between second and third layer	-4.85
on top of Pt	-5.88
tin-oxide	-2.4
on top of Pt	-5.79
Interface of Pt and tin-oxide	-5.28
Interface of Pt and tin-oxide	-4.73
on metallic site	-5.78

Table C.14. Calculated CH₃CO adsorption energies on different sites over Pt-SnO₂

Adsorption site	Adsorption energy (eV)
on Pt-first layer	-2.21
on Pt-second layer	-2.6
on Pt-third layer	-2.55
on Pt-third layer	-2.52
on Pt- top-vertical	-2.56
on Pt- second layer	-2.79
on Pt-third layer	-2.61
Tin-oxide	-1.34
on Pt-second layer	-2.78
on Pt-O and C bond to surface	-3

Table C.15. Calculated CH adsorption energies on different sites over Pt-SnO₂

Adsorption site	Adsorption energy (eV)
on border	-6.52
on-oblique metallic site	-6.86
on-oblique-top-near-sno2	-6.37
on-sn	-2.47
on-top	-6.75
on-top-top site	-5.14

Table C.16. Calculated CH₃ adsorption energies on different sites over Pt-SnO₂

Adsorption site	Adsorption energy (eV)
Pt-vertical	-2.51
Pt-top layer-hollow	-2.49
Pt-top layer-hollow	-2.61
Pt-top layer-hollow	-2.47
Pt-second layer-top	-2.22
Pt-second layer-top	-2.14
Pt-third layer-top	-2.04
Pt-third layer-top	-2
Pt-third layer-top	-2.06
Pt-first layer-hollow	-2.37
Pt-second layer-hollow	-2.34
Pt-second layer-hollow	-2.48
Pt-second layer-hollow	-2.42
Pt-third layer-hollow	-2.12
Pt-third layer-hollow	-2.06
Pt-third layer-top	-2.32
Tin-oxide	-1.67

Table C.17. Calculated CHCO adsorption energies on different sites over Pt-SnO₂

Adsorption site	Adsorption energy (eV)
Between first and second layer	-3.16
on the interface of metallic site and tin-oxide	-2.76
on tin-oxide	-0.79
on top of metallic site	-2.9
on tin	-1.07
on third layer of Pt	-2.3

Table C.18. Calculated CO adsorption energies on different sites over Pt-SnO₂

Adsorption site	Adsorption energy (eV)
border	-1.96
on-oblique	-2.31
on top of oblique site	-2.18
on-sn-hcp	-0.35
on-sn-top	-0.6
on top of oblique site	-2.29

Table C.19. Calculated CH₃CO adsorption energies on different sites over Pt-Rh-SnO₂ (first model)

Adsorption site	Adsorption energy (eV)
on metallic surface-top layer- bond through Rh	-2.63
on metallic surface-second layer-bond through Pt	-2.43
on metallic surface-third layer-bond through Pt	-2.07
on metallic surface-third layer-bond through Pt	-2.2
on metallic surface- vertical- bond through Rh	-2.49
on metallic surface-second layer-bond through Rh	-2.64
on metallic surface-third layer-bond through Pt	-2.53
on tin-oxide	-1.42
on metallic surface-second layer-bond through Pt	-2.66

Table C.20. Calculated CH₃ adsorption energies on different sites over Pt-Rh-SnO₂ (first model)

Adsorption site	Adsorption energy (eV)
on metallic surface-vertical-bond through Pt	-2.34
on metallic surface-vertical-bond through Pt and Rh	-2.3
on metallic surface-vertical-bond through Pt and Rh	-2.34
on metallic surface-first layer-bond through Pt	-2.5
on metallic surface-first layer-bond through Rh	-2.1
on metallic surface-second layer-bond through Rh	-1.94
on metallic surface-second layer-bond through Pt	-2.27
on metallic surface-third later-bond through Rh	-1.56
on metallic surface-third layer-bond through Rh and Pt	-1.69
on metallic surface-second layer-bond through Pt	-2.37
on metallic surface-second layer-bond through Rh	-2.48
on metallic surface-second layer-bond through Rh and Pt	-2.18
on metallic surface-between second and third layer-bond through Rh and Pt	-1.78
on metallic surface-between second and third layer-bond through Rh and Pt	-2.2
on metallic surface-between second and third layer-bond through Rh and Pt	-2.15
on metallic surface-between second and third layer-bond through Rh and Pt	-2.17
on tin-oxide	-1.68

Table C.21. Calculated CHCO adsorption energies on different sites over Pt-Rh-SnO₂ (first model)

Adsorption site	Adsorption energy (eV)
bond with tin	-0.69
on metallic surface-third layer-bond with Rh and Pt	-1.91
on top of metallic surface-bond with Pt	-2.81

Table C.22. Calculated CH adsorption energies on different sites over Pt-Rh-SnO₂ (first model)

Adsorption site	Adsorption energy (eV)
on metallic site-between first and second layer-bond with Pt and Rh	-7.33
bond with Pt-vertical	-4.86
on metallic site-between second and third layer-bond with Pt and Rh	-6.64
Tin-oxide	-2.39
on first layer-bond with Pt and Rh	-6.76
interface on metallic site and tin-oxide	-6.35

Table C.23. Calculated CO adsorption energies on different sites over Pt-Rh-SnO₂ (first model)

Adsorption site	Adsorption energy (eV)
between first and second layer, bond with Rh and Pt	-2.71
bond with Pt, on third layer	-1.73
bond with Pt, on first layer	-2.14
Tin oxide	-0.42
Tin oxide	-0.57

Table C.24. Calculated CH₂ adsorption energies on different sites over Pt-Rh-SnO₂ (first model)

Adsorption site	Adsorption energy (eV)
first layer-bond with one Rh and one Pt	-5.85
between second and third layer-bond with two Rh and one Pt	-4.96
first layer-bond with one Rh and one Pt	-5.82

Table C.25. Calculated CH₂CO adsorption energies on different sites over Pt-Rh-SnO₂ (first model)

Adsorption site	Adsorption energy (eV)
Tin-oxide	-0.06
top of metallic site-bond with two Rh and one Pt	-1.35
bond with Rh-third layer of metallic site	-0.56
second layer of metallic site-one Rh and one Pt	-1.58
Tin-oxide	-0.44

Table C.26. Calculated CH₃CO adsorption energies on different sites over Pt-Rh-SnO₂ (second model)

Adsorption site	Adsorption energy (eV)
Rh surface-first layer	-2.3
Rh surface-second layer	-2.36
Rh surface-third layer	-2.02
Rh surface-third layer	-2.17
Rh surface-top of Rh	-2.42
Pt surface-first layer	-2.45
Pt surface-second layer	-2.4
Pt surface-second layer	-2.48
Tin-oxide	-1.29

Table C.27. Calculated CH₃ adsorption energies on different sites over Pt-Rh-SnO₂ (second model)

Adsorption site	Adsorption energy (eV)
Rh surface-vertical	-2
Rh surface-vertical	-2.3
Rh surface-vertical	-2.33
Rh surface-first layer	-2.06
Rh surface-vertical	-2.39
Rh surface-second layer	-2.01
Rh surface-between second and third layers	-1.72
Rh surface-third layer	-1.69
Between Rh and Pt	-2
Pt surface-first layer	-2.13
Pt surface-first layer	-2.2
Pt surface-second layer	-2.08
Pt surface-second layer	-2.12
Pt surface-second layer	-1.99
Tin-oxide	-1.67

Table C.28. Calculated CH adsorption energies on different sites over Pt-Rh-SnO₂ (second model)

Adsorption site	Adsorption energy (eV)
on Rh-between first and second layer	-7.69
on Rh-between first and second layer	-7.39
on Rh-between second and third layer	-7.32
on Pt-between first and second layer	-7.31
on Pt-between first and second layer	-7.34

Table C.29. Calculated CH₂CO adsorption energies on different sites over Pt-Rh-SnO₂ (second model)

Adsorption site	Adsorption energy (eV)
on Rh (Pt side)	-1.77
Interface of Rh and Pt	-1.74
on Rh, between first and second layers of Rh	-1.52
on Rh, second layer	-1.43
on Rh, between second and third layer	-1.54

Table C.30. Calculated CH₂ adsorption energies on different sites over Pt-Rh-SnO₂ (second model)

Adsorption site	Adsorption energy (eV)
on Rh, between first and second layer	-5.32
on Rh, between Rh and Pt layer	-5.54
on Pt, between first and second layer	-5.38

Table C.31. Calculated CHCO adsorption energies on different sites over Pt-Rh-SnO₂ (second model)

Adsorption site	Adsorption energy (eV)
on Metallic site, between Rh and Pt	-4.31
on Pt, between first and second layer	-4.21
on Pt, between first and second layer	-4.13

Table C.32. Calculated CO adsorption energies on different sites over Pt-Rh-SnO₂ (second model)

Adsorption site	Adsorption energy (eV)
on Rh, next to Pt	-2.77
on Rh, between first and second layers	-2.8
on Rh, between first and second layers	-2.99

Table C.33. Calculated CH₃CO adsorption energies on different sites over Pt-Rh-SnO₂ (third model)

Adsorption site	Adsorption energy (eV)
on Rh-first layer	-2.34
on Rh-second layer	-2.53
on Pt	-2.5
on Pt	-2.6
on Rh-vertical	-3
on Rh-second layer	-2.62
on Pt	-2.62
Tin-oxide	-1.29
on Rh-second layer	-2.65

Table C.34. Calculated CH₃ adsorption energies on different sites over Pt-Rh-SnO₂ (third model)

Adsorption site	Adsorption energy (eV)
on Rh-vertical-top	-1.11
on Rh-vertical-hollow	-1.37
on Rh-vertical-hollow	-1.42
on Rh-first layer	-1.06
on Rh-first layer	-1.1
on Rh-second layer	-1.05
on Pt	-1.15
on Pt	-1.07
on Pt	-0.92
on Rh-between first and second layers	-1.28
on Rh-between first and second layers	-1.17
on Rh-second layer	-1.2
on Pt	-1.43
Between Rh and Pt-hollow site	-1.09
on Pt	-1.4
on Pt	-1.22
Tin-oxide	-0.81

Table C.35. Calculated CH₂CO adsorption energies on different sites over Pt-Rh-SnO₂ (third model)

Adsorption site	Adsorption energy (eV)
on SnO ₂	-0.48
on Rh, between first and second layers	-1.85
on Rh, second layer	-1.28
on Rh, second layer	-1.19

Table C.36. Calculated CH₂ adsorption energies on different sites over Pt-Rh-SnO₂ (third model)

Adsorption site	Adsorption energy (eV)
on Rh, between first and second layers	-5.07
on Rh, between first and second layers	-5.08

Table C.37. Calculated CH adsorption energies on different sites over Pt-Rh-SnO₂ (third model)

Adsorption site	Adsorption energy (eV)
on metallic surface, between Pt and Rh	-7.08
on metallic surface, between Pt and Rh	-6.79
on metallic surface, between Pt and Rh	-7.16
on metallic surface, between Pt and Rh	-7.16
on Rh, between first and second layer of Rh	-7.59
on Rh, between first and second layer of Rh	-7.3
on Pt, between first and second layer of Pt	-7.34

Table C.38. Calculated CO adsorption energies on different sites over Pt-Rh-SnO₂ (third model)

Adsorption site	Adsorption energy (eV)
on metallic surface, between first and second layer of Rh	-2.66
on metallic surface, between Rh and Pt	-2.33
bond with Rh, first layer	-2.35

C.5. Pt-SnO₂ interface model verification

Table C.39. Number of layers' effect on oxygen vacancy formation energy for the Pt-SnO₂ system

Number of layers	Oxygen vacancy formation energy(eV)	
	Including freezing	Without freezing
3	2.72	2.90
4	2.86	2.80
5	3.03	2.99
6	2.87	2.90
7	3.04	2.89
8	2.72	2.69

Table C.40. Number of layers' effect on oxygen vacancy formation energy for SnO₂ system

Number of layers	Oxygen vacancy formation energy(eV)	
	Including freezing	Without freezing
3	1.46	1.35
4	1.46	1.63
5	1.45	1.38
6	1.35	1.50
7	1.37	1.35
8	1.18	1.53

Table C.41. Number of layers' effect on platinum adsorption energy for Pt-SnO₂ system

Number of layers	Platinum adsorption energy(eV)	
	Including freezing	Without freezing
3	-14.57	-15.44
4	-14.63	-13.81
5	-14.55	-14.94
6	-14.76	-14.47
7	-14.70	-14.75
8	-14.67	-14.58

Table C.42. Number of layers' effect on platinum adsorption energy for Pt-SnO₂ system with oxygen vacancy

Number of layers	Platinum adsorption energy(eV)	
	Including freezing	Without freezing
3	-13.31	-13.88
4	-13.22	-12.65
5	-12.97	-13.33
6	-13.24	-13.07
7	-13.03	-13.21
8	-13.13	-13.41

C.6. CH_xCO C-C bond breaking over Pt, Pt-SnO₂, and three models of Pt-Rh-SnO₂ surfaces is depicted in Figures C.46-C.48:

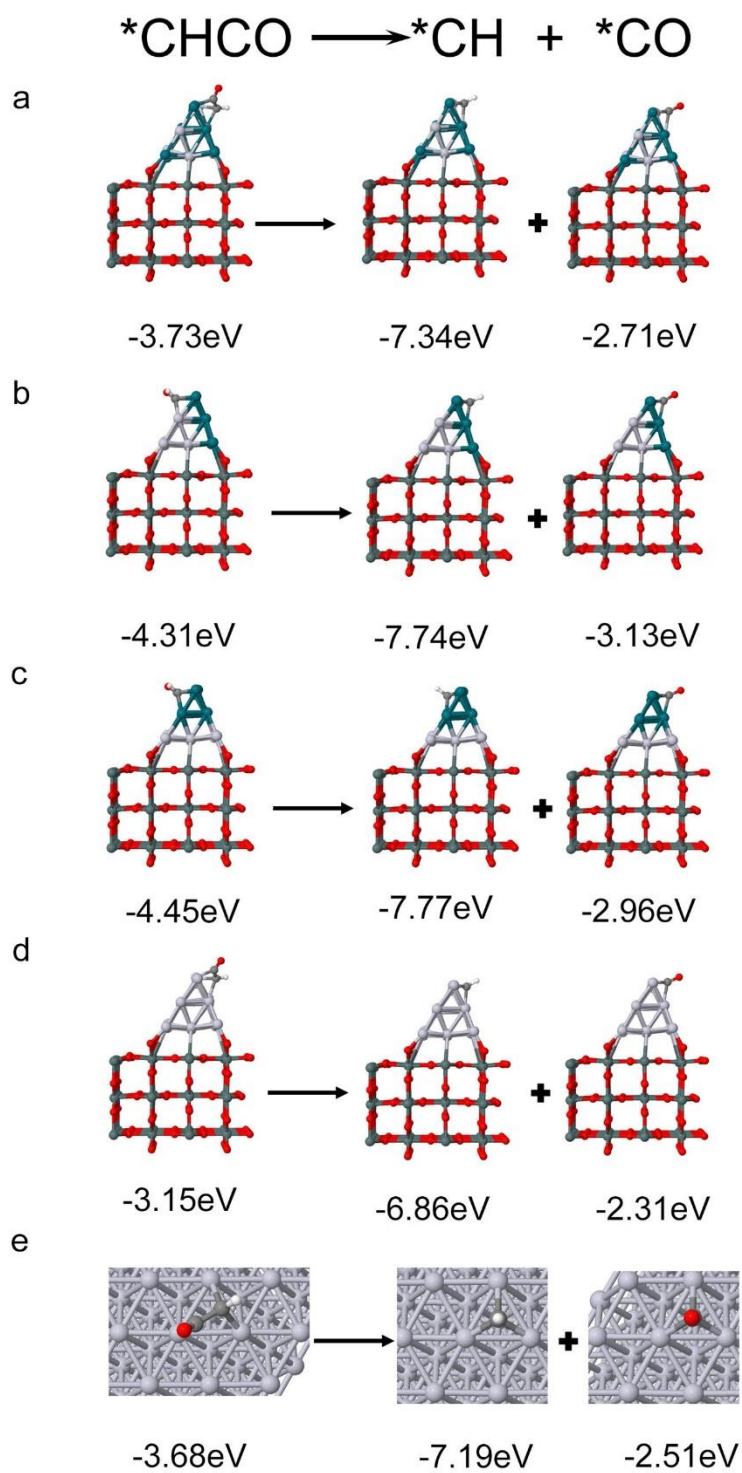


Figure C.46. Reaction energy of C-C bond scission of CHCO on various catalyst surfaces: (a) PtRh-SnO₂ (1st model), (b) PtRh-SnO₂ (2nd model), (c) PtRh-SnO₂ (3rd model), (d) Pt-SnO₂ and (e) Pt (111). The adsorption energies are listed below each structure.

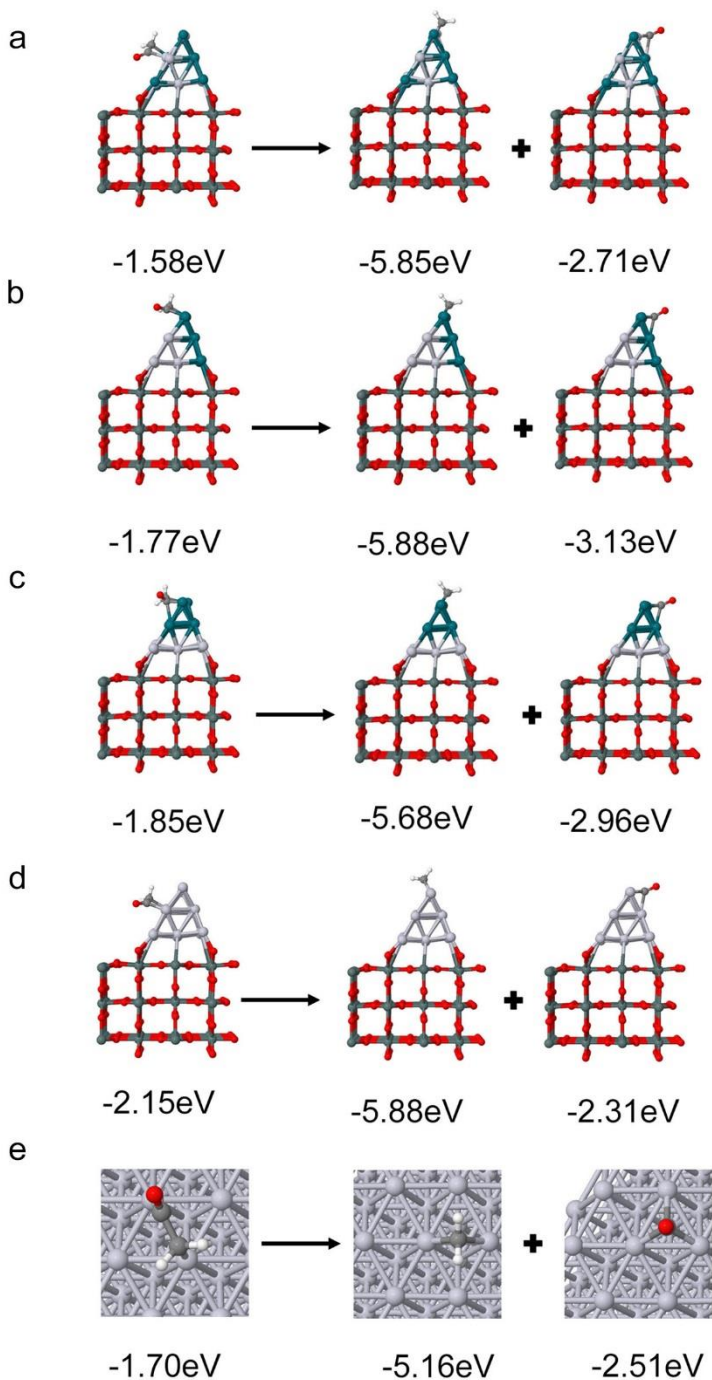
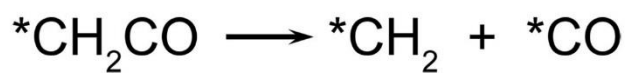


Figure C.47. Structures for C-C bond scission of CH_2CO on various catalyst surfaces: (a) PtRh-SnO₂ (1st model), (b) PtRh-SnO₂ (2nd model), (c) PtRh-SnO₂ (3rd model), (d) Pt-SnO₂ and (e) Pt (111). The adsorption energies are listed below each structure.

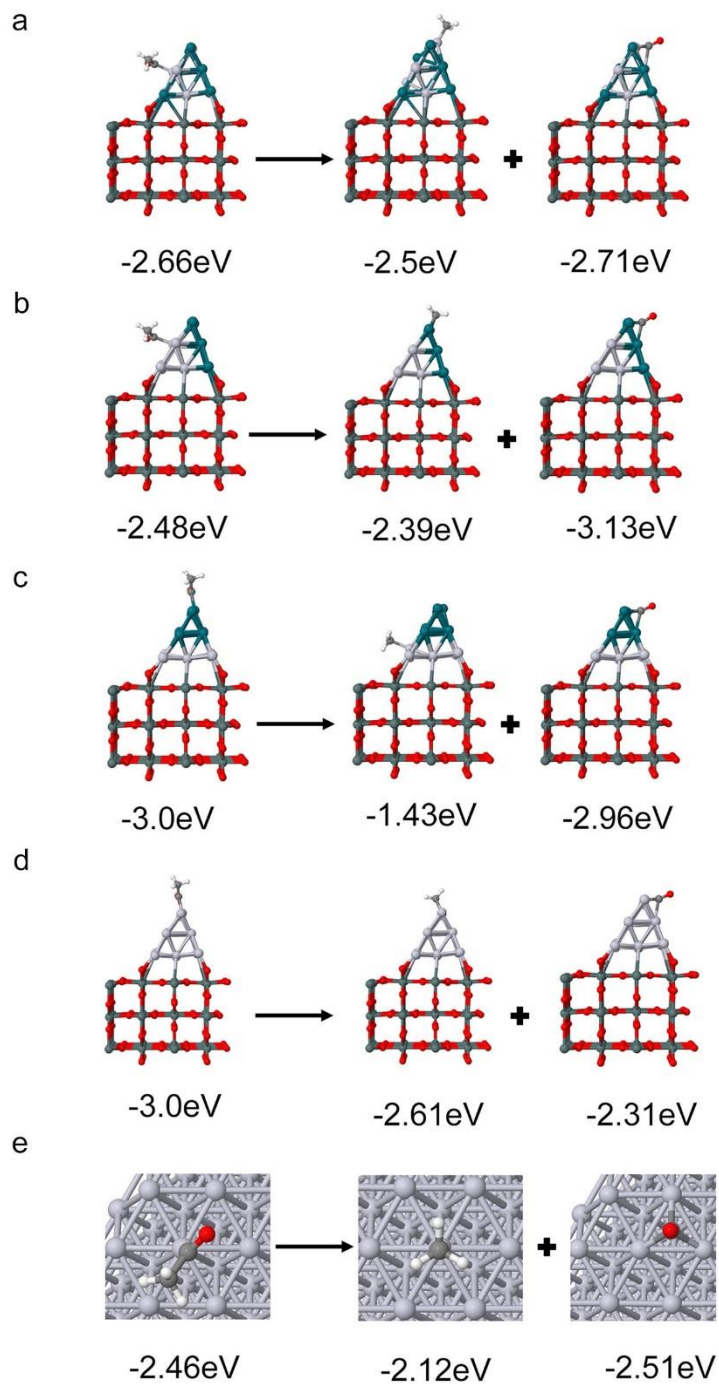


Figure C.48. Reaction energy of C-C bond scission of CH₃CO on various catalyst surfaces: (a) PtRh-SnO₂ (1st model), (b) PtRh-SnO₂ (2nd model), (c) PtRh-SnO₂ (3rd model), (d) Pt-SnO₂ and (e) Pt (111). The adsorption energies are listed below each structure.

C.7. CH_xCO C-C bond breaking over Rh₂O₃

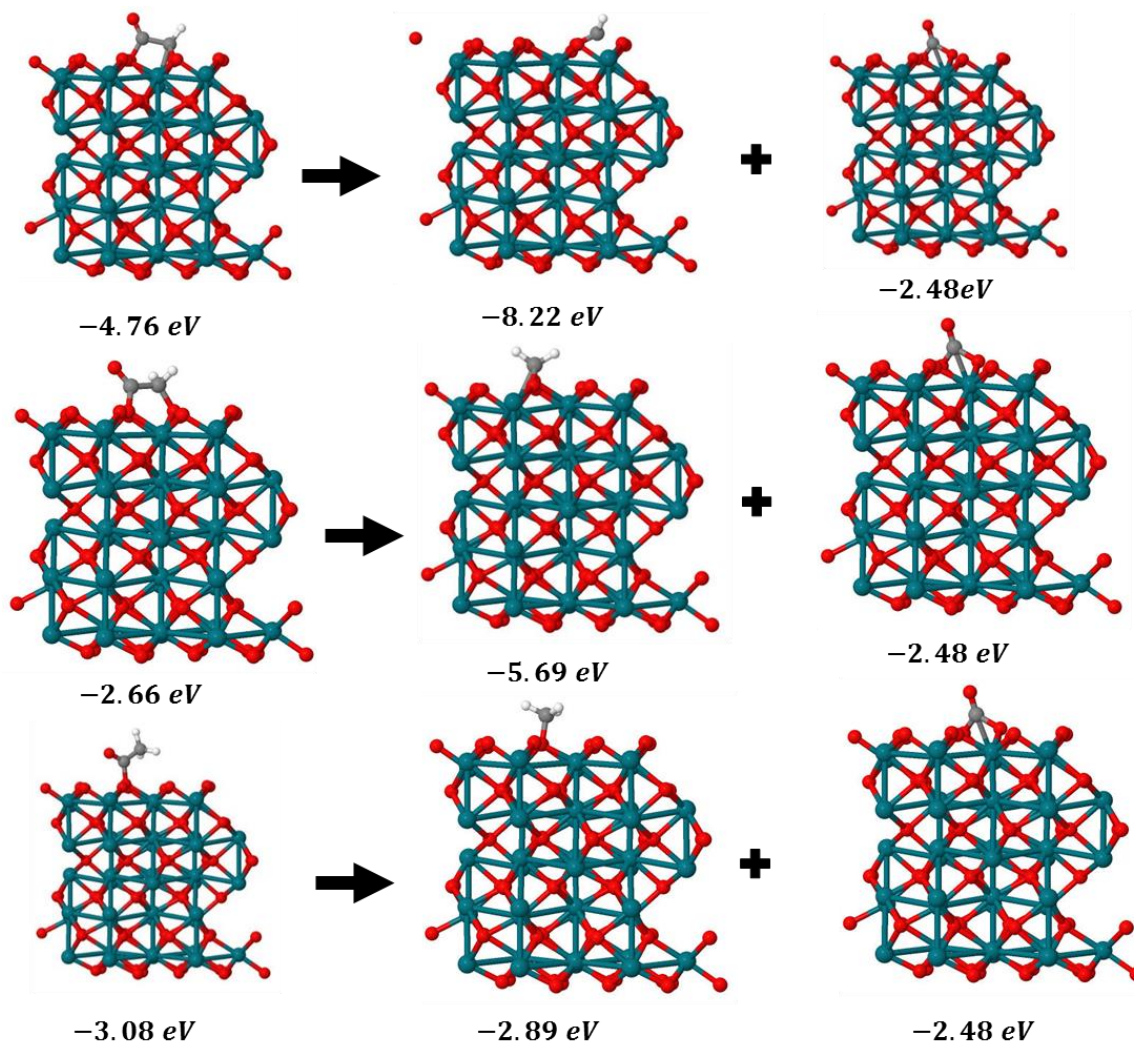


Figure C.49. Reaction energy of C-C bond scission of CH_xCO (x=1,2,3) on Rh₂O₃. The adsorption energies are listed below each structure.

C.8. CH_x and CO oxidation over Rh and Rh₂O₃ surfaces

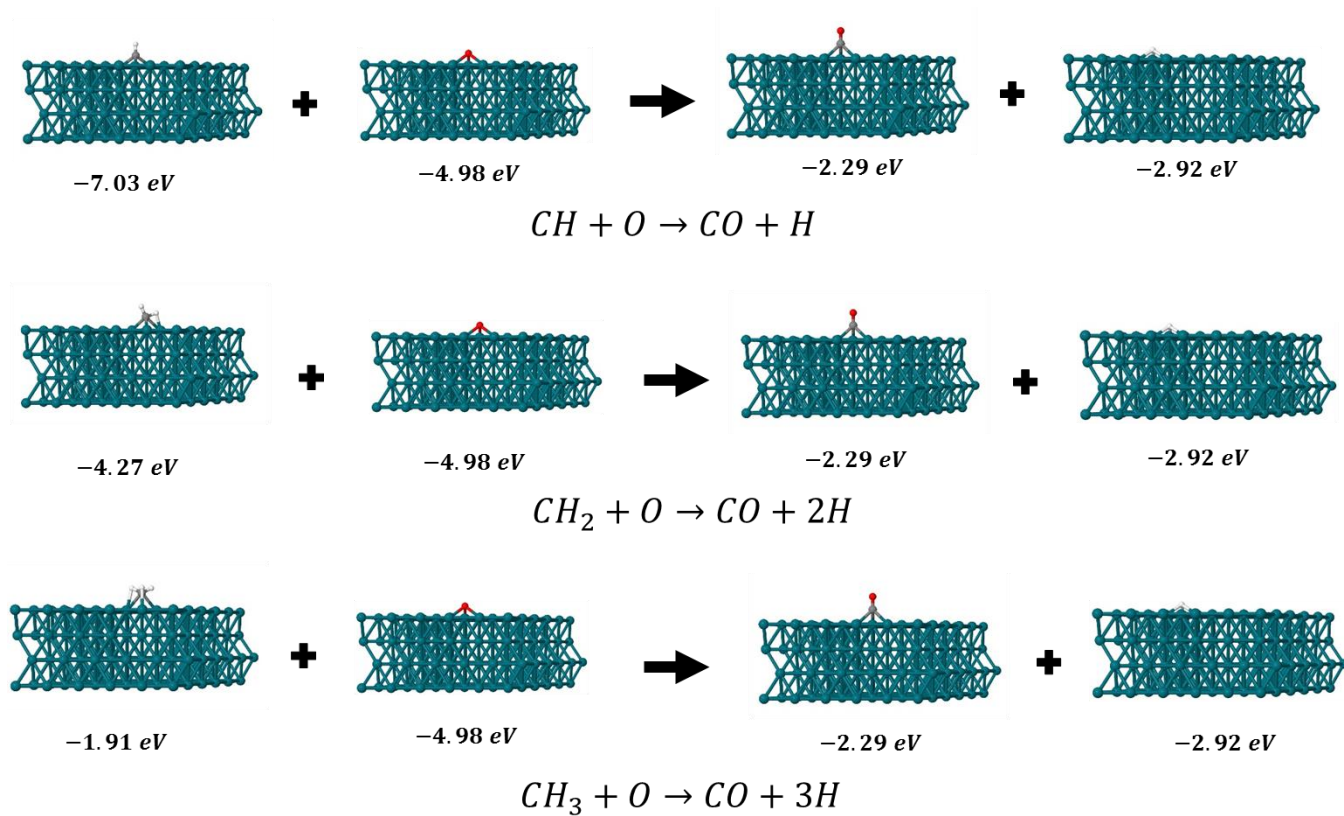


Figure C.50. Reaction energy of oxidation of CH_x species (x=1,2,3) on Rh. The adsorption energies are listed below each structure.

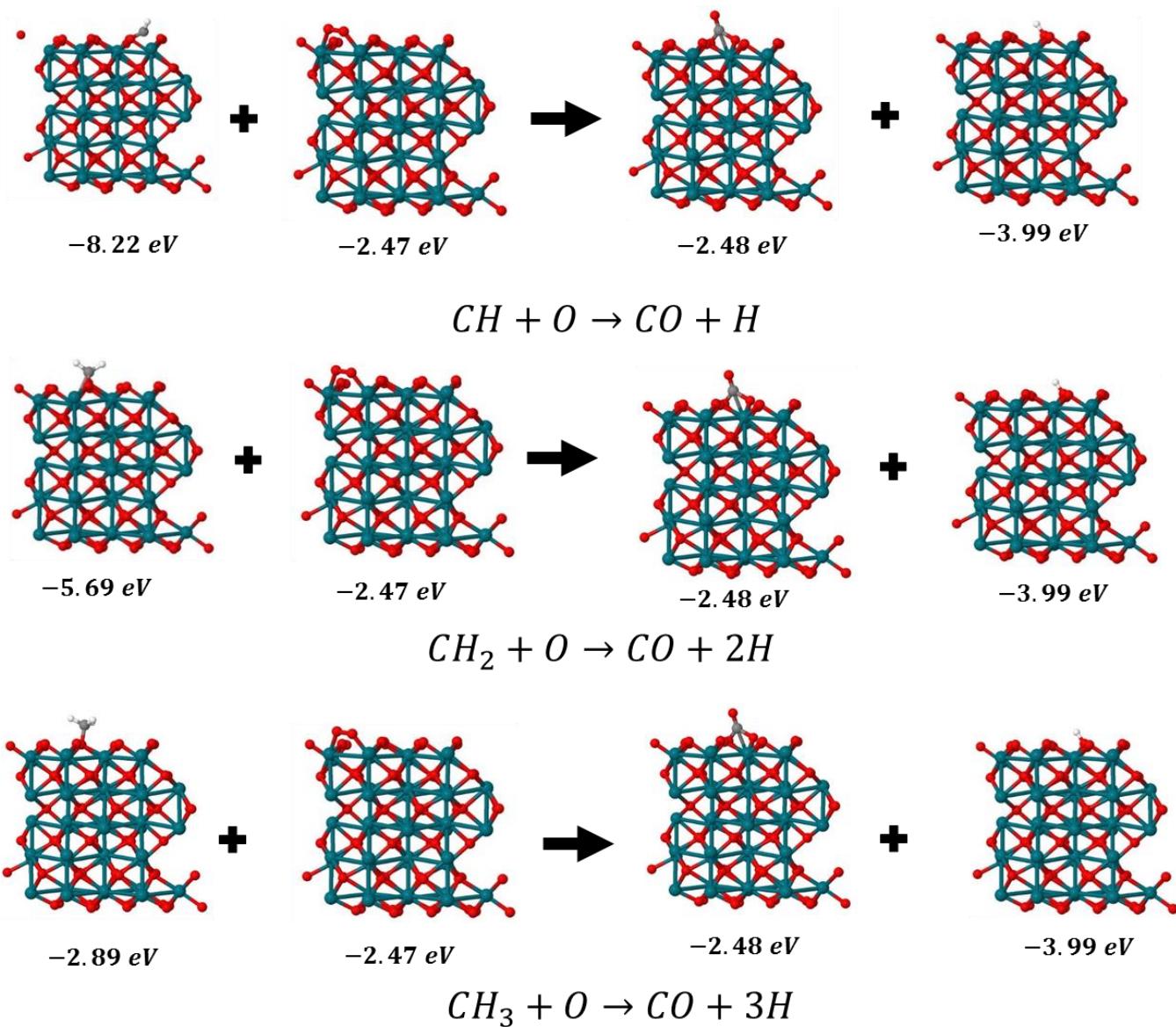


Figure C.51. Oxidation reaction of CH_x species ($x=1,2,3$) on Rh_2O_3 . The adsorption energies are listed below each structure.

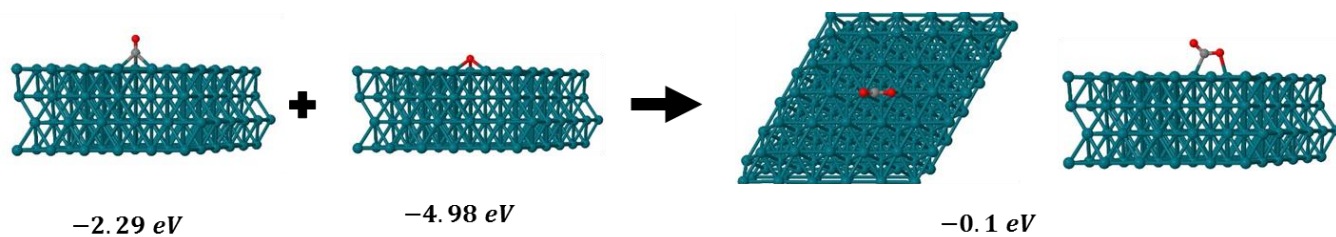


Figure C.52. Oxidation reaction of CO species on Rh. The adsorption energies are listed below each structure.

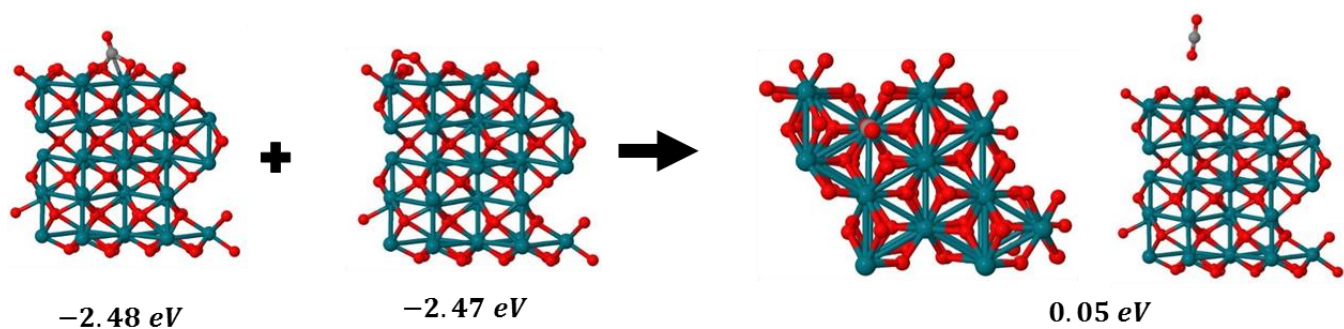


Figure C.53. Oxidation reaction of CO species on Rh_2O_3 . The adsorption energies are listed below each structure.

Table C.43. Calculated reaction energies (eV) for oxidation of CH_x and CO species ($\text{CH}_x + \text{O} \rightarrow \text{CO} + x\text{H}$) and $\text{CO} + \text{O} \rightarrow \text{CO}_2$. From this table, preferential effect of Rh_2O_3 in oxidation reactions is evident.

Oxidation reaction	Rh	Rh_2O_3
$\text{CH} + \text{O} \rightarrow \text{CO} + \text{H}$	-0.5	-3.07
$\text{CH}_2 + \text{O} \rightarrow \text{CO} + 2\text{H}$	-1.27	-5.08
$\text{CH}_3 + \text{O} \rightarrow \text{CO} + 3\text{H}$	-1.63	-6.57
$\text{CO} + \text{O} \rightarrow \text{CO}_2$	1.01	-1.15

References

1. <https://www.e-education.psu.edu/egee102/node/1951>.
2. Beering, S. C., *Building a Sustainable Energy Future: US Actions for an Effective Energy Economy Transformation*. DIANE Publishing: 2011.
3. https://web.archive.org/web/20140209080834/http://www.worldenergy.org/focus/fuel_cells/377.a.sp.
4. Brown, L. F., A comparative study of fuels for on-board hydrogen production for fuel-cell-powered automobiles. *Int J Hydrogen Energ* **2001**, 26 (4), 381-397.
5. Farrell, A. E.; Plevin, R. J.; Turner, B. T.; Jones, A. D.; O'Hare, M.; Kammen, D. M., Ethanol can contribute to energy and environmental goals. *Science* **2006**, 311 (5760), 506-508.
6. Antolini, E., Catalysts for direct ethanol fuel cells. *Journal of Power Sources* **2007**, 170 (1), 1-12.
7. Teng, X., Anodic catalyst design for the ethanol oxidation fuel cell reactions. *Materials and Processes for Energy: Communicating Current Research and Technological Developments, Formatex Research Center* **2013**, 473-484.
8. Camara, G. A.; Iwasita, T., Parallel pathways of ethanol oxidation: The effect of ethanol concentration. *J Electroanal Chem* **2005**, 578 (2), 315-321.
9. Chang, S. C.; Leung, L. W. H.; Weaver, M. J., Metal Crystallinity Effects in Electrocatalysis as Probed by Real-Time Ftir Spectroscopy - Electrooxidation of Formic-Acid, Methanol, and Ethanol on Ordered Low-Index Platinum Surfaces. *J Phys Chem-Us* **1990**, 94 (15), 6013-6021.
10. Wang, H.; Jusys, Z.; Behm, R. J., Ethanol electrooxidation on a carbon-supported Pt catalyst: Reaction kinetics and product yields. *J Phys Chem B* **2004**, 108 (50), 19413-19424.
11. Willsau, J.; Heitbaum, J., Elementary Steps of Ethanol Oxidation on Pt in Sulfuric-Acid as Evidenced by Isotope Labeling. *J Electroanal Chem* **1985**, 194 (1), 27-35.
12. Shin, J. W.; Tornquist, W. J.; Korzeniewski, C.; Hoaglund, C. S., Elementary steps in the oxidation and dissociative chemisorption of ethanol on smooth and stepped surface planes of platinum electrodes. *Surface Science* **1996**, 364 (2), 122-130.
13. Tarnowski, D. J.; Korzeniewski, C., Effects of surface step density on the electrochemical oxidation of ethanol to acetic acid. *J Phys Chem B* **1997**, 101 (2), 253-258.
14. Iwasita, T.; Pastor, E., A Dems and Ftir Spectroscopic Investigation of Adsorbed Ethanol on Polycrystalline Platinum. *Electrochim Acta* **1994**, 39 (4), 531-537.
15. Schmiemann, U.; Muller, U.; Baltruschat, H., The Influence of the Surface-Structure on the Adsorption of Ethene, Ethanol and Cyclohexene as Studied by Dems. *Electrochim Acta* **1995**, 40 (1), 99-107.
16. Ferrin, P.; Simonetti, D.; Kandoi, S.; Kunkes, E.; Dumesic, J. A.; Norskov, J. K.; Mavrikakis, M., Modeling Ethanol Decomposition on Transition Metals: A Combined Application of Scaling and Bronsted-Evans-Polanyi Relations. *Journal of the American Chemical Society* **2009**, 131 (16), 5809-5815.
17. Alcalá, R.; Mavrikakis, M.; Dumesic, J. A., DFT studies for cleavage of C-C and C-O bonds in surface species derived from ethanol on Pt (111). *Journal of Catalysis* **2003**, 218 (1), 178-190.
18. Lamy, C.; Belgsir, E. M.; Leger, J. M., Electrocatalytic oxidation of aliphatic alcohols: Application to the direct alcohol fuel cell (DAFC). *J Appl Electrochem* **2001**, 31 (7), 799-809.
19. Cong, Y.; Van Spaendonk, V.; Masel, R., Low temperature C-C bond scission during ethanol decomposition on Pt (331). *Surface science* **1997**, 385 (2-3), 246-258.
20. Lee, A. F.; Gawthrop, D. E.; Hart, N. J.; Wilson, K., A Fast XPS study of the surface chemistry of ethanol over Pt {111}. *Surface science* **2004**, 548 (1), 200-208.
21. Wang, H.-F.; Liu, Z.-P., Comprehensive mechanism and structure-sensitivity of ethanol oxidation on platinum: new transition-state searching method for resolving the complex reaction network. *Journal of the American Chemical Society* **2008**, 130 (33), 10996-11004.

22. Houtman, C.; Barteau, M., Divergent pathways of acetaldehyde and ethanol decarbonylation on the Rh (111) surface. *Journal of Catalysis* **1991**, *130* (2), 528-546.
23. Papageorgopoulos, D.; Ge, Q.; King, D., Synchronous Thermal Desorption and Decomposition of Ethanol on Rh {111}. *The Journal of Physical Chemistry* **1995**, *99* (49), 17645-17649.
24. Vesselli, E.; Baraldi, A.; Comelli, G.; Lizzit, S.; Rosei, R., Ethanol Decomposition: C-C Cleavage Selectivity on Rh (111). *ChemPhysChem* **2004**, *5* (8), 1133-1140.
25. Cui, G.; Song, S.; Shen, P. K.; Kowal, A.; Bianchini, C., First-principles considerations on catalytic activity of Pd toward ethanol oxidation. *The Journal of Physical Chemistry C* **2009**, *113* (35), 15639-15642.
26. Davis, J.; Barteau, M., The influence of oxygen on the selectivity of alcohol conversion on the Pd (111) surface. *Surface science* **1988**, *197* (1-2), 123-152.
27. Davis, J.; Barteau, M., Spectroscopic identification of alkoxide, aldehyde, and acyl intermediates in alcohol decomposition on Pd (111). *Surface Science* **1990**, *235* (2-3), 235-248.
28. Liang, Z.; Zhao, T.; Xu, J.; Zhu, L., Mechanism study of the ethanol oxidation reaction on palladium in alkaline media. *Electrochim Acta* **2009**, *54* (8), 2203-2208.
29. Wang, E.; Xu, J.; Zhao, T., Density functional theory studies of the structure sensitivity of ethanol oxidation on palladium surfaces. *The Journal of Physical Chemistry C* **2010**, *114* (23), 10489-10497.
30. Bittinscattaneo, B.; Wilhelm, S.; Cattaneo, E.; Buschmann, H. W.; Vielstich, W., Intermediates and Products of Ethanol Oxidation on Platinum in Acid-Solution. *Ber Bunsen Phys Chem* **1988**, *92* (11), 1210-1218.
31. Gootzen, J. F. E.; Visscher, W.; vanVeen, J. A. R., Characterization of ethanol and 1,2-ethanediol adsorbates on platinized platinum with Fourier transform infrared spectroscopy and differential electrochemical mass spectrometry. *Langmuir* **1996**, *12* (21), 5076-5082.
32. Hitmi, H.; Belgsir, E. M.; Leger, J. M.; Lamy, C.; Lezna, R. O., A Kinetic, Analysis of the Electrooxidation of Ethanol at a Platinum-Electrode in Acid-Medium. *Electrochim Acta* **1994**, *39* (3), 407-415.
33. Monyoncho, E. A.; Steinmann, S. N.; Michel, C.; Baranova, E. A.; Woo, T. K.; Sautet, P., Ethanol Electro-oxidation on Palladium Revisited Using Polarization Modulation Infrared Reflection Absorption Spectroscopy (PM-IRRAS) and Density Functional Theory (DFT): Why Is It Difficult To Break the C-C Bond? *Acs Catal* **2016**, *6* (8), 4894-4906.
34. Schmidt, V. M.; Ianniello, R.; Pastor, E.; Gonzalez, S., Electrochemical reactivity of ethanol on porous Pt and PtRu: Oxidation/reduction reactions in 1 M HClO₄. *J Phys Chem-US* **1996**, *100* (45), 17901-17908.
35. Souza-Garcia, J.; Herrero, E.; Feliu, J. M., Breaking the C-C Bond in the Ethanol Oxidation Reaction on Platinum Electrodes: Effect of Steps and Ruthenium Adatoms. *ChemPhysChem* **2010**, *11* (7), 1391-1394.
36. Alcalá, R.; Shabaker, J. W.; Huber, G. W.; Sanchez-Castillo, M. A.; Dumesic, J. A., Experimental and DFT studies of the conversion of ethanol and acetic acid on PtSn-based catalysts. *J Phys Chem B* **2005**, *109* (6), 2074-2085.
37. Li, M.; Guo, W. Y.; Jiang, R. B.; Zhao, L. M.; Shan, H. H., Decomposition of Ethanol on Pd(111): A Density Functional Theory Study. *Langmuir* **2010**, *26* (3), 1879-1888.
38. Li, M.; Guo, W. Y.; Jiang, R. B.; Zhao, L. M.; Lu, X. Q.; Zhu, H. Y.; Fu, D. L.; Shan, H. H., Density Functional Study of Ethanol Decomposition on Rh(111). *J Phys Chem C* **2010**, *114* (49), 21493-21503.
39. Choi, Y. M.; Liu, P., Understanding of ethanol decomposition on Rh(1 1 1) from density functional theory and kinetic Monte Carlo simulations. *Catal Today* **2011**, *165* (1), 64-70.
40. Guo, W. Y.; Li, M.; Lu, X. Q.; Zhu, H. Y.; Li, Y.; Li, S. R.; Zhao, L. M., Ethanol decomposition on a Pd(110) surface: a density functional theory investigation. *Dalton T* **2013**, *42* (6), 2309-2318.
41. Wu, Z. P.; Zhang, M. H.; Jiang, H. X.; Zhong, C. J.; Chen, Y. F.; Wang, L. C., Competitive C-C and C-H bond scission in the ethanol oxidation reaction on Cu(100) and the effect of an alkaline environment. *Phys Chem Chem Phys* **2017**, *19* (23), 15444-15453.

42. Xu, H.; Miao, B.; Zhang, M. H.; Chen, Y. F.; Wang, L. C., Mechanism of C-C and C-H bond cleavage in ethanol oxidation reaction on Cu₂O(111): a DFT-D and DFT plus U study. *Phys Chem Chem Phys* **2017**, *19* (38), 26210-26220.
43. Rodriguez, J. A.; Liu, P. *Theoretical Studies in Heterogenous Catalysis: Towards a Rational Design of Novel Catalysts for Hydrodesulfurization and Hydrogen Production*; Brookhaven National Laboratory: 2008.
44. Perez, J.; Paganin, V. A.; Antolini, E., Particle size effect for ethanol electro-oxidation on Pt/C catalysts in half-cell and in a single direct ethanol fuel cell. *J Electroanal Chem* **2011**, *654* (1), 108-115.
45. Markovic, N. M.; Gasteiger, H. A.; Ross, P. N.; Jiang, X. D.; Villegas, I.; Weaver, M. J., Electrooxidation Mechanisms of Methanol and Formic-Acid on Pt-Ru Alloy Surfaces. *Electrochim Acta* **1995**, *40* (1), 91-98.
46. Gojkovic, S. L.; Vidakovic, T. R.; Durovic, D. R., Kinetic study of methanol oxidation on carbon-supported PtRu electrocatalyst. *Electrochim Acta* **2003**, *48* (24), 3607-3614.
47. Iwasita, T., Electrocatalysis of methanol oxidation. *Electrochim Acta* **2002**, *47* (22-23), 3663-3674.
48. Christensen, P. A.; Hamnett, A.; Troughton, G. L., The Role of Morphology in the Methanol Electrooxidation Reaction. *J Electroanal Chem* **1993**, *362* (1-2), 207-218.
49. Giorgi, L.; Pozio, A.; Bracchini, C.; Giorgi, R.; Turtu, S., H₂ and H₂/CO oxidation mechanism on Pt/C, Ru/C and Pt-Ru/C electrocatalysts. *J Appl Electrochem* **2001**, *31* (3), 325-334.
50. Zhou, W. J.; Song, S. Q.; Li, W. Z.; Sun, G. Q.; Xin, Q.; Kontou, S.; Pouliaitis, K.; Tsiakaras, P., Pt-based anode catalysts for direct ethanol fuel cells. *Solid State Ionics* **2004**, *175* (1-4), 797-803.
51. Zhou, W. J.; Zhou, Z. H.; Song, S. Q.; Li, W. Z.; Sun, G. Q.; Tsiakaras, P.; Xin, Q., Pt based anode catalysts for direct ethanol fuel cells. *Appl Catal B-Environ* **2003**, *46* (2), 273-285.
52. Wang, Y.; Ren, J. W.; Deng, K.; Gui, L. L.; Tang, Y. Q., Preparation of tractable platinum, rhodium, and ruthenium nanoclusters with small particle size in organic media. *Chem Mater* **2000**, *12* (6), 1622-1627.
53. Vigier, F.; Coutanceau, C.; Perrard, A.; Belgsir, E. M.; Lamy, C., Development of anode catalysts for a direct ethanol fuel cell. *J Appl Electrochem* **2004**, *34* (4), 439-446.
54. Lamy, C.; Rousseau, S.; Belgsir, E.; Coutanceau, C.; Léger, J.-M., Recent progress in the direct ethanol fuel cell: development of new platinum-tin electrocatalysts. *Electrochim Acta* **2004**, *49* (22), 3901-3908.
55. Riberio, J.; dos Anjos, D. M.; Kokoh, K. B.; Coutanceau, C.; Leger, J. M.; Olivi, P.; de Andrade, A. R.; Tremiliosi-Filho, G., Carbon-supported ternary PtSnIr catalysts for direct ethanol fuel cell. *Electrochim Acta* **2007**, *52* (24), 6997-7006.
56. Calegario, M. L.; Suffredini, H. B.; Machado, S. A. S.; Avaca, L. A., Preparation, characterization and utilization of a new electrocatalyst for ethanol oxidation obtained by the sol-gel method. *Journal of Power Sources* **2006**, *156* (2), 300-305.
57. Zhang, D. Y.; Ma, Z. F.; Wang, G. X.; Konstantinov, K.; Yuan, X. X.; Liu, H. K., Electro-oxidation of ethanol on Pt-WO₃/C electrocatalyst. *Electrochim Solid St* **2006**, *9* (9), A423-A426.
58. Spinace, E. V.; Neto, A. O.; Vasconcelos, T. R. R.; Linardi, M., Electro-oxidation of ethanol using PtRu/C electrocatalysts prepared by alcohol-reduction process. *Journal of Power Sources* **2004**, *137* (1), 17-23.
59. Tanaka, S.; Umeda, M.; Ojima, H.; Usui, Y.; Kimura, O.; Uchida, I., Preparation and evaluation of a multi-component catalyst by using a co-sputtering system for anodic oxidation of ethanol. *Journal of Power Sources* **2005**, *152* (1), 34-39.
60. Zhou, W. J.; Li, W. Z.; Song, S. Q.; Zhou, Z. H.; Jiang, L. H.; Sun, G. Q.; Xin, Q.; Pouliaitis, K.; Kontou, S.; Tsiakaras, P., Bi- and tri-metallic Pt-based anode catalysts for direct ethanol fuel cells. *Journal of Power Sources* **2004**, *131* (1-2), 217-223.
61. Antolini, E.; Colmati, F.; Gonzalez, E. R., Effect of Ru addition on the structural characteristics and the electrochemical activity for ethanol oxidation of carbon supported Pt-Sn alloy catalysts. *Electrochim Commun* **2007**, *9* (3), 398-404.

62. Rousseau, S.; Coutanceau, C.; Lamy, C.; Leger, J. M., Direct ethanol fuel cell (DEFC): Electrical performances and reaction products distribution under operating conditions with different platinum-based anodes. *Journal of Power Sources* **2006**, *158* (1), 18-24.
63. Spinace, E. V.; Linardi, M.; Neto, A. O., Co-catalytic effect of nickel in the electro-oxidation of ethanol on binary Pt-Sn electrocatalysts. *Electrochem Commun* **2005**, *7* (4), 365-369.
64. Ha, S.; Larsen, R.; Masel, R. I., Performance characterization of Pd/C nanocatalyst for direct formic acid fuel cells. *Journal of Power Sources* **2005**, *144* (1), 28-34.
65. Chen, Y. G.; Zhuang, L.; Lu, J. T., Non-Pt anode catalysts for alkaline direct alcohol fuel cells. *Chinese J Catal* **2007**, *28* (10), 870-874.
66. He, Q. G.; Chen, W.; Mukerjee, S.; Chen, S. W.; Laufek, F., Carbon-supported PdM (M = Au and Sn) nanocatalysts for the electrooxidation of ethanol in high pH media. *Journal of Power Sources* **2009**, *187* (2), 298-304.
67. Nguyen, S. T.; Law, H. M.; Nguyen, H. T.; Kristian, N.; Wang, S. Y.; Chan, S. H.; Wang, X., Enhancement effect of Ag for Pd/C towards the ethanol electro-oxidation in alkaline media. *Appl Catal B-Environ* **2009**, *91* (1-2), 507-515.
68. de Souza, J. P. I.; Queiroz, S. L.; Bergamaski, K.; Gonzalez, E. R.; Nart, F. C., Electro-oxidation of ethanol on Pt, Rh, and PtRh electrodes. A study using DEMS and in-situ FTIR techniques. *J Phys Chem B* **2002**, *106* (38), 9825-9830.
69. Su, H. Y.; Gu, X. K.; Ma, X. F.; Zhao, Y. H.; Bao, X. H.; Li, W. X., Structure evolution of Pt-3d transition metal alloys under reductive and oxidizing conditions and effect on the CO oxidation: a first-principles study. *Catal Today* **2011**, *165* (1), 89-95.
70. Christoffersen, E.; Liu, P.; Ruban, A.; Skriver, H. L.; Norskov, J. K., Anode materials for low-temperature fuel cells: A density functional theory study. *Journal of Catalysis* **2001**, *199* (1), 123-131.
71. Du, W. X.; Mackenzie, K. E.; Milano, D. F.; Deskins, N. A.; Su, D.; Teng, X. W., Palladium-Tin Alloyed Catalysts for the Ethanol Oxidation Reaction in an Alkaline Medium. *Acs Catal* **2012**, *2* (2), 287-297.
72. Cao, L.; Sun, G. Q.; Li, H. Q.; Xin, Q., Carbon-supported IrSn catalysts for a direct ethanol fuel cell. *Electrochem Commun* **2007**, *9* (10), 2541-2546.
73. Du, W. X.; Wang, Q.; Saxner, D.; Deskins, N. A.; Su, D.; Krzanowski, J. E.; Frenkel, A. I.; Teng, X. W., Highly Active Iridium/Iridium-Tin/Tin Oxide Heterogeneous Nanoparticles as Alternative Electrocatalysts for the Ethanol Oxidation Reaction. *Journal of the American Chemical Society* **2011**, *133* (38), 15172-15183.
74. Du, W. X.; Deskins, N. A.; Su, D.; Teng, X. W., Iridium-Ruthenium Alloyed Nanoparticles for the Ethanol Oxidation Fuel Cell Reactions. *Acs Catal* **2012**, *2* (6), 1226-1231.
75. Sholl, D.; Steckel, J. A., *Density functional theory: a practical introduction*. John Wiley & Sons: 2011.
76. Simons, J., *An introduction to theoretical chemistry*. Cambridge University Press: 2003.
77. Peleg, Y.; Pnini, R.; Zaarur, E.; Hecht, E., *Quantum mechanics*. 2nd ed.; McGraw-Hill Companies: New York, 2010; p ix, 361 p.
78. Martin, R. M., *Electronic structure: basic theory and practical methods*. Cambridge university press: 2004.
79. Kohn, W.; Sham, L. J., Self-consistent equations including exchange and correlation effects. *Physical review* **1965**, *140* (4A), A1133.
80. Parr, R. G.; Yang, W., Density-functional theory of the electronic structure of molecules. *Annu Rev Phys Chem* **1995**, *46* (1), 701-728.
81. Kittel, C., *Introduction to solid state physics*. Wiley New York: 1976; Vol. 8.
82. Lippert, G.; Hutter, J.; Parrinello, M., A hybrid Gaussian and plane wave density functional scheme. *Mol Phys* **1997**, *92* (3), 477-487.
83. Frigo, M.; Johnson, S. G., The design and implementation of FFTW3. *P Ieee* **2005**, *93* (2), 216-231.

84. Hutter, J.; Iannuzzi, M.; Schiffmann, F.; VandeVondele, J., CP2K: atomistic simulations of condensed matter systems. *Wires Comput Mol Sci* **2014**, *4* (1), 15-25.
85. VandeVondele, J.; Hutter, J., An efficient orbital transformation method for electronic structure calculations. *J Chem Phys* **2003**, *118* (10), 4365-4369.
86. VandeVondele, J.; Krack, M.; Mohamed, F.; Parrinello, M.; Chassaing, T.; Hutter, J., QUICKSTEP: Fast and accurate density functional calculations using a mixed Gaussian and plane waves approach. *Comput Phys Commun* **2005**, *167* (2), 103-128.
87. Lerch, D.; Wieckhorst, O.; Hart, G. L. W.; Forcade, R. W.; Muller, S., UNCLE: a code for constructing cluster expansions for arbitrary lattices with minimal user-input. *Model Simul Mater Sc* **2009**, *17* (5).
88. Jin, H. M.; Wu, P., Coefficient of thermal expansion for solder alloys based on cluster expansion method. *J Mater Chem* **2002**, *12* (4), 1090-1093.
89. Cheng, F. Y.; Ma, H.; Li, Y. M.; Chen, J., Ni_{1-x}Pt_x (x=0-0.12) hollow spheres as catalysts for hydrogen generation from ammonia borane. *Inorg Chem* **2007**, *46* (3), 788-794.
90. Akbayrak, S.; Tonbul, Y.; Ozkar, S., Ceria supported rhodium nanoparticles: Superb catalytic activity in hydrogen generation from the hydrolysis of ammonia borane. *Appl Catal B-Environ* **2016**, *198*, 162-170.
91. Biloen, P.; Dautzenberg, F. M.; Sachtler, W. M. H., Catalytic Dehydrogenation of Propane to Propene over Platinum and Platinum-Gold Alloys. *Journal of Catalysis* **1977**, *50* (1), 77-86.
92. Gryaznov, V. M.; Ermilova, M. M.; Morozova, L. S.; Orekhova, N. V.; Polyakova, V. P.; Roshan, N. R.; Savitsky, E. M.; Parfenova, N. I., Palladium Alloys as Hydrogen Permeable Catalysts in Hydrogenation and Dehydrogenation Reactions. *J Less-Common Met* **1983**, *89* (2), 529-535.
93. Rochefort, A.; Lepeltier, F.; Boitiaux, J. P., Particle-Size Effect in Supported Platinum - Methylcyclohexane Dehydrogenation. *Journal of Catalysis* **1992**, *138* (2), 482-490.
94. Burch, R., Platinum-Tin Reforming Catalysts .1. The Oxidation-State of Tin and the Interaction between Platinum and Tin. *Journal of Catalysis* **1981**, *71* (2), 348-359.
95. Burch, R.; Garla, L. C., Platinum-Tin Reforming Catalysts .2. Activity and Selectivity in Hydrocarbon Reactions. *Journal of Catalysis* **1981**, *71* (2), 360-372.
96. Colon-Mercado, H. R.; Popov, B. N., Stability of platinum based alloy cathode catalysts in PEM fuel cells. *Journal of Power Sources* **2006**, *155* (2), 253-263.
97. Shao, Y. Y.; Yin, G. P.; Gao, Y. Z., Understanding and approaches for the durability issues of Pt-based catalysts for PEM fuel cell. *Journal of Power Sources* **2007**, *171* (2), 558-566.
98. Zhang, S. S.; Yuan, X. Z.; Hin, J. N. C.; Wang, H. J.; Friedrich, K. A.; Schulze, M., A review of platinum-based catalyst layer degradation in proton exchange membrane fuel cells. *Journal of Power Sources* **2009**, *194* (2), 588-600.
99. Ferrando, R.; Jellinek, J.; Johnston, R. L., Nanoalloys: From theory to applications of alloy clusters and nanoparticles. *Chem Rev* **2008**, *108* (3), 845-910.
100. Dowben, P. A.; Miller, A., *Surface Segregation phenomena*. CRC Press: 1990.
101. Wang, G. F.; Van Hove, M. A.; Ross, P. N.; Baskes, M. I., Quantitative prediction of surface segregation in bimetallic Pt-M alloy nanoparticles (M = Ni, Re, Mo). *Prog Surf Sci* **2005**, *79* (1), 28-45.
102. Ma, Y. G.; Balbuena, P. B., Pt surface segregation in bimetallic Pt₃M alloys: A density functional theory study. *Surface Science* **2008**, *602* (1), 107-113.
103. Mayrhofer, K. J. J.; Juhart, V.; Hartl, K.; Hanzlik, M.; Arenz, M., Adsorbate-Induced Surface Segregation for Core-Shell Nanocatalysts. *Angew Chem Int Edit* **2009**, *48* (19), 3529-3531.
104. Kitchin, J. R.; Norskov, J. K.; Barteau, M. A.; Chen, J. G., Modification of the surface electronic and chemical properties of Pt(111) by subsurface 3d transition metals. *J Chem Phys* **2004**, *120* (21), 10240-10246.
105. Stamenkovic, V. R.; Fowler, B.; Mun, B. S.; Wang, G. F.; Ross, P. N.; Lucas, C. A.; Markovic, N. M., Improved oxygen reduction activity on Pt₃Ni(111) via increased surface site availability. *Science* **2007**, *315* (5811), 493-497.

106. Wang, G. F.; Van Hove, M. A.; Ross, P. N.; Baskes, M. I., Monte Carlo simulations of segregation in Pt-Ni catalyst nanoparticles. *J Chem Phys* **2005**, *122* (2).
107. Ramirez-Caballero, G. E.; Balbuena, P. B., Surface segregation of core atoms in core-shell structures. *Chem Phys Lett* **2008**, *456* (1-3), 64-67.
108. Lovvik, O. M., Surface segregation in palladium based alloys from density-functional calculations. *Surface Science* **2005**, *583* (1), 100-106.
109. Wang, L. L.; Johnson, D. D., Predicted Trends of Core-Shell Preferences for 132 Late Transition-Metal Binary-Alloy Nanoparticles. *Journal of the American Chemical Society* **2009**, *131* (39), 14023-14029.
110. Yu, Y. L.; Xiao, W.; Wang, J. W.; Wang, L. G., Understanding the surface segregation behavior of transition metals on Ni(111): a first-principles study. *Phys Chem Chem Phys* **2016**, *18* (38), 26616-26622.
111. Nilekar, A. U.; Ruban, A. V.; Mavrikakis, M., Surface segregation energies in low-index open surfaces of bimetallic transition metal alloys. *Surface Science* **2009**, *603* (1), 91-96.
112. Ruban, A. V.; Skriver, H. L., Calculated surface segregation in transition metal alloys. *Comp Mater Sci* **1999**, *15* (2), 119-143.
113. Ruban, A. V.; Skriver, H. L.; Norskov, J. K., Surface segregation energies in transition-metal alloys. *Phys Rev B* **1999**, *59* (24), 15990-16000.
114. Zhang, Y. H.; Duan, Z. Y.; Xiao, C.; Wang, G. F., Density functional theory calculation of platinum surface segregation energy in Pt₃Ni (111) surface doped with a third transition metal. *Surface Science* **2011**, *605* (15-16), 1577-1582.
115. Chen, S.; Ferreira, P. J.; Sheng, W. C.; Yabuuchi, N.; Allard, L. F.; Shao-Horn, Y., Enhanced activity for oxygen reduction reaction on "Pt(3)CO" nanoparticles: Direct evidence of percolated and sandwich-segregation structures. *Journal of the American Chemical Society* **2008**, *130* (42), 13818-13819.
116. Guesmi, H.; Louis, C.; Delannoy, L., Chemisorbed atomic oxygen inducing Pd segregation in PdAu(111) alloy: Energetic and electronic DFT analysis. *Chem Phys Lett* **2011**, *503* (1-3), 97-100.
117. Barcaro, G.; Fortunelli, A.; Polak, M.; Rubinovich, L., Patchy Multishell Segregation in Pd-Pt Alloy Nanoparticles. *Nano Lett* **2011**, *11* (4), 1766-1769.
118. Gauthier, Y.; Baudoing, R.; Jupille, J., Metastability of the Segregation-Reversal Composition Profile at the Pt_xNi_{1-x}(110) Surface - a Low-Energy Electron-Diffraction Study. *Phys Rev B* **1989**, *40* (3), 1500-1510.
119. Gauthier, Y.; Baudoing, R.; Lundberg, M.; Rundgren, J., Surface-Sandwich Segregation and Multilayer Relaxation on Pt_{0.5}Ni_{0.5}(110) Measured by Low-Energy Electron-Diffraction - an Observation of Face-Related Segregation Reversal. *Phys Rev B* **1987**, *35* (15), 7867-7878.
120. Luyten, J.; Schurmans, M.; Creemers, C.; Bunnik, B. S.; Kramer, G. J., Surface segregation in Pt₂₅Rh₇₅ alloys studied by Monte Carlo simulations and the modified embedded atom method. *Surface Science* **2007**, *601* (7), 1668-1676.
121. Matveev, A., Physical and mathematical model of the surface segregation in binary alloys of transition metals. *Journal of Surface Investigation. X-ray, Synchrotron and Neutron Techniques* **2013**, *7* (4), 774-783.
122. Rubinovich, L.; Polak, M., Prediction of distinct surface segregation effects due to coordination-dependent bond-energy variations in alloy nanoclusters. *Phys Rev B* **2009**, *80* (4), 045404.
123. Shin, Y. K.; Gai, L. L.; Raman, S.; van Duin, A. C. T., Development of a ReaxFF Reactive Force Field for the Pt-Ni Alloy Catalyst. *J Phys Chem A* **2016**, *120* (41), 8044-8055.
124. Tomanek, D.; Aligia, A. A.; Balseiro, C. A., Calculation of Elastic Strain and Electronic Effects on Surface Segregation. *Phys Rev B* **1985**, *32* (8), 5051-5056.
125. Treglia, G.; Legrand, B., Surface-Sandwich Segregation in Pt-Ni and Ag-Ni Alloys - 2 Different Physical Origins for the Same Phenomenon. *Phys Rev B* **1987**, *35* (9), 4338-4344.
126. Foiles, S. M.; Baskes, M. I.; Daw, M. S., Embedded-Atom-Method Functions for the Fcc Metals Cu, Ag, Au, Ni, Pd, Pt, and Their Alloys. *Phys Rev B* **1986**, *33* (12), 7983-7991.

127. Anderson, R. M.; Zhang, L.; Loussaert, J. A.; Frenkel, A. I.; Henkelman, G.; Crooks, R. M., An Experimental and Theoretical Investigation of the Inversion of Pd@Pt Core@Shell Dendrimer-Encapsulated Nanoparticles. *Acs Nano* **2013**, *7* (10), 9345-9353.
128. Duan, Z. Y.; Wang, G. F., Monte Carlo simulation of surface segregation phenomena in extended and nanoparticle surfaces of Pt-Pd alloys. *J Phys-Condens Mat* **2011**, *23* (47).
129. Hansen, P. L.; Molenbroek, A. M.; Ruban, A. V., Alloy formation and surface segregation in zeolite-supported Pt-Pd bimetallic catalysts. *J Phys Chem B* **1997**, *101* (10), 1861-1868.
130. VandeVondele, J.; Hutter, J., Gaussian basis sets for accurate calculations on molecular systems in gas and condensed phases. *J Chem Phys* **2007**, *127* (11).
131. Perdew, J. P.; Burke, K.; Ernzerhof, M., Generalized gradient approximation made simple. *Phys Rev Lett* **1996**, *77* (18), 3865-3868.
132. Goedecker, S.; Teter, M.; Hutter, J., Separable dual-space Gaussian pseudopotentials. *Phys Rev B* **1996**, *54* (3), 1703-1710.
133. Krack, M., Pseudopotentials for H to Kr optimized for gradient-corrected exchange-correlation functionals. *Theor Chem Acc* **2005**, *114* (1-3), 145-152.
134. Brako, R.; Sokcevic, D.; Lazic, P.; Atodiresei, N., Graphene on the Ir(111) surface: from van der Waals to strong bonding. *New J Phys* **2010**, *12*.
135. Haas, P.; Tran, F.; Blaha, P., Calculation of the lattice constant of solids with semilocal functionals (vol 79, 085104, 2009). *Phys Rev B* **2009**, *79* (20).
136. Feibelman, P. J.; Hammer, B.; Norskov, J. K.; Wagner, F.; Scheffler, M.; Stumpf, R.; Watwe, R.; Dumesic, J., The CO/Pt(111) puzzle. *J Phys Chem B* **2001**, *105* (18), 4018-4025.
137. Boscoboinik, J. A.; Plaisance, C.; Neurock, M.; Tysoc, W. T., Monte Carlo and density functional theory analysis of the distribution of gold and palladium atoms on Au/Pd(111) alloys. *Phys Rev B* **2008**, *77* (4).
138. Ke, X. Z.; Kramer, G. J.; Lovvik, O. M., The influence of electronic structure on hydrogen absorption in palladium alloys. *J Phys-Condens Mat* **2004**, *16* (34), 6267-6277.
139. Lovvik, O. M.; Olsen, R. A., Density functional calculations on hydrogen in palladium-silver alloys. *J Alloy Compd* **2002**, *330*, 332-337.
140. Lovvik, O. M.; Olsen, R. A., Density functional calculations of hydrogen adsorption on palladium-silver alloy surfaces. *J Chem Phys* **2003**, *118* (7), 3268-3276.
141. Sonwane, C. G.; Wilcox, J.; Ma, Y. H., Solubility of hydrogen in PdAg and PdAu binary alloys using density functional theory. *J Phys Chem B* **2006**, *110* (48), 24549-24558.
142. Dieguez, O.; Marzari, N., First-principles characterization of the structure and electronic structure of alpha-S and Rh-S chalcogenides. *Phys Rev B* **2009**, *80* (21).
143. Frechard, F.; van Santen, R. A.; Siokou, A.; Niemantsverdriet, J. W.; Hafner, J., Adsorption of ammonia on the rhodium (111), (100), and stepped (100) surfaces: An ab initio and experimental study. *J Chem Phys* **1999**, *111* (17), 8124-8130.
144. Inderwildi, O. R.; Lebiez, D.; Deutschmann, O.; Warnatz, J., Coverage dependence of oxygen decomposition and surface diffusion on rhodium (111): A DFT study. *J Chem Phys* **2005**, *122* (3).
145. Chelikowsky, J. R., Predictions for Surface Segregation in Intermetallic Alloys. *Surface Science* **1984**, *139* (2-3), L197-L203.
146. Mukherjee, S.; Moran-Lopez, J., Theory of surface segregation in transition-metal alloys. *Surface Science* **1987**, *188* (3), L742-L748.
147. Sutton, A. P., *Electronic structure of materials*. Clarendon Press: 1993.
148. Niessen, A. d.; De Boer, F.; Boom, R.; De Chatel, P.; Mattens, W.; Miedema, A., Model predictions for the enthalpy of formation of transition metal alloys II. *Calphad* **1983**, *7* (1), 51-70.
149. Brejnak, M.; Modrak, P., Electronic theory of surface segregation for dilute transition metal alloys: predictions based on rigid-band-like approach. *Surface Science* **1991**, *247* (2-3), 215-221.
150. Cyrot-Lackmann, F., On the electronic structure of liquid transitional metals. *Advances in Physics* **1967**, *16* (63), 393-400.
151. Friedel, J., Physics of Clean Metal-Surfaces. *Ann Phys-Paris* **1976**, *1* (6), 257-307.

152. Sun, K.; Zhang, M. H.; Wang, L. C., Effects of catalyst surface and hydrogen bond on ethanol dehydrogenation to ethoxy on Cu catalysts. *Chem Phys Lett* **2013**, *585*, 89-94.
153. Abad, A.; Concepcion, P.; Corma, A.; Garcia, H., A collaborative effect between gold and a support induces the selective oxidation of alcohols. *Angew Chem Int Edit* **2005**, *44* (26), 4066-4069.
154. Gong, J. L.; Mullins, C. B., Selective Oxidation of Ethanol to Acetaldehyde on Gold. *Journal of the American Chemical Society* **2008**, *130* (49), 16458-+.
155. Kwon, Y.; Lai, S. C. S.; Rodriguez, P.; Koper, M. T. M., Electrocatalytic Oxidation of Alcohols on Gold in Alkaline Media: Base or Gold Catalysis? *Journal of the American Chemical Society* **2011**, *133* (18), 6914-6917.
156. Tremiliosi-Filho, G.; Gonzalez, E. R.; Motheo, A. J.; Belgsir, E. M.; Leger, J. M.; Lamy, C., Electro-oxidation of ethanol on gold: analysis of the reaction products and mechanism. *J Electroanal Chem* **1998**, *444* (1), 31-39.
157. Wachs, I. E.; Madix, R. J., The oxidation of ethanol on Cu (110) and Ag (110) catalysts. *Applications of Surface Science* **1978**, *1* (3), 303-328.
158. Bergamaski, K.; Gonzalez, E. R.; Nart, F. C., Ethanol oxidation on carbon supported platinum-rhodium bimetallic catalysts. *Electrochim Acta* **2008**, *53* (13), 4396-4406.
159. Shen, S. Y.; Zhao, T. S.; Xu, J. B., Carbon supported PtRh catalysts for ethanol oxidation in alkaline direct ethanol fuel cell. *Int J Hydrogen Energ* **2010**, *35* (23), 12911-12917.
160. Du, W.; Yang, G.; Wong, E.; Deskins, N. A.; Frenkel, A. I.; Su, D.; Teng, X., Platinum-tin oxide core-shell catalysts for efficient electro-oxidation of ethanol. *Journal of the American Chemical Society* **2014**, *136* (31), 10862-10865.
161. Jiang, L.; Colmenares, L.; Jusys, Z.; Sun, G. Q.; Behm, R. J., Ethanol electrooxidation on novel carbon supported Pt/SnO_x/C catalysts with varied Pt : Sn ratio. *Electrochim Acta* **2007**, *53* (2), 377-389.
162. Antolini, E.; Colmati, F.; Gonzalez, E., Ethanol oxidation on carbon supported (PtSn) alloy/SnO₂ and (PtSnPd) alloy/SnO₂ catalysts with a fixed Pt/SnO₂ atomic ratio: effect of the alloy phase characteristics. *Journal of Power Sources* **2009**, *193* (2), 555-561.
163. Jiang, L.; Zhou, Z.; Li, W.; Zhou, W.; Song, S.; Li, H.; Sun, G.; Xin, Q., Effects of treatment in different atmosphere on Pt₃Sn/C electrocatalysts for ethanol electro-oxidation. *Energy & Fuels* **2004**, *18* (3), 866-871.
164. Silva, J.; De Souza, R.; Parreira, L.; Neto, E. T.; Calegari, M.; Santos, M., Ethanol oxidation reactions using SnO₂@ Pt/C as an electrocatalyst. *Applied Catalysis B: Environmental* **2010**, *99* (1-2), 265-271.
165. De Souza, R.; Parreira, L.; Rascio, D.; Silva, J.; Teixeira-Neto, E.; Calegari, M.; Spinace, E.; Neto, A.; Santos, M., Study of ethanol electro-oxidation in acid environment on Pt₃Sn/C anode catalysts prepared by a modified polymeric precursor method under controlled synthesis conditions. *Journal of Power Sources* **2010**, *195* (6), 1589-1593.
166. Godoi, D. R. M. d.; Perez, J.; Villullas, H., Alloys and oxides on carbon-supported Pt-Sn electrocatalysts for ethanol oxidation. *Journal of Power Sources* **2010**, *195* (11), 3394-3401.
167. Silva, J.; Parreira, L.; De Souza, R.; Calegari, M. L.; Spinacé, E.; Neto, A. O.; Santos, M., PtSn/C alloyed and non-alloyed materials: differences in the ethanol electro-oxidation reaction pathways. *Applied Catalysis B: Environmental* **2011**, *110*, 141-147.
168. Zhu, M.; Sun, G.; Yan, S.; Li, H.; Xin, Q., Preparation, structural characterization, and activity for ethanol oxidation of carbon-supported PtSnIn catalyst. *Energy & Fuels* **2008**, *23* (1), 403-407.
169. Vajda, S.; Pellin, M. J.; Greeley, J. P.; Marshall, C. L.; Curtiss, L. A.; Ballentine, G. A.; Elam, J. W.; Catillon-Mucherie, S.; Redfern, P. C.; Mehmood, F., Subnanometre platinum clusters as highly active and selective catalysts for the oxidative dehydrogenation of propane. *Nat Mater* **2009**, *8* (3), 213.
170. Pacchioni, G., Electronic interactions and charge transfers of metal atoms and clusters on oxide surfaces. *Phys Chem Chem Phys* **2013**, *15* (6), 1737-1757.
171. Antolini, E.; Gonzalez, E. R., A simple model to assess the contribution of alloyed and non-alloyed platinum and tin to the ethanol oxidation reaction on Pt-Sn/C catalysts: application to direct ethanol fuel cell performance. *Electrochim Acta* **2010**, *55* (22), 6485-6490.

172. Wei, Z. D.; Guo, H. T.; Tang, Z. Y., Methanol electro-oxidation on platinum and platinum-tin alloy catalysts dispersed on active carbon. *Journal of Power Sources* **1996**, *58* (2), 239-242.
173. Rahimpour, M. R.; Jafari, M.; Iranshahi, D., Progress in catalytic naphtha reforming process: A review. *Applied energy* **2013**, *109*, 79-93.
174. Srinivasan, R.; Davis, B. H., The structure of platinum-tin reforming catalysts. *Platinum Metals Review* **1992**, *36* (3), 151-163.
175. Deng, L.; Miura, H.; Shishido, T.; Hosokawa, S.; Teramura, K.; Tanaka, T., Dehydrogenation of Propane over Silica-Supported Platinum–Tin Catalysts Prepared by Direct Reduction: Effects of Tin/Platinum Ratio and Reduction Temperature. *ChemCatChem* **2014**, *6* (9), 2680-2691.
176. Stagg, S.; Querini, C.; Alvarez, W.; Resasco, D., Isobutane Dehydrogenation on Pt–Sn/SiO₂ Catalysts: Effect of Preparation Variables and Regeneration Treatments. *Journal of Catalysis* **1997**, *168* (1), 75-94.
177. Janssen, M.; Moolhuysen, J., Binary systems of platinum and a second metal as oxidation catalysts for methanol fuel cells. *Electrochim Acta* **1976**, *21* (11), 869-878.
178. Janssen, M.; Moolhuysen, J., Platinum—tin catalysts for methanol fuel cells prepared by a novel immersion technique, by electrocodeposition and by alloying. *Electrochim Acta* **1976**, *21* (11), 861-868.
179. Janssen, M.; Moolhuysen, J., State and action of the tin atoms in platinum-tin catalysts for methanol fuel cells. *Journal of catalysis* **1977**, *46* (3), 289-296.
180. Katayama, A., Electrooxidation of methanol on a platinum-tin oxide catalyst. *The Journal of Physical Chemistry* **1980**, *84* (4), 376-381.
181. Mingyuan, Z.; Gongquan, S.; Huanqiao, L.; Lei, C.; Qin, X., Effect of the Sn (II)/Sn (IV) redox couple on the activity of PtSn/C for ethanol electro-oxidation. *Chinese J Catal* **2008**, *29* (8), 765-770.
182. Zhu, M.; Sun, G.; Xin, Q., Effect of alloying degree in PtSn catalyst on the catalytic behavior for ethanol electro-oxidation. *Electrochim Acta* **2009**, *54* (5), 1511-1518.
183. Assmann, J.; Crihan, D.; Knapp, M.; Lundgren, E.; Löffler, E.; Muhler, M.; Narkhede, V.; Over, H.; Schmid, M.; Seitsonen, A. P.; Varga, P., Understanding the structural deactivation of ruthenium catalysts on an atomic scale under both oxidizing and reducing conditions. *Angew Chem Int Edit* **2005**, *44* (6), 917-920.
184. Castelli, I. E.; Landis, D. D.; Thygesen, K. S.; Dahl, S.; Chorkendorff, I.; Jaramillo, T. F.; Jacobsen, K. W., New cubic perovskites for one- and two-photon water splitting using the computational materials repository. *Energ Environ Sci* **2012**, *5* (10), 9034-9043.
185. Goodenough, J. B.; Manoharan, R.; Paranthaman, M., Surface Protonation and Electrochemical Activity of Oxides in Aqueous-Solution. *Journal of the American Chemical Society* **1990**, *112* (6), 2076-2082.
186. Grenier, J. C.; Wattiaux, A.; Doumerc, J. P.; Dordor, P.; Fournes, L.; Chaminade, J. P.; Pouchard, M., Electrochemical Oxygen Intercalation into Oxide Networks. *J Solid State Chem* **1992**, *96* (1), 20-30.
187. Gustafson, J.; Westerstrom, R.; Resta, A.; Mikkelsen, A.; Andersen, J. N.; Balmes, O.; Torrelles, X.; Schmid, M.; Varga, P.; Hammer, B.; Kresse, G.; Baddeley, C. J.; Lundgren, E., Structure and catalytic reactivity of Rh oxides. *Catal Today* **2009**, *145* (3-4), 227-235.
188. Lundgren, E.; Gustafson, J.; Resta, A.; Weissenrieder, J.; Mikkelsen, A.; Andersen, J. N.; Kohler, L.; Kresse, G.; Klikovits, J.; Biederman, A.; Schmid, M.; Varga, P., The surface oxide as a source of oxygen on Rh(111). *J Electron Spectrosc* **2005**, *144*, 367-372.
189. McCalla, E.; Abakumov, A. M.; Saubanière, M.; Foix, D.; Berg, E. J.; Rouse, G.; Doublet, M.-L.; Gonbeau, D.; Novák, P.; Van Tendeloo, G., Visualization of OO peroxo-like dimers in high-capacity layered oxides for Li-ion batteries. *Science* **2015**, *350* (6267), 1516-1521.
190. Mefford, J. T.; Hardin, W. G.; Dai, S.; Johnston, K. P.; Stevenson, K. J., Anion charge storage through oxygen intercalation in LaMnO₃ perovskite pseudocapacitor electrodes. *Nat Mater* **2014**, *13* (7), 726.
191. Over, H.; Kim, Y. D.; Seitsonen, A. P.; Wendt, S.; Lundgren, E.; Schmid, M.; Varga, P.; Morgante, A.; Ertl, G., Atomic-scale structure and catalytic reactivity of the RuO₂(110) surface. *Science* **2000**, *287* (5457), 1474-1476.

192. Suntivich, J.; Hong, W. T.; Lee, Y.-L.; Rondinelli, J. M.; Yang, W.; Goodenough, J. B.; Dabrowski, B.; Freeland, J. W.; Shao-Horn, Y., Estimating hybridization of transition metal and oxygen states in perovskites from Ok-edge x-ray absorption spectroscopy. *The Journal of Physical Chemistry C* **2014**, *118* (4), 1856-1863.
193. Yang, G. X.; Frenkel, A. I.; Su, D.; Teng, X. W., Enhanced Electrokinetics of C-C Bond Splitting during Ethanol Oxidation by using a Pt/Rh/Sn Catalyst with a Partially Oxidized Pt and Rh Core and a SnO₂ Shell. *Chemcatchem* **2016**, *8* (18), 2876-2880.
194. Kresse, G.; Furthmüller, J., Efficient iterative schemes for ab initio total-energy calculations using a plane-wave basis set. *Phys Rev B* **1996**, *54* (16), 11169.
195. Kresse, G.; Furthmüller, J., Efficiency of ab-initio total energy calculations for metals and semiconductors using a plane-wave basis set. *Comp Mater Sci* **1996**, *6* (1), 15-50.
196. Kresse, G.; Hafner, J., Ab initio molecular dynamics for open-shell transition metals. *Phys Rev B* **1993**, *48* (17), 13115.
197. Kresse, G.; Hafner, J., Ab initio molecular dynamics for liquid metals. *Phys Rev B* **1993**, *47* (1), 558.
198. Kresse, G.; Hafner, J., Ab initio molecular-dynamics simulation of the liquid-metal–amorphous-semiconductor transition in germanium. *Phys Rev B* **1994**, *49* (20), 14251.
199. Molina, L. M.; Rasmussen, M. D.; Hammer, B., Adsorption of O₂ and oxidation of CO at Au nanoparticles supported by TiO₂(110). *J Chem Phys* **2004**, *120* (16), 7673-7680.
200. Scherson, Y. D.; Aboud, S. J.; Wilcox, J.; Cantwell, B. J., Surface Structure and Reactivity of Rhodium Oxide. *J Phys Chem C* **2011**, *115* (22), 11036-11044.
201. Erini, N.; Loukrakpam, R.; Petkov, V.; Baranova, E. A.; Yang, R.; Teschner, D.; Huang, Y.; Brankovic, S. R.; Strasser, P., Ethanol electro-oxidation on ternary platinum–rhodium–tin nanocatalysts: Insights in the atomic 3D structure of the active catalytic phase. *Acs Catal* **2014**, *4* (6), 1859-1867.
202. Green, I. X.; Tang, W.; Neurock, M.; Yates, J. T., Spectroscopic observation of dual catalytic sites during oxidation of CO on a Au/TiO₂ catalyst. *Science* **2011**, *333* (6043), 736-739.
203. Laursen, S.; Linc, S., Geometric and electronic characteristics of active sites on TiO₂-supported Au nano-catalysts: insights from first principles. *Phys Chem Chem Phys* **2009**, *11* (46), 11006-11012.
204. Molina, L. M.; Hammer, B., Active role of oxide support during CO oxidation at Au/MgO. *Phys Rev Lett* **2003**, *90* (20).
205. Song, W.; Hensen, E. J., A computational DFT study of CO oxidation on a Au nanorod supported on CeO₂ (110): on the role of the support termination. *Catalysis Science & Technology* **2013**, *3* (11), 3020-3029.
206. Delpeuch, A. B.; Asset, T.; Chatenet, M.; Cremers, C., Electrooxidation of Ethanol at Room Temperature on Carbon-Supported Pt and Rh-Containing Catalysts: A DEMS Study. *J Electrochem Soc* **2014**, *161* (9), F918-F924.
207. Rao, L.; Jiang, Y. X.; Zhang, B. W.; Cai, Y. R.; Sun, S. G., High activity of cubic PtRh alloys supported on graphene towards ethanol electrooxidation. *Phys Chem Chem Phys* **2014**, *16* (27), 13662-13671.
208. Sheng, T.; Lin, W.-F.; Hardacre, C.; Hu, P., Significance of β -dehydrogenation in ethanol electro-oxidation on platinum doped with Ru, Rh, Pd, Os and Ir. *Phys Chem Chem Phys* **2014**, *16* (26), 13248-13254.
209. Ioroi, T.; Yasuda, K., Platinum-iridium alloys as oxygen reduction electrocatalysts for polymer electrolyte fuel cells. *J Electrochem Soc* **2005**, *152* (10), A1917-A1924.
210. Singh, S. K.; Xu, Q. A., Bimetallic nickel-iridium nanocatalysts for hydrogen generation by decomposition of hydrous hydrazine. *Chem Commun* **2010**, *46* (35), 6545-6547.
211. Chen, W.; Chen, S., Iridium-platinum alloy nanoparticles: Composition-dependent electrocatalytic activity for formic acid oxidation. *J Mater Chem* **2011**, *21* (25), 9169-9178.
212. Dees, M.; Ponc, V., On the influence of sulfur on the platinum/iridium bimetallic catalysts in n-hexane/hydrogen reactions. *Journal of Catalysis* **1989**, *115* (2), 347-355.

213. Miles, M.; Klaus, E.; Gunn, B.; Locker, J.; Serafin, W.; Srinivasan, S., The oxygen evolution reaction on platinum, iridium, ruthenium and their alloys at 80 C in acid solutions. *Electrochim Acta* **1978**, 23 (6), 521-526.
214. Sinfelt, J.; Via, G.; Lytle, F., Structure of bimetallic clusters. Extended x-ray absorption fine structure (EXAFS) studies of Pt–Ir clusters. *The Journal of Chemical Physics* **1982**, 76 (6), 2779-2789.
215. Kuttiyiel, K. A.; Sasaki, K.; Chen, W.-F.; Su, D.; Adzic, R. R., Core–shell, hollow-structured iridium–nickel nitride nanoparticles for the hydrogen evolution reaction. *Journal of Materials Chemistry A* **2014**, 2 (3), 591-594.
216. Nakagawa, K.; Ikenaga, N.; Teng, Y.; Kobayashi, T.; Suzuki, T., Partial oxidation of methane to synthesis gas over iridium–nickel bimetallic catalysts. *Applied Catalysis A: General* **1999**, 180 (1-2), 183-193.
217. Singh, S. K.; Xu, Q., Bimetallic nickel-iridium nanocatalysts for hydrogen generation by decomposition of hydrous hydrazine. *Chem Commun* **2010**, 46 (35), 6545-6547.
218. Kiran, V.; Ravikumar, T.; Kalyanasundaram, N.; Krishnamurthy, S.; Shukla, A.; Sampath, S., Electro-Oxidation of Borohydride on Rhodium, Iridium, and Rhodium–Iridium Bimetallic Nanoparticles with Implications to Direct Borohydride Fuel Cells. *J Electrochem Soc* **2010**, 157 (8), B1201-B1208.
219. Bao, J.; Dou, M.; Liu, H.; Wang, F.; Liu, J.; Li, Z.; Ji, J., Composition-Dependent Electrocatalytic Activity of Palladium–Iridium Binary Alloy Nanoparticles Supported on the Multiwalled Carbon Nanotubes for the Electro-Oxidation of Formic Acid. *ACS applied materials & interfaces* **2015**, 7 (28), 15223-15229.
220. Meitzner, G.; Via, G.; Lytle, F.; Sinfelt, J., Structure of bimetallic clusters. Extended x-ray absorption fine structure (EXAFS) studies of Re–Cu, Ir–Cu, and Pt–Cu clusters. *The Journal of chemical physics* **1985**, 83 (1), 353-360.
221. Olsson, P.; Abrikosov, I. A.; Vitos, L.; Wallenius, J., Ab initio formation energies of Fe–Cr alloys. *Journal of Nuclear Materials* **2003**, 321 (1), 84-90.
222. Lavrentiev, M. Y.; Drautz, R.; Nguyen-Manh, D.; Klaver, T.; Dudarev, S., Monte Carlo study of thermodynamic properties and clustering in the bcc Fe–Cr system. *Phys Rev B* **2007**, 75 (1), 014208.
223. Hu, W.; Zhang, B.; Shu, X.; Huang, B., Calculation of formation enthalpies and phase stability for Ru–Al alloys using an analytic embedded atom model. *Journal of alloys and compounds* **1999**, 287 (1), 159-162.
224. Cieslak, J.; Tobola, J.; Dubiel, S., Formation energy in σ -phase Fe–V alloys. *Journal of Physics and Chemistry of Solids* **2013**, 74 (9), 1303-1307.
225. Lu, Z.; Klein, B.; Zunger, A., Ordering tendencies in Pd–Pt, Rh–Pt, and Ag–Au alloys. *Journal of phase equilibria* **1995**, 16 (1), 36-45.
226. Sluiter, M.; Kawazoe, Y., Prediction of the mixing enthalpy of alloys. *EPL (Europhysics Letters)* **2002**, 57 (4), 526.
227. Taylor, J., Thermodynamic Assessment of Platinum Group Metal Systems. *Platinum Metals Review* **1985**, 29 (2), 74-80.
228. Muller, S., Bulk and surface ordering phenomena in binary metal alloys. *J Phys-Condens Mat* **2003**, 15 (34), R1429-R1500.
229. Sanchez, J., Cluster expansion and the configurational theory of alloys. *Phys Rev B* **2010**, 81 (22), 224202.
230. Yuge, K.; Okawa, R., Cluster expansion approach for modeling strain effects on alloy phase stability. *Intermetallics* **2014**, 44, 60-63.
231. Yuge, K.; Seko, A.; Kuwabara, A.; Oba, F.; Tanaka, I., First-principles study of bulk ordering and surface segregation in Pt–Rh binary alloys. *Phys Rev B* **2006**, 74 (17).
232. Garbulsky, G.; Ceder, G., Linear-programming method for obtaining effective cluster interactions in alloys from total-energy calculations: Application to the fcc Pd–V system. *Phys Rev B* **1995**, 51 (1), 67.
233. Walker, R.; Darby, J., Thermodynamic properties of solid nickel-platinum alloys. *Acta Metallurgica* **1970**, 18 (12), 1261-1266.

234. Blum, V.; Hart, G. L.; Walorski, M. J.; Zunger, A., Using genetic algorithms to map first-principles results to model Hamiltonians: Application to the generalized Ising model for alloys. *Phys Rev B* **2005**, *72* (16), 165113.
235. Yuge, K.; Saito, R.; Kawai, J., Formalism to model stacking fault effects on surface phase stability in alloys. *Phys Rev B* **2013**, *87* (2), 024105.
236. Monkhorst, H. J.; Pack, J. D., Special points for Brillouin-zone integrations. *Phys Rev B* **1976**, *13* (12), 5188.
237. Yuge, K., GCVC manual. © Copyright 2013, K. Yuge. Last updated on Nov 18, 2014. Created using Sphinx 1.2b2., 2014.
238. Tanaka, R.; Takeuchi, K.; Yuge, K., Application of grid increment cluster expansion to modeling potential energy surface of cu-based alloys. *Materials Transactions* **2015**, *56* (7), 1077-1080.
239. Yuge, K., Modeling configurational energetics on multiple lattices through extended cluster expansion. *Phys Rev B* **2012**, *85* (14), 144105.
240. Müller, S., Bulk and surface ordering phenomena in binary metal alloys. *Journal of Physics: Condensed Matter* **2003**, *15* (34), R1429.
241. Massalski, T.; Okamoto, H.; Subramanian, P.; Kacprzak, L., Binary Alloys Phase Diagrams (ASM International, Materials Park, Ohio, 1990). *Vol. II* **2001**.
242. Kwon, S.; Ham, D. J.; Lee, S. G., Enhanced H₂ dissociative phenomena of Pt–Ir electrocatalysts for PEMFCs: an integrated experimental and theoretical study. *RSC Advances* **2015**, *5* (68), 54941-54946.
243. Tayal, J.; Rawat, B.; Basu, S., Bi-metallic and tri-metallic Pt–Sn/C, Pt–Ir/C, Pt–Ir–Sn/C catalysts for electro-oxidation of ethanol in direct ethanol fuel cell. *Int J Hydrogen Energ* **2011**, *36* (22), 14884-14897.
244. Kolb, B.; Muller, S.; Botts, D. B.; Hart, G. L. W., Ordering tendencies in the binary alloys of Rh, Pd, Ir, and Pt: Density functional calculations. *Phys Rev B* **2006**, *74* (14).
245. Hart, G. L.; Curtarolo, S.; Massalski, T. B.; Levy, O., Comprehensive search for new phases and compounds in binary alloy systems based on platinum-group metals, using a computational first-principles approach. *Physical Review X* **2013**, *3* (4), 041035.
246. Miedema, A.; De Boer, F.; Boom, R., Model predictions for the enthalpy of formation of transition metal alloys. *Calphad* **1977**, *1* (4), 341-359.
247. Linares, J. J.; Zignani, S. C.; Rocha, T. A.; Gonzalez, E. R., Ethanol oxidation on a high temperature PBI-based DEFC using Pt/C, PtRu/C and Pt₃Sn/C as catalysts. *J Appl Electrochem* **2013**, *43* (2), 147-158.
248. Lobato, J.; Canizares, P.; Rodrigo, M. A.; Linares, J. J., Study of different bimetallic anodic catalysts supported on carbon for a high temperature polybenzimidazole-based direct ethanol fuel cell. *Appl Catal B-Environ* **2009**, *91* (1-2), 269-274.
249. Wang, M. Y.; Chen, J. H.; Fan, Z.; Tang, H.; Deng, G. H.; He, D. L.; Kuang, Y. F., Ethanol electro-oxidation with Pt and Pt-Ru catalysts supported on carbon nanotubes. *Carbon* **2004**, *42* (15), 3257-3260.
250. Zhang, F.-Z.; Xue, H.-T.; Tang, F.-L.; Li, X.-K.; Lu, W.-J.; Feng, Y.-D., Phase equilibrium of Cd_{1-x}Zn_xS alloys studied by first-principles calculations and Monte Carlo simulations. *Chinese Physics B* **2015**, *25* (1), 013103.
251. Gyenge, E.; Atwan, M.; Northwood, D., Electrocatalysis of borohydride oxidation on colloidal Pt and Pt-alloys (Pt- Ir, Pt-Ni, and Pt-Au) and application for direct borohydride fuel cell anodes. *J Electrochem Soc* **2006**, *153* (1), A150-A158.
252. Xu, Z.; Kitchin, J. R., Relationships between the surface electronic and chemical properties of doped 4d and 5d late transition metal dioxides. *The Journal of chemical physics* **2015**, *142* (10), 104703.
253. Michaelides, A.; Scheffler, M., An introduction to the theory of metal surfaces. *Textbook of Surface and Interface Science* **2010**, *1*.